SPH STUDIES OF COMPLEX FLUID FLOW IN PIPES AND STIRRED VESSELS

By

XUE LIAN

A thesis submitted to
the University of Birmingham
for the degree of
DOCTOR OF PHILOSOPHY

School of Chemical Engineering
College of Engineering and Physical Sciences
University of Birmingham
April 2025

ABSTRACT

Fluid dynamics is extremely vital in the 21^{st} century and to develop it, both experimental and numerical studies are necessary. Complex flows in industrial devices present many challenges, especially from a modeling point of view. Research is needed to improve the understanding and prediction of the flow behavior of solid-liquid flow systems and to investigate novel numerical modeling to guide the design of flows in different geometries. This thesis focuses primarily on numerical modeling and includes three main research areas. First, the Smooth Particle Hydrodynamics (SPH) method, coupled with the Discrete Element Method (DEM), was employed to study the influence of various parameters, including particle size, shape and density, pipe Reynolds number, and carrier fluid rheology on the Lagrangian migration trajectories of solid particles. Second, a coupled SPH-DEM model was developed to predict and obtain the velocity and solid concentration distributions of the particle-laden flows in the pipes, as well as information on flow field details, such as particle angular velocities, slip velocities, and vorticity of the liquid. Finally, the SPH method was applied to simulate Newtonian and non-Newtonian fluid flows in mechanically agitated stirred vessels with different impellers and Reynolds numbers. The velocity fields provided by SPH agree well with the Positron Emission Particle Tracking (PEPT) experimental data.

The investigation focuses on the inertial migration of a individual solid particle within a horizontal pipe flow, encompassing a broad range of tube Reynolds numbers spanning 350 to 3500. To model the flow dynamics, a coupled approach employing SPH in conjunction with the DEM is employed. Initially, the study focused on the behavior of single-phase flows comprising both Newtonian and non-Newtonian fluids, with a keen emphasis on validating the SPH-DEM predicted equilibrium

radial position of a single particle. This validation process involves experimental validation utilizing a pipe flow loop configuration equipped with digital imaging technique. Subsequently, the validated SPH-DEM methodology is utilized to explore the impact of various parameters, including particle size, particle density, pipe Reynolds number, carrier fluid rheology, and particle shape, on the equilibrium radial position of a solitary particle within the flow. The insights garnered from this comprehensive investigation are expected to offer valuable contributions to the understanding and characterization of particle-laden flows across a diverse array of engineering applications.

A Lagrangian–Lagrangian particle-based SPH–DEM numerical approach was applied to simulate the horizontal laminar pipe flow of coarse particle–liquid food suspensions. SPH–DEM was able to predict the single-phase flow of various non-Newtonian fluid rheologies including the carrier fluid used to convey food particles with a high degree of accuracy, as validated by analytical solutions of radial velocity profiles. The particle–liquid flow simulations were also successfully validated using experimental measurements obtained by a technique of PEPT. The radial particle velocity profiles, radial solid phase distributions, as well as particle passage time distributions were accurately predicted at solid loadings varying from 10 to 40vol.%. Radial particle velocity profiles are asymmetric, with the maximum being located above the centerline. Such asymmetry disappears at high solid concentrations, and the maximum moves to the center. Simulations yielded detailed information on the local dynamics of the two-phase flows investigated, including translational as well as rotational particle slip velocities, flow pressure field, and fluid vorticity. While local translational particle slip velocities, as expected for nearly neutrally buoyant particles, were vanishingly small, particle angular (slip) velocities were significant. Spin is positive (anticlockwise) in the top half of the pipe cross section and negative (clockwise) in the bottom half. Particle spin is fastest closest to the wall where liquid velocity gradients are highest, reducing to zero at the center of the pipe before switching direction. As the solid load increases, close to the particle packing fraction, the particles pack so densely that their motion (e.g., rotation or spin) is limited. Spin becomes negligible except near the walls. The capability of the SPH-DEM methodology was also successfully validated in non-Newtonian single-phase as well as in two-phase particle-liquid flows by

comparing the local phase velocity flow field, radial particle distribution and particle passage times in three-dimensional (3D) simulations. The simulations also yielded accurate predictions of flow pressure drop. In addition, detailed information was afforded on local particle spin, fluid pressure and carrier fluid vorticity. The results demonstrate the high capability of the proposed numerical framework to predict the complex features of complex particle-liquid flows in pipes.

As is known, the mixing characteristics of non-Newtonian fluids in a mixing vessel are quite different from Newtonian fluids mixing flows due to the special relationship between viscosity and shear rate. The pseudo cavern and cavern are, respectively, the classic mixing features of shear-thinning fluids and viscous fluids. The accuracy of the SPH model in simulating different mixing features of non-Newtonian fluids within stirred vessels was validated through comparisons with experimental data obtained from particle image velocimetry (PIV), PEPT, and planar laser-induced fluorescence (PLIF) measurements. Flow fields generated by the mixing of Newtonian and non-Newtonian fluids in single-phase flows with different Reynolds numbers in transitional and laminar flow regimes are well predicted by the SPH model. Detailed 3D distributions of liquid-phase velocities can be captured using the SPH model. However, due to the complex flow mechanisms and shortcomings of SPH model, SPH modelling at high Reynolds numbers, especially turbulent flows, is still a great challenge for SPH at present.

ACKNOWLEDGMENTS

This thesis marks as the end of a long journey that I could never forget in my whole life. First, I would like to express my gratitude to my supervisor Prof. Mostafa Barigou for his valuable guidance during my Ph.D. research. It has been an absolute pleasure working with him, and I have gained a lot of knowledge from his meticulous approach to research.

I would like to thank Dr. Chiya Savari, Dr. Kun Li, and Dr. Zhuangjian Yang for their kind introduction and advice on experimental and numerical work. Dr. Chiya and Kun have been instrumental in assisting me throughout my thesis journey, particularly in writing, modeling, and data analysis. Their invaluable support and guidance have significantly contributed to the development and refinement of my research. I would also like to thank the staff from IT service especially Simon Hartley, for his help in installing and running DualSPHysics on BlueBEAR. I would also like to express my appreciation to China Scholarship Council (CSC) and Department of Chemical Engineering, University of Birmingham, for the significant contribution in funding this work.

At the end, to my parents and grandparents who give me life and the opportunity to achieve happiness. To my husband Ning Zhang, who complete my soul, without his support and encouragement I could not have achieved so much. This thesis is dedicated to my daughter, Leyi (Chloe) Zhang, and I hope my sweetheart grows up to be a happy, brave, and independent woman.

Ride waves amid great transformations, neither merriment nor terror interferes.

In managing great affairs, one should not be pleased too early nor lose heart too soon.

Yuanming Tao

Contents

List of Figures

List of Tables

Chapter One

INTRODUCTION

1.1 Scope of the research

The scope of this research is to explore the phenomenon of solid particle motion in complex, non-Newtonian flows, with a focus on flows in horizontal pipes, and three-dimensional (3D) mixing flows of non-Newtonian fluids in mechanically stirred vessels. This work was part of the wider aim to develop and enhance the capabilities of particle-based meshfree method, Smoothed Particle Hydrodynamics (SPH), for predicting the velocity and solid concentration distribution in both pipe and stirred vessel. The research is conducted as a part of the EPSRC Programme (Grant No. EP/R045046/1): "Probing Multiscale Complex Multiphase Flows with Positrons for Engineering and Biomedical Applications," led by Professor Mostafa Barigou at the University of Birmingham.

1.2 Motivation

The solid-liquid flow is a complex and widespread subject, and solid-liquid system usually is ubiquitous in industry and physiological processes, such as food, power, chemical industry, nuclear

power, refrigeration, mining, petroleum, metallurgy, and so on. A critical challenge for modern engineering is to model the complex multi-scale particle-liquid flows that are the foundation of so many industrial and physiological processes. Despite such a wide range of applications, industrial practice and processes and clinical practice are neither efficient nor satisfactory due to a limited understanding of the nature of the complex, multi-scale interactions within these systems. These flows may involve viscous with non-Newtonian rheological properties. In addition, the particles present in these industrial processes vary widely in size, shape, density, and surface characteristics, further complicating the flow dynamics. The capability to analyze and predict multi-scale particle-liquid flows with reliability will bring significant economic, scientific, and societal benefits. At present, our basic understanding is limited by the enormous practical difficulties in imaging such flows, measuring their local properties, and design hybrid numerical models to predict the flow details.

The solid-liquid flow and single-phase flow in pipe and stirred vessel are the canonical cases representing these varied applications. However, the solid-liquid flow prediction of the liquid velocity profile is quite different from single-phase flow in the pipe and stirred vessel, the addition of a solid phase to the flow system can cause dramatic changes in the flow structure and mechanism. The flow characteristics of solid-liquid suspensions are affected by factors such as liquid viscosity, particle shape, size, concentration, and flow velocity. Pipe transport of food materials is also a common operation in food manufacturing. For example, continuous in-line processing of particulate foods relies on the conveying of particle-liquid mixtures through pipes. Typically, the challenge in a heat-hold-cool process is to ensure a safe and uniform level of sterility whilst preventing over-processing. Often, in such processes, the food particles are coarse solids (up to 20 mm), their loading is high, and the carrier fluid is viscous. Basic understanding of these flow details and local properties has been limited to date due to the challenging nature of measuring and imaging them. Mixtures of practical within flows are often concentrated and opaque, making optical flow visualization very difficult. The inherent opacity of solid-liquid flows limits the

application of advanced laser-optical measurement techniques such as Laser Doppler Velocimetry (LDV) and Particle Image Velocimetry (PIV), especially when the flow is not dilute, which imposes a significant challenge for imaging solid-liquid flows (Fang et al., 2021; Leary et al., 2017; Riis et al., 2020). Positron emission particle tracking (PEPT) is able to visualize concentrated opaque particle-liquid flows by providing the long-term three-dimensional (3D) trajectories of both solid and liquid phases, and is also non-invasive (Fairhurst et al., 2001; Nadeem et al., 2018). The flow components are tracked in space and time utilizing tiny radiolabeled tracers in PEPT with an accuracy comparable to that of LDV and PIV (Guida et al., 2010; Pianko-Oprch et al., 2009). PEPT has been used to study both single-phase and complex multiphase flows, and the data provided have been successfully used to guide, drive and validate various numerical modeling approaches (Li et al., 2023a; Moreira et al., 2020; Savari et al., 2022; Pellico et al., 2024). The technique is, however, very expensive to run and not widely available, which makes any available data very rare and precious. Thus, advanced numerical modeling strategies need to be developed to reduce the reliance on experimental work in this challenging field.

Moreover, following the rapid development of numerical techniques and computing power, various numerical modelling techniques, especially grid-based models, have been successfully applied to simulate single-phase flows in pipelines and stirred vessels. However, the problem is even further complicated when introducing coarse solid particles into the flow systems with different geometries. It is challenging to simulate complex multiphase flows using a single modeling technique with various assumptions, so in solid-liquid flow studies, a coupled approach of different modeling techniques is more beneficial to obtain detailed information about the flow field, such as the angular velocity of rotation of the particles, the slip velocity, the force analysis of the particles, and the vorticity of the liquid. In particular, the simplifying assumption that modeling the large size of solid particles implies a homogeneous mixture for fine particle suspensions is clearly not suitable, and thus the mixture cannot be modeled as a single phase (Meyers, 1992).

Solid-liquid mixture flows have been extensively studied in the scientific literature, with a fo-

cus on experimental and grid-based approaches. The literature mainly investigates macroscopic flow properties through conventional experimental techniques and grid-based computational fluid dynamics (CFD). However, experimental methods often face limitations due to high costs, time constraints, and the challenge of capturing detailed particle-fluid interactions on smaller scales. Experimental techniques also typically require specialized equipment and are limited by measurement accessibility, especially in high solids loadings or opaque mixtures with limited visibility. Similarly, grid-based CFD methods, although highly developed, still have difficulties in modeling complex interfaces and high particle concentrations. These methods rely on a fixed grid structure, which can lead to numerical dispersion and loss of accuracy when capturing sharp interfaces and complex flow structures such as those found in multiphase flows. In addition, grid-based methods are computationally intensive, especially when modeling suspensions of dense particles, as they require significant refinement to resolve interactions on smaller scales. These limitations highlight the need for alternative modeling approaches, such as particle-based methods, to overcome the challenges inherent in traditional experimental and CFD techniques for accurately simulating solid-liquid flows.

The Smoothed Particle Hydrodynamics (SPH) method, which is one of the most commonly used particle-based methods for modeling incompressible viscous flows, provides an alternative framework. In the SPH method, the Navier-Stokes equations are discretized into a set of particles, each particle carrying the physical properties of a fluid. By using a smoothing kernel function, this method provides an interpolating framework that allows the particles to interact smoothly, thus creating an adaptable system. The SPH has a clear advantage in terms of robustness: it is based on a variational framework, which, as demonstrated in previous studies, ensures the conservation of key physical quantities. In addition, the Lagrangian formulation is capable of accurately advecting fluid properties and facilitates the implicit description of interfaces such as free surfaces. This formulation also simplifies coupling with the discrete element method (DEM), which is essential for accurately modeling particle-fluid interactions, especially in dense and complex suspended flows.

Given these advantages, the further development and application of the SPH method, especially when coupled with DEM, is expected to solve significant challenges in the modeling of non-Newtonian fluids and high particle loading flow fields, where traditional CFD methods often suffer from great limitations. This study is essential for optimizing industrial processes involving these mixtures, improving the design and operational strategies of equipment such as pipelines and mixing vessels, and improving our overall understanding of multiphase flow systems. Therefore, this research aims to develop a hybrid particle-based model to investigate the multi-phase flows in both pipes and stirred vessels. In addition, the mesh-free numerical models are validated using a substantial set of rare experimental data from Positron Emission Particle Tracking (PEPT). The validated model can then be applied to study and gain insights into complex particle-liquid flows under various conditions.

1.3 Objectives

The main aim of this study is to broaden the applicability of Smoothed Particle Hydrodynamics method to problems involving multi-scale fluid dynamics, especially focusing on the particle-liquid pipe flows and mixing flows. The objectives of this research are as follows:

• Gain insights into the performance and limitations of the SPH method for simulating non-Newtonian pipe flows and mixing flows using the open-source code DualSPHysics.

• Apply the SPH model to predict pipe flow behavior for Newtonian and non-Newtonian fluids over a range of Reynolds numbers.

• Couple the SPH method with the DEM to accurately simulate solid-liquid systems under high solids loading conditions. The coupled SPH-DEM method aims to expand the application of SPH in environments where traditional modeling methods encounter limitations and solve key problems

in the simulation of dense suspensions.

• Investigate the effects of particle size, shape, density, and flow Reynolds number on the radial migration dynamics of inertial particles in viscous flows using SPH-DEM modeling.

• Improve SPH modeling capabilities to accurately simulate the behavior of non-Newtonian fluids in stirred vessels with different impeller configurations and rheological properties.

1.4 Thesis layout and publications

The structure and contents of this thesis are outlined as follows:

Chapter 2 presents an extensive review of the current literature focusing on experimental techniques and numerical applied to fluid dynamics in pipes and stirred vessels, covering both single-phase and multi-phase flow situations. Lagrangian approach are introduced to study and analyse complex flow systems, and visualization techniques as well as numerical simulation methods are reviewed.

Chapter 3 mainly focuses on Smoothed Particle Hydrodynamics (SPH) approach, in which a detailed review of the literature on SPH methods used to model different flow phenomena is presented. Then, the SPH basic formulation is listed in detail and the rheological modeling in the SPH framework is introduced. The details and framework of SPH-DEM coupling method is presented here. Finally, the post-processing of SPH raw data is given.

Chapter 4 reports an investigation of SPH approach to modelling Newtonian and non-Newtonian fluids in pipe flows. The fluids used are of the power-law, Bingham plastic, and Herschel-Bulkley types to assess the rheology model in SPH. The non-Newtonian pipe flow simulations are in laminar regime. The affection of different rheological parameters in pipe flows are discussed.

Chapter 5 reports on a detailed numerical study of the complex dynamics of inertial particle radial migration in viscous flow. In this chapter, extensive theoretical and experimental validations were conducted for particle-liquid flow. The SPH-DEM model is then used to study the role of various parameters, including particle size, shape, density, pipe Reynolds number and carrier fluid rheology on the Lagrangian migration trajectories of particles and, in particular, their final equilibrium radial position in the flow.

In Chapter 6, a novel SPH-DEM model is applied to model the flow of nearly neutrally buoyant alginate particles within non-Newtonian carrier fluid in horizontal pipe. The SPH-DEM model is validated by using experimental data and empirical and semi-empirical correlations from the literature. This chapter also introduces the SPH-DEM simulation set-up in both 2D and 3D simulations. The model is then utilized to perform a parametric study of the effects of particle size and solid loading on the solid and fluid phase velocity profile, particle concentration profile.

In Chapter 7, the accuracy of the SPH model in simulating different mixing features of non-Newtonian fluids within stirred vessels was validated through comparisons with experimental data obtained from PIV, PEPT, and PLIF measurements. Detailed 3D distributions of liquid-phase velocities can be captured using the SPH model.

Chapter 8 summarizes the major conclusions of this work and proposes recommendations for further work.

This research has led to the following journal publications:

[1] Lian, X., Savari, C., Li, K., Barigou, M., 2023. Coupled smoothed particle hydrodynamics and discrete element method for simulating coarse food particles in a non-Newtonian conveying fluid. Physics of Fluids 35(4).

[2] Yang Z J., Lian X., Savari C., Barigou, M., 2024. Evaluating the effectiveness of CFD-DEM and SPH-DEM for complex pipe flow simulations with and without particles[J]. Chemical Engi-

neering Science: 119788.

[3] Lian X., Savari C., Barigou, M., 2024. Effects of particle size, particle density, particle shape and Reynolds number on equilibrium position in a horizontal pipe: A SPH-DEM simulation study. (To be submitted).

[4] Lian, X., Savari, C., Barigou, M., 2025. Application of the Lagrangian meshfree approach to modelling viscoplastic fluid in stirred vessels (In draft).

Chapter Two

LITERATURE REVIEW

2.1 Introduction

This thesis primarily focuses on exploring solid-liquid pipe flows and mixing flows using meshless particle-based methods, investigating their behaviors under various conditions. In this chapter, a comprehensive literature review of each area is conducted to provide the necessary background information to identify existing research gaps. Fluid mixing and solid-liquid flows represent fundamental phenomena encountered across diverse industries, including chemicals, biochemicals, polymers, crystallization, minerals, food, and pharmaceuticals. The efficient operation and control of these processes are crucial for optimizing product quality, enhancing production efficiency, and ensuring operational safety (Paul et al., 2004; Wright et al., 2017). Thus, a deep understanding of the fundamentals of fluid mixing and solid-liquid interactions is fundamental to designing, operating, and enhancing industrial processes.

In the chemical and biochemical industries, fluid mixing plays a central role in promoting chemical reactions, improving mass and heat transfer, and ensuring product homogeneity. Whether mixing components to a uniform mixture or dispersing reactants in a reactor vessel, effective fluid mixing has a direct impact on reaction kinetics and product yields. Similarly, in polymerization processes,

achieving the desired molecular weight distribution and polymer morphology is highly dependent on controlled mixing conditions. The pharmaceutical and food industries face unique challenges in handling solid-liquid mixture flows, where the processing of particulate materials in carrier flow demands precise control to maintain product integrity and consistency. From pharmaceutical tablet coating to food particle suspension, understanding the dynamics of solid-liquid interactions is crucial for ensuring product quality, stability, and shelf-life. Moreover, in mineral processing and crystallization, the effective suspension and transport of solid particles in liquid streams are vital for achieving desired product specifications and minimizing process inefficiencies.

In-depth studying the fluid dynamics of solid-liquid food flows is thus crucial for an efficient design of food processing operations. Assessing the complex fluid dynamics phenomena of multiphase systems remains challenging, particularly when the system is opaque. As mentioned in Chapter 1, some experimental approaches are capable of capturing flow with high solid fraction. However, experiments can provide accurate velocity and solid concentration field distributions, these experimental approaches cannot provide details of particle interactions, as well as study the influencing factors of slight changes in local velocity fields. With the advent of supercomputers and the rapid development of CFD, it has become possible to investigate the details of solid-liquid flow. The CFD results of single-phase pipe flow can be verified by the theoretical analytical solution and experimental data. However, due to the lack of accurate analytical solutions, the solid-liquid pipe flow is mostly verified by the experimental results. At the same time, validated CFD models can also provide effective suggestions for the design of experiments and pipe transportation in industries. Therefore, an advanced CFD tool should be carefully selected in this work.

For mixing flows in stirred vessels, this work focused on applying SPH to model flow behaviours in a baffled tank. As illustrated in Figure 2.1, a typical configuration of a baffled tank which consists of a centrally-located shaft, an impeller (shown as a pitched blade turbine), and four baffles. Baffled tanks offer several advantages over unbaffled tanks, particularly in industrial processes where efficient fluid mixing is essential. Baffles disrupt the flow pattern within the tank, and enhancing

mixing efficiency. This leads to more uniform distribution of components, improved mass and heat transfer rates, and reduced mixing time. In processes where thorough blending or reaction kinetics are critical, baffled tanks offer superior performance compared to unbaffled tanks. Baffles help to inhibit the formation of vortices in tanks, which can occur in tanks without baffles under certain flow conditions. Vortices can carry air or foreign particles into the process fluid, leading to contamination or inefficient mixing. By disrupting vortex formation, baffled tanks ensure a cleaner, more controlled mixing process. Unbaffled tanks are often used for high-viscosity fluid mixing, where vertexing is rare. Close-clearance impellers like helical-ribbon, helical screw, or anchor types, occupying 85 to 95% of the tank diameter, are commonly employed for efficient mixing while minimizing vortex formation (Paul et al., 2004). The mixing of fluids in a mixing vessel under the rotation of a rotating impeller produces various flow patterns. The rheological properties of the fluid and the configuration of the mixing tank have a great influence on these flow patterns.

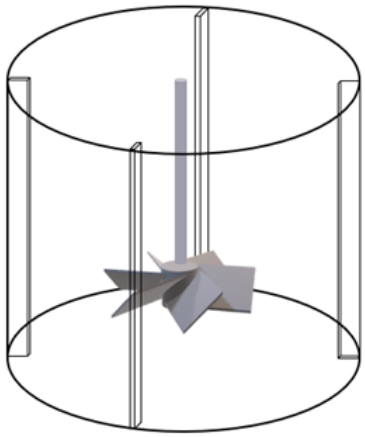

Figure 2.1: Configuration of a mechanically agitated vessel

This chapter begins a review of theoretical studies of fluid rheology and flow mechanics in pipe and stirred vessel, followed by a critical analysis of experimental and numerical approaches used to investigate mixing flows and pipe flows in different aspects.

In view of the broad applicability of fluid mixing and solid-liquid food flow across multiple indus-

tries, research efforts have been directed towards deepening our understanding of these phenomena and developing innovative strategies for process optimization. Considering the broad applicability of mixing and solid-liquid food flows across many industries, research efforts have been dedicated to improving understanding of these phenomena and advancing practical applications. By using advanced experimental techniques and computational modeling to explore the details of solid-liquid and mixing flows.

2.2 Fluid rheology

The flow rheology characteristics are critical in both physical and chemical processing, since they can significantly govern both in-process efficiency and final product quality in many industries (Chhabra et al., 2011). For example, in food, polymer, catalyst, oil and mining exhibit non-Newtonian rheological properties, like plasticity, elasticity, yields stress, and thixotropy. The more obvious the non-Newtonian behaviour of the carrier fluid, the more complex the hydrodynamic behaviour in solid-liquid multi-phase flows. This study primarily focuses on time-independent fluid behavior. Based on the relationship between shear stress and shear rate, fluids are classified into four types: pseudoplastic, viscoplastic, dilatant, and Bingham plastic.

Since most of the industrial complex fluids are non-Newtonian, the development of accurate and simple in-line rheometers becomes very important. Wall slip, thixotropy, shear-induced phase migration, and shear bands can occur during the industrial processing of most complex fluids (Chhabra et al., 2011; Kalyon et al., 2014). Complex interpretation via conventional rheology measurements is often demanding and complex. In a study conducted by Machin et al. (2018), the inline electrical resistance rheometer technique is successfully applied to obtain the rheological information of a range of fluids, based on electrical resistance sensing. Once an accurate velocity distribution of the flow in the pipeline and stirred vessels is obtained, choosing the appropriate

rheology model in the simulation will improve the accuracy of the simulation study.

Fluid rheology models reflect the relationship between fluid viscosity and shear rate. Research (Kelessidis et al., 2006) was carried out to investigate the effects of the rheological parameters of the fluid on the radial velocity distribution and the pressure drop through the annulus are significant in pipe flows. Their study showed that the rheology models play an important role in the pressure loss estimation, especially for the non-Newtonian pipe flow. Researchers also investigated the variations in the values of all rheological parameters (i.e. consistency index (k), power law index (n) and fluid yield stress (τ_y)) on stirred vessels (Patel et al., 2015). Based on the relationship between the fluid viscosity and shear rate, non-Newtonian fluids have been generally classified into four groups, i.e. shear-thinning, shear-thickening, Bingham and viscoplastic fluids (Irgens, 2014). The shapes of curves of shear stress as a function of shear rate for these cases are presented in Figure 2.2. The flow behaviours of different models, ie, Newtonian (a), Shear-thinning or pseudoplastic (b, e.g., ice, blood, paint), Shear-thickening or dilatant (c, e.g. wet sand, wet starch), Bingham (d, e.g., toothpaste, margarine), viscoplastic (e). The shear-thinning and viscoplastic fluids are mainly considered in this thesis, and their rheological characteristics are discussed in more detail as follows.

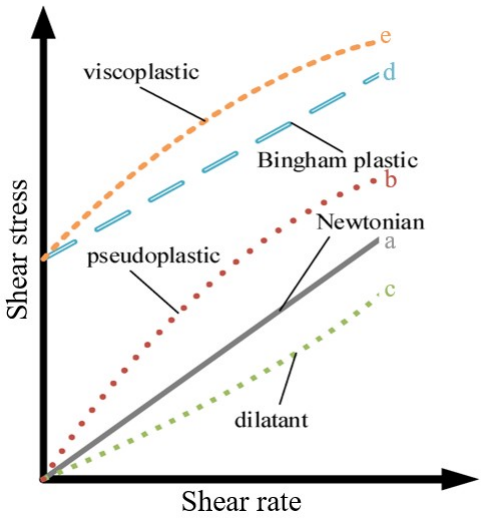

Figure 2.2: Shear stress as a function of shear rate

2.2.1 Shear-thinning fluids

Shear-thinning fluids, usually called pseudoplastic fluids, in which the viscosity decreases with increasing shear rate, are a common and important class of non-Newtonian fluids used in chemical production. Various constitutive laws can be employed to describe the rheological properties of shear-thinning fluids. Power-law fluids can exhibit either shear-thinning or shear-thickening behavior, depending on the value of the flow behavior index. When the flow behavior index is less than 1, the fluid exhibits shear-thinning behavior, which is the most commonly studied case:

$$\tau = k\dot{\gamma}^n \tag{2.1}$$

where τ represents the shear stress, $\dot{\gamma}$ refers to the shear rate, k and n are the fluid consistency coefficient and flow behavior index, respectively.

The viscosity of shear-thinning fluids plays a pivotal role in both pipe flow and agitated vessel mixing. Shear-thinning fluids, characterized by a viscosity that decreases with increasing shear rate, exhibit unique flow behaviors that significantly impact industrial operations. In both pipe flow and agitated vessel applications, understanding the rheological properties of shear-thinning fluids is essential for optimizing process performance, product quality, and energy efficiency. The viscosity of shear-thinning fluids decreases noticeably near the impeller due to the high shear rate, and is relatively high in the low shear regions away from the impeller. Therefore, the fluid mixing is constrained in the region around the impeller, termed a pseudo-cavern. The fluid has been found to be generally well mixed within the pseudo-cavern, while beyond it the shear-thinning fluids move with very small velocity ($\ll 1\% u_{\text{tip}}$) (Adams et al., 2007). One of the earliest experimental methods involves flow visualization techniques such as particle image velocimetry (PIV) (Guida et al., 2010a; Li et al., 2011) and laser-induced fluorescence (LIF) (Barigou, 2009; Busciglio et al., 2014). These methods are able to provide qualitative insights into flow patterns and

mixing efficiency. Ultrasonic Doppler Velocimetry (UDV) enables the measurement of flow velocity profiles in stirred vessels with high spatial and temporal resolution. It has been utilized to study non-Newtonian fluid flows, providing insights into velocity gradients, shear rates, and flow homogeneity (Bouillard et al., 2001). Additionally, Positron Emission Particle Tracking (PEPT) has been utilized as a non-intrusive Lagrangian flow visualization technique to obtain complete 3D velocity and concentration fields of both continuous and dispersed phases in opaque mixing equipment (Guida et al., 2011; Barigou et al., 2009).

Similarly, in pipe flow, the viscosity of shear-thinning fluids influences the velocity profile and pressure drop along the pipe length, affecting pumping power requirements and overall system efficiency. The non-uniform velocity distribution and viscosity gradient can affect flow stability, leading to phenomena such as flow instabilities, vortex shedding, or transition to turbulence. Transportation of shear-thinning non-Newtonian fluids and slurries through pipelines is common in a variety of practical applications in the process industries (Pinho et al., 1990). In the case of fluids with significant yield stresses or high effective viscosities, laminar flow phenomena may occur at flow rates associated with industrial operations. Understanding these flow characteristics is crucial for maintaining flow stability and control the performance of pipe transportation.

2.2.2 Viscoplastic fluids

Viscoplastic fluids are a type of non–Newtonian fluid that exhibit yield stress, which constitute a very important class of non-Newtonian fluids. The modeling of viscoplastic fluids is of crucial importance in industrial applications, since a large variety of materials (e.g. foams, pastes, slurries, oils, ceramics, etc.) exhibit the fundamental character of viscoplasticity. Apparent yield stress is an important characteristic of viscoplastic fluids, also known as yield stress fluids (Balmforth et al., 2014). As a result, the external force must overcome the apparent yield stress required for a viscoplastic fluid to flow, otherwise it behaves like a solid. The rheological behavior of viscoplastic

fluids is typically characterized as:

$$\tau = \tau_y + k\dot{\gamma}^n \tag{2.2}$$

where τ_y is the yield stress, k and n are the fluid consistency coefficient and the flow behaviour index, respectively. When the value of n is equal to 1, Eq. 2.2 is called Bingham fluid model, and is called Herschel-Bulkley model when n value less than 1. Both Bingham fluids and Herschel-Bulkley fluid are investigated in this thesis for rheology model validation and applications.

The mixing characteristics of viscous fluids are typical of shear-thinning fluids, where fluid mixing is mainly restricted to the area around the impeller area. As distinguished from shear-thinning fluids, for viscoplastic fluids, there is a fixed boundary due to the apparent yield stress, and there is no fluid motion beyond the cavern boundary (Adams et al., 2007; Adams et al., 2009). The term 'cavern' was originally created by Wichterle and Wein in 1975 to characterize the flow region around an impeller (Wichterle et al., 1975). The formation materials of cavern around the impeller is a distinctive feature of viscoplastic fluid mixing.

The formation of cavern negatively affects the mixing efficiency and scholars have been trying to measure the cavern size in order to eliminate the dead zone outside the cavern. The size and configuration of the cavern can be defined through various theoretical models, with the cylindrical model (Elson et al., 1986), spherical model (Solomon et al., 1981) and toroidal model (Amanullah et al., 1998) are the three most commonly used models. The cavern size and shape described by these three classical models have also been widely used as a tool to validate the numerical and experimental works in literature (Adams et al., 2007; Amanullah et al., 1998).

Similar to viscoplastic fluids in mixing flows, viscoplastic fluids as carrier fluids also exhibit different velocity profiles in pipe flows than Newtonian fluids. The response of viscoelastic fluids to applied stresses varies with time and is characterized by phenomena such as stress relaxation

and creep. This time-varying behavior is a result of the fluid's ability to store and dissipate energy over time, which can lead to complex flow dynamics in pipe flow. Viscoelastic fluids exhibit shear thinning or shear thickening behavior, i.e., the viscosity of the fluid decreases or increases with increasing shear rate. Such non-Newtonian behavior complicates the flow pattern and affects the stability and efficiency of pipeline flow. For single phase flow, the velocity distribution are described by different theoretical models, velocity profiles calculated from these models were used as validation for numerical works. When a second phase is introduced in a viscous non-Newtonian pipe flow, the velocity distribution changes due to the details of the distribution of the second term. The change in the velocity distribution can have a direct and significant effect on the transport characteristics of the system (King, 2002; Ruiz-Viera et al., 2006).

2.2.3 Solid-liquid suspensions

Our work mainly focus on solid-liquid flow in pipe flow. Particles in fluids are ubiquitous in both natural and industrial processes. For example, suspensions of blood, fluidized beds, detergents, pipeline transfers, paints, fiber-reinforced polymers, sewage sludges and drilling muds contain particles (hard particles, droplets or bubbles). Flowing behavior and rheological properties of these suspensions are determined by parameters of particle shape, size and concentration, particle-particle interactions, particle surface properties, fluid rheology and type of flow.

The solid-liquid flow in a pipe is the canonical case representing these varied applications. However, the prediction of the liquid velocity profile is different from single-phase flow in the pipe, the addition of a solid or gas phase to the flow system can cause dramatic changes in the flow structure. The flow characteristics of solid-liquid suspensions in pipes are affected by factors such as liquid viscosity, particle shape, size, concentration, and flow velocity. Depending on the density of solid particles, the solid particles may settle at the pipe bottom or float on the liquid surface. A major issue and point of continuing confusion in solid-liquid flows is the shortage of proper equations

and supporting assumptions that fit both solid and liquid phases (Meyers, 1992). Historically, fluid mechanics has been developing along three different paths of experiments, theoretical analysis, and numerical methods. When particles are added to the flow system, the system becomes more complex. It is a great challenge to reveal the real mechanism of fluid-solid coupling. Especially when the solid volume fractions are up to 40-60%, the flow system is opaque, detailed experimental studies on multi-phase pipe flow are extraordinarily difficult. Opaque systems require the use of different tracing principles such as particle image velocimetry (PIV), electrical resistivity tomography (ERT), and also the positron emission particle tracking (PEPT) methodology (Nadeem et al., 2018).

Intensive study of the fluid dynamics of food solid-liquid flow is therefore essential for the effective design of food processing operations (Lareo et al., 1997). Assessing the complex fluid dynamics phenomena of multiphase systems remains challenging, particularly when the system is opaque. PEPT is a flow measurement technique, which is based on the tracking of radiolabelled flow tracers (Parker, 2017). PEPT, a noninvasive method provides information on particle or fluid element trajectories, velocity fields, residence time distributions, flow mechanisms in different regions of the mixer geometry and on mixing quality by analyzing the auto-correlation of particle movement. Although PEPT is able to provide satisfactory and reliable results, it also has several shortcomings like high device costs. Therefore, a simple measurement method needs to be developed for solid-liquid two-phase flows pertaining to transportation.

Nowadays, with the rapid development of large-scale electronic computers, Computational Fluid Dynamics (CFD) has also been rapidly developed, and it has been regarded as a powerful method to simulate detailed flow characteristics. There are two main approaches to model the liquid phase in CFD for carrying fluids: particle-based and mesh/grid -based approaches. Usually, liquid flow is simulated by the locally averaged Navier–Stokes equations in the grid-based method. Based on conventional finite element (Deb et al., 2014) and finite volume method (Chen et al., 2011)), the traditional CFD can solve with the locally averaged Navier–Stokes equations. In the particle-

based method, both lattice Boltzmann method (LBM) and the smoothed particle hydrodynamics (SPH) are potential and maturity. They consider the fluid phase as a series of particles, and they are easier to couple with Discrete Element Method (DEM), which is a powerful and common numerical metho proposed by Cundall in 1979 to model the solid particles in engineering systems (Cundall et al., 1979). The coupling between SPH and DEM has obvious benefits in appropriately handle the interaction between the carried flow and solid particles. The SPH-DEM model has many advantages in simulating flow details, such as the rotational angular velocity of particles and a large number of particle trajectories.

2.3 Flow mechanism

Whether laminar or turbulent flow, it is very important to distinguish if the flow in the pipeline is fully developed, and many researchers in the past have proposed a series of studies on the hydrodynamic development length of laminar flow, and summarised in a review work (Durst et al., 2005). Usually, the research on the requirement of steady flow development length is carried out theoretically or experimentally. As pointed out by Durst et al. (2005), the nonlinear convection term is involved in the momentum equation, so theoretical studies cannot provide a correct solution. In most theoretical studies, these terms are either ignored or linearized by greatly simplified assumptions. On the other hand, experimental studies also failed to produce satisfactory results with sufficient precision due to the limitations of the adopted test setup. At the same time, most measurement methods produce huge inaccuracies in determining developmental length, due to the asymptotic nature of physical phenomena. Therefore, it may be concluded that only CFD simulations can provide more accurate results for the development through pipes and channels, ultimately determining the axial length required for fully developed flow. For pipe flows, their correlation for development length has been reported by Durst et al. (2005),

$$\frac{L}{D} = \left[(0.619)^{1.6} + (0.0567\,Re)^{1.6}\right]^{1/1.6} \tag{2.3}$$

where L is the required development length, D is the pipe diameter and Re is the Reynolds number based on the diameter of the pipe. Reynolds number of pipe flow is defined as follows:

$$Re = \frac{\rho_L \overline{u} D}{\mu_L} \tag{2.4}$$

where ρ_L and μ_L are the density and viscosity of the liquid phase, respectively. The local velocities and solid phase distributions in a horizontal pipe are not only influenced by the fluid rheology mentioned above but also significantly influenced by the pressure drop. Reynolds number (Re),flow rate, size, density and shape of solid particles. Different particle size distributions and sizes of solid particles can significantly impact the interaction between the solid particles and the carrier fluid. When the particles sizes are in range of 70 and 200 μm, it is easier to interact with the eddies of the carrier fluid, keeping them dispersed, in which case the contact between particles can be ignored (Messa et al., 2014). Interactions through particle collisions or more permanent contact interactions mainly exist with coarser solid particle in pipe flow, which usually shows a stratified phenomenon (Bartosik, 2020; Uzi et al., 2018). The degree of stratification of the coarse particle-liquid pipe flow is related to the type of particle-to-particle collision, the solids concentration in the mixture, and the flow rate, which both affect the stratification behaviour.

For nano-particles (Talebizadehsardari et al., 2020), Brownian diffusion plays the most important role in deposition mechanism. The solid phase concentration and density of the solid particles all have effects on the radial distribution of the solid phase concentration in the pipe flow. The solid concentration distribution profiles of neutrally buoyant Particles often present parabolic curve in a pipeline (McKetta, 2022). However, for the heavy particles whose particle density is greater than the carrier fluids, the solid concentration distribution shows an obvious non-pair obvious

asymmetry feature (Zheng et al., 2021). In this thesis, the diameter of the solid particles ranges from 2 to 10 mm, thus particle collisions should be carefully considered in the CFD model. This particle size range was chosen because it belongs to the category of coarse particles, which are often encountered in industrial processes such as fluidized beds, sediment transport, and mixing processes. Coarse particles are characterized by significant inertial effects, so particle-fluid and particle-particle interactions are critical to understand the system dynamics. In addition, this range enables research to focus on practical situations while ensuring that models are computationally efficient and consistent with experimental data for validation purposes.

2.4 Experimental approach

Investigation of flow dynamics with complex conditions are challenging by experimental approach. Both invasive and non-invasive techniques are applied to measure the flow parameters. The study of flow dynamics under complex conditions using only experimental methods is difficult on complex fluid systems. This is mainly due to the inherent complexity of accurately capturing and analysing the finer differences in fluid behavior under various conditions. As a result, researchers typically employ invasive or non-invasive techniques to comprehensively measure and understand various flow parameters. These techniques include a variety of experimental methods, each of which offers unique advantages and provides insight into the fluid dynamics. By using both invasive and non-invasive methods, researchers have gained an understanding of complex flow phenomena and have played a significant role in the development and validation of numerical models.

To study industrial pipe transportation, high design, and requirements of probes for invasive methods are important. Multi-hole pressure probes often applied to measure mean velocity components and the local pressure field in three-dimensional solid-liquid flows (Bryer et al., 1971; Musgrove et al., 1993). Shepherd firstly used cobra probe to measure the flow rate of pipe flows (Shepherd,

1981). Based on work of Hooper et al. (1997) and Musgrove et al. (1993), they improved the cobra probe to investigate turbulent structures. Comparing with normal full scale flow meters, electromagnetic flow velocity probes (Baker et al., 2002) show the advantages of more accurate measurement results in pipe flow rate.

When the invasive method is impossible to use or creates unacceptable risks, the non-invasive method is a better choice. Invasive methods can accurately achieve single-point measurement in pipe flow and obtain the temperature, flow rate and pressure drop. Therefore, it is almost impossible to study the fluid hydrodynamic details of solid-liquid pipeline flow map by invasive methods. And the probe of invasive methods in pipe flow can create a disturbance, which resulting measurement errors. It is hard to avoid these errors, despite great effort in the design of the probes. At the experimental level, the velocity field, flow structure and solid phase concentration distribution of solid-liquid two-phase flow are mainly studied through non-invasive method.

In industrial pipe transportation, invasive methods sometimes create uncontrollable risks, so it is safer and more accurate to use non-invasive methods in such cases (Gebhardt et al., 2018; Liptak, 2003). Due to the errors associated with the flow disturbance caused by the probes, non-intrusive measuring techniques are preferred over intrusive methods. Non-invasive methods can be installed outside the pipe without interfering with local flow, do not need to cut the pipe, and keep the system in a completely sealed state. Non-invasive velocity measurement is safe, convenient, superior flexible in practice and operates without interfering with local flow (Eesa et al., 2008; Xu et al., 2019). Currently non-invasive methods are mainly based on ultrasonic and electromagnetic techniques. These techniques, however, are expensive and complex in calibrating. Ultrasonic techniques and Electromagnetic techniques have been applied to study phase fraction and phase velocity measurements (Suzuki et al., 2000; Thorn et al., 2012; Hossein et al., 2024). In the last two decades, non-intrusive techniques rapidly developed, such as Particle Image Velocimetry (PIV), particle tracking velocimetry (PTV), Laser Doppler Velocimetry (LDV), electrical resistivity tomography (ERT), and the positron emission particle tracking (PEPT).

Experimental techniques for multiphase pipe flows based on LDV can also be found in literature (Hosokawa et al., 2013; Wang et al., 2019), LDV can accurately realize the single-point measurement in pipe flow (Xu et al., 2019). LDV is commonly used to investigate multiphase behavior in industrial-scale measurement applications, providing precise, non-intrusive velocity measurements of fluid and particle motion (Yan et al., 2024). However, PIV has ability to capture the transient state of the flow field (Xu et al., 2017), thus obtain other physical parameters of the flow field. Since the solid fraction reaches 40-60% v/v, solid-liquid pipe flow is usually opaque, most optical methods have serious limitations in measuring opaque solid-liquid flow and high-concentration solid-liquid flow. Although some researchers combined PIV with UDV, in which flow field images were extracted using PIV and the flow velocity was measured by UDV (Fang et al., 2021; Leary et al., 2017; Riis et al., 2020). For opaque systems, it is better to apply different tracking principles to investigate flow mechanics, such as ERT, PTV, and PEPT used in this thesis.

PEPT, A tracer is labelled with a positron-emitting radioisotope, and the position of the tracer is reconstructed by examining a collection of coincident gamma rays associated with the annihilation of the emitted positrons with nearby electrons. In the work of Fairhurst et al. (2001), they used PEPT to study almost spherical coarse alginate particles in a 45 mm internal diameter pipe positioned either vertically or horizontally. PEPT tracks a tracer particle radiolabelled with a positron-emitting radionuclide 18F in the field of view of a PET scanner. The solid delivery concentration is in the range of 20 to 40% v/v, with mean mixture velocities of 20 to 125 mm/s. The asymmetry of the horizontal velocity profiles was found to depend strongly on the solid concentration and the particle Reynolds number in the work of Fairhurst. 3D-PTV was applied to investigate the particle and the carrier phase turbulence for 0.4 mm ceramic beads and water in a downward channel flow at Re = 7500 in work of Suzuki et al. (2000). Recently, Romano et al. (2023) conducted a comparison between Reynolds-Averaged Navier-Stokes simulations and 3D-PTV measurements for Newtonian and non-Newtonian fluid flows in a stirred vessel operating in the transitional regime.

The contribution of experimental methods to the study of the flow mechanism of pipe flow and

mixing flow is enormous. However, it is difficult to give satisfactory results for flow studies with extremely strict experimental conditions. For example, an experimental investigation of buoyant solid particles dispersion in pipe flow was conducted using a pulsed ultrasonic Doppler velocimeter (Le Guer et al., 2003), the solid phase concentration radial distribution did not follow parabolic shape as discussed in CFD study (Puri et al., 1983). Combining experiment and CFD methods will make solid-liquid pipe flow studies faster and more accurate. CFD results can be validated by experimental data, and the validated CFD models can simulate more cases without much cost.

2.4.1 Invasive method

Invasive methods in fluid dynamics typically rely on a variety of techniques designed to directly probe and interact with the fluids. Examples of intrusive techniques include hot-wire anemometers and intrusive flow probes. Each of these invasive methods requires the physical insertion of a probe, sensor, or instrument into the flow field to directly measure parameters such as velocity, pressure, and turbulence characteristics (Silva, 2022). Although these intrusive methods may disturb the flow field to some extent, they provide accurate local measurements and are valuable tools for providing complex fluid conditions, such as temperature, pointed-velocity, and pressure.

In the field of process pipe systems, the precise measurement and monitoring of fluid parameters such as temperature, pressure, and velocity are often common and important. While immersion sensors represent a highly accurate and responsive solution for capturing changes in these parameters, they do come at the cost of being highly invasive. This intrusiveness can come into direct contact with the process fluids in the pipeline, raising concerns about increased maintenance costs and potential downtime. In addition, the intrusive nature of these sensors complicates adding or repositioning sensing locations, further exacerbating operational challenges. Capturing transient velocity flow fields using intrusive methods is nearly impossible to achieve. This is particularly obvious in the case of heat transfer analyses of pipes and mixed flows where accurate capture of

the velocity field is required.

2.4.2 Non-invasive method

Laser Doppler Velocimetry

Laser Doppler Velocimetry (LDV) has emerged as a powerful tool for studying fluid flow dynamics in pipe flows. In the mid-1960s, Yeh and Cummins (1964) were the first to demonstrate the feasibility of measuring fluid velocity using LDV in the USA. LDV is a laser-based technique for measuring flow velocity based on the Doppler shift of tracer particles which scatter laser light as they flow through a gaseous or liquid medium and an optical technique that allows the measurement of localized velocities in transparent systems (Drain, 1980). LDV is capable of accurately measuring the velocity profile of pipeline flow, providing insight into the flow behavior near the wall, core, and boundary layer. The theoretical mechanism of the LDV technique to estimate the velocity of the measurement region is based on the Doppler shift, which is directly proportional to the velocity of the scattering particle (Brown et al., 2003).

Molki et al. (2013) showed that the LDV is effective in capturing velocity gradients at different Reynolds numbers in laminar regime, which can help to accurately obtain the velocity profile. LDV has also played an important role in the study of transition and turbulent flows in piping systems (Molki et al., 2013). Researchers applied LDV to analyse the volume-cycled oscillatory flow of a Newtonian viscous fluid in a straight circular tube within turbulent regime (Eckmann et al., 1991). In addition, LDV measurements also serve as essential validation tools for numerical models and computational simulations of pipe flow. But it is hard to obtain the velocity in opaque systems (Yan et al., 2024). LDV relies on dispersed particles or tracers in the flow to measure velocity. Variations in particle density or size distribution can affect the accuracy and consistency of the measurement, especially in dilute or inhomogeneous flows. LDV is a powerful tool for fluid

flow measurements but comes with some limitations. It requires clear optical access, which makes it unsuitable for opaque or dense fluids where light scattering or absorption occurs. The method also relies on tracer particles that must accurately follow the flow, and improper seeding can lead to erroneous results.

Particle image velocimetry

Over the past three decades, the Particle Image Velocimeter (PIV) has become a standard tool in fluid dynamics experiments. PIV can be characterized as an imaging-based flow diagnostic technique that relies on seeding a fluid flow with tiny tracer particles and discovering the motion associated with the tracer particles to deduct the fluid velocity. Its main feature is the ability to measure the instantaneous velocity field at multiple points simultaneously, typically on the order of 103-105, with a spatial resolution sufficient to calculate instantaneous fluid vorticity and strain rates. To date, PIV is one of the few experimental methods that can provide such information in rapidly developing flows. The typical workflow of PIV experiment (Buchhave, 1992) is shown in Figure 2.3. The experimental setup of the PIV technique usually consists of a laser emitting sheet and a camera for recording the displacement of the flows within different geometries, such as pipe and stirred vessels (Jahanmiri, 2011).

The development of slug flow along a horizontal pipe was quantitatively investigated through particle image velocimetry (Xu et al., 2020). The application of PIV to boundary layer flows has also received a great deal of attention, provides accurate experimental measurements at low wave numbers (Atkinson et al., 2011; Coudert et al., 2011). Significant amount of information on the single-phase flow field in stirred vessels has been obtained through PIV measurements (Chung et al., 2009, Li et al., 2011). Some researchers have also utilized PIV to measure multiphase flows, and since the fluid transparency requirements of this technique are limited to very dilute systems (Aubin et al., 2004; Zade et al., 2018). Despite the outstanding contribution of PIV for velocity

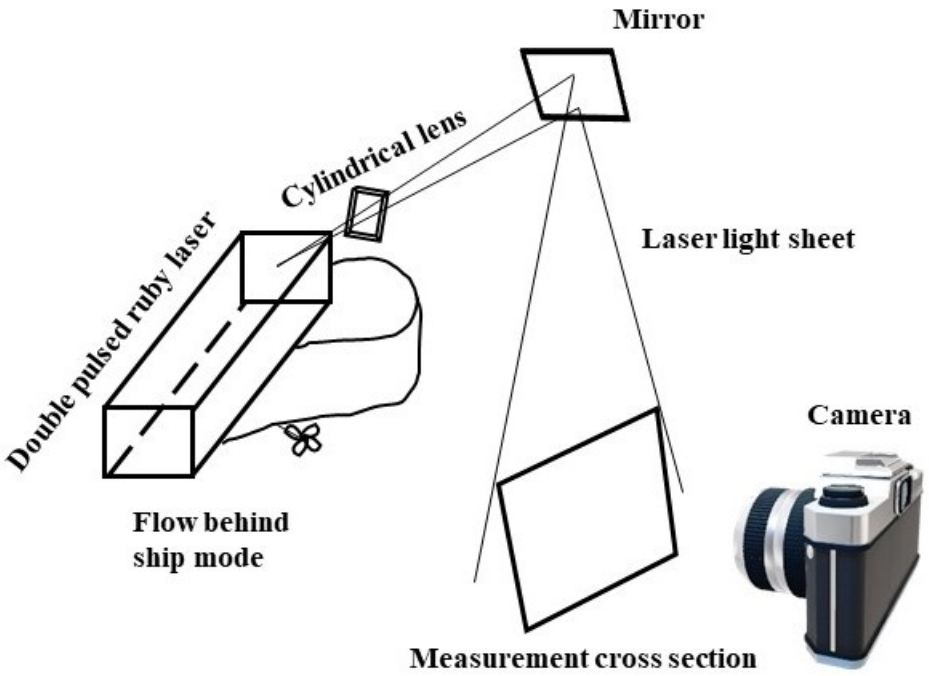

Figure 2.3: Typical workflow of PIV experiment

flow field obtaining, the measurements are performed in a sheet field of irradiation and therefore detailed and three-dimensional (3D) flow information are challenging (Sozzi et al., 2005). PIV provides detailed velocity measurements in various flow studies, but it also faces notable limitations. PIV usually requires optical transparency, making it impractical to conduct experiments in opaque or highly scattering media (Wang et al., 2023). PIV also relies on tracer particles that must accurately follow the flow such as LDV. Complex three-dimensional or high-speed flows may demand specialized configurations (e.g., stereoscopic or time-resolved PIV), which significantly increases the complexity and cost of the setup.

Positron emission particle tracking

PEPT is a non-invasive imaging technique, which is applied to track the movement of tiny particles within different type of complex fluid flow, providing a 3D long-term Lagrangian trajectory with

time and space information (Barigou, 2004). PEPT is particularly useful for studying complex fluid flows in various applications such as chemical engineering, environmental engineering, and biomedical research. PEPT has a comparable accuracy with the leading optical techniques (e.g. PIV, LDV), but has advantages to image opaque fluids and inside opaque equipment (Pianko-Oprych et al., 2009). Currently PEPT is successfully applied to study flow and mixing in pipes and vessels (Guida et al., 2010a; Li et al., 2023a; Lian et al., 2023; Yang et al., 2022).

Mixing by nature is a Lagrangian process, and although Eulerian methods such as LDV and PIV are very useful and have contributed significantly to the investigation of multiphase hydrodynamics through the point-determination of the velocity field, a Lagrangian study method is necessary for its complete characterization. In addition, localized measurements in suspensions are not easy to carry out by LDV or PIV. Both LDV or PIV method, tiny tracer particles ($\sim$10 μm) are selected to track the liquid movement, and these techniques cannot be operated with large/coarse particle sizes or high solid concentrations. The details set-up and data collecting process are illustrated in the following sections in this thesis.

The schematic of PEPT experimental set-up is shown in Figure 2.4(a). PEPT consists of two face-to-face gamma ray detectors, between which the flow domain of interest. The tracer is labelled with a positron-emitting nuclide, and two back-to-back 511 keV γ-rays are emitted once a positron annihilates with an electron. In order to capture gamma rays from positron annihilation, a commonly used radioisotope is fluorine-18 (18F), which emits positrons as shown in Figure 2.4(b).

As mentioned above, the quality of data collection is highly related to the radiolabelled tracer, due to the PEPT technique relying on the emission of collinear photons from the same annihilation. The requirements for PEPT tracers can be summarized as follows:

1. **Radioactive Properties**: PEPT tracers must be radioactive to emit positrons, which can be detected by the imaging system. Commonly used radioactive isotopes for PEPT include

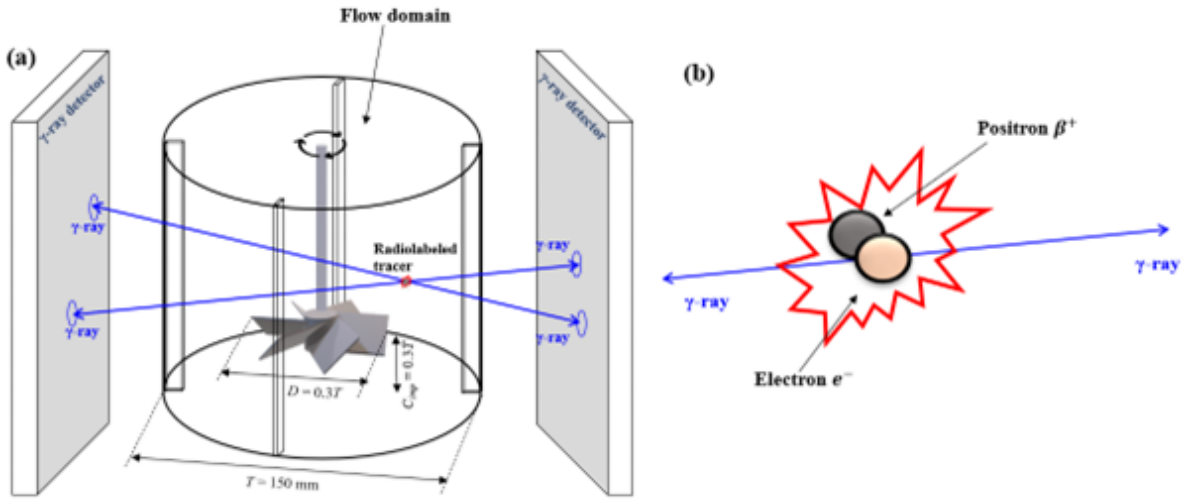

Figure 2.4: The schematic of (a) PEPT experimental set-up and (b) positron and electron annihilation

fluorine -18 (^{18}F) and carbon-11 (^{11}C).

2. **Stability**: Tracers should have a sufficiently long half-life to allow for extended tracking periods without significant decay. This ensures that the tracer remains active throughout the experiment.

3. **Chemical Compatibility**: Tracers should be chemically compatible with the fluid or material being tracked to prevent unwanted interactions or reactions that could alter their behavior or properties.

4. **Physical Properties**: Ideally, the tracer must be fully identical to the system under investigation or be able to characterize the main properties of the system.

In mixing processes and suspension flows, where there is not significant heat transfer, the main factors affecting the quality of the raw experimental data include particle density and size, and controlled levels of radioactivity (Parker, 2017). Ideally, the density of the radioactive tracer should be

the same as that of the tracked fluid or solid particles. Until now, preparing the neutrally buoyant tracers for tracking phase information has been challenging. As a solution to this problem, PEPT raw data can be used to validate CFD results, then using validated CFD models to simulate neutrally buoyant cases. The raw data of PEPT is three Cartesian coordinates (x, y, z) at corresponding times. There are two ways to post-process the PEPT raw data:

1. **Lagrangian-Eulerian Analysis**: This method extracts local Eulerian quantities, such as the three velocity components of the tracking phase, local phase occupancy, and time-averaged concentration, from the pure Lagrangian information contained in the tracer trajectory.

2. **Lagrangian Statistical Analysis**: This method uses the concepts of residence time, circulation time, and trajectory length distributions to perform statistical analysis on the tracer trajectories.

These approaches ensure comprehensive analysis and interpretation of the PEPT data, enhancing the understanding of complex fluid dynamics in various systems. Although PEPT is a rare and valuable technique for tracking particle motion in fluid experiments, it requires specialized equipment, including positron-emitting tracer particles, which can be expensive and difficult to prepare. The size of the tracer particles must closely match the fluid flow characteristics, and deviations can lead to inaccurate measurements. The technique also involves radiation and therefore must comply with strict safety protocols and regulations. These limitations, along with the need for accurate calibration and the limited accessibility of facilities, can restrict its widespread use in fluid mechanics research.

Electrical resistance tomography

Electrical resistance tomography (ERT) is a non-invasive imaging technique used to reconstruct the internal conductivity distribution of an object or medium. The theory behind ERT is that different

materials have different electrical conductivities, which can be exploited to create contrasts in the image. This method is capable of extracting flow information when imaging in two neighboring planes of the pipe. With various advantages such as high speed, low cost, no radiation hazard and non-invasiveness, ERT has emerged as a promising technology for monitoring various existing industrial streams, providing both conductivity images and measurement of flow parameters such as velocity distribution and flow pattern identification (Lucas et al., 1999).

Over twenty years ago, ERT was successfully applied to measure two-phase flow of non-conductive solids and conductive liquids in vertical and inclined pipelines (Loh et al., 1999; Lucas et al., 1999). The accuracy of the velocity profile information generated by the ERT has been validated in the literature through comparisons with other techniques, such as fiber optic probes, PEPT and magnetic resonance imaging (Edwards et al., 2009; Razzak et al., 2010; Stevenson et al., 2010). Key benefits of ERT applications also include non-invasive 3D visual insight into opaque systems and fluids to detect anomalies and faults. ERT also can provide qualitative and quantitative flow information in the opaque systems (Sharifi et al., 2012). ERT has several limitations that impact its effectiveness and applicability in imaging conductivity distributions. One major drawback is its poor spatial resolution, making it less suitable for detecting fine-scale structures. Even small measurement errors or noise can result in significant inaccuracies in the reconstructed images. Additionally, ERT has limited depth penetration and non-uniform sensitivity, with higher sensitivity near the electrodes and lower accuracy in deeper regions. The technique is highly dependent on the configuration, quality and number of electrodes, and improper placement can lead to incomplete reconstructions.

Planar laser-induced fluorescence

Planar Laser Induced Fluorescence (PLIF) is a non-invasive technique for measuring the concentration of a standard volume in a fluid flow. As far back as the 19^{th} century, the use of soluble dyes for water flow visualisation first came to light when Osbourne Reynolds famously experimented

with laminar and turbulent flows in circular pipes (Reynolds, 1883). Over the next century, significant advancements were made in the field of flow visualization, culminating in the development of laser-induced fluorescence (LIF) technology. This technology marked a transition from qualitative to quantitative research in fluid flow analysis. LIF involves the use of fluorescent dyes that are excited by a laser, emitting light at different wavelengths. The intensity of this emitted light is proportional to the concentration of the dye, allowing for precise measurements of fluid concentration. The most common application of LIF in fluid flows is two-dimensional PLIF, which provides a detailed two-dimensional map of the concentration field within a fluid flow, enabling researchers to study complex flow phenomena with high spatial resolution (Crimaldi, 2008). This technique is widely used in various fields, including aerodynamics, combustion, and environmental science, to investigate flow structures, mixing processes, and chemical reactions. For example, PLIF can accurately capture the size and shape of cavities in non-Newtonian fluid flows. Understanding the detailed structure and dynamics of a fluid region is critical in a variety of applications (Adams et al., 2007).

PLIF is mainly used in fluid dynamics to visualize and quantify scalar fields such as concentration or temperature. However, its application comes with limitations. PLIF requires the use of a tracer dye that fluoresces under laser excitation, which may alter the fluid properties if not carefully chosen. The method is sensitive to laser sheet alignment and intensity variations, which can introduce errors in measurements. PLIF is also limited to optically transparent or semi-transparent flows, as light scattering and absorption in opaque or dense fluids can compromise the technique.

Electrical capacitance tomography

Electrical capacitance tomography (ECT) is used to visualize and monitor the distribution of dielectric materials within a given domain, typically a closed vessel or pipe. It works by measuring the capacitance values between pairs of electrodes placed around the periphery of the domain

and using these measurements to reconstruct an image of the material's permittivity distribution (Zhang et al., 2014). Both ECT and ERT generate images, providing cross-sectional distribution information that can yield a real-time picture of the flow, concentration and liquid holdup in two-phase flows. Recent research has demonstrated the potential feasibility of combining ECT with Microwave cavity resonance (MCR) to measure liquid holdup and identify flow patterns in both oil-continuous and water-continuous systems. For slug flow patterns, which exhibit relatively higher liquid holdup due to the liquid phase occupying a larger fraction of the pipe volume, various correlations have been developed to predict the liquid holdup under such conditions (Almutairi et al., 2020).

ECT is an efficient, real-time imaging method suitable for industrial applications, particularly when dealing with non-conductive materials. However, due to its spatial resolution and sensitivity limitations, there is a need for continuous hardware and algorithm improvements to enhance its capabilities. Key issues for the application of ECT in fluidized beds, mixing and pipe flows are discussed in a review, including sensor design and data analysis (Wang et al., 2020).

2.5 Numerical approach

CFD deals mainly with conversation equations such as mass and momentum to describe physical phenomena mathematically. In the past two decades, with the rapid development of computer performance, CFD has gradually developed different computational numerical methods for complex flows. Building on past theoretical and experimental studies in fluid dynamics, different numerical methods have been validated and further developed. Numerical approaches play a crucial part in the investigation of pipe flow and mixing phenomena, providing an in-depth view of fluid dynamics, transport processes, and mixing performance. In this section, two types of numerical methods are examined: mesh-based methods and particle-based methods, focusing on the application to

pipe and mixing flows. Mesh-based methods are widely utilized in the numerical simulation of pipe flow and mixing phenomena, offering accurate solutions to the governing equations of fluid dynamics. This literature review examines the applications of mesh-based methods in pipe flow and mixing, focusing on their versatility, reliability, and computational efficiency.

The complexity of the numerical methods often depends on the nature of the numerical method employed as well as other factors such as discretisation technology, mesh size and properties, and the boundary conditions applied. In investigating complex solid-liquid two-phase and mixing flows, the choice of numerical model could seriously affect the reliability of the results of numerical performance assessment. Typically, two important numerical complicating factors in CFD simulations are numerical diffusion (or pseudo-diffusion) and numerical dispersion effects. Numerical diffusion is introduced by discretization schemes, particularly when solving convection-dominated equations such as the advection equation in CFD. Numerical dispersion refers to the artificial oscillations in a numerical solution that occur due to errors in the discretization of wave-like phenomena. Both are forms of numerical error and affect the simulation reliability of detailed analyses for solid-liquid flow and mixing. Numerical diffusion arises from the numerical approximation of the advection term in the flow control conservations. The control conservations in fluid dynamics are described by partial differential equations (PDEs), which serve as fundamental mathematical tools for expressing the governing principles of fluid flow and capturing the intricate interplay of various physical phenomena within fluid systems. These equations cannot be solved directly by a digital computer, since digital computers can only recognize and process numerical data. Thus, these PDEs should be converted into numerical equations that contain only numbers without derivatives. This process of generating a numerical analogue of the PDE is called 'numerical discretisation'. The discretization process produces an error because the numerical terms are only approximations of the original partial differential equation terms. Such error, however, can be reduced to a very low level and is therefore acceptable.

The mesh method is a mature, reliable and widely used method, including the finite element meth-

ods (FEM), the finite volume methods (FVM), and the finite difference methods (FDM) and it contributes to many fields with different application backgrounds under a variety of geometries, scales and conditions, such as fluidized bed (Zbib et al., 2018), stirred vessel (Liu et al., 2013), particle combustion (Kong et al., 2021), viscous pipe flow (Eesa et al., 2008), and blood flow (Bose et al., 2015). The similarity of these approaches is that a pre-defined mesh or grid is required, which provides the links between each numerical element (or cells). Thus, in a general fluid flow problem, the primary fluid phase is normally simulated by solving the differential equations or PDEs of the elements inside the mesh (Wendt, 2008). The FVM and FEM are the two numerical techniques that are most commonly used in predicting the velocity and solid volume distributions in the solid-liquid flows. Specifically for the Eulerian mesh method, the primary phase is solved by a particular series of PDEs named the Navier–Stokes equations (McLean, 2012). And when the secondary or multiple phases (such as particulate phases) are introduced into the primary Euerlian phase for modelling multiphase flow problems, two different approaches are widely used: the Eulerian-Eulerian (EE) approach and the Eulerian-Lagrangian (EL) approach.

Particle-based method has developed as a powerful tool for modeling complex fluid flows, providing a general method for capturing free-surface flows, mixed flows, and solid-liquid two-phase flows. Unlike traditional mesh-based methods that discretize the fluid domain into fixed cells, particle-based methods represent the fluid as a collection of individual particles that interact with each other according to specified rules. This particle-based approach can accurately represent the behavior of fluids on both macro- and microscopic scales and is therefore well suited for modeling phenomena such as turbulence, multiphase flow, and fluid-solid coupling. In this chapter, the fundamentals of particle-based methods for modelling fluid flow are examined, including Smoothed Particle Hydrodynamics (SPH), Discrete Element Method (DEM) and Lattice Boltzmann Method (LBM). One of the main advantages of particle-based methods over mesh-based methods is the ability to deal with highly nonlinear and discontinuous flow behaviors with much higher fidelity. By directly tracking the motion of individual particles, these methods can naturally capture com-

plex flow features such as vortexes, shear layers, and mixing zones. In addition, particle-based methods offer inherent flexibility in modeling complex geometries and boundary conditions because particles can move freely within the fluid domain without the constraints of a fixed mesh structure. In section 2.5.2, a detailed review of the SPH, LBM and DEM are conducted.

2.5.1 Mesh-based method

Finite Volume Method

Finite volume methods (FVM) are a category of classical discretization techniques that have demonstrated to be highly successful in approximating the solution of a wide variety of systems of conservation laws (Barth et al., 2018). They are widely employed in fluid dynamics, porous media flow, multiphase flows, electromagnetism, bioprocess modeling, semiconductor device simulation, and numerous other engineering fields governed by conservative systems that can often be defined and described in the form of integral control volumes (Moukalled et al., 2016). In contrast to other numerical models, the FVM employs a distinctive discretization procedure that consists of two basic steps. In the first step, integrate the partial differential equations and convert them to equilibrium equations on the units. The surface and volume integrals over elements and its surfaces are converted into discrete algebraic relations using integral quadrature of a specified order of accuracy. Finally obtained is a group of semi-specific equations. The second step focuses on selecting interpolating profiles to approximate the variation of variables within an element and relate the surface values of the variables to their cell values, thus transforming algebraic relationships into algebraic equations.

FVM is a common technique used in CFD codes, and the advantages are in terms of memory usage and high efficiency in solution speed, particularly in large problems, high Reynolds number turbulence, and source term dominated flows (Surana et al., 2007). FVM computes partial differential

equations for the Navier-Stokes equations, mass and energy conservation equations, and turbulence equations unfolded in a conservative form and then solved on a discrete control volume. FVM has been extensively applied in pipe flow simulations to study velocity profiles, pressure distributions, and turbulence characteristics (Chu et al., 2020; Koo, 2022; Zhou et al., 2017). In the work of Eesa and Barigou, the radial solid concentrations distribution was obtained through E-E mesh-based method within FEM principle, and simulation results were validated by PEPT experimental data (Eesa et al., 2008; Eesa et al., 2010). Then Eesa applied the validated FEM model to show that the imposition of a transverse vibration motion on a steady laminar flow generates sufficient chaotic fluid motion which leads to considerable radial mixing in solid-liquid pipe flow.

FVM was also applied to predict the performance of micromixer devices, such as liquid mixing and solid-liquid mixing stirred vessels. In mixing flows and solid-liquid two-phase flows, false diffusive quantities are produced with calculations, and in order to reduce the impact of false diffusive quantities on the accuracy of simulations, Bailey investigated the effect of false diffusive quantities in a two-dimensional test problem using the FVM on structured and unstructured grids, applying the first-order and second-order upper wind methods, and quantifying the resulting false diffusive quantities (Bailey, 2017). Researchers also studied flow dynamics and mixing flows by using FVM and discussed several options for investigating and minimizing numerical diffusion effects at moderate cell Pe numbers (Soleymani et al., 2008). Higher-order QUICK schemes were introduced to perform spatial discretization in the FVM computational framework, locally refine the mesh, and artificially increase the diffusion constants to reduce the high computational cost. Based on their study, the results obtained from FVM numerical simulations can be used for optimization purposes while the physical mixing of the mixer cannot be evaluated. However, one significant drawback is its reliance on grid discretization, which can lead to numerical diffusion and inaccuracies, particularly in complex geometries or high-gradient regions. The method struggles with handling highly unstructured grids efficiently, leading to increased computational costs for intricate geometries. Additionally, its reliance on predefined control volumes limits its flexibil-

ity in handling moving boundaries or deformable domains, which are common in fluid-structure interaction and multiphase problems.

Finite Element Method

The basic idea of Finite Element Method (FEM) is to subdivides the domain into finite elements, where the governing equations are numerically solved. The name of FEM was firstly proposed and appeared by Clough in 1960 at a ASCE Conference (Clough, 1960). Extensive finite element work was conducted at the University of California at Berkeley during the period 1957 to 1970 (Clough, 2004). Its formulation has been adapted for use with fluid dynamics governing equations.

Unsteady pipe flow was studied by using modified FEM (Szymkiewicz et al., 2005), which yields a six-point scheme with two weighting parameters. The proposed scheme provides higher accuracy compared to the standard FEM. Compared experimental data and modified FEM results show that the desired damping and smoothing of the pressure wave can be acquired when numerical diffusion raising from numerical model. This phenomenon indicates that the physical dissipation process is not properly represented in its mathematical model. FEM has been employed to model fluid-structure interactions and heat transfer phenomena in pipe systems (Tijsseling, 1996). Talebizadehsardari et al. in 2020 derived the Lagrangian particle tracking method, which follows the rule of FEM, is able to predict the deposition of nano-particles in annular pipe flows under laminar flow conditions (Talebizadehsardari et al., 2020). This model was validated by simulating nano-particle in pipe flows and comparing the numerical data with the analytical solutions. A detailed study on the effects of various parameters such as particle size, pipe length, pipe diameter, air temperature, and the flow rate were performed.

As mentioned above, although FVM shows well performance in application of pipe and mixing flows. FVM still needs particular attention to ensure that conservative solutions. The finite element method must be carefully designed to keep it sustainable, but it is still much more stable than the

finite volume method (Zawawi et al., 2018). Nevertheless, the finite element method probably requires more memorization and slower solving times compared to the finite volume method (Bakker et al., 2001).

Finite Difference Method

The Finite Difference Method (FDM) is based on the calculus of finite differences. It is a relatively straightforward method in which the governing PDE is satisfied at a set of prescribed interconnected points within the computational domain, referred to as nodes. while the boundary conditions are satisfied at a prescribed set of nodes on the boundary of the computational domain. The framework of interconnected nodes is referred to as a mesh or grid (Mazumder, 2015). High order finite difference methods on Cartesian grids are a key player in High-Performance Computing due to the simplicity, low memory storage and efficiency of the traditional five-point (in 2D) or seven-point (in 3D) schemes together with high scalability when using dimensional splitting techniques such as the Alternative Direction Implicit (ADI) method (Jammy et al., 2019).

However, one of the main disadvantage of the FDM is that it uses rectilinear grids that are inflexible for fitting the problem geometry, and for locally refinement of point. In order to overcome this challenge, the FDM as well follows the trends of meshless methods by proposing algorithms that allow the use of unstructured nodes. A generalized finite difference method was proposed, combining Taylor series and moving least squares approximation with weighting functions (Benito et al., 2001). In common with other localized meshless methods (Wei et al., 2023) , the generalized finite difference method results in sparse matrices, which can be efficiently solved without the need for fast algorithms. The accuracy of generalized finite difference method is controlled by the number of terms retained in the sequence and the degree of refinement of the points. Similar to the finite element h-p scheme, large local errors can be improved in the approximation order by increasing the node concentration and including more points in the template (Benito et al., 2003) .

Volume of Fluid (VOF) Method is not a stand-alone numerical method like FDM, FVM, or FEM. Instead, it is an interface-capturing technique implemented within the Eulerian-Eulerian framework to handle multiphase flows efficiently. The VOF method is commonly used to simulate free surface and multiphase flows, including mixing phenomena in pipe and stirred vessels. This method is flexible and efficient when dealing with complex free boundary configurations (Hirt et al., 1981). The VOF method with interfacial reconstruction follows strict conservation of mass. This technique is capable of modelling immiscible mixed fluids by solving a single set of momentum equations and keeping track of the volume fraction of each fluid throughout the domain. The VOF method not only accounts for surface tension and wall adhesion effects, but also can be implemented as a ready-to-use model into many commercially developed CFD software packages, including ANSYS Fluent, GERRIS Flow solver (GFS), and STAR-CCM.

The single phase and solid-liquid flows in stirred vessels, concerning the free liquid surface, the influence of the rotating speed, clearance and diameter of the impeller on the vortex depth have been studied via VOF method in the gas-liquid uncovered unbaffled stirred vessel (Li et al., 2017). VOF is successfully applied to capture the gas-liquid interface and turbulence in the stirred vessel. The suitable representation of two-phase flows is a hot topic of recent industrial interest. VOF model and Eulerian model are commonly used to simulate two-phase flows. The differences in the mathematical description of the Navier-Stokes equations underlying these models lead to differences in their convergence, computational time and accuracy (Guerrero et al., 2017). In two-phase upward flow simulations in vertical pipes, the Eulerian and VOF models exhibit distinct advantages and limitations. By comparing the results with the experimental results, it is found that the Eulerian model has a lower mean square error than the VOF model. Eulerian model takes less computational time than the VOF model. However, only the VOF model is able to predict the flow pattern. For simulating the solid-liquid flows in pipe and stirred vessels, VOF is commonly coupled with other grid-based methods to capture the details velocity and solid volume fraction distribution.

2.5.2 Particle-based method

Lattice Boltzmann Method

The lattice Boltzmann method (LBM) is an innovative tool applied to the investigation of modeling fluid flow, heat transfer, and other complex physical phenomena (Kuznik et al., 2010). In comparison with traditional grid-based CFD methods, LBM is suitable for studying micro- and meso-scale modelling methods based on particle motion dynamics. It has many strengths such as natural parallelism, simple coding, easy implementation, flexible geometry characteristics, and high precision. So far, LBM has been applied with great success in multiphase flow, chemical reaction flow, porous media flow, thermohydrodynamics, suspended particle flow, and magnetohydrodynamics. LBM has developed rapidly in the past years, especially in the simulation of solid-liquid flows. LBM provides a new approach to multiscale analysis with a unique physical background and efficient algorithms based on the theory of molecular dynamics. Compared to traditional CFD methods, LBM saves significant computational time by eliminating the need to solve the Poisson equation for pressure. In addition, since most of the simulation works are limited to local nodes, it is cleanly programmed and well suited for implementation using parallelised algorithms and hardware (Kefayati et al., 2017).

Fluid dynamics analysis is closely related to graphics data in several aspects, particularly in simulation and visualization. Graphics data refers to any form of data used to represent visual elements in a digital or computational environment. Graphics Processing Units (GPUs) provide a massively parallel architecture with low cost making them suitable for computational fluid dynamics (CFD) simulations. This connection allows for the acceleration of certain CFD models using GPUs, originally designed for processing graphics data. Runtime of CFD simulations can be reduced by using hardware acceleration and parallel computing. Graphics data is essential in fields like computer graphics, visualization, virtual reality, gaming, and simulation. GPUs are particularly effective due to their ability to handle the advanced data structures and algorithms common to both fields, such

as grids, meshes, and numerical approximations, which facilitate both accurate fluid simulations and their visualization. Unlike the central processing unit (CPU), GPUs feature a significantly higher number of parallel, multithreaded processors and boast superior memory bandwidth. This architectural distinction enables GPUs to excel in executing compute-intensive and highly parallel tasks at remarkable speeds. The advent of compute unified device architecture (CUDA) has further streamlined parallelization implementation, leading to substantial performance enhancements by leveraging GPU capabilities (Cheng et al., 2018). The integration of the LBM with GPU technology offers a compelling solution for achieving efficient compute performance and remarkable acceleration rates in handling big data applications. In the work of Cheng et al, they provided an overview of the fundamental concepts and models of the LBM, followed by a detailed exploration of its implementation on GPU architectures (Cheng et al., 2018).

The application of LBM for the steady flow in a pipe of square cross-section has been performed, the carrier liquid is non-Newtonian Bingham fluid. Yield stress effects on momentum transport using the Bingham model were also investigated for certain pertinent parameters of the Oldroyd number (Kefayati et al., 2017). LBM offers significant advantages in the study of velocity, pressure and phase distributions in complex fluid simulations, especially when it involves non-Newtonian fluid-carrying fluids, opaque flow behaviours, three-dimensional flow patterns, and elastic interactions with pipe and vessel walls. Due to its inherent versatility and efficiency, LBM excels in capturing the complex dynamics of such systems with high fidelity. By discretising the fluid domain into a lattice structure and simulating particle interactions within this framework, the LBM can analyse complex flow phenomena in detail, including non-Newtonian fluid rheology, turbulence properties, and complex flow-wall interactions. In addition, the parallel computing capability of the LBM makes it well suited to handle large-scale simulations with high computational efficiency, which further enhances its usefulness in solving complex fluid dynamics problems. In conclusion, LBM is a powerful tool for gaining insight into the behaviour of complex fluids in a wide range of industrial and scientific applications. Although LBM is a powerful and increasingly popular

approach in CFD, particularly for complex flows and multiphase systems. However, it has several limitations compared to traditional CFD methods. LBM requires a high spatial resolution to accurately capture fine-scale flow features, especially for high Reynolds number flows or turbulent flows, which leads to significant memory and computational demands compared to traditional Navier-Stokes solvers. LBM is inherently designed for weakly compressible flows. Simulating highly compressible flows requires significant modifications, which may reduce accuracy and efficiency.

Smoothed particle hydrodynamics

Smoothed Particle Hydrodynamics (SPH) is a mesh-free method that has gained significant attention and popularity in recent years due to its versatility and effectiveness in simulating liquid/gas driven flows. SPH is a truly Lagrangian particle method for modeling complex fluid flows. Unlike traditional grid-based methods, SPH represents fluid as a collection of discrete particles, enabling the accurate modeling of complex flow phenomena with high fidelity. Developed initially by Gingold and Monaghan in the 1970s for astrophysical simulations, SPH has since been adapted and extended to a wide range of engineering applications, including aerospace, automotive, maritime, and biomedical engineering (Gingold et al., 1977). SPH was firstly developed to investigate astrophysical applications (Lucy, 1977), then Monaghan (1994) further developed the SPH method for simulating the slightly compressible flows by introducing a virtual speed of sound and attaining a very low Mach number to control density variation within 1%, which is called weakly compressible SPH (WCSPH) (Liang et al., 2015; Monaghan, 1994).

Since its inception, the Smoothed Particle Hydrodynamics (SPH) method has been widely applied to a variety of problems in fluid mechanics and solid mechanics (Monaghan, 1992). This wide range of applications can be attributed to SPH's remarkable ability to effectively incorporate complex physics into its formulation. In SPH, flow domain variables such as density, velocity, and

acceleration are calculated by approximating a set of governing equations on a set of particles. It is worth noting that the connections between particles are not predetermined, but dynamically evolve over time. Therefore, SPH provides a straightforward way to deal with situations involving very large deformations while maintaining excellent conservation properties. These properties include energy, linear momentum, angular momentum, mass and entropy, provided that no artificial viscosity is introduced into the system (Monaghan, 2012). In addition, SPH has some distinct advantages over traditional mesh-based numerical methods for modelling complex fluid flows. By appropriately deploying boundary particles and ghost particles at specific locations in the initial period, free surfaces and moving boundaries can be automatically tracked during the simulation regardless of the complexity of the particle motion, which has always been a challenge for Eulerian mesh-based methods (Ming et al., 2017). SPH naturally meets the interface tracking requirements in multiphase flow simulation.

The Lagrangian meshfree approach, SPH, offers several advantages over both traditional grid-based Euler and Euler-Lagrangian methods for modeling viscoplastic fluids in stirred vessels. For example, SPH can handle large deformations and complex geometries more efficiently, and it can accurately capture the complex fluid-structure interactions and moving boundaries that occur during mixing (Sefid et al., 2015). Additionally, SPH also can easily couple with other particle-based method like DEM to simulate particle-laden flows, which are important in many industrial applications (Lian et al., 2023). Although the SPH method may causing some complexities, it is a general easy and appropriate way to study mixing flow, free surface and moving boundary problems (Shadloo et al., 2016), which will simultaneously be applied in the present study. Due to its Lagrangian nature, SPH is a proper way to model mixing processes, and there is no need to model convective terms in SPH modeling because these convective terms are satisfied by the motion of the particles. Hence the false diffusion introduced by the modeling of mesh-based method does not occur in SPH modeling. Moving boundary and fluid–structure interaction are other complex problems for the mesh-based methods, in which the motion of the rigid body should be defined

by moving mesh, sliding mesh, or immersed boundary methods. However, in the SPH and meshfree methods, the motion of the rigid bodies can be modeled easily (Sefid et al., 2015). All of the above-mentioned qualities show that SPH is a convenient method to model mixers involving rotating blades and with free surface flow. In this thesis, a SPH algorithm is developed to simulate mixing processes involving rotating blades in stirred vessels. The application of the Lagrangian meshfree approach to modeling viscoplastic fluids in stirred vessels was established and review the fundamental concepts of SPH model and discuss its advantages and limitations. A number of case studies that demonstrate the effectiveness of the Lagrangian meshfree approach in simulating viscoplastic fluid mixing in stirred vessels and discuss some of the challenges and future directions for this exciting area of research. To date, there have been limited applications of the SPH method for modelling mixing flows in stirred vessels, especially for non-Newtonian fluids.

One major drawback of SPH is its sensitivity to particle distribution and density fluctuations, which can lead to inaccuracies in pressure and velocity fields. SPH also struggles with handling boundaries, as boundary conditions require specialized treatments that may introduce errors. SPH is computationally expensive, particularly for large-scale simulations, due to its reliance on neighboring particle interactions. Additionally, the accuracy of the results depends heavily on the smoothing kernel and the number of particles, requiring careful parameter selection. High Reynolds number flows and capturing sharp interfaces, such as those in multiphase simulations, remain challenging for SPH, limiting its applicability in certain complex fluid dynamics problems.

Discrete Element Method

Granular materials are very common in industry and food processing. The behavior of food granular and powder materials differs from that of other materials, mainly because of their different biological origin. As a result of the understanding of natural phenomena and the need for control of technological processes, granular medium forces have gradually matured and many tasks have

been solved by applying continuum mechanics and approximate methods for solving differential equations (Drescher, 1991). Computer and numerical methods, especially the FEM, can analyse complex shapes and variations in material properties. However, it fails to deal effectively with the inherent heterogeneity, discontinuities and anisotropy of granular medium (Horabik et al., 2016). Discrete Element Method (DEM) firstly proposed by Cundall and Strack (1979), which has been successfully used to solve granular flows. The second solid phased introduced to the carrier flow, can be modeled by contact model in DEM. In the DEM, solid particles are controlled by the motion governing equations, the contact forces are calculated following the laws of physics (Cundall et al., 1979).

DEM modeling requires a detailed information about the interactions between particles under different solid loadings in the pipe and mixing flows. The correct values of the physical parameters of the solid particles as well as the properly selected and applied physical model of the particle interactions are key inputs for DEM modeling. DEM simulations have proven to be effective in examining many technological processes in agriculture, such as transportation, compression, silo loading and discharge dynamics (Raji et al., 2004). Dem was successfully applied in fluidization and spray drying of food powders and simulating the interaction between soft materials (González-Montellano et al., 2014; Woo et al., 2010). Typically, particles in food processing are soft materials, characterized by variable shapes during flow and mixing, which is a challenge to simulate with DEM, especially to deal with deformed surfaces in a reasonable way. DEM has proven valuable for simulating particle-particle and particle-fluid interactions in multiphase flows, but it has several limitations in fluid simulations. DEM is computationally intensive, particularly for systems with a large number of particles, as it requires resolving interactions at a granular level, which makes simulating large-scale or highly dynamic systems impractical without significant computational resources. Additionally, DEM often requires coupling with other numerical methods, such as CFD, to model fluid behavior, which can introduce complexity and compatibility challenges.

2.5.3 Numerical approaches coupling

In recent years, there has been a growing interest in the development of Numerical approaches coupling with different simulation methods to tackle multi-physics and multi-scale problems more effectively. However, coupling numerical approaches poses several challenges, including ensuring numerical stability, maintaining computational efficiency, and achieving seamless data transfer between different simulation domains. Overcoming these challenges requires the development of robust coupling algorithms, efficient parallel computing techniques, and advanced data interpolation methods. Since this work mainly focuses on using SPH-DEM model to simulate solid-liquid pipe flows, this section mainly focuses on coupling models in multiphase pipe flows.

The numerical approaches have non-negligible advantages in revealing the flow mechanism of solid-liquid suspensions. For carried fluid, there are two main simulation methods to simulate liquid phase in CFD: particle-based and mesh-based methods. Based on conventional FEM (Deb et al., 2014) and FVM (Chen et al., 2011), the traditional CFD can solve with the locally averaged Navier–Stokes equations. In the particle-based method, LBM, Moving Particle Semi-Implicit (MPS), and the SPH are potential and maturity. In CFD, many mesh-based numerical methods have been applied to solve and study the solid-liquid pipe flow. Mahmud et al. (2009) adopted Eulerian-Eulerian method coupled with the VOF method to capture the free liquid interface in the gas-liquid-solid system. Nevertheless, the predicted vortex depth is lower than the actual value. Sun et al. (2015) have developed a DEM-VOF coupling method for simulating solid–liquid flows with free surface based on programming code for the first time and applied it to a rotating drum. Fluid-particle interaction forces were solved by an empirical correlation on accounting of the volume averaging technique. Recently, DEM-VOF coupling algorithm was developed for turbulent free-surface flows with buoyant particles in complex geometries based on FLUENT and EDEM software package, and it has been also applied to stirred tanks (Wu et al., 2018). Researchers have used the Eulerian-Eulerian mesh-based approach to study the solid-liquid flows with differ-

ent geometries, flow regions, and solid loadings, numerical models were validated with different experimental techniques (Chen et al., 2011; Jiradilok et al., 2006; Li et al., 2018; Treinen et al., 2015). In the work of Eesa, the radial solid concentrations distribution of solid-liquid pipe flow was obtained through E-E mesh-based method (Eesa et al., 2008). However, it may be hard for a mesh-based method to track particle trajectories, rotation angular velocity, and collision problems between particles (Washino et al., 2013). Therefore, coupled attracted researchers in solid-liquid pipe flows. According to the investigation of particle-liquid coupling by mesh methods, grid distortion may frequently occur due to the geometric complexity of particle shapes. The meshing process for a complex-shaped boundary is extremely complicated (Markauskas et al., 2017). Compared with mesh-based method, SPH and MPS are easier to couple with Discrete DEM, which has been acknowledged as a powerful and common numerical method proposed by Cundall (1979) to simulate the dynamics of granular materials (Lu et al., 2015). Based on Newton's equation of motion, DEM calculates the position and velocity of each solid particle, also trajectories of solid particles can be obtained. The biggest difference between SPH and MPS is in the calculation way of the particle pressure term (Xu et al., 2021). The coupling between SPH and DEM is well-suited to appropriately handle the interaction between the carried flow and solid particles, and obtain flow details, such as the rotational angular velocity of particles, particle trajectories of each solid particle. Even for different particles shapes and sizes with a high robustness performances, SPH-DEM model is more flexible compared with Reynolds averaged Navier-Stokes (RANS) VOF (Sasson et al., 2016). Based on these superiority, to date, SPH-DEM the coupled SPH-DEM method has already been applied to complex flows, such as solid-liquid flows, debris flow, and molten slag trickle flow (Natsui et al., 2018).

Martin Robinson et al. proposed a mesoscale SPH–DEM model (M. Robinson et al., 2014), which reproduces the flow behaviour in sedimentation simulation. In the past few years most of the coupled SPH-DEM studies are focus on two-dimensional simulations (Xu et al., 2022) or limited to a very small scale (Markauskas et al., 2018). Thus, Superior computer hardware is also important

in CFD calculations, especially for SPH method. In the SPH framework, Xu et al. proposed the particle shifting (PS) method in 2009, which moves particles to the area less populated, avoiding therefore inter-particle penetrations, also improving stability (Lyu et al., 2022; Xu et al., 2009). As Pazouki and Negrut pointed out, Boundary Condition Enforcing markers introduced into SPH-DEM boundary conditions can ensures the no-slip condition on the solid surface in SPH-DEM model, both velocity and solid concentration distribution in this work were validated (Pazouki et al., 2015). However, few studies have used both particle velocity and solid phase distribution profiles to validate the simulation results. Hence, numerical models are urgently needed to show both solid- and liquid-phase behaviors in solid-liquid pipe flow.

Compared to FVM-DEM and other grid-based coupling models, SPH-DEM is better suited for handling very coarse particles and complex boundary interactions. The mesh-free nature of SPH allows for a more accurate representation of curved and moving boundaries, which is particularly important in mixing tanks and solid-liquid pipe flows. In contrast, FVM relies on grid-based boundary conditions, which can introduce staircase effects when modeling complex geometries, leading to inaccuracies in predicting near-wall fluid behavior and particle-boundary interactions. Additionally, SPH naturally captures free-surface flows and interface deformations without requiring extra tracking methods like VOF, reducing numerical diffusion. SPH-DEM is also more effective for high solid concentration flows, as it directly resolves particle-fluid interactions without relying on empirical drag models, unlike FVM-DEM. Its Lagrangian framework ensures numerical stability and adaptability in multiphase flows, avoiding grid-induced errors and diffusion. These advantages make SPH-DEM the preferred choice for solid-liquid multiphase pipe flows.

A coupled SPH-DEM framework, therefore, should be able to appropriately and efficiently handle the interactions between the carrier fluid and solid particles to yield flow details such as the rotational angular velocity (or spin) of the particles and Lagrangian trajectories of both particles and fluid. The coupled SPH-DEM model is highly robust and flexible with regard to the shape and size of the solid particles considered compared to conventional mesh-based CFD approaches

(Sasson et al., 2016) and has recently been successfully applied to simulate different flow systems including packed beds (Natsui et al., 2018), particle sedimentation (Robinson et al., 2014) and debris flow (Liu et al., 2021). In the past few years most of the coupled SPH-DEM studies are focus on two-dimensional simulations (Wu et al., 2018) or limited to a very small (Markauskas et al., 2018) flow domain. However, few studies have been validated due to the lack of appropriate experimental data, and food flows have not been investigated in this way.

Chapter Three

METHODOLOGY

3.1 Smoothed particle hydrodynamics formulation

SPH is a pure Lagrangian numerical framework that is based on numerical particle interpolation to compute smooth field variables. The numerical particles act as control masses and carry all physical properties of the system to be simulated in the computational domain. In this section, the principle and equations are detailed illustrated. SPH is one of the earliest particle-based method and widely applied to model liquids and gas flow with different geometries. In SPH method, a flow domain can be characterized by spatial convolution:

$$A(\mathbf{r}) = \int A(\mathbf{r}')W(\mathbf{r}-\mathbf{r}',h)d\mathbf{r}' \tag{3.1}$$

where, W and h represent the kernel function and smoothing length, respectively. r is a position vector. To apply the approximation on discretized SPH particles, the function A in Eq. (3.1) can be interpolated at a particle a where a summation is performed over all the particles that fall within its region of compact support of W. Eq. (3.1) can be written as follow:

$$A(\mathbf{r}_a) \approx \sum_b A(\mathbf{r}_b) W(\mathbf{r}_a - \mathbf{r}_b, h) \frac{m_b}{\rho_b} \tag{3.2}$$

where subscripts indicate individual particles, a is the target particle in calculation, b is the neighbouring particles of target particle determined by kernel function W. m and ρ are mass and the density of numerical particles.

3.1.1 Smoothing kernel

The governing equations at each SPH particle are solved in a weighted averaged formulation in an influenced domain Ω, as shown in Figure 3.1. The influence domain and weighting of neighbouring particles are defined by a kernel function W, whose derivative is used to calculate the gradient and divergence operators. The kernel is expressed as a function of the normalized distance between SPH particles ($q = |r_{ab}|/h$), where r_{ab} is the distance between any two given numerical particles a and b and the parameter h is the smoothing length (Figure 3.1). The smoothing length controls the size of the area around the target numerical particle in which neighbouring particles are considered. The choice of kernel function is not unique, here two kernel functions, Cubic Spline and a quintic class 2 Wendland function, are widely used as kernel functions (Monaghan et al., 1985) in SPH simulations (Robinson, 2009). Cubic Spline kernel function is defined as:

$$W(r_{ab}, h) = \alpha_D \begin{cases} 1 - \frac{3}{2}q^2 + \frac{3}{4}q^3, & 0 \le q \le 1 \\ \frac{1}{4}(3-q)^3, & 1 \le q \le 2 \\ 0, & q \ge 2 \end{cases} \tag{3.3}$$

where, $\alpha_D = 10/7\pi h^2$ in 2D simulations and $\alpha_D = 1/\pi h^3$ in 3D simulations, q is the distance between two SPH particles and h is the smoothing length. The quintic class 2 Wendland function is:

$$W(r_{ab},h) = \alpha_D \begin{cases} (1-q)^4(4q+1), & 0 \leq q \leq 1 \\ 0, & q \geq 1 \end{cases} \tag{3.4}$$

where $\alpha_D = 7\pi h^2/4$ in 2D simulations and $\alpha_D = 21\pi h^3/16$ in 3D simulations. The quintic class 2 Wendland kernel offers a good balance between computational cost and accuracy. It provides higher-order approximations compared to lower-order kernels, which improves the accuracy of the simulation while maintaining computational efficiency. In this thesis, the quintic class 2 Wendland smooth kernel is employed in all simulations.

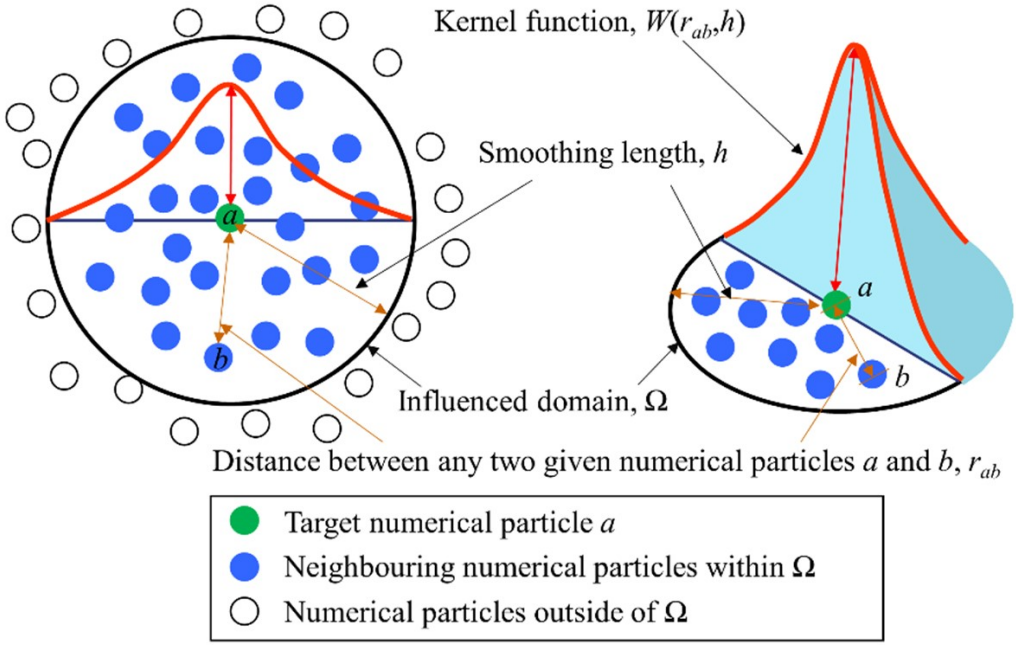

Figure 3.1: Schematic of the SPH approach for simulating numerical particles.

3.1.2 Momentum Equation

The motion of the liquid phase is governed by continuity and momentum conservation equations. Monaghan (1992b) proposed the Lagrangian form of the momentum conservation equation in a

continuum as:

$$\frac{d\mathbf{v}_a}{dt} = -\frac{1}{\rho}\nabla P + \mathbf{g} + \mathbf{\Gamma} \tag{3.5}$$

where, $\mathbf{v}_a$ is the velocity of target particle a. $\mathbf{\Gamma}$ represents the dissipative terms. SPH framework offers different options for including the effects of dissipation.

Artificial Viscosity

Artificial viscosity is a numerical technique commonly employed in fluid dynamics simulations to stabilize the solution and handle shock waves, discontinuities, and other high-gradient regions. The artificial viscosity scheme is a common method within fluid simulation using SPH due primarily to its simplicity. In SPH notation, Eq. (3.5) can be written as:

$$\frac{d\mathbf{v}_a}{dt} = -\sum_b m_b \left(\frac{P_a + P_b}{\rho_a \cdot \rho_b} + \Pi_{ab} \right) \nabla_a W_{ab} + \mathbf{g} \tag{3.6}$$

P_a and ρ_a are the pressure and density that correspond to a target particle a, and P_b and ρ_b are the pressure and density corresponding to a given neighbouring particle b (Figure 3.1). The viscosity term is Π_{ab} calculated by:

$$\Pi_{ab} = \begin{cases} -\frac{\alpha c_{ab} \mu_{ab}}{\rho_{ab}}, & \text{if } v_{ab} \cdot r_{ab} < 0 \\ 0, & \text{if } v_{ab} \cdot r_{ab} > 0 \end{cases} \tag{3.7}$$

Where α is a coefficient that needs to be tuned in order to introduce the appropriate dissipation. The value of $\alpha = 0.01$ has been validated to provide the best results in the fluids-structure flows (Altomare et al., 2015). c_{ab} is the mean sound speed, defined as $c_{ab} = 0.5(c_a - c_b)$. $r_{ab} = r_a - r_b$

and $v_{ab} = v_a - v_b$ with r_i as the particle position, and v_i as the velocity. $\mu_{ab} = hv_{ab} \cdot r_{ab}/(r_{ab}^2 + \eta^2)$, here $\eta^2 = 0.01h^2$. In this thesis, the simulation of laminar flow in pipes is conducted using the artificial viscosity technique to enhance numerical stability.

Laminar viscosity and Sub-Particle Scale (SPS) Turbulence

The laminar viscous stresses $(\nu_0 \nabla^2 \mathbf{v})_a$ in the momentum conversation can be represented as (Lo et al., 2002):

$$(\nu_0 \nabla^2 \mathbf{v})_a = \sum_b m_b \left(\frac{4\nu_0 r_{ab} \cdot \nabla_a W_{ab}}{(\rho_a + \rho_b)(r_{ab}^2 + \eta^2)} \right) \mathbf{v}_{ab} \tag{3.8}$$

where, ν_0 is the kinematic viscosity, $r_{ab} = \mathbf{r}_a - \mathbf{r}_b$ is the separation distance between numerical particles, and $\eta^2 = 0.01h^2$. During the whole simulation process, the mass of each particle remains constant. In SPH discrete notation this can be described as:

$$(\nu_0 \nabla^2 \mathbf{v})_a = -\sum_b m_b \left(\frac{P_a + P_b}{\rho_a \cdot \rho_b} \right) \nabla_a W_{ab} + \mathbf{g} + \sum_b m_b \left(\frac{4\nu_0 r_{ab} \cdot \nabla_a W_{ab}}{(\rho_a + \rho_b)(r_{ab}^2 + \eta^2)} \right) \mathbf{v}_{ab} \tag{3.9}$$

The basic equations of the Sub-Particle Scale (SPS) was first proposed by Gotoh et al (2004) to study the effects of turbulence in simulations of Moving Particle Semi-implicit (MPS) model (Gotoh et al., 2004). The momentum conservation equation is defined as:

$$\frac{d\mathbf{v}_a}{dt} = -\frac{1}{\rho} \nabla P + \mathbf{g} + (\nu_0 \nabla^2 \mathbf{v})_a + \frac{1}{\rho} \nabla \cdot \vec{\tau} \tag{3.10}$$

where laminar term is defined following Eq. (3.8), and $\bar{\tau}$ refers to SPS stress tensor. Favre-averaging is needed to account for compressibility in weakly compressible SPH (Dalrymple et al., 2006). Equation of eddy viscosity is assumed for modelling the SPS stress tensor, and the shear

stress components in coordinate directions i and j are expressed in Einstein notation i and j.

$$\tau^{ij} = 2\nu_{SPS}\left(s^{ij} - \frac{1}{3}s^{ij}\delta^{ij}\right) - \frac{2}{3}C_L\Delta^2\delta^{ij}|s^{ij}|^2 \tag{3.11}$$

The turbulence eddy viscosity is $\nu_{SPS} = [C_{Sm}\Delta]^2|s^{ij}|^2$, where C_{Sm} is the Smagorinsky constant with a value of 0.12; Δ is the particle spacing at the start of simulation, the quantity of δ^{ij} defined as $\delta^{ij} = 2\frac{\delta^i\delta^j}{\delta^i+\delta^j}$, s^{ij} is an element of the SPS strain tensor, and $C_L = 0.0066$. The turbulent flows in pipes and mixing flows are modeled using the SPS turbulence model to capture the turbulent effects in the simulations.

3.1.3 Continuity equation

Throughout a weakly compressible SPH simulation, the mass of each particle remains constant and only the associated density changes. These density fluctuations are calculated by solving the mass conservation or continuity equations in the SPH form (Monaghan et al., 1992):

$$\frac{d\rho_a}{dt} = \rho_a\sum_b m_b\frac{\mathbf{v}_{ab}\cdot\nabla_a W_{ab}}{\rho_b} \tag{3.12}$$

In SPH, the carrier fluid is represented through a set of Lagrangian form equations. Mass conservation is employed to quantify variations in fluid density. In order to mitigate fluctuations in fluid density during simulations, an additional density diffusion term is incorporated into the continuity equation:

$$\frac{d\rho_a}{dt} = \sum_b m_b\mathbf{v}_{ab}\cdot\nabla_a W_{ab} + \delta h c_0\sum_b 2(\rho_{ba}^T - \rho_{ab}^H)\frac{\mathbf{r}_{ab}\cdot\nabla_a W_{ab}}{r_{ab}^2}\frac{m_b}{\rho_b} \tag{3.13}$$

$$\rho_{ab}^{H} = \rho_0 \left(\gamma \sqrt{\frac{P_{ab}^{H} + 1}{c_0^2 \rho_0}} - 1 \right) \tag{3.14}$$

where, $\mathbf{v_{ab}} = \mathbf{v_a} - \mathbf{v_b}$ and $r_{ab} = r_a - r_b$ are the velocity difference and distance between numerical particles a and b, respectively. The second term on the right-hand side corresponds to the density diffusion term, where c_0 denotes the speed of sound at the reference density and δ represents a coefficient governing the extent of density diffusion. The variables T and H denote the total and hydrostatic components of liquid density. The hydrostatic density difference between particle a and b can be calculated by Eq. (3.13). P_{ab}^{H} refers to the computation of the hydrostatic pressure difference between numerical particles a and b, which is expressed as:

$$P_{ab}^{H} = \rho_0 g z_{ab} \tag{3.15}$$

where, ρ_0 represents the reference density, typically associated with the density of water, while z_{ab} represents the vertical separation between particles a and b.

3.1.4 Equation of state

There are two common approaches for solving the momentum conservation equation in SPH, namely incompressible SPH (ISPH), and weakly compressible SPH (WCSPH). In ISPH, the pressure term in the equation is computed by solving the pressure Poisson's equation, while the pressure is computed explicitly from the density variations using an artificial equation of state in WCSPH (Monaghan et al., 2005):

$$P = B \left[\left(\frac{\rho}{\rho_0} \right)^{\gamma} - 1 \right] \tag{3.16}$$

where, P is pressure, γ is the fluid polytropic index (here, $\gamma = 7$), and $B = c_0^2\rho_0/\gamma$, ρ_0 is the reference density, and c_0 refers to the speed of sound at the reference density. It should be noted that it is common practice in WCSPH not to actually use the physical speed of sound but to impose c_0 to be typically at least 10 times the maximum velocity of the system. In WCSPH simulations, the density variation factor ($|\rho/\rho_0 - 1|$) must be less than 1% to keep the relative incompressibility of the fluid (Gomez-Gesteira et al., 2010).

3.2 Rheology model in SPH

In this thesis, the non-Newtonian rheology of the carrier fluid was modelled using the Herschel-Bulkley-Papanastasiou (HBP) model (Han et al., 2020), which includes an apparent yield stress. This is a general viscoplastic model which has the advantage of being able to represent various time-independent rheological behaviours including Newtonian, pseudoplastic and dilatant with and without a yield stress, making it popular for use in numerical simulations. In this model, the effective viscosity (μ_{eff}) is a function of shear rate ($\dot{\gamma}$) and yield stress (τ_y), thus:

$$\mu_{\text{eff}} = \mu(\dot{\gamma})^{n-1} + \frac{\tau_y}{2\dot{\gamma}}\left(1 - e^{-m\dot{\gamma}}\right) \tag{3.17}$$

where, μ is the apparent dynamic viscosity. Details of shear rate calculations are widely discussed in the literature (Fourtakas et al., 2016; Han et al., 2019; Wang et al., 2016). Compared to the well-known Bingham model, two additional coefficients, the Papanastasiou parameter (m) and power-law index (n) are included in the HBP model. As m tends to infinity and $n \neq 1$, the HBP model reduces to the original Herschel-Bulkley model. When $\tau_y \neq 0$, $m \neq 0$ and $n = 1$ the model reduces to the simple Bingham model. When $\tau_y = 0$, and $n \neq 1$ the model reduces to the power-law model and, consequently, when $\tau_y = 0$, and $n = 1$ it represents Newtonian behavior.

3.3 Time step in SPH

The SPH framework includes a widely used numerical integration scheme. The momentum v_a, density ρ_a, and position r_a equations are first described as:

$$\frac{dv_a}{dt} = F_a \tag{3.18}$$

$$\frac{d\rho_a}{dt} = D_a \tag{3.19}$$

$$\frac{dr_a}{dt} = v_a \tag{3.20}$$

where v_a is sometimes also optimized by an XSPH correction when these equations are time-integrated using either the computationally simple Verlet-based scheme or the numerically more stable but computationally intensive two-stage enantiomer approach (Monaghan, 1989).

3.3.1 Verlet scheme

The algorithm follows the classic Verlet method (Verlet, 1967) which offers the advantage of minimal computational overhead compared to other integration techniques. This efficiency stems from avoiding multiple computations per iteration such as the predictor and correction steps. The predictor step calculates the variables based on the following equations:

$$v_a^{\chi+1} = v_a^{\chi-1} + 2\Delta t F_a^{\chi} \tag{3.21}$$

$$r_a^{\chi+1} = r_a^{\chi} + \Delta t v_a^{\chi} + 0.5\Delta t^2 F_a^{\chi} \tag{3.22}$$

$$\rho_a^{\chi+1} = \rho_a^{\chi-1} + 2\Delta t D_a^{\chi} \tag{3.23}$$

where F_a^{χ} and D_a^{χ} are calculated respectively by Eq. (3.18) and Eq. (3.19). The χ refers to the time step $t = \chi\Delta t$. In this thesis, all simulations are conducted using the symplectic scheme, ensuring accurate long-term integration and the preservation of system properties.

3.3.2 Symplectic scheme

Without friction or viscous influence, the symplectic integral algorithm is time-reversible (Leimkuhler et al., 1996). The symplectic scheme maintains geometrical properties such as the symmetry of the energy over time described in the equations of motion. Therefore, it improves the accuracy of the long-term solution behavior. An explicit second-order Symplectic scheme is introduced featuring two stages: a predictor stage followed by a corrector stage. Firstly, in the predictor stage, the values of acceleration and density are calculated at the midpoint of the time step by:

$$r_a^{\chi+\frac{1}{2}} = r_a^{\chi} + \frac{\Delta t}{2} v_a^{\chi} \tag{3.24}$$

$$\rho_a^{\chi+\frac{1}{2}} = \rho_a^{\chi} + \frac{\Delta t}{2} D_a^{\chi} \tag{3.25}$$

In the corrector stage, $\frac{dv_a^{\chi+\frac{1}{2}}}{dt}$ is used to estimate the corrected velocity and position of the target particle at the end of the time step calculated as:

$$v_a^{\chi+1} = v_a^{\chi+\frac{1}{2}} + \frac{\Delta t}{2} F_a^{\chi+\frac{1}{2}} \tag{3.26}$$

$$r_a^{\chi+1} = r_a^{\chi+\frac{1}{2}} + \frac{\Delta t}{2} v_a^{\chi+1} \tag{3.27}$$

The updated values of velocity and position obtained by Eq. (3.26) are then applied to estimate the corrected value of density $\frac{d\rho_a^{\chi+1}}{dt} = D_a^{\chi+1}$.

3.3.3 Variable time step

To ensure the robustness of the SPH or SPH-DEM simulations, the Courant-Friedrichs-Lewy (CFL) condition needs to be satisfied (Monaghan et al., 1999). There are viscous diffusion and forcing terms in the CFL condition. The simulation time step Δt is estimated as:

$$\Delta t_f = \min_a \left(\sqrt{\frac{h}{|f_a|}} \right) \tag{3.28}$$

$$\Delta t_{cv} = \min_a \left(\frac{h}{c_0 + \max_b \left(\frac{h v_a \cdot r_{ab}}{r_{ab}^2 + \eta} \right)} \right) \tag{3.29}$$

$$\Delta t = C_{\mathrm{CFL}} \cdot \min(\Delta t_f, \Delta t_{cv}) \tag{3.30}$$

where, Δt_f is influenced by the force per unit mass ($|f_a|$); Δt_{cv} combines the Courant and the viscous time step controls.

3.4 Boundary conditions in SPH

In SPH framework, flow geometry and boundary are comprised of group of the numerical boundary particles. These particles are treated as a distinct set from the numerical fluid particles. Solid immiscible boundaries and periodic open boundaries are described in detail in this section. In addition, different methods are provided to allow boundary particles to move according to a fixed forcing function.

3.4.1 Dynamic Boundary Condition

The Dynamic Boundary Condition (DBC) is a default approach supplied by DualSPHysics (Crespo et al., 2007). Numerical boundary particles in this method meet the identical equations as numerical fluid particles, however, they do not shift in response to the forces applied to them. Conversely, they either remain in a fixed position or move according to an imposed/specified motion function (i.e., a moving object, such as a door or a wavemaker).

As numerical fluid particles close to the boundary and the distance between boundary particles and the fluid particles is less than twice the smoothing length h, the density of the affected boundary particles increases, leading to an increase in pressure. At the same time, due to the pressure term in the momentum equation, this in turn produces a repulsive force on the fluid particles. The stability of this method depends on the proper time step to accommodate the highest velocity of any fluid particles currently interacting with the boundary particles. Therefore, calculating a variable time step is critical to ensure stability.

The DBC suffers some weaknesses, e.g., excessive dissipation, the unphysical values at these points due to the evolution of the density and pressure of the particles at the fixed boundary, and an unphysical boundary layer which is too large for describing boundary. Another disadvantage of

DBC is that when considering steady state 2D pipe flows such as Poiseuille and Couette flows, the boundary layer cannot be solved accurately without using high resolution. SPH simulations at low resolution, directly setting the velocity of each boundary particle to zero to approximate no-slip does not capture the correct boundary flow. This results in higher velocity close to the boundary and throughout the flow than expected. Nevertheless, DBC can still be successfully applied to solve coastal engineering challenges because it allows the discretisation of complex 3D geometries without the need to implement complex mirroring techniques or semi-analytical wall boundary conditions. Although the DBC is widely used in SPH methods, it has been observed that, in certain cases, some numerical fluid particles penetrate the boundary or fail to reflect specularly. To address this issue, this thesis employs multiple layers of boundary particles to effectively prevent solid particles from crossing the pipe wall boundary. These additional layers enhance numerical stability and prevent unexpected behaviors such as particle leakage or penetration, and can also improve the accuracy of the simulations.

3.4.2 Periodic open boundary condition

Periodic boundary conditions are usually applied to both inlet and outlet of pipe flows, following the methodology outlined by Gomez-Gesteira et al (2012) and illustrated in Figure 3.2. Implementation involves enabling numerical particles in proximity to the open lateral boundary to interact with numerical fluid particles near the corresponding open lateral boundary on the opposite side of the domain (Gomez-Gesteira et al., 2012). When a suspended particle exits the outflow zone, its velocity is automatically reset to zero and temporarily stored in a buffer reservoir (Figure 3.2). Subsequently, each time a suspended particle enters the flow domain, a particle is extracted from the buffer reservoir and inserted into the upstream side of the inflow zone with the specified prescribed velocity and density.

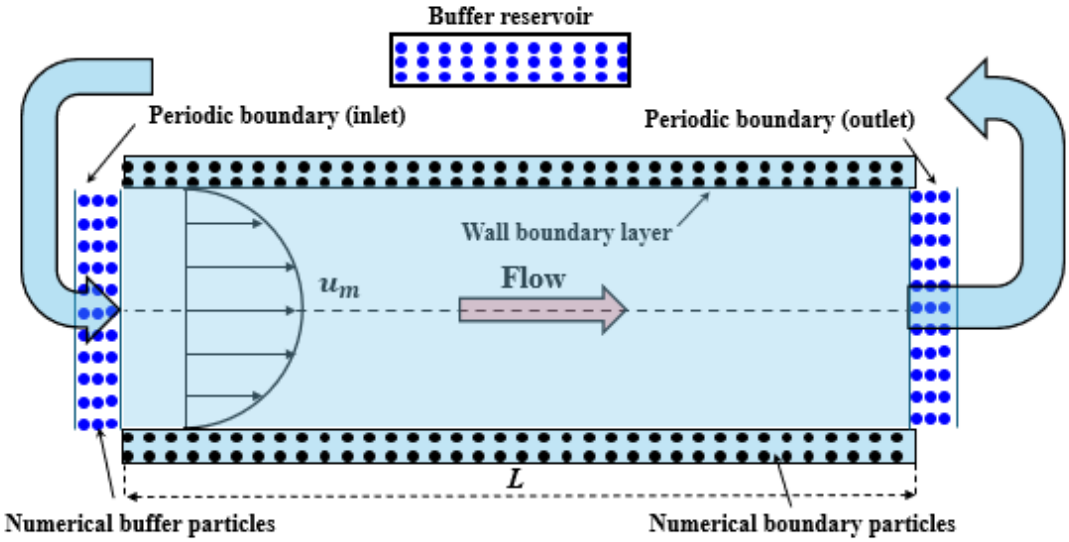

Figure 3.2: Configuration of periodic open boundary condition.

3.4.3 Modified dynamic Boundary Condition

To overcome the drawbacks of DBC mentioned in section 3.7.1, a modification of DBC (mDBC) has been proposed to enhance the accuracy of the boundary flow condition (English et al., 2019). The boundary particles in this implementation are aligned in the same configuration as the boundary particles in the original DBC, with the boundary interface located at the half-particle spacing of the innermost layer of the boundary particles. A ghost node is projected across the boundary interface into the fluid for each boundary particle, and the projection process is similar to the method described by Marrone et al. (2011). As illustrated in Figure 3.3(a), the ghost nodes are mirrored across the boundary interface along the direction of the boundary normal pointing into the fluid domain. The physics properties of numerical fluid particles are calculated at the ghost node in a corrected SPH sum by the neighbouring particles in the support domain in Figure 3.3(b). Both Figure 3.3(a) and Figure 3.3(b) are focus on the flat geometry boundary, for boundary particles located

at corners, the situation is further complicated by the presence of multiple normal. As shown in Figure 3.3(c), the boundary interfaces of each solid boundary intersect to form an interface corner through which the ghost node mirrors the fluid domain. Finally, the physics properties of numerical fluid particles are calculated at the ghost node in a corrected SPH sum by the neighbouring particles in the support domain as well in Figure 3.3(d).

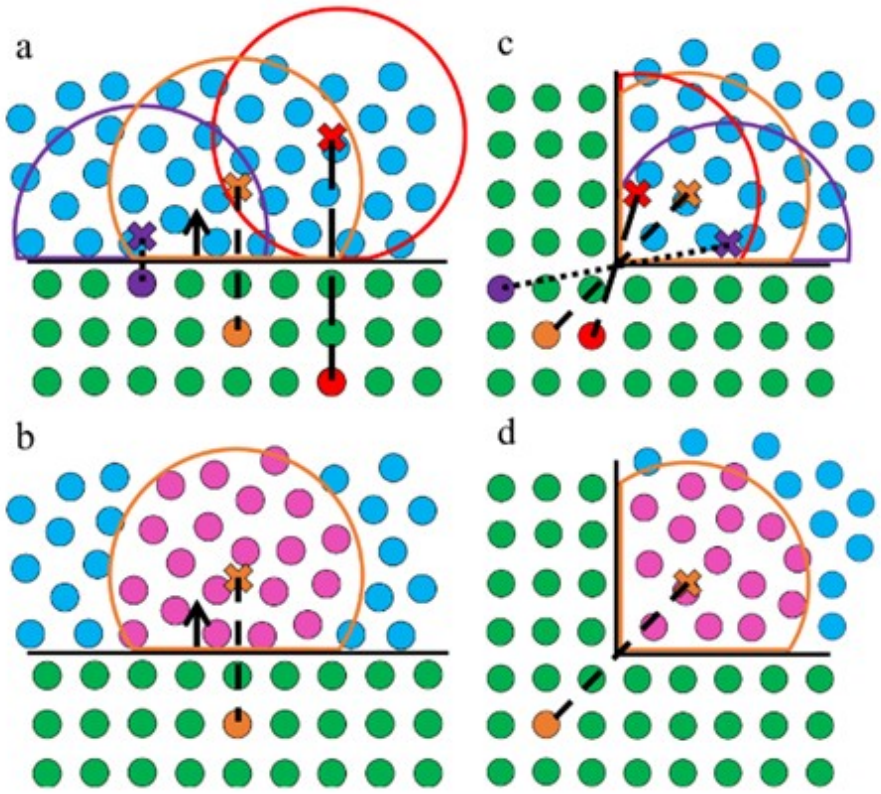

Figure 3.3: Schematics of Mirroring of ghost nodes in flat surface (ab) and corner (cd). Fluid particles (pink) included in the kernel sum around ghost nodes for boundary particles (English et al., 2019).

The parameter values of boundary particles are determined by the properties of numerical fluid particles, utilizing the values computed at the ghost node. This process involves employing an extrapolation method akin to the one employed for open boundaries in the model proposed by Tafuni et al. (2018). For the density of the boundary particle ρ_{bou}, the density ρ_g and its gradient

are calculated at the ghost node via the first order consistent SPH interpolation (Liu et al., 2006), which requires solving the following linear system for each ghost node g:

$$\mathbf{A}_g \begin{bmatrix} \rho_g \\ \partial_x \rho_g \\ \partial_y \rho_g \\ \partial_z \rho_g \end{bmatrix} = \mathbf{B}_g \tag{3.31}$$

To calculate the matrix $\mathbf{A}_g$ and the vector $\mathbf{B}_g$ at each ghost node g, a new particle interaction loop needs to be computed.

3.5 Discrete element method formulation

The Discrete Element Method (DEM) is a numerical technique used to model and simulate the behavior of systems composed of discrete particles, such as granular materials, powders, or assemblies of solid particles. DEM tracks the motion and interaction of individual particles over time by solving equations of motion for each particle. One of the most famous laws in physics is basic to understand the motion of any particle group. It describes the relation between a body, the forces acting on it and the effect it has on its motion. The second Newton's Law states that:

$$m\vec{a} = \vec{F}_t \tag{3.32}$$

Where m is the mass of the body, a is the acceleration and F_t is the total force that acts on the previous mass.

The accuracy of DEM simulations is heavily influenced by the choice of contact models, which define the forces and interactions between particles. The linear spring-dashpot model and the

Hertz-Mindlin (non-linear) model are currently the most widely used contact models in DEM simulations due to their reliability and applicability in representing particle interactions. In the linear contact model, the contact force F_c is decomposed into a linear (spring) component F_l and damping component F_d,

$$F_c = F_l + F_d \tag{3.33}$$

Then the linear component can be further decomposed into normal (n) and tangential (t) components,

$$F_n^l = k_n \delta_n \tag{3.34}$$

$$F_t^l = (F_t^t)_0 + k_t \Delta\delta_t \tag{3.35}$$

where k_n refers to normal direction constant stiffness and k_t is the constant stiffness in tangential directions. δ_n is the total normal overlap and $\Delta\delta_t$ is the increment in tangential overlap. The normal force is typically calculated in absolute terms by multiplying the total overlap at a given moment by the stiffness. As particle rotation is computed and updated, the tangential force is adjusted incrementally, with $(F_t^l)_0$ representing the shear force from the previous time step (Wren et al., 1997). A Coulomb-type frictional slip is incorporated in the tangential direction, requiring the computed tangential force to be validated against the following condition:

$$F_t^l = \begin{cases} F_{l*}^t & \text{if } F_{l*}^t \leq \mu F_n^l \\ \mu F_n^l & \text{otherwise} \end{cases} \tag{3.36}$$

The damping forces in the normal and tangential directions are given by:

$$F_d^n = c_n \dot{\delta}_n, \quad F_d^t = c_t \dot{\delta}_t \tag{3.37}$$

where c_n and c_t are the damping coefficients in the normal and tangential directions, respectively, with units of Ns/m. The damping coefficients can also be expressed in terms of the critical damping

ratio β as:

$$c_n = 2\beta_n \sqrt{m_c k_n}, \quad c_t = 2\beta_t \sqrt{m_c k_t} \tag{3.38}$$

where m_c can be express as:

$$m_c = \frac{m_1 m_2}{m_1 + m_2} \tag{3.39}$$

m_c for contact between particles with a mass of m_1 and m_2, respectively. Under certain conditions, the normal force may enter a tensile state, and it is up to the user to determine whether this behavior should be permitted or if the normal force should be constrained to zero in such cases. The implementation of the tangential contact model varies across different codes. While some codes rely solely on the linear spring force to define the maximum sliding or frictional force, as in Eq. 3.37, others integrate both spring and damping forces into the calculation (Thakur et al., 2016). It is crucial for users to recognize these differences and understand their potential impact on simulation results. Most importantly, caution should be exercised when transferring parameter sets from one code to another to ensure consistent and accurate outcomes.

In the Hertz-Mindlin contact model, the contact force F_c is resolved into a non-linear Hertz component F_h and damping component F_d:

$$F_c = F_h + F_d \tag{3.40}$$

The Hertz component can be further decomposed into normal (n) and tangential (t) components (Boac et al., 2014),

$$F_h^n = k_n \delta_n^{3/2} \tag{3.41}$$

$$F_h^t = (F_l^t)_0 + k_t \Delta\delta_t \tag{3.42}$$

Coulomb-type frictional slip is considered in the tangential direction, meaning that the tangential shear force computed above is verified against specific constraints given in Eq. 3.36. The normal stiffness is determined by the material's elasticity modulus and particle radius as:

$$k_n = \frac{4}{3} E^* \sqrt{R^*} \tag{3.43}$$

and the shear stiffness is given by:

$$k_t = 8G^* \sqrt{R^* \delta_n} \tag{3.44}$$

where R^*, E^* and m^* can be calculated as:

$$R^* = \left(\frac{1}{R_i} + \frac{1}{R_j} \right)^{-1}, \quad E^* = \left(\frac{1-\nu_i^2}{E_i} + \frac{1-\nu_j^2}{E_j} \right)^{-1}, \quad m^* = \left(\frac{1}{m_i} + \frac{1}{m_j} \right)^{-1}$$

E and G refer to the Young's modulus and shear modulus of the two particles in contact, ν representing Poisson's ratio, and R is the particle radius, respectively (Boac et al., 2014).

The damping forces in the normal and tangential directions are described as:

$$F_d^n = c_n \dot{\delta}_n \delta_n^{1/4} \tag{3.45}$$

$$F_d^t = c_t \dot{\delta}_t \delta_t^{1/4} \tag{3.46}$$

where c_n and c_t are the damping coefficients in the normal and shear directions, respectively and can be calculated as:

$$c_n = \frac{\ln e}{\sqrt{\ln^2 e + \pi^2}} \sqrt{m^* k_n} \tag{3.47}$$

$$c_t = \frac{\ln e}{\sqrt{\ln^2 e + \pi^2}} \sqrt{m^* k_t} \tag{3.48}$$

where e is the coefficient of restitution. Alternatively, the damping coefficients can also be expressed in terms of the critical damping ratio. For a more comprehensive review of contact normal force models can be found in the work of Kruggel-Emden et al. (2007).

Based on the traditional DEM method, a novel Distributed Contact Discrete Element Method (DCDEM) has been proposed (Cummins et al., 2011). The uniqueness of this method is that it no longer represents a single solid particle by a numerical particle, instead it is represented by a group of numerical particles. Similar to the Smoothed Particle Hydrodynamics (SPH) method, any physical object is discretized into a set of numerical particles for modeling and computation. Instead of solving the stress–strain equations at the discretisation numerical particles, a traditional DEM contact force model is applied between interacting points on different particles. A given numerical particle on a given solid object then has force contributions from nearby particles. The DCDEM method was introduced and compared to traditional DEM by scholars (Cummins et al., 2011; Canelas et al., 2016). In this thesis, DCDEM was applied to simulate the disperse phase in simulations. The details of coupling between DCDEM and SPH are illustrated in next section.

3.6 Coupling with distributed contact discrete element method

In DCDEM, the suspended solid particles are treated as a discrete phase whose motion is described by Newton's second law:

$$m_i \frac{d^2 \mathbf{r}_i}{dt^2} = \sum_j \mathbf{c}_{ij} + \mathbf{f}_i + m_i \mathbf{g} \tag{3.49}$$

where, m_i represents the mass of particle i at position $\mathbf{r}_i$, $\mathbf{c}_{ij}$ represents the contact force between solid particles and $\mathbf{f}_i$ is the coupling force of the particle-liquid flow acting on solid particle i.In the coupled SPH-DEM approach, the force exerted on solid particle i by the numerical SPH particles is estimated as (Anderson et al., 1967):

$$\mathbf{f}_i = V_i(-\nabla P + \nabla \cdot \tau) + \mathbf{f}_d(\varepsilon_i, \mathbf{u}_s) \tag{3.50}$$

where, V_i is the volume of the solid particle. The first two terms account for fluid forces such as shear stress, pressure and buoyancy. The force $\mathbf{f}_d$ is the particle drag force which is affected by the local porosity ε_i and the superficial fluid velocity $\mathbf{u}_s$ given by:

$$\mathbf{u}_s = \varepsilon_i(\mathbf{u}_L - \mathbf{u}_p) \tag{3.51}$$

where, $\mathbf{u}_L$ and $\mathbf{u}_p$ are, respectively, the velocity of the SPH fluid and DEM solid particles. The drag force is defined as (Coulson et al., 1990):

$$\mathbf{f}_d = \frac{1}{8} C_d \varepsilon_i^{-\varphi} \pi d_p^2 \rho_f \mathbf{u}_s |\mathbf{u}_s| \tag{3.52}$$

where, ρ_f is the fluid density. The drag coefficient C_d and the constant φ are related to the particle

Reynolds number, $Re_p = \rho u d_p / \mu$:

$$C_d = \left(0.63 + \frac{4.8}{\sqrt{Re_p}}\right)^2 \tag{3.53}$$

$$\varphi = 3.7 - 0.65 \times \exp\left[-\left(\frac{1.5 - \log_{10} Re_p}{2}\right)^2\right] \tag{3.54}$$

The total contact force (F_{ij}^T) acting on particle i resulting from collision with particle j is resolved into normal ($F_{n,ij}$) and tangential ($F_{t,ij}$) components, as shown in Figure 3.4. Both forces are further decomposed into a repulsion force (F^r) and a damping force (F^d) arising, respectively, from deformation of the material and dissipation of energy during the deformation.

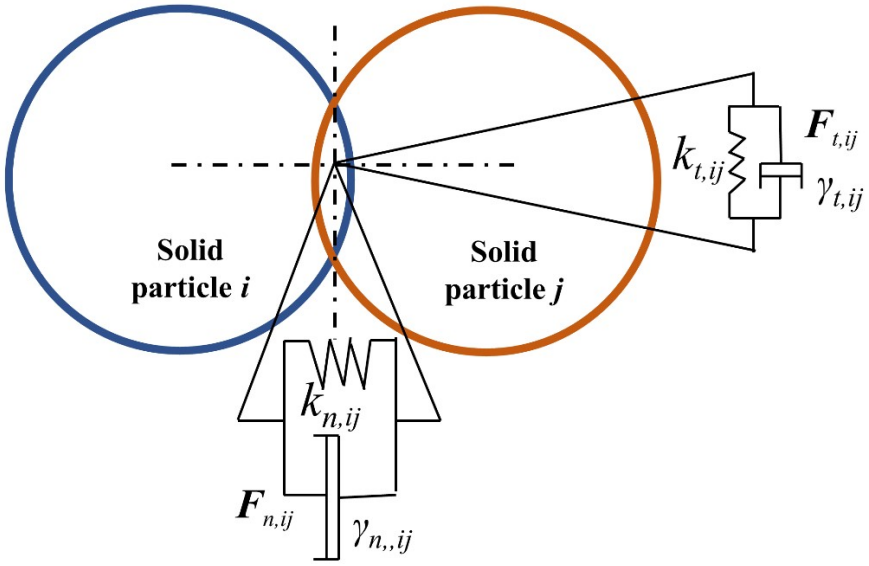

Figure 3.4: Illustration of viscoelastic DEM model for interaction between solid particles.

The normal force is expressed as:

$$F_{n,ij} = F_{n,ij}^r + F_{n,ij}^d = k_{n,ij}\delta_{ij}^{3/2} e_{ij}^n - \gamma_{n,ij}\delta_{ij}^{1/2}\delta_{ij}\dot{e}_{ij}^n \tag{3.55}$$

where, the stiffness is given by:

$$k_{n,ij} = -\frac{4}{3}E^*\sqrt{R^*} \tag{3.56}$$

and the damping coefficient is:

$$\gamma_{n,ij} = -\frac{\log e_{ij}}{\sqrt{\pi^2 + \log^2 e_{ij}}} \tag{3.57}$$

where, $\delta_{ij} = \max(0, (d_i + d_j)/2 - |r_{ij}|)$ is the particle overlap (approximating deformation), e^n_{ij} is the unit vector between the centres of particles i and j, and $\dot{\delta}_{ij} = v_{ij} \cdot e^n_{ij}$ is the rate of normal deformation. The parameter e_{ij} is the restitution coefficient defined as the ratio of the velocities after and before particle collision, and its value controls viscous dissipation during collision.

The reduced radius R^* and reduced elasticity E^* are defined as:

$$R^* = \left(\frac{1}{r_i} + \frac{1}{r_j}\right)^{-1}; \quad E^* = \left(\frac{1-v^2_{p_i}}{E_i} + \frac{1-v^2_{p_j}}{E_j}\right)^{-1} \tag{3.58}$$

where, r is particle radius, E is Young's modulus and v_p is Poisson's ratio.

Similarly, the tangential force is also decomposed into a repulsion F^r_t and a damping force F^d_t, thus:

$$F_{t,ij} = F^r_t + F^d_t = k_{t,ij}\delta^t_{ij}e^t_{ij} - \gamma_{t,ij}\delta_{ij}\dot{\delta}_{ij}e^t_{ij} \tag{3.59}$$

where the stiffness and damping constants for tangential force are:

$$k_{t,ij} = \frac{2}{7} k_{n,ij}, \quad \gamma_{t,ij} = \frac{2}{7} \gamma_{n,ij} \tag{3.60}$$

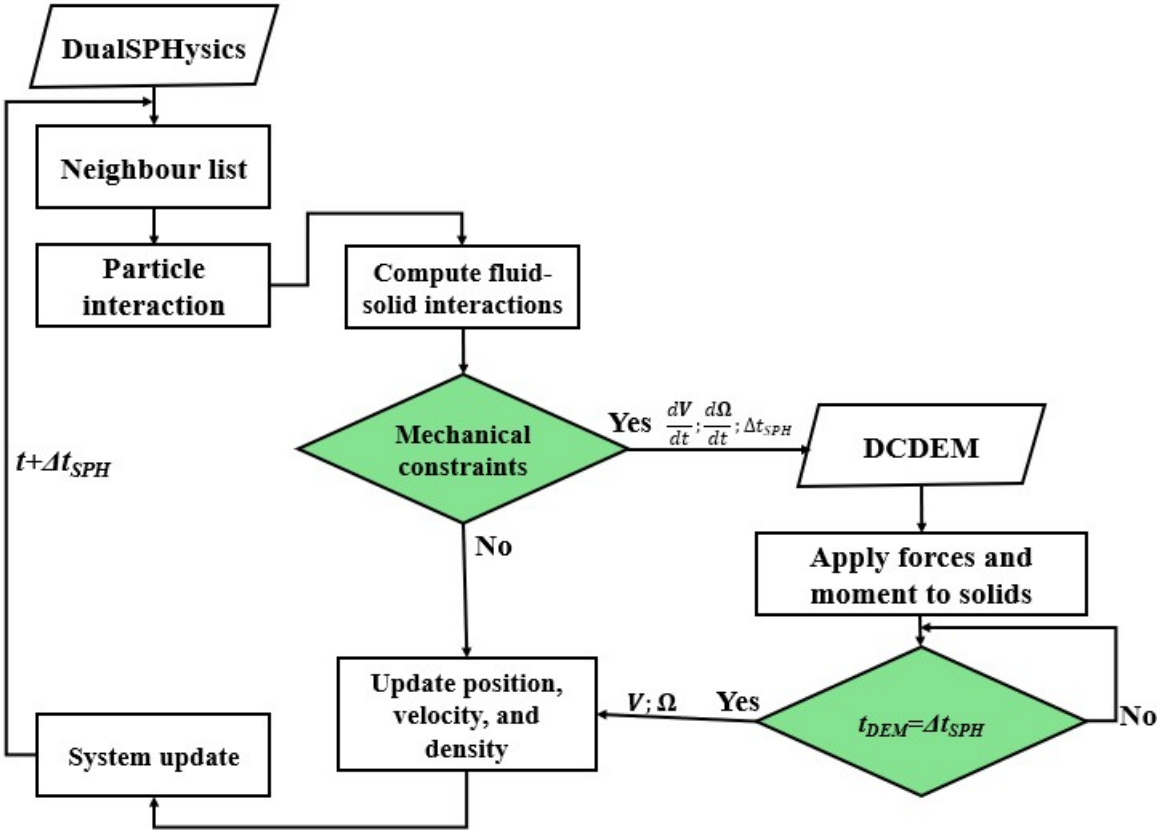

Figure 3.5: Flow chart of the coupling between DualSPHysics and DCDEM.

The SPH-DEM coupling process is illustrated in the flowchart of Figure 3.5. The governing equations for the liquid and solid phases are solved for each numerical particle. Initially, DualSPHysics generates a list of neighboring particles, facilitating the calculation of particle interactions based on localized dynamics (Domínguez et al., 2011). These interactions include the computation of forces between fluid and solid particles, each boundary particle (k) inside the solid particle experiences a force per unit mass denoted by:

$$f_k = \sum_a f_{ka} \tag{3.61}$$

where, f_{ka} represents the force per unit mass exerted by fluid particle (a) on boundary particle (k), given by:

$$m_k f_{ka} = -m_a f_{ak} \tag{3.62}$$

After calculating the force on each boundary particle (k), the fundamental equations of rigid body dynamics are then employed, thus:

$$M\frac{d\mathbf{V}}{dt} = \sum_k m_k f_k \tag{3.63}$$

$$I\frac{d\mathbf{\Omega}}{dt} = \sum_k m_k(\mathbf{r}_k - \mathbf{R}_0) \times f_k \tag{3.64}$$

where, M represents the mass of the object, I denotes the moment of inertia, $\mathbf{V}$ signifies velocity, $\mathbf{\Omega}$ represents rotational velocity, and $\mathbf{R}_0$ denotes the centre of mass. Equations 3.63 and 3.64 are then numerically integrated over time to predict the values of $\mathbf{V}$ and $\mathbf{\Omega}$ at the next timestep.

Each boundary particle of the body possesses a velocity $\mathbf{u}$, given by:

$$\mathbf{u}_k = \mathbf{V} + \mathbf{\Omega} \times (\mathbf{r}_k - \mathbf{R}_0) \tag{3.65}$$

If mechanical constraints—defined by changes in velocity and angular momentum within a specified time step are met, the simulation progresses to incorporate DCDEM principles. Here, additional forces and moments are applied to solid particles to simulate detailed physical responses, such as collisions or deformations. If the time threshold is exceeded, the process recalculates the fluid-solid interaction with updated conditions. Otherwise, the system updates all particle states, including position, velocity and density in preparation for the next time-step simulation. The in-

tegration ensures that mechanical constraints (due to collisions or other interactions between solid particles and fluids) are consistently managed to reflect realistic physical behaviors.

Chapters 5 and 6 of this thesis employ the Smoothed Particle Hydrodynamics (SPH) method coupled with the Discrete Element Method (DEM) to model particle migration and solid-liquid flows in the horizontal pipe. The rheological behavior of all non-Newtonian fluids considered in this study is governed by the Herschel-Bulkley-Papanastasiou (HBP) model. This model is applied to investigate a range of scenarios, including non-Newtonian single-phase flows in pipes and mixing processes in stirred vessels.

Chapter Four

SPH APPROACH FOR MODELING SINGLE-PHASE NEWTONIAN AND NON-NEWTONIAN FLUIDS IN PIPES

4.1 Introduction

Newtonian fluids are the starting point of fluid mechanics, however various industrial processes involve complex rheological fluids flow, which are characterised by a variety of rheological properties and can no longer be described by simple Newtonian behaviour. Indeed, in the process industries, Newtonian fluids are often the exception rather than the rule. Non-Newtonian fluids are commonly used in a wide range of industrial applications, including most multiphase mixtures, high molecular weight systems and their solutions, usually these multiple mixtures exist as emulsions, suspensions, foams/foams, dispersions. High molecular weight systems and their solutions, food, pharmaceuticals, personal care products, agrochemicals and industrial applications, pharmaceuticals, personal care products, agrochemicals, synthetic propellants, and slurry fuels. Non-Newtonian fluids exhibit a wide variety of behaviours that depart from the linear relationship

between shear stress and shear rate observed in Newtonian fluids. These characteristic properties that distinguish them play a key role in different industrial and natural processes, ranging from food processing and pharmaceutical manufacturing to geophysical phenomena. A signature feature of non-Newtonian fluids is their shear rate dependence, i.e., the viscosity varies with the rate of deformation. Unlike Newtonian fluids, which maintain a constant viscosity regardless of the applied shear rate, non-Newtonian fluids can exhibit shear-thinning, shear-thickening or viscoelastic behaviour. The viscosity of shear-thinning fluids (such as some polymer solutions and suspensions) decreases with increasing shear rate. Conversely, the viscosity of shear-thickening fluids (e.g., corn starch suspensions) increases with increasing shear rate. Viscoelastic fluids (e.g. polymer solutions such as poly (ethylene oxide) or biological fluids such as blood) respond to deformation with both viscous and elastic responses, resulting in complex flow behaviour. Another characteristic of non-Newtonian fluids is dependence on time, stress history and flow conditions. These fluids may exhibit time-dependent behaviour known as thixotropy or rheology. These fluids may exhibit time-dependent behaviour, known as thixotropy or rheology, where the viscosity changes over time at a constant shear stress or shear rate. In addition, the flow behaviour of non-Newtonian fluids can be affected by factors such as temperature, pressure and additives, leading to changes in viscosity and flow properties.

Understanding the typical characteristics of non-Newtonian fluids in pipe is essential for designing efficient processes, optimizing product performance, and predicting flow behavior in various applications. By elucidating the complexities of non-Newtonian fluid behavior, researchers and engineers can develop tailored solutions to meet specific industrial and scientific needs, driving innovation and progress in diverse fields. In mesh-based method, there are various non-Newtonian rheology models installed into commercial software like Ansys (CFX). The key issue of applying SPH to simulate the non-Newtonian flows is lack of proper numerical rheology models. HBP-SPH model has been proved to simulate debris flow behavior over bed sediment in 3D simulations (Han et al., 2020).

The SPH simulation results were compared to other numerical technique and theoretical solutions. The objective of this chapter is to employ a numerical model to simulate the flow behavior of both laminar Newtonian and non-Newtonian fluids within a straight and horizontal pipe. This numerical approach, utilizing the Herschel-Bulkley-Papanastasiou (HBP) model within the Smoothed Particle Hydrodynamics (SPH) framework, facilitates the investigation of fluid flow characteristics. Specifically, it enables the analysis of velocity profiles, pressure distributions, and shear stress distributions under varying conditions and rheological properties. By integrating the HBP model into the SPH framework, this study aims to provide insights into the complex behavior of non-Newtonian fluids in pipe flow scenarios.

4.2 Theory

In this section, the basic formulas and velocity distributions of pipe flow velocities for Newtonian and three classical non-Newtonian fluids (e.g., the power law, Bingham's model, and the Herschel-Buckley model) are discussed.

4.2.1 Newtonian Fluids

To simulate fluids of Newtonian rheology in viscous flow by SPH, the Newtonian model ($\tau = \eta\dot{\gamma}$) with a constant viscosity (η) was used.

4.2.2 Non-Newtonian Fluids

Shear thinning fluids, also known as pseudoplastic fluids, are characterised by an apparent viscosity which decreases with increasing shear rate. Most shear thinning fluids, however, exhibit

a Newtonian behaviour at very low and very high shear rates, resulting in two limiting values of the apparent viscosity, a zero-shear viscosity, μ_0, and an infinite shear viscosity, μ_∞, respectively. Shear thinning behaviour can be represented using different mathematical models, as described below.

Power Law Model

The power law model is the fundamental constitutive equation used to describe the flow behaviour of non-Newtonian fluids. It describes how the shear stress to which a fluid is subjected varies with the rate of deformation (i.e., shear rate) of the fluid. This model represents the correlation between shear stress and shear rate through a Power law expression, which takes the form:

$$\tau = k\dot{\gamma}^n \tag{4.1}$$

where τ is the shear stress, k is the consistency index, $\dot{\gamma}$ is the shear rate, and n is the flow behaviour index.

where τ is the shear stress, the constants k and n are, respectively, flow consistency index and flow behaviour index. The coefficient of consistency reflects a fluid's resistance to deformation, whereas the index of flow behaviour indicates the degree to a fluid exhibiting shear-thinning or shear-thickening behaviour. By fitting experimental data to power law models, engineers and researchers can determine the rheological properties of non-Newtonian fluids and predict their behaviour in a variety of industrial processes and applications. And n value is in range of 0 to 1, when n = 1, this model is reduced to a simple Newtonian one with a constant viscosity equal to k.

In pipe flow, the power law model can describe the velocity profile of non-Newtonian fluids. This model relates the velocity (μ_f) of the fluid at different radial positions (r) within the pipe to the shear stress (τ) experienced by the fluid. The power law expression for the velocity profile is given

by:

$$u_f(r) = \frac{1}{2n}\left(\frac{R^n \cdot \tau_w}{K}\right)\left(\left(\frac{R}{r}\right)^n - 1\right) \tag{4.2}$$

where R is the radius of the pipe, τ_w refers to wall shear stress. This equation represents the variation of velocity across the radial direction of the pipe, with the velocity being maximum at the center ($r = 0$) and decreasing towards the wall ($r = R$). By analysing and comparing the velocity profile predicted by the power law model to experimental data and numerical data, researchers can validate the experimental set-up and numerical model, also gain insights into the flow behavior of non-Newtonian fluids in pipe flow, aiding in the design and optimization of industrial processes.

Bingham model

The Bingham model characterizes the flow behavior of viscoplastic fluids, which exhibit a yield stress below which they behave like solids and above which they flow like fluids. The model is used in a wide variety of industrial applications because of its ability to represent such materials simply and effectively. The basic apparent viscosity (μ) of the liquid phase in Bingham model is given by:

$$\mu = \begin{cases} K\dot{\gamma}^{n-1} + \tau_y & \tau > \tau_y \\ \mu \to \infty & \tau \leq \tau_y \end{cases} \tag{4.2}$$

where τ_y is the shear stress and apparent yield stress. The mean velocity profile outside the plug region is defined by:

$$u_f(r) = \frac{\Delta P}{L}\left(\frac{R^2 - r^2}{4\mu}\right) - \frac{\tau_y}{\mu}[R - r], \quad r > R_P \tag{4.3}$$

where R_P represents the radius of the plug region, L is the pipe length. Radius of plug region can be calculated as:

$$R_P = \frac{2L\tau_y}{\Delta P} \tag{4.4}$$

For $r < R_P$, the velocity is calculated by:

$$u_f(r) = \left(\frac{\Delta P}{L}\right) \cdot \left(\frac{R^2}{4\mu}\right) \cdot \left(1 - \frac{R_P}{R}\right)^2, \quad r < R_P \tag{4.5}$$

Herschel-Bulkley model

For more complex rheology, the Herschel-Bulkley (HB) model is used to estimate the apparent viscosity (μ) of the liquid phase as follow:

$$\mu = \begin{cases} K\dot{\gamma}^{n-1} + \frac{\tau_y}{\dot{\gamma}} & \tau > \tau_y \\ \infty & \tau \leq \tau_y \end{cases} \tag{4.7}$$

Where, for $n = 1$, HB model is transferred to Bingham plastic fluids. The velocity radial distribution is described as:

$$u_f(r) = \left(\frac{nR}{n+1}\right) \cdot \left(\frac{\tau_w}{K}\right)^{1/n} \left[\left(1 - \frac{\tau_y}{\tau_w}\right)^{(n+1)/n} - \left(\frac{r}{R} - \frac{\tau_y}{\tau_w}\right)^{(n+1)/n}\right] \tag{4.8}$$

The Reynolds number of a non-Newtonian fluid is given in terms of the effective viscosity of the fluid, μ_{eff}, thus,

$$Re = \frac{\rho \bar{u} D}{\mu_{eff}} \tag{4.9}$$

where, $\bar{u}$ denotes the mean flow velocity, and D is the pipe diameter. For a non-Newtonian fluid, the effective viscosity is calculated by:

$$\mu_{eff} = m' \left(\frac{8\bar{u}D}{D} \right)^{n'-1} \tag{4.10}$$

For power law type flows,

$$m' = K \left(\frac{3n+1}{4n} \right)^{n}, \quad n' = n \tag{4.11}$$

For Bingham and HB model fluids,

$$m' = \tau_w \left(\frac{\mu}{\tau_w \left(1 - \frac{4}{3}\Phi + \frac{\Phi^4}{3} \right)} \right)^{n'}, \quad n' = \frac{1 - \frac{4}{3}\Phi + \frac{\Phi^4}{3}}{1 - \Phi^4} \tag{4.12}$$

Where, $\Phi = \frac{\tau_y}{\tau_w}$, refers to the ratio of yield stress to wall shear stress.

4.3 FVM simulations

We used a pipe with 40 mm diameter, and 70 mm length to simulate Newtonian and non-Newtonian in horizontal pipe flows. Simulation of multiphase flow by FVM used the Eulerian-Lagrangian approach by solving the fluid phase as a continuum (Eulerian) and the dispersed phase as a discrete phase within a Langrangian framework by resolving the force balance on each numerical particle.

The mass and momentum conservation equations are expressed, respectively, as (Yeoh et al., 2019):

$$\frac{\partial}{\partial t}(\alpha_L \rho_L) + \nabla \cdot (\alpha_L \rho_L \vec{u}_L) = 0 \tag{4.6}$$

and

$$\frac{\partial}{\partial t}(\alpha_L \rho_L \vec{u}_L) + \nabla \cdot (\alpha_L \rho_L \vec{u}_L \vec{u}_L) = -\alpha_L \nabla p + \nabla \cdot \left[\alpha_L \mu_L \left(\nabla \vec{u}_L + \nabla \vec{u}_L^T\right)\right] + \alpha_L \rho_L \vec{g} + \vec{F} \tag{4.7}$$

where, α_L, ρ_L, $\vec{u}_L$, and μ_L are the volume fraction, density, velocity, and viscosity of the liquid phase. p is the pressure of the whole flow system, and $\vec{g}$ is the gravitational acceleration. $\vec{F}$ represents the forces due to interaction with the discrete phase. When simulating single-phase liquid flow, $\alpha_L = 1$ and $\vec{F} = 0$.

A number of turbulence models exist. Here, the Reynolds-averaged Navier-Stokes (RANS) k-ε model was used:

$$\frac{\partial}{\partial t}(\alpha_L \rho_L k_L) + \nabla \cdot (\alpha_L \rho_L \vec{u}_L k_L) = \nabla \cdot \left(\alpha_L \left(\mu_L + \frac{\mu_{t,L}}{\sigma_k}\right) \nabla k_L\right) + \alpha_L G_{k,L} - \alpha_L Y_k + \alpha_L G_{kb,L} \tag{4.8}$$

and

$$\frac{\partial}{\partial t}(\alpha_L \rho_L \varepsilon_L) + \nabla \cdot (\alpha_L \rho_L \vec{u}_L \varepsilon_L) = \nabla \cdot \left(\alpha_L \left(\mu_L + \frac{\mu_{t,L}}{\sigma_\varepsilon}\right) \nabla \varepsilon_L\right) + \alpha_L G_{\varepsilon,L} - \alpha_L Y_\varepsilon + \alpha_L G_{\varepsilon b,L} \tag{4.9}$$

where, k and ε are the turbulent kinetic energy and its dissipation rate; $G_{k,L}$ and $G_{\varepsilon,L}$ are the generation of turbulence kinetic energy and specific dissipation rate; Y_k and Y_ε are the dissipation of turbulence kinetic energy and specific dissipation rate; and $G_{\varepsilon b,L}$ and $G_{eb,L}$ are the generation of turbulence kinetic energy and specific dissipation rate due to buoyancy effects. For flows of low turbulence ($Re < 10,000$), the shear stress transportation (SST) model was used (Menter et al., 2003).

4.4 SPH simulations

4.4.1 Geometry

The pipe boundary is consisting of a group of numerical boundary particles in SPH simulations, the length L is 0.07 m length, and D is 0.04 m. As shown in Figure 4.1, the geometry is discretised with numerical particles of a specified particle spacing (S_p). Optimisation of the particle spacing is essential to carry out the Sp-independence study, which is done by performing several simulations with different particle spacings, starting with a larger spacing and improving until the results are no longer dependent on the proximity of the particle spacings. With this approach, the particle spacing was determined for the whole region, taking into account the balance between computational time and accuracy, in this chapter the particle spacing was 0.006 m.

As a result of the no-slip condition of the pipe wall, a high variable gradient usually exists near the wall, and here up to 60 boundary layers are created near the wall in order for the wall liquid particles to penetrate the pipe surface. This allowed a more accurate prediction of the flow variables in this region.

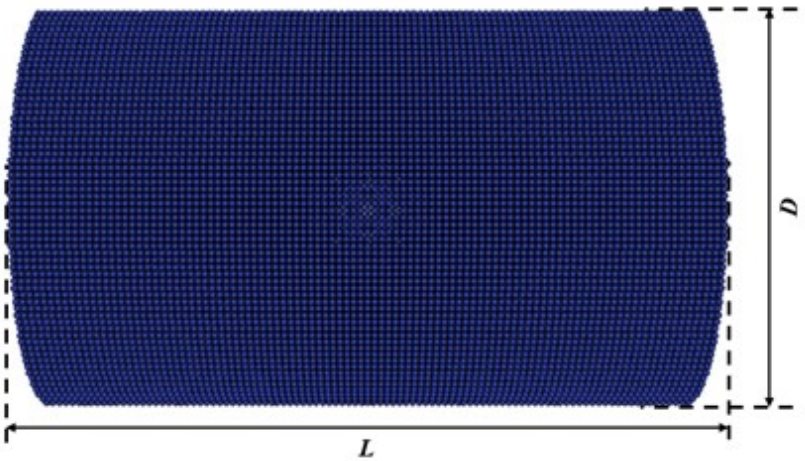

Figure 4.1: The snapshot of 3D pipe geometry in SPH simulations

4.4.2 Simulation setup

The HBP rheology model details are illustrated in section 3.2, which was used to model the rheology of carrier fluids. Time step is following the variable time step methodology described in section 3.4.3. In SPH, periodic boundary conditions are applied at the inlet and outlet of the pipe in all single-phase simulations, which reduces computational work significantly. Buffer layers are implemented to enforce open boundaries at the inlet and outlet, as shown in Figure 4.2, which serve to mitigate errors that arise due to kernel truncation near boundaries. Within these buffer regions, particles are introduced or removed to avoid the occurrence of voids. The physical quantities, such as velocity and pressure, of the buffer numerical particles can be extrapolated from the fluid domain. The numerical representation of the wall boundary introduces a set of boundary particles. In SPH cases, up to sixty layers of such particles were utilized. SPH particles representing the liquid phase are initialized within the pipe domain using a uniform distribution to ensure smooth density and pressure calculations. The pipe flow is driven by a constant pressure gradient, which gradually establishes the expected velocity profile. Initially, all fluid particles are assigned a velocity of zero, allowing the flow to develop naturally over time under the applied pressure difference, ensuring a stable and physically accurate simulation.

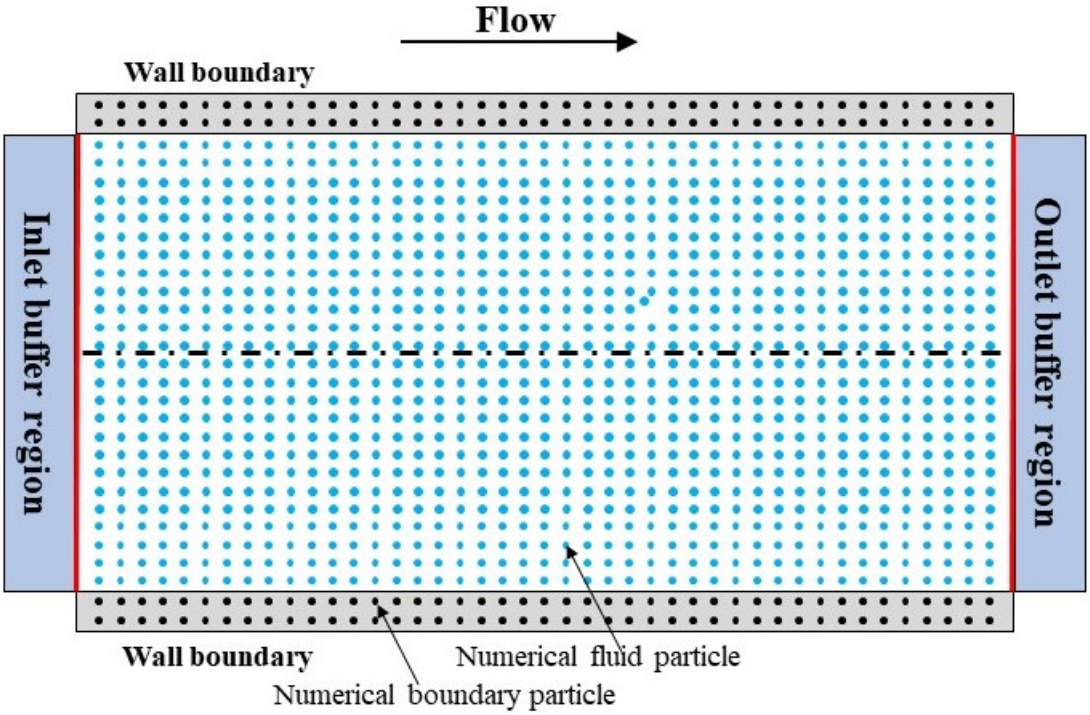

Figure 4.2: Schematic of the boundary conditions in single phase flow

Table 4.1: Modelling parameters used in SPH and FVM simulations.

Liquid phase	**SPH**	**FVM**
Papanastasiou parameter, m (-)	10	-
Power-law index, n (-)	0.89	0.89
Mesh size (m)	-	0.001-0.004
Numerical particle spacing (m)	0.0006	-
Kernel function	Wendland	-
Kernel smooth length, h (m)	$h = 0.1 \cdot \sqrt{3Sp}$	-
Time step, Δt_{Liquid} (s)	0.000005	0.001

In this chapter, SPH simulation results are validated by theoretical solutions and FVM data, the

FVM data in this work is in-house and provided by Dr. Zhuangjian Yang, details set-up of FVM can be founded in the paper (Yang et al., 2024), in which SPH data are come from this thesis. The numerical parameters used in SPH simulations are listed in Table 4.1.

4.5 Results and discussion

To thoroughly assess the capability and performance of both the mesh-based FVM method and meshfree particle-based SPH method, investigated single-phase and two-phase particle-liquid flows of various levels of complexity, including: (i) single-phase viscous flow of Newtonian fluids as well as non-Newtonian fluids represented by various rheology models, namely power-law, Bingham plastic and Herschel-Bulkley covering a wide range of rheological parameters; (ii) single-phase turbulent flow of Newtonian fluids. Finally, a comprehensive computational cost analysis of these two methods was conducted.

4.5.1 Laminar simulation of Newtonian fluids

The radial velocity profiles predicted by FVM and SPH at Reynolds numbers (Re) from 20 to 1,000 are presented in Figure 4.3, alongside their corresponding theoretical parabolic profiles (Bird et al., 1977). Overall, the plots show very good agreement between simulation data and theory. However, whilst FVM results demonstrate excellent adherence to the theoretical profiles, SPH results exhibit a minor deviation (overestimation) near the pipe wall which may be attributed to the fact that the SPH wall boundary gives a reasonable approximation of the no-slip condition but does not perfectly enforce it.

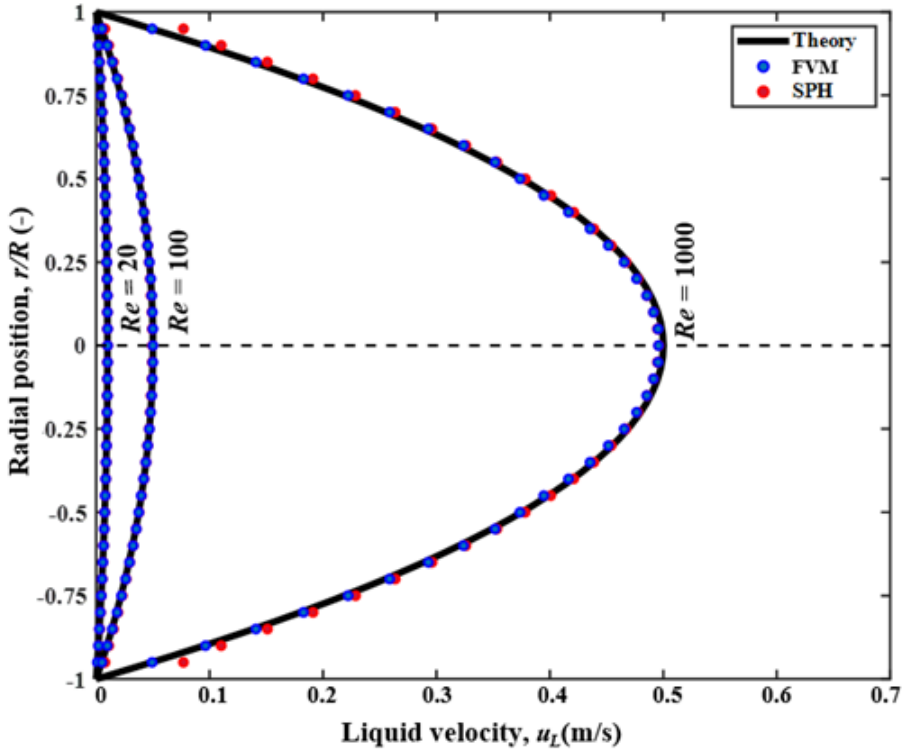

Figure 4.3: FVM and SPH predictions of radial velocity profile in laminar Newtonian flow compared to analytical solution: $\rho_L = 1{,}000$ kg m^{-3}; $\mu_L = 0.001$ Pa s.

4.5.2 Laminar simulation of power law fluids

The radial velocity profiles predicted by FVM and SPH for power law fluids of varying flow behaviour index (n) are plotted in Figure 4.4, alongside their analytical solutions (Bird et al., 1977). Over a wide range of n values from 0.6 to 1.4, FVM produces excellent predictions matching very closely the theoretical velocity profiles across almost the entire pipe cross-section. The SPH method demonstrates very good agreement with the theory in the central region, but displays some significant near the wall, probably arising from the approximated treatment of the no-slip condition, as pointed out above.

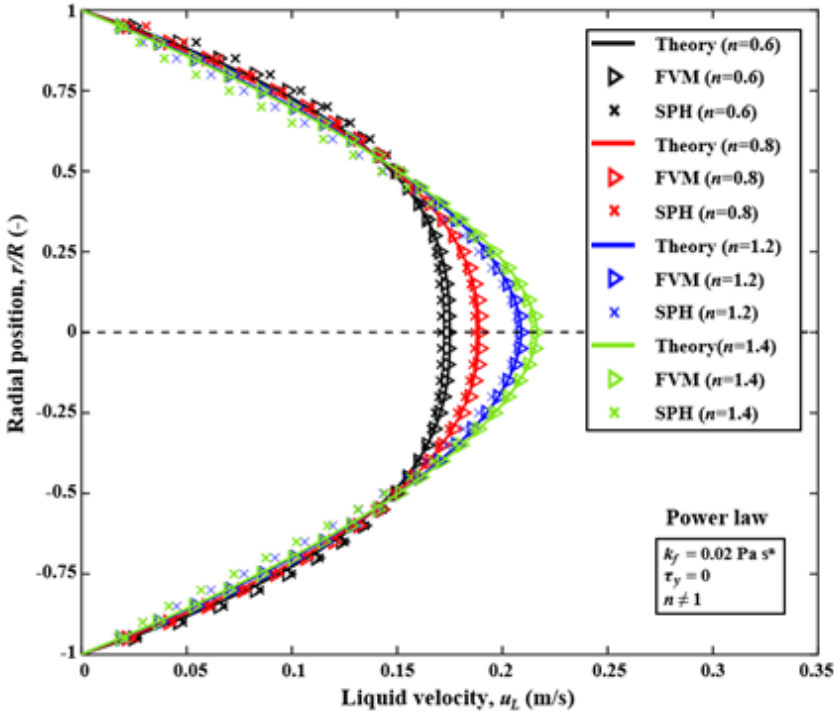

Figure 4.4: FVM and SPH predictions of radial velocity profile in laminar flow of different power-law fluids compared to analytical solution.

4.5.3 Laminar simulation of Bingham fluids

In the flow of Bingham plastic fluids, a critical parameter is the apparent yield stress (τ_y) which is the variable under investigation here, while the fluid consistency index (k) is kept constant. As shown in Figure 4.5, both FVM and SPH exhibit excellent agreement with the theoretical predictions over a range of τ_y values from 1 to 7 Pa, particularly in the central plug region. However, there SPH yields tends to underestimate the fluid velocity in the vicinity of the wall compared to the theoretical solution. Despite incorporating more accurate modified dynamic boundary condition, the predictive ability of SPH near the wall still requires further refinement. This limitation is attributed to the current state-of-the art of the meshfree particle-based method, wherein 3D curved surface boundaries need further improvement (English et al., 2022).

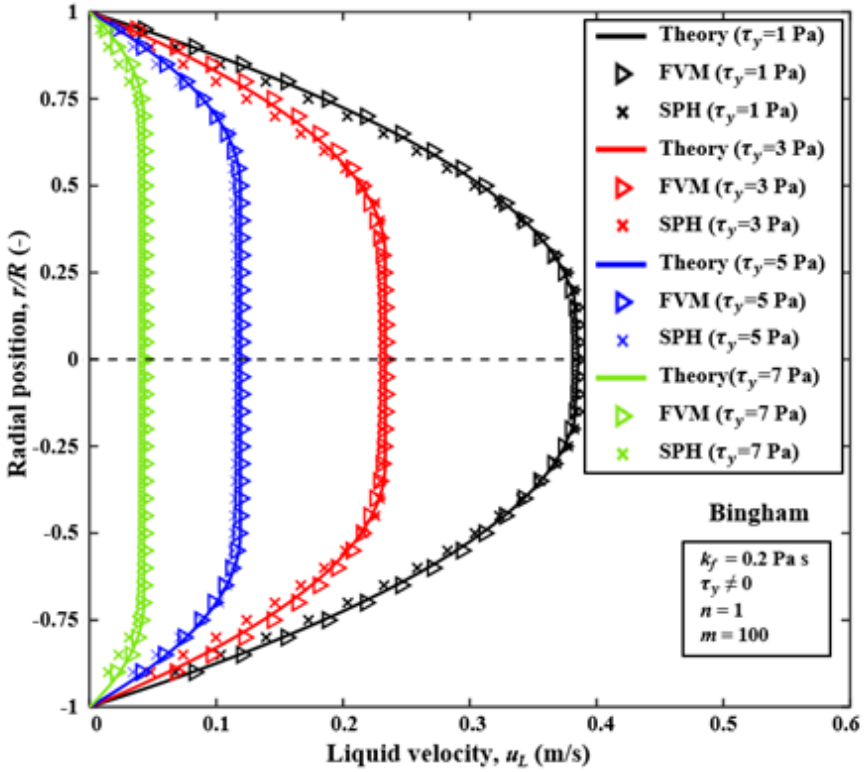

Figure 4.5: FVM and SPH predictions of radial velocity profile in laminar flow of different Bingham plastic fluids compared to analytical solution.

4.5.4 Laminar simulation of Herschel–Bulkley fluids

The Figure 4.6 depicts the comparison of liquid velocity profiles for a Herschel-Bulkley fluid across different shear-thinning indices (n). The radial position normalized by the pipe radius (r/R) is plotted against the liquid velocity (u_L). The black, red, blue, and green curves represent the theoretical predictions for n values of 0.6, 0.8, 1.2, and 1.4, respectively. The Herschel-Bulkley fluid parameters used in the simulations include a consistency factor (k_f) of 0.2 Pa·s^n, a yield stress (τ_y) of 3 Pa, and a Papanastasiou parameter (m) of 10,000. This figure demonstrates the agreement between the theoretical, FVM, and SPH velocity profiles across different shear-thinning indices, validating the numerical methods' accuracy in simulating the behavior of Herschel-Bulkley fluids in pipe flow. Notably, both CFD and SPH exhibit excellent accuracy compared to theory.

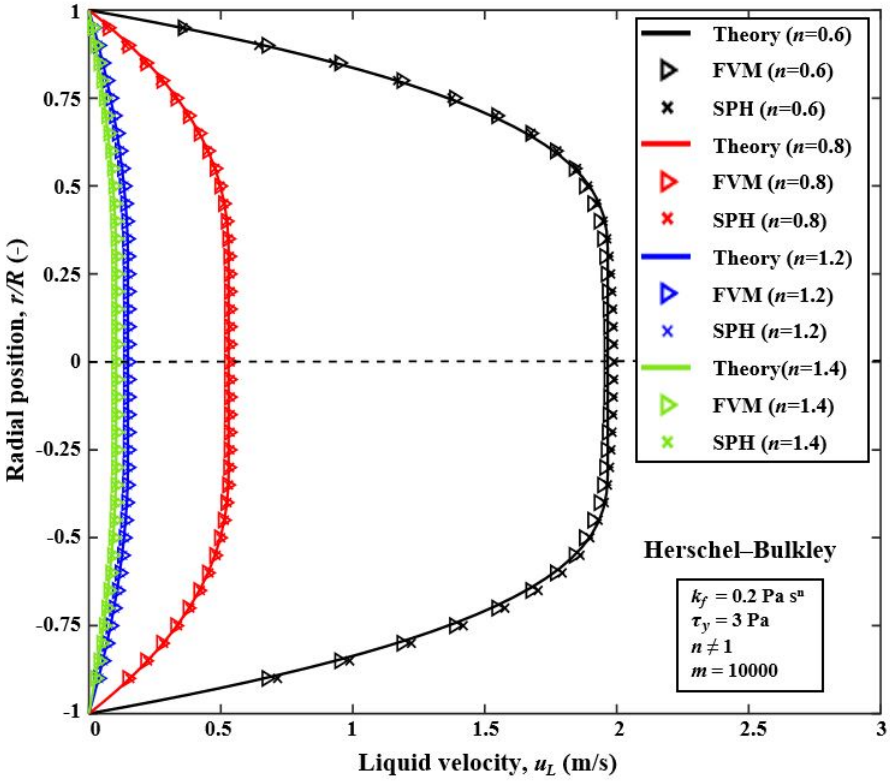

Figure 4.6: FVM and SPH predictions of radial velocity profile in laminar flow of different Herschel–Bulkley fluids compared to analytical solution.

4.5.5 Turbulent flow of single-phase Newtonian fluids

The capability and predictive performance of FVM and SPH is examined in the turbulent regime across a range of Reynolds numbers from 4,500 to 108,000 and presented in Figure 4.7. At low turbulence ($Re = 4,500$), slightly above the transition regime, both FVM and SPH exhibit good agreement across most of the pipe cross-section with the well-known theoretical one-seventh power law relationship which is valid for $4,500 < Re < 20,000$ (Chant, 2005). At $Re = 7,800$, PEPT data are also shown alongside the one-seventh power law relationship. The FVM predictions coincide very well with the theoretical and experimental results, SPH produces some deviations, particularly in the wall region. At low turbulence ($Re = 4,500$), slightly above the transition regime, both

FVM and SPH exhibit good agreement across most of the pipe cross-section with the well-known theoretical one-seventh power law relationship which is valid for $4,500 < Re < 20,000$ (Chant, 2005). At $Re = 7,800$, PEPT data are also shown alongside the one-seventh power law relationship. The FVM predictions coincide very well with the theoretical and experimental results, SPH produces some deviations, particularly in the wall region.

At $Re = 12,000$, the FVM accuracy remains unchanged, but the SPH discrepancies become more significant over most of the pipe radius. Although applying the SPS model and shifting algorithm has been reported to improve SPH stability and precision for treating turbulent flows, the method encountered serious challenges in achieving accurate results for $Re > 12,000$ (Vacondio et al., 2013). The ability of SPH to simulate turbulent flows is limited at present because of the lack of appropriate turbulence models. This is an area in need of further development.

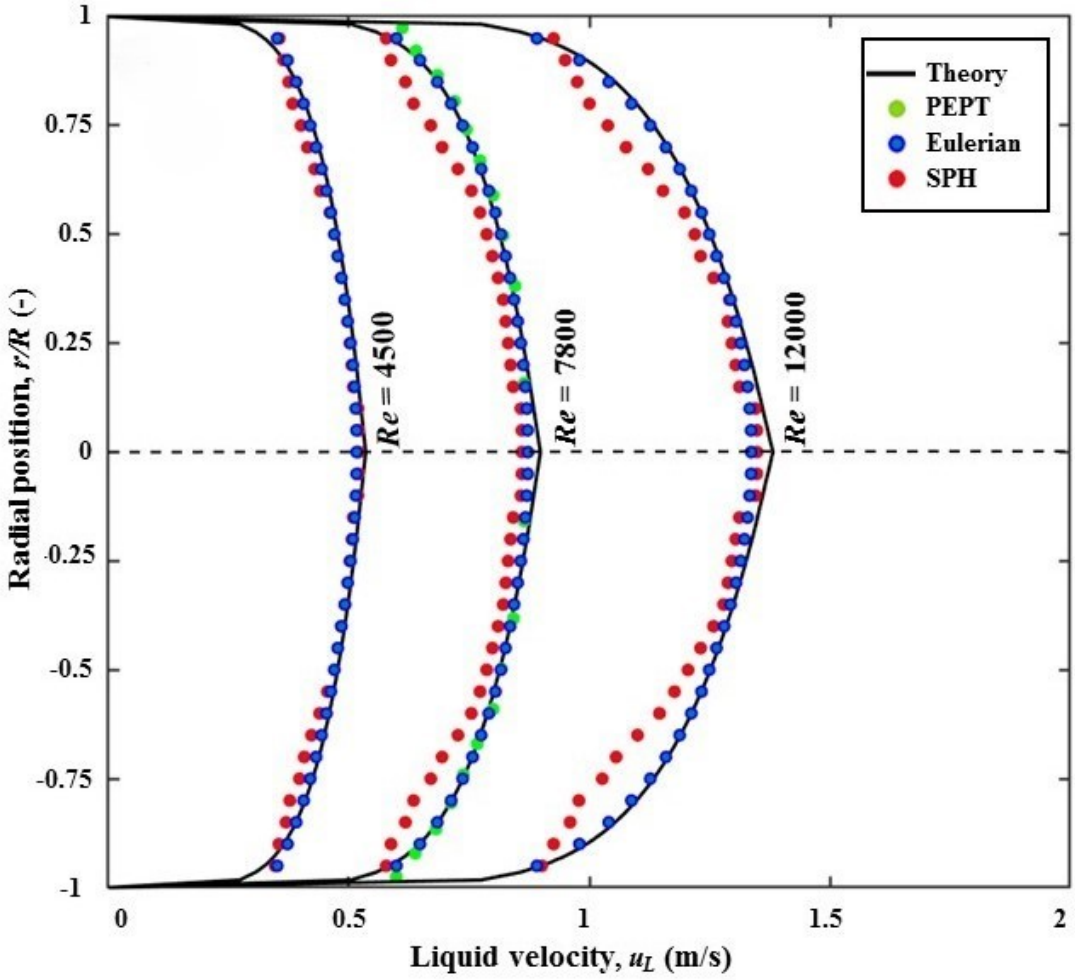

Figure 4.7: FVM and SPH predictions of radial velocity profile in turbulent Newtonian flow compared to one-seventh power law correlation and experimental measurements.

Computational cost is an important element in assessing the cost-effectiveness of numerical modelling in practical applications. Recent advancements in computer science have led to significant increases in both CPU and GPU computational power, making the implementation of CPU-GPU solutions possible. An illustrative study utilizing 12 CPUs (Intel® Xeon® Silver 4214 Processor) and a GPU (NVIDIA® GeForce® RTX 2080) was used to estimate the computational time for different numerical FVM and SPH simulations, as summarised in Table 4.2. For single-phase

flow (Re=100, section 4.1.1) , the computational time was negligible in FVM simulations. For the FVM simulation, with 228,456 mesh particles, the simulation time is 0.05 hours on a CPU and 0.03 hours on a CPU-GPU system. In contrast, the SPH model, which uses 533,019 numerical particles, takes significantly longer to simulate. The SPH simulation time is 12.6 hours on a CPU and 0.4 hours on a CPU-GPU system. This table highlights the substantial reduction in simulation time achieved by using GPU acceleration, particularly in the SPH simualtions.

Table 4.2: Computational cost comparison of SPH and FVM.

	Number of mesh/numerical particles	Simulation time (hr)	
		CPU	CPU-GPU
FVM	228,456	0.05	0.03
SPH	533,019	12.6	0.4

4.6 Conclusion

In this charpter, the capabilities and performance of the mesh-based Finite Volume Method (FVM) and the mesh-free particle-based Smoothed Particle Hydrodynamics (SPH) in simulating single-phase Newtonian and non-Newtonian flows are compared. Through a comprehensive analysis encompassing both laminar and turbulent flow regimes, as well as various fluid rheologies, the study highlights the strengths and limitations of each approach.

In single-phase flow, the FVM method shows excellent agreement with the theoretical model and provides accurate predictions in a wide range of conditions, including laminar and turbulent states. This shows the robustness of the FVM in dealing with different flow conditions and its reliability in predicting the flow behaviour. Meanwhile, the SPH approach, despite its approximations in terms of boundary conditions, excels in capturing complex fluid dynamics, especially laminar flows.The

meshless nature of SPH allows it to easily handle deformable boundaries and complex geometries, which makes it particularly effective in situations that may be difficult to resolve with conventional mesh methods. However, the ability of SPH to simulate turbulence is currently limited due to the lack of appropriate turbulence models in the SPH framework. Improving the applicability of SPH to a wider range of turbulent flows is also one of the current challenges and development directions for SPH.

In laminar regime, SPH is able to capture accuracy velocity distribution in pipe flow. The turbulent SPH simulations are limited to by turbulence model in SPH framework. This chapter has proved that the HBP rheology model in SPH is flexible and excellent to predict different non-Newtonian flow behaviors. HBP model successfully applied in SPH provides a foundation for the study of complex flows such as solid-liquid two-phase flows and mixed flows.

Chapter Five

INVESTIGATING INERTIAL PARTICLE MIGRATION: NUMERICAL MODELLING VIA INTEGRATION OF SPH WITH DEM

5.1 Introduction

Particle-laden flows are prevalent in both natural and industrial settings, serving diverse applications across the scales, including blood flow, food and chemical processing, river engineering, energy generation and construction. Consequently, extensive theoretical and experimental efforts have been devoted to unravelling the complexities of particle behaviour in such flows. One notable phenomenon, the radial migration of particles in viscous pipe flow, where neutrally-buoyant spheres move laterally away from the wall towards a stable equilibrium position, was first reported by Segré and Silberberg and came to be generally recognised as the Segré-Silberberg effect (Segre et al., 1961). Building on Segré and Silberberg's work, subsequent experimental studies explored

cross-streamline migration at moderately high Reynolds (*Re*) numbers up to 2,400 (Matas et al., 2004), revealing a shift towards the wall of the equilibrium radial position as Re increased. Karnis (1966) attributed the phenomenon to inertial effects, and later Tachibana (Tachibana, 1973) determined that the clarity of the phenomenon increases when the particle-to-pipe diameter ratio surpasses 0.2. Such findings were corroborated by other researchers such as Eloot, et al. (2004) in particle migration experiments, highlighting the critical influence of parameters like the carrier liquid flowrate, solids volume fraction, particle-to-liquid density ratio, particle-to-pipe diameter ratio, particle shape and pipe length on the trajectories of particles and their lateral particle equilibrium positions.

The challenge of conducting particle migration studies under various flow conditions arises from the complex experimental design and strict in-process control, especially when dealing with neutrally buoyant particles. Such challenges are compounded by numerous factors, including flow configuration, particle characteristics and fluid rheology. Consequently, in the absence of adequate theoretical treatments, diverse numerical modelling methodologies have been developed, each possessing distinct advantages and drawbacks, to study particle migration in diverse flow scenarios. Computational Fluid Dynamics (CFD) in its various forms has been the prevalent numerical technique for simulating particle migration. A number of researchers such as Feng et al., (1994) employed direct numerical simulation (DNS) to investigate the migration of a single circular particle in a two-dimensional (2D) Poiseuille flow. Joseph and Ocando (2002) explored the correlation between lift force and angular slip velocity through DNS, while Yu, et al. (2004) utilized a finite-difference-based distributed Lagrange multiplier (DLM) method to obtain results on radial, angular, and axial velocities for both neutrally and non-neutrally buoyant spherical particles in a vertical Poiseuille flow at Reynolds numbers up to 300. Pan and Glowinski (2005) simulated the motion of neutrally buoyant balls in a circular Poiseuille flow also using DNS. Yang et al. (2005) delved into correlations for lift force on a neutrally buoyant particle undergoing rotational and forward movement without radial velocity at Re values up to 250, employing packages based

on both moving and adaptive grids and distributed Lagrange multipliers (DLM) on a fixed grid . Shao et al. (2008) employed a fictitious domain method to numerically examine the inertial migration of neutrally buoyant spherical particles in a tube at moderately high Reynolds numbers up to 2,200. A substantial body of literature has also been generated, focusing on various aspects such as neutrally and non-neutrally buoyant particles with a particle-to-liquid density ratio of 0.98-1.02 in a linear shear flow-dominated channel with Reynolds numbers up to 500 (Liu et al., 2021; Safa et al., 2019).

Another major technique which has been employed is the lattice Boltzmann method (LBM) (Hu et al., 2017; Li et al., 2004). In LBM, any given phase or component is represented as clusters of molecules situated on lattice sites, engaging in interactions with neighbouring clusters through 'streaming' and 'collision' processes. Its kinetic foundation obviates the need for explicit phase-interface tracking. The algorithm exhibits efficiency and programming simplicity, facilitating parallelization. Furthermore, LBM has been synergistically coupled with the discrete element method (DEM) or immersed boundary method (IBM) to enhance predictive capabilities. In this way, simulations of particle migration in channels with varying contraction-expansion ratios, yielded detailed particle migration trajectories that would be hard to observe experimentally (Jiang et al., 2019; Zhang et al., 2018). Recently, Hu et al. (2019) applied the LBM-IBM method to inertial particle migration in the Poiseuille flow of a power-law fluid, exploring the influences of Reynolds number, power-law index, and blockage ratio on the formation of particle trains.

Thus, a number of pertinent factors influence particle migration, including particle size, shape and density, flow Reynolds number and fluid rheology. Despite the number of modelling attempts, however, the comprehensive study of these parameters remains limited, being piecemeal with no single technique capable of addressing all factors. Each numerical method has its constraints, leading to investigations focusing on specific subsets of influential parameters within confined flow scenarios. For example, certain numerical methodologies (e.g., LBM) are better at analysing the effects of particle properties (Zhu et al., 2007), while others (e.g., DNS) are more suitable

for simulating the influence of fluid rheology, and some (e.g., DLM) are more adept at exploring the impact of flow regime (Lixing, 2010). Although considerable numerical simulation work has been conducted in this area by previous researchers, most of it focuses on the variation of specific parameters. For example, much of the research is based on grid-based methods, where the particle size typically does not exceed 2 cm, and the fluid involved lacks complex rheological properties. This chapter aims to present a generalized meshless approach to simulating particle migration that addresses these limitations and extends the applicability of such simulations. Therefore, there is still a need for powerful modeling methods that can comprehensively and effectively reveal all phenomena of particle migration so that successful numerical studies can be performed at any time when experiments are limited, too costly, or infeasible.

SPH stands out as a fully Lagrangian, particle-based approach that has gained significant popularity in recent years due to its versatile applications and straightforward implementation (Pozorski et al., 2023). In the SPH framework, the state of fluid is represented by a finite set of numerical particles, wherein the physical properties of a given particle are derived from its proximate neighbours through an interpolation function. This mechanism enables numerical particles to interact within the confined spherical support of the smoothing kernel. The resultant collective motion of SPH numerical particles emulates fluid flow and can be modelled using classical hydrodynamic equations. Notably, SPH has emerged as a promising numerical technique, particularly when coupled with other particle-based methods like DEM, showcasing numerous advantages (Moreira et al., 2020; Tran-Duc et al., 2022). SPH exhibits exceptional adaptability in handling intricate boundary conditions owing to its mesh-free construction (Monaghan et al., 2009; Ye et al., 2019), rendering it well-suited for simulating particle migration problems. When combined with DEM, the SPH-DEM model facilitates facile adjustments to particle characteristics, including shape, size, as well as parameters governing particle-wall and particle-particle collisions (Chen et al., 2020; Sizkow et al., 2021). This heightened flexibility in fluid modelling by SPH, coupled with DEM's efficacy in handling the discrete phase, positions SPH-DEM as a robust methodology for investigating particle

migration across diverse parameters and a wide spectrum of changes.

This chapter investigates the inertial migration of single particles in viscous flow using the technique of SPH-DEM. Through theoretical and experimental validation using high-speed flow visualisation, we demonstrate the significant merits of coupling SPH with an enhanced variant of DEM, namely distributed contact DEM (DCDEM) for superior predictive capability. This variant of DEM can handle the physical properties of the discrete phase much better than traditional DEM, e.g., more complex particle shapes and particle-particle/wall collisions. More importantly in this study, however, DCDEM uses the same principle as SPH to represent suspended particles with clusters of numerical particles and, therefore, is more readily amenable to efficient coupling with SPH. Using this coupling, we analyse the effects of particle size, shape and density, flow Reynolds number and fluid rheology, in significant detail, covering a wide range of parameters: (i) particle-pipe diameter ratios of spheres in the range of 0.00125 - 0.25; (ii) particle-fluid density ratios in the range of 1 - 1.5; (iii) ellipsoidal particles of aspect ratio in the range 0.25 - 0.75; (iv) flow Reynolds numbers in the range 10 - 3,500; and (v) non-Newtonian power-law fluids with varying flow index in the range 0.6 – 1.4. This work serves to underscore the versatility and accuracy of the SPH-DEM methodology in simulating complex multiphase flow phenomena.

5.2 Experiment

Aiming to validate the SPH and SPH-DEM strategies, a closed-loop pipe flow system was employed to observe the equilibrium radial position of a neutrally-buoyant particle in a horizontal Newtonian laminar flow, the experimental set-up was shown in Figure 5.1. A vortex pump (T21-32 HF4 LB1, Turo vortex pump, EGGER, Switzerland) was used to drive fluid through a 3 m long Perspex pipe of internal diameter $D = 0.04$ m. The volumetric flowrate was measured in-line using a Doppler ultrasonic flowmeter (UF D5500, Doppler flow meter, Micronics). Experiments were

conducted under ambient conditions, and a temperature probe was employed to monitor the fluid temperature. The fluid was a 52 wt/wt% glycerol-water solution, while the suspended particle was a Nylon-66 sphere of diameter d_p = 4 mm and density ρ_p = 1,130 kg m^{-3}. The concentration of Glycerol was adjusted to match that of the Nylon-66 particle. The density and viscosity of the carrier fluid were determined before and after each run to ensure they remained constant. To establish fully developed flow and mitigate entrance effects flow visualization was performed downstream of a 60D entrance length (i.e., 2.4 m), as illustrated in Figure 5.1. A Basler acA1300-200um digital camera was employed to capture images of the particle at a rate of 100 frames/s. Front-light illumination was utilised to enhance the quality of the images.

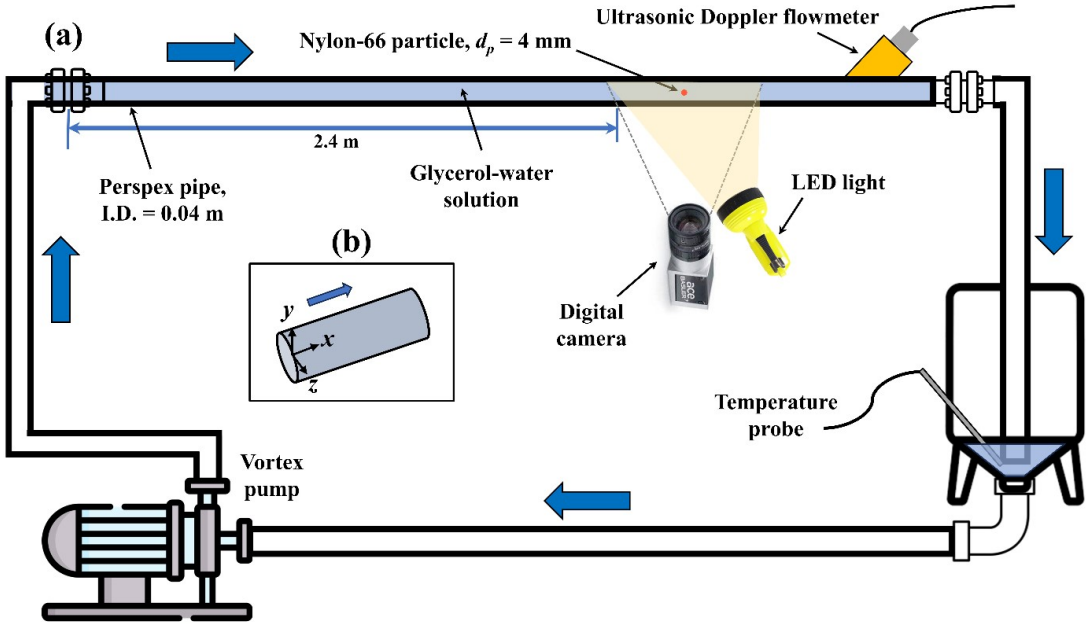

Figure 5.1: Experimental set-up: (a) flow loop and imaging instrumentation; (b) Cartesian coordinate frame.

5.3 Numerical modelling of particle migration

The following sections describe the numerical methodologies employed for simulating the continuous and discrete phases in a viscous particle-laden flow.

5.3.1 Basic governing equations

Mass conservation is employed to quantify variations in fluid density. In order to mitigate fluctuations in fluid density during simulations, an additional density diffusion term is incorporated into the continuity equation:

$$\frac{d\rho_a}{dt} = \sum_b m_b \mathbf{v}_{ab} \cdot \nabla_a W_{ab} + \delta h c_0 \sum_b 2(\rho_{ab}^T - \rho_{ab}^H) \frac{\mathbf{r}_{ab} \cdot \nabla_a W_{ab}}{r_{ab}^2} \frac{m_b}{\rho_b} \tag{5.1}$$

where, a is the target numerical particle and b is anyone of its neighbour particles. The summation is carried out over all particles other than a, and $\nabla_a W_{ab}$ is the gradient of the kernel taken with respect to the position of particle a. Subscript ab denotes the difference in value between numerical particles a and b, e.g., $\mathbf{v}_{ab} = \mathbf{v}_a - \mathbf{v}_b$; ρ, m, $\mathbf{v}$ and $\mathbf{r}$ are density, mass, velocity and distance, respectively. The second term on the right-hand side corresponds to the density diffusion term, where $c_0 = \sqrt{\frac{\partial P}{\partial \rho}}$ denotes the speed of sound at the reference density, and δ represents a coefficient governing the extent of density diffusion. In this formulation, the dynamic density (ρ^D) in the continuity equation is replaced by $\rho^D = \rho^T - \rho^H$ where superscripts T and H denote the total and hydrostatic components, respectively. In a weakly compressible SPH framework, the relationship between total pressure (P) and density is expressed by an artificial equation of state. Using equation of state only considering the hydrostatic part of the pressure, the hydrostatic density difference (ρ_{ab}^H) can be calculated as:

$$\rho_{ab}^{H} = \rho_0 \left(\sqrt[\gamma]{\frac{P_{ab}^{H} + 1}{C_B}} - 1 \right) \tag{5.2}$$

The term P_{ab}^{H} is the hydrostatic pressure difference between numerical particles a and b:

$$P_{ab}^{H} = \rho_0 g z_{ab} \tag{5.3}$$

where, z_{ab} represents the vertical separation between a and b. The parameter c_0 is conventionally set to a value at least 10 times greater than the maximum velocity observed in the flow. To obtain this maximum velocity, the velocity of each numerical liquid particle is tracked through the simulation. At every timestep the model identifies the particle with the highest velocity among all the particles present in the simulation domain, and the value multiplied by 10 is then assigned to c_0. To ensure the reliability of results, it is imperative that at the end of the simulation, the density fluctuations among numerical particles remain below 1% (Gomez-Gesteira et al., 2010). The Lagrangian form of the momentum conservation equation in single particle migration and sub-particle scale model (SPS) are illustrated in section 3.1.2.

The above SPH approach for modelling fluid flow, can also facilitate two-way coupling with rigid body dynamics by treating body geometries as moving boundaries (Domínguez et al., 2022), so that the full particle-liquid flow is modelled by SPH. This methodology resolves the motion of a suspended object (suspended particles) by accounting for its interaction with fluid numerical particles and utilizing these interactions to propel its movement. This begins with the summation of the force contributions across the entire object. Assuming the object is rigid, the net force acting on each boundary particle of the object is computed by adding up the contributions from all surrounding numerical fluid particles. Here, the number of these boundary particles ranged from 20 to 80, depending on the size and shape of the suspended particles and S_p value. Thus, each boundary particle (k) experiences a force per unit mass denoted by:

$$f_k = \sum_a f_{ka} \tag{5.4}$$

where, f_{ka} represents the force per unit mass exerted by fluid particle (a) on boundary particle (k), given by:

$$m_k f_{ka} = -m_a f_{ak} \tag{5.5}$$

To describe the motion of the suspended object, the fundamental equations of rigid body dynamics are then employed, thus:

$$M\frac{d\mathbf{V}}{dt} = \sum_k m_k f_k \tag{5.6}$$

$$I\frac{d\mathbf{\Omega}}{dt} = \sum_k m_k(\mathbf{r}_k - \mathbf{R}_0) \times f_k \tag{5.7}$$

where, M represents the mass of the object, I denotes the moment of inertia, $\mathbf{V}$ signifies velocity, $\mathbf{\Omega}$ represents rotational velocity, and $\mathbf{R}_0$ denotes the centre of mass. Equations 5.6 and 5.7 are then numerically integrated over time to predict the values of $\mathbf{V}$ and $\mathbf{\Omega}$ at the next timestep.

Each boundary particle of the body possesses a velocity $\mathbf{u}$, given by:

$$\mathbf{u}_k = \mathbf{V} + \mathbf{\Omega} \times (\mathbf{r}_k - \mathbf{R}_0) \tag{5.8}$$

Ultimately, the boundary particles constituting the body are displaced by integrating Equation 5.8 over time. If the particle contacts with the pipe wall boundary, the DEM module will be used to calculate the contact force following section 3.5.

5.3.2 Simulation setup and boundary conditions

The simulations were executed in a 2D domain employing DualSPHysics software for 30 s. Pipe flow is essentially unidimensional, so that 2D simulations are sufficient for its accurate representation. Numerous studies in the literature have employed analogous 2D simulations (e.g., CFD, SPH) to investigate diverse flow phenomena (Kim et al., 2021; Ng et al., 2021; Xu et al., 2022). The pipe was simulated over a length of $L = 0.07$ m. DBC is a standard conventional condition to model solid surfaces in SPH simulations, such as the pipe wall. However, a small unphysical gap between the fluid and solid boundaries can arise, contributing to a reduction in the precision of pressure measurements along the boundary. Here, mDBC was introduced wherein the density of solid particles is acquired through linear extrapolation from ghost positions situated within the fluid domain, as shown in Figure 5.2 (English et al., 2022). Through mDBC, the separation between the fluid and boundary is diminished, leading to pressure convergence in undisturbed conditions, including cases involving a sharply cornered bed configuration.

Periodic boundary conditions were applied to both inlet and outlet illustrated in Figure 5.2. Implementation involves enabling numerical particles in proximity to the open lateral boundary to interact with numerical fluid particles near the corresponding open lateral boundary on the opposite side of the domain. When a suspended particle exits the outflow zone, its velocity is automatically reset to zero and temporarily stored in a buffer reservoir. Subsequently, each time a suspended particle enters the flow domain, a particle is extracted from the buffer reservoir and inserted into the upstream side of the inflow zone with the specified prescribed velocity and density.

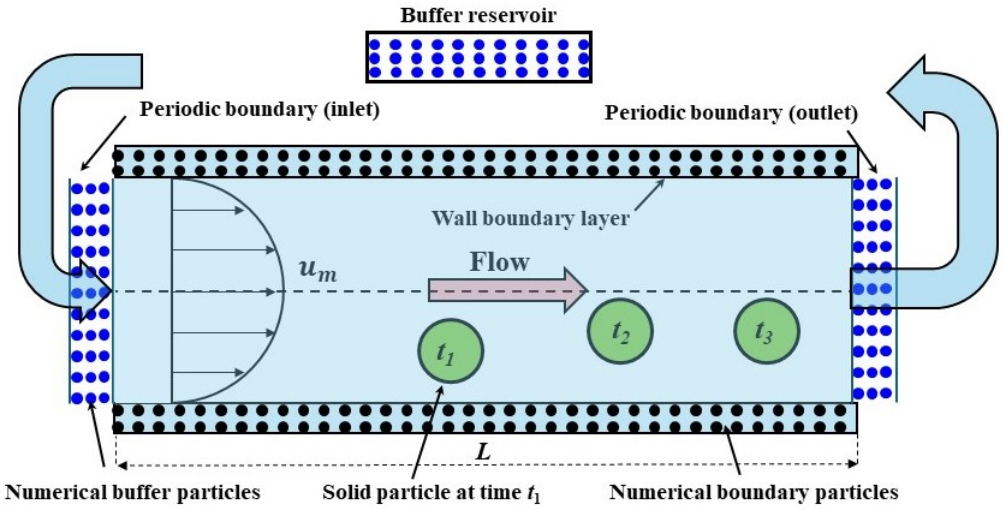

Figure 5.2: Schematics of radial migration of solid particle in a pipe and boundary settings.

The simulation timestep is calculated based on the Courant- Friedrichs-Lewy (CFL) condition. For single particle in the pipe flow, there are three different definitions based on the viscous diffusion and forcing terms in the CFL condition:

$$\Delta t_f = \min_a \left(\sqrt{\frac{h}{|f|}} \right) \tag{5.9}$$

$$\Delta t_{cv} = \min_a \left(\frac{h}{c_0 + \max_b \frac{|h\mathbf{v}_a \cdot \mathbf{r}_a|}{r_{ab}^2 + \eta}} \right) \tag{5.10}$$

$$\Delta t_{DEM} = \frac{3.21}{50} \left(\frac{-M^*}{k_n} \right)^{2/5} v_n^{-1/5} \tag{5.11}$$

where, Δt_f is influenced by the force per unit mass ($|f|$); Δt_{cv} combines the Courant and the viscous timestep controls; v_n is the normal relative velocity, M^* is the reduced mass of the system where there is a contact, and k_n is the stiffness of DEM contact model.

The simulation timestep is taken to be the minimum of the above three values weighted by the C_{CFL} coefficient:

$$\Delta t = C_{CFL} \cdot \min(\Delta t_f, \Delta t_{cv}, \Delta t_{DEM}) \tag{5.10}$$

where, $C_{CFL} = 0.2$.

Initially, the simulation of single-phase laminar flow is conducted using the SPH module in isolation and validated against existing theoretical solutions. A new independent simulation is then conducted where a single neutrally-buoyant particle representing the discrete phase is introduced in the static liquid and the whole particle-fluid flow is analysed. The particle-liquid flow is then modelled independently as described by SPH-DEM. The effects of particle size, density, and geometry of the moving suspended particle are examined. In SPH-DEM simulations, the numerical DEM particles represent the solid phase and interact with the surrounding SPH fluid particles. All numerical particles (both SPH particles and DEM particles) have an initial velocity of zero to ensure that any motion observed in the simulation results is completely from the applied pressure gradient and particle-fluid interaction.

The simulation workflow for single particle migrate in pipe, commences with the generation of numerical particles, succeeded by the establishment of a neighbour list for a designated numerical particle based on the kernel function domain. Subsequently, the contact relationship between the target numerical particle and its neighbouring particles is evaluated. If the interaction between fluid and suspended particle necessitates consideration, it is estimated using either SPH or DEM, as discussed above. The physical properties of the SPH numerical particles are updated, followed by the adjustment of the suspended particle and liquid physical properties. Similarly, in the DEM approach, the interaction between the fluid and suspended solid particles is computed based on the methodology described above. The physical properties of the suspended particle and liquid are then updated for the subsequent timestep calculation. The simulation concludes once the specified

target time (t_{target}) is exceeded.

5.3.3 Optimization of numerical particle spacing

The optimization of numerical particle spacing constitutes a critical input parameter in the context of SPH particle-liquid simulations, most crucially for simulating particle flow as the requirements are more stringent than for single-phase flow. Therefore, a numerical particle distance sensitivity analysis was initially conducted to identify potential numerical errors stemming from inadequate spatial discretization of the geometric domain. To this end, the particle radial migration of a single suspended neutrally-buoyant particle ($d_p = 4$ mm) was simulated by SPH-DEM at $Re = 350$, using varying numerical particle spacings (S_p). The suspended particle was introduced at a radial position $r/R = 0.1$ and its Lagrangian trajectory examined in the x-direction as a function of S_p, while keeping all other parameters constant (see Figure 5.3). Results show that values of $S_p \geq \frac{D}{400}$ do not affect the particle trajectory and its ultimate equilibrium position resulting from radial migration. Hence, considering the balance between computational cost and numerical accuracy achieved, the particle spacing of S_p = D/400 was adopted for all subsequent simulations.

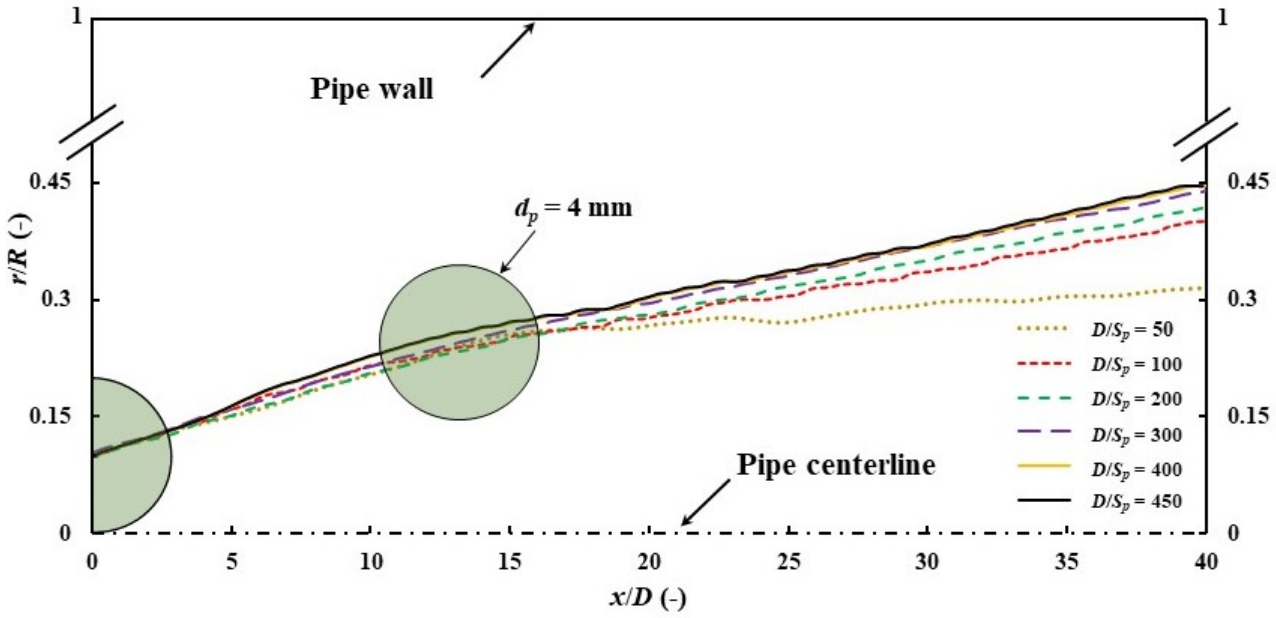

Figure 5.3: Effects of numerical particle spacing on simulated particle trajectory: $d_p = 4$ mm, ρ_r = 1, Re = 350.

5.4 Validation of SPH-DEM model

Initially, to evaluate the efficacy of SPH in modelling the carrier fluid, a series of simulations were conducted for single-phase flow of Newtonian and non-Newtonian (power-law) fluids. The SPH simulations yielded local Lagrangian velocities throughout the simulation domain which were used to construct radial velocity profiles by considering 40 annular sections across the pipe, as depicted in Figure 5.4. The SPH prediction of parabolic Newtonian laminar velocity profiles are excellent (Figure 5.4(a)). In transient flow (Re = 3,500), the SPH profile showed good agreement with the 1/6 power-law correlation commonly used to approximate turbulent pipe flow (Bird et al., 1977; Chant, 2005). The slight discrepancies observed may be attributed to the reduced accuracy of the power-law relationship in the transient regime. The radial velocity profiles predicted by SPH for power-law fluids of varying flow behaviour index (n) at Re =350 show excellent agreement with

analytical solutions in Figure 5.4(b) (Bird et al., 1977). Clearly, these results demonstrate the robust capability of SPH method to simulate single-phase flow with different rheologies, particularly in the laminar regime.

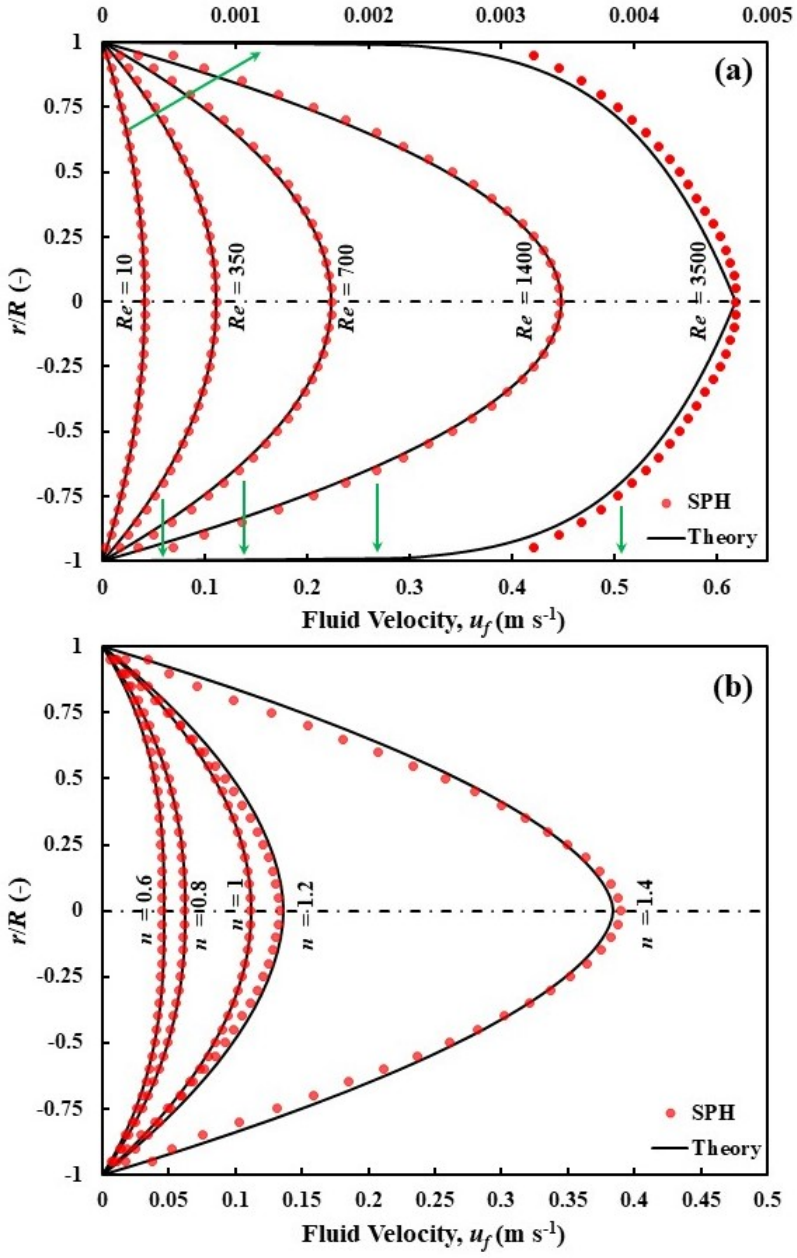

Figure 5.4: SPH predictions of radial velocity profiles in single-phase flow compared to analytical solutions: (a) Newtonian fluid at varying Re values; (b) power-law fluids at Re = 350.

As described above, a digital imaging technique was utilized to determine the equilibrium radial position of a single 4 mm neutrally-buoyant sphere introduced at various radial positions in the laminar flow of an aqueous glycerol solution. The use of a high frame rate (100 frames/s) together with a high image resolution facilitated the precise detection of a single particle across multiple frames by the circle Hough transform algorithm (Atherton et al., 1999) enabling the determination of the circle's centre and radius. Conversion from image pixel coordinates was achieved using a linear scale incorporated in the image. In the experiment, 25 particle trajectories were randomly released and analyzed to determine equilibrium radial positions in the top and bottom regions of the pipe, two equilibrium positions were displayed in Figure 5.5. Six simulations were performed, three of which were located above the centerline and three below it. For each group, one simulation was initialized near the centerline, another at the midpoint of the pipe's cross-sectional radius, and the third near the pipe wall. The reason for setting the initial positions in this way is that the initial shear rates at different locations of the pipe are considered to be different, and in order to fully validate the accuracy of the model, three representative locations are chosen for the simulations. As shown in Figure 5.5, the trajectories are plotted across a normalized pipeline distance (x/D), with D representing the diameter of the pipeline. Each trajectory represents the path of a particle released from different initial positions within the pipe. These trajectories provide a clear comparison between numerical predictions and experimental data, highlighting the accuracy of the SPH-DEM simulation in predicting particle migration behaviors under given flow conditions with a Reynolds number of 350. SPH-DEM simulations yielded final particle equilibrium positions (r_{eq}) very close to the experimentally determined values, the difference being less than 5%. The SPH-DEM coupling provides good predictions and modeling of particle-liquid flow and will be adopted for the rest of this study.

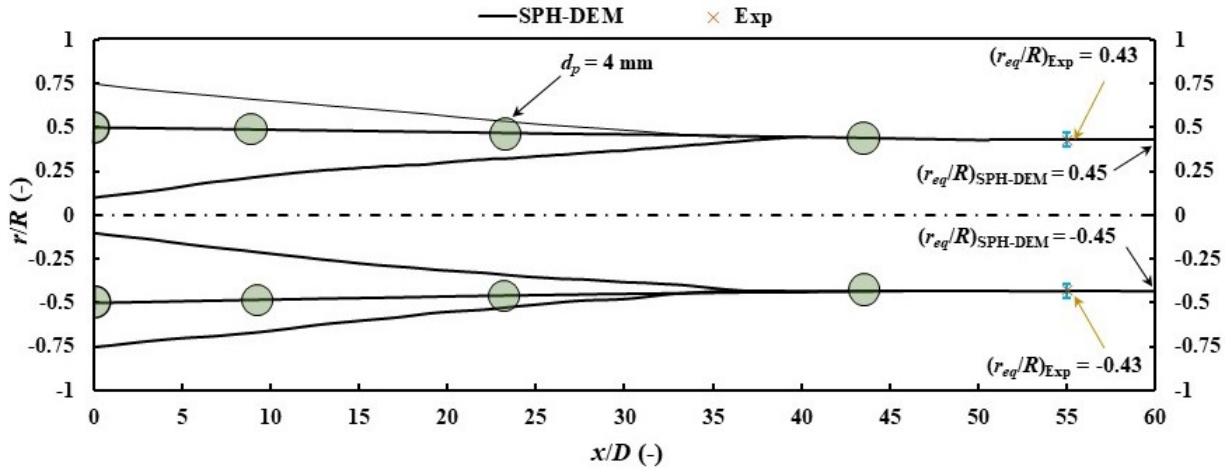

Figure 5.5: SPH-DEM particle trajectory with experimental equilibrium particle positions: $d_p = 4$ mm, $\rho_r = 1$, $Re = 350$.

5.5 Results and discussion

Using the SPH-DEM approach, a parametric investigation was undertaken to investigate the impact of various pertinent parameters on the equilibrium radial position of a suspended particle migrating within viscous flows. The study included the initial position at which the suspended particle is introduced in the flow, particle diameter and shape, particle-liquid density ratio (ρ_r) and pipe Reynolds number. Whilst the study focuses mainly on Newtonian flow, cases of non-Newtonian flow of power-law rheology are also examined.

5.5.1 Effects of initial particle position

The simulated lateral migration trajectories of neutrally-buoyant particles introduced at different initial positions in the flow are depicted in Figure 5.6 for particle diameters of 1 mm, 4 mm and 10 mm. Regardless of their initial release location above the centreline, particles invariably migrate

towards a common lateral equilibrium position (r_{eq}), in accordance with the Segre–Silberberg effect. Particle behaviour below the centreline mirrors exactly that above it. Thus, a neutrally-buoyant particle settles into a radial position characterized by steady rectilinear motion with no linear or angular acceleration, and the hydrodynamic lift force reduces to zero.

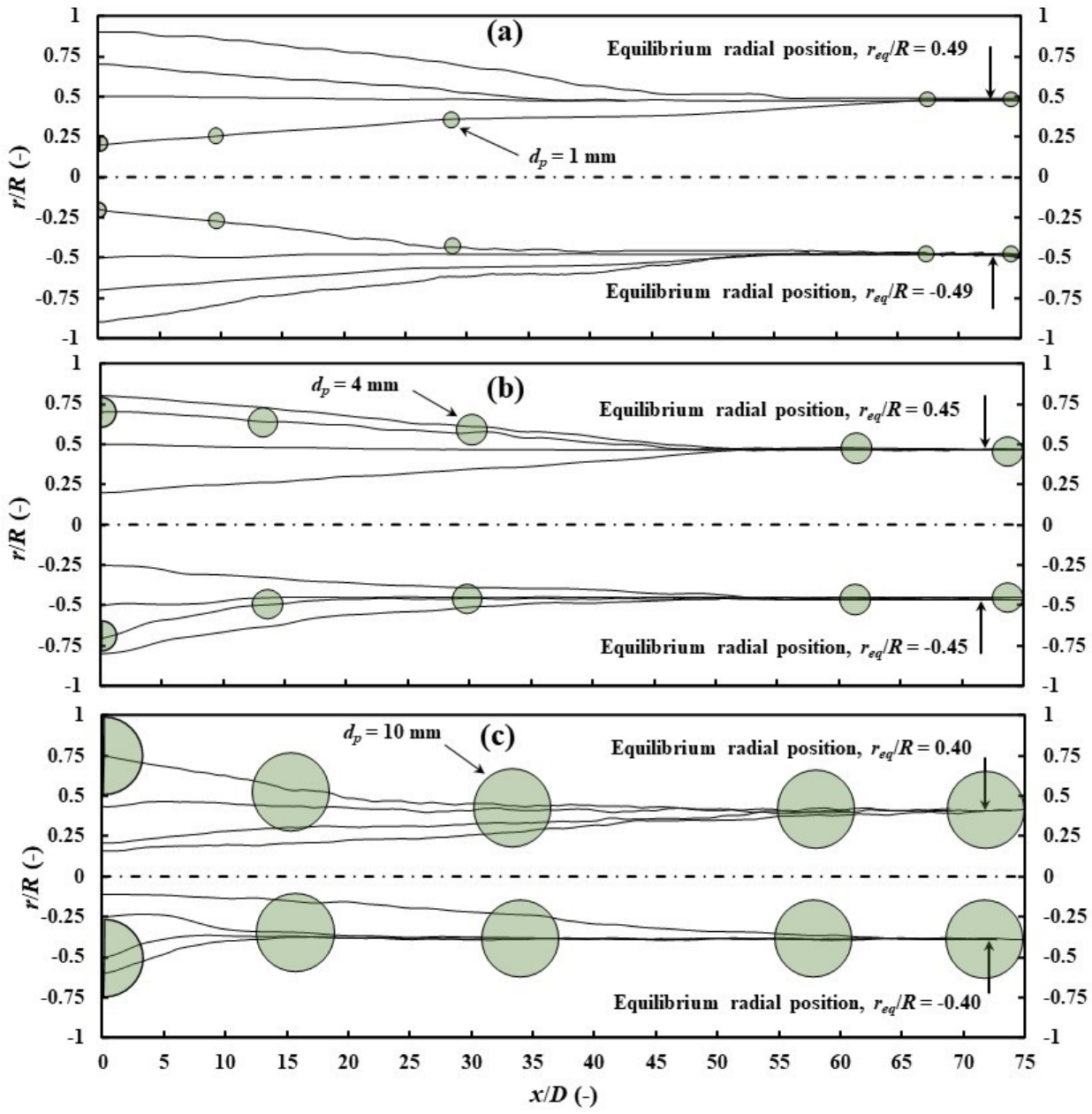

Figure 5.6: Effects of the initial position of a neutrally-buoyant particle on its equilibrium radial position, illustrated for different particle sizes: $\rho_r = 1$, $Re = 350$.

The stability of the particle equilibrium at a zero-lift point can be established by examining the slope of the lift force as a function of radial position (Hu et al., 2019). The centreline corresponds

to a segment of the lift force curve characterized by a negative slope. In this configuration, any deviation of a particle from the centreline induces a negative lift force, thereby propelling the particle further away from the axis. Consequently, the centreline represents an unstable equilibrium position. Conversely, another zero-lift point exists between the centreline and the wall, situated on a segment of the curve with a positive slope. In this scenario, when a particle is displaced from this equilibrium point, the lift force acts in a direction opposing the displacement, effectively exerting a corrective force towards the equilibrium position. Thus, the zero-lift point between the centreline and the wall denotes a stable equilibrium position. Given the symmetry of particle trajectories around the centreline, subsequent simulations will focus exclusively on the bottom region of the pipe below the centreline.

The stability of the particle equilibrium at a zero-lift point can be established by examining the slope of the lift force as a function of radial position (Hu et al., 2019). The centreline corresponds to a segment of the lift force curve characterized by a negative slope. In this configuration, any deviation of a particle from the centreline induces a negative lift force, thereby propelling the particle further away from the axis. Consequently, the centreline represents an unstable equilibrium position. Conversely, another zero-lift point exists between the centreline and the wall, situated on a segment of the curve with a positive slope. In this scenario, when a particle is displaced from this equilibrium point, the lift force acts in a direction opposing the displacement, effectively exerting a corrective force towards the equilibrium position. Thus, the zero-lift point between the centreline and the wall denotes a stable equilibrium position. Given the symmetry of particle trajectories around the centreline, subsequent simulations will focus exclusively on the bottom region of the pipe below the centreline.

5.5.2 Effects of particle size

The effects of particle size on the migration trajectories of a neutrally-buoyant particle released from different initial positions in the lower half of the pipe are illustrated in Figure 5.7. Particles of differing sizes migrate along disparate trajectories towards distinct equilibrium positions. Notably, an increase in particle size prompts migration further from the pipe wall across liquid streamlines towards the centreline. Extremely small particles ($d_p = 0.05$ mm) do not deviate from their starting radial position because of their negligible inertia and follow streamlines closely. These observations are consistent with previous findings (Feng et al., 1994). The lateral migration of neutrally-buoyant particles in horizontal pipe flow is governed by four principal mechanisms: wall repulsion induced by lubrication, inertial lift stemming from shear slip, lift generated by particle rotation, and lift attributed to the curvature of the undisturbed velocity profile of the carrier liquid. Shear slip refers to the relative motion or slip between the liquid phase and solid particles suspended within the liquid (Tehrani, 1996). If the fluid is viscous and the particles are small or lightweight, they may experience less resistance from the fluid and move at a different velocity compared to the surrounding liquid. It influences parameters like the distribution of particles across the pipe cross-section. This would be the major factor in the case of dense particles, but its contribution would diminish becoming negligible as particles tend to become more neutrally-buoyant. Wall repulsion induced by lubrication is the force generated by the lubricating layer between particles and the pipe wall, preventing particle adhesion, reducing friction, and facilitating smoother transport. In single-particle flow, as is the case here, this would only be significant in case of large particle-to-pipe diameter ratios (Bureau et al., 2023; Cook, 2001). Lift generated by particle rotation is an upward force arising from particle spin, influencing particle trajectory and promoting dispersion and suspension within the liquid (Brandt et al., 2022). Lift attributed to the curvature of the undisturbed velocity profile of the carrier liquid is an upward force on particles caused by velocity differences, aiding particle suspension (Brandt et al., 2022). As particle size increases, the contributions from inertial lift due to shear slip and particle rotation become more pronounced,

consequently shifting the equilibrium position of larger particles closer towards the pipe centre.

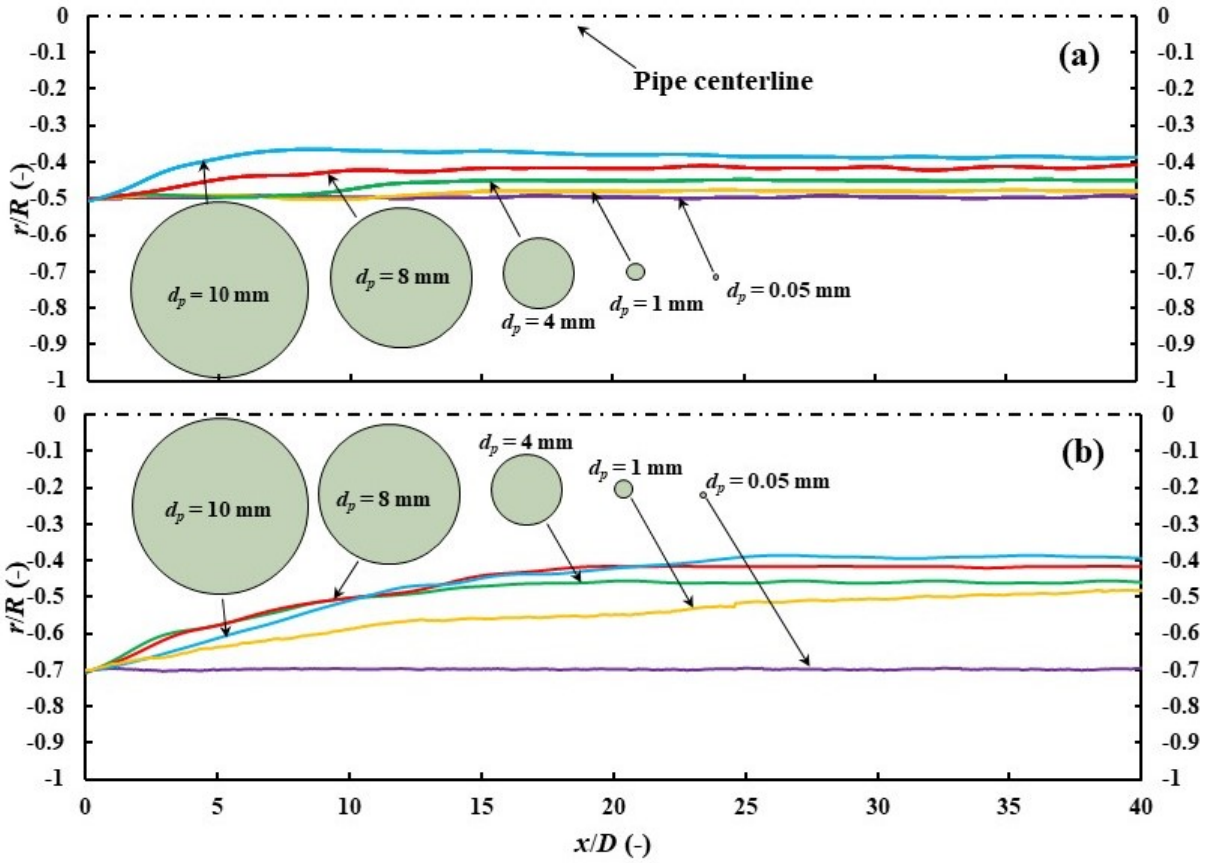

Figure 5.7: Effects of the size of a neutrally-buoyant particle on its equilibrium radial position, illustrated for two different initial particle positions: $\rho_r = 1$, $Re = 350$.

5.5.3 Effects of particle-liquid density ratio

The effects of particle-liquid density ratio (ρ_r) on the migration trajectories of particles released from three initial positions are depicted in Figures 5.9 and 5.10, for 4 mm and 10 mm particles, respectively. Irrespective of their initial release position, particles tend to migrate towards the bottom of the pipe as the density ratio increases, with higher density ratios leading to faster attainment of equilibrium. Inspection of Figure 5.8 reveals that density ratios of 1.1 and under cause the smaller

(4 mm) particle to suspend in the flow at a distinct equilibrium position, while density ratios of 1.2 and higher cause the particle to settle at the bottom wall.

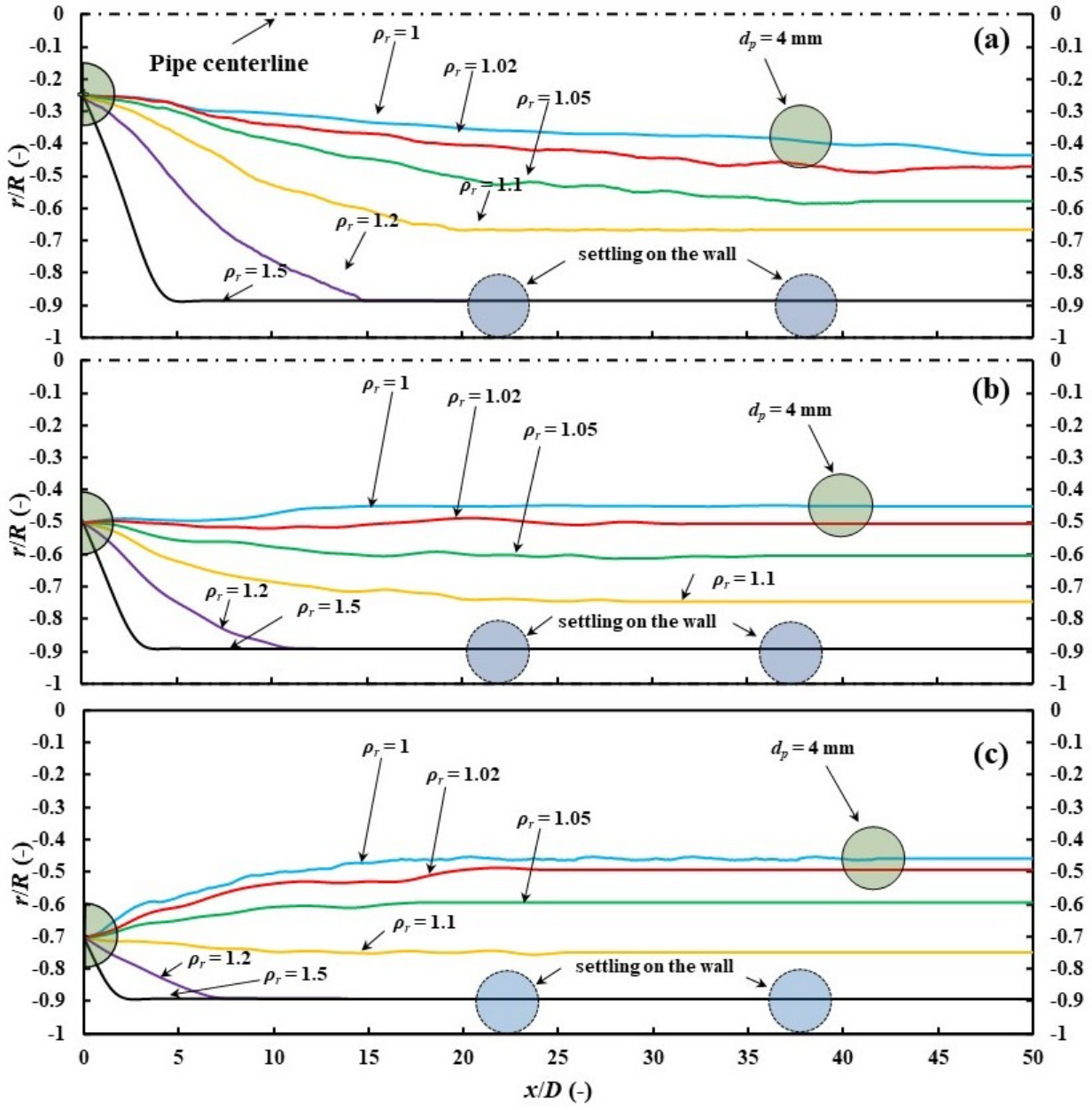

Figure 5.8: Effects of the particle-liquid density ratio on the particle equilibrium radial position, illustrated for three different initial particle positions: $d_p = 4$ mm; $Re = 350$.

Results in Figure 5.9 show that the larger (10 mm) particle settles at the bottom of the pipe for all density ratios of 1.1 or higher, while it reaches a stable equilibrium position for smaller density ratios 1.05 and lower. Denser particles also reach their equilibrium position faster than lighter particles. Particle settling time for $d_p = 4$ and 10 mm is plotted as a function of particle density ratio in Figure 5.10. Whilst neutrally-buoyant particles do not settle, for a given density ratio larger particles settle faster than smaller ones, and for a given particle size, denser particles settle much faster.

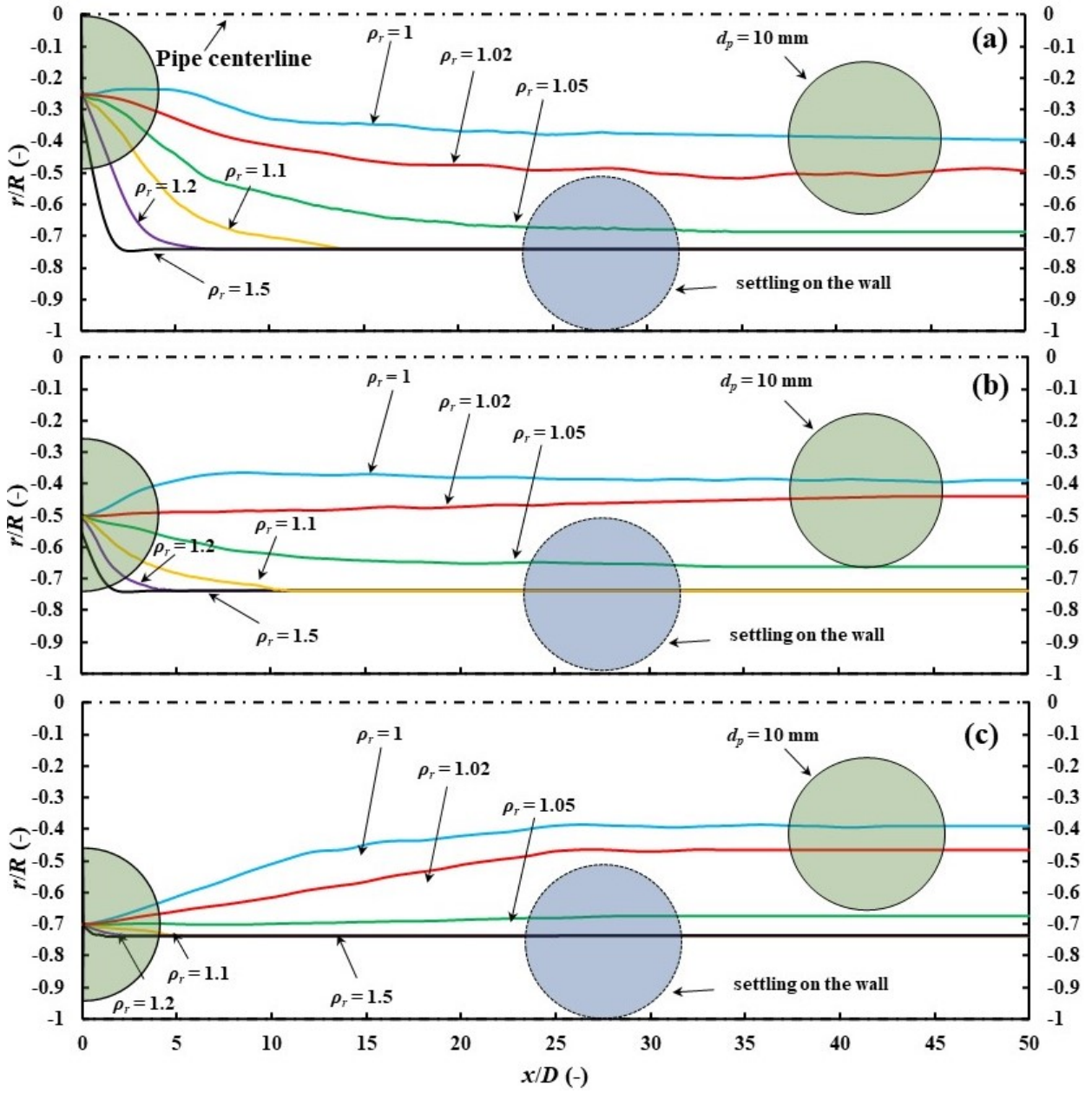

Figure 5.9: Effects of particle-liquid density ratio on the radial equilibrium position of a migrating particle in a viscous flow: $d_p = 10$ mm; $Re = 350$.

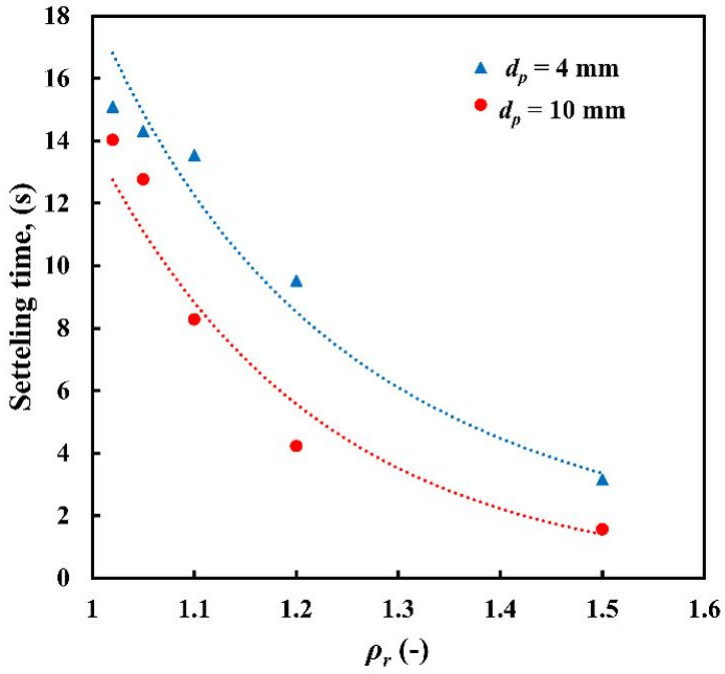

Figure 5.10: Effects of the particle-liquid density ratio on the particle settling time, illustrated for different particle sizes: $Re = 350$.

These phenomena are also illustrated in Figure 5.11, which is a snapshot of four particles ($d_p = 4$ mm) of different density ratios are released in the bottom half of the pipe flow ($Re = 350$) at radial position $r/R = -0.25$; the multimedia was constructed by combining SPH-DEM simulation data for the four individual particles. These observations together with those in Figure 5.8 indicate that particle density has more impact on particle migration than particle size, which is in line with the classical Segré–Silberberg effect.

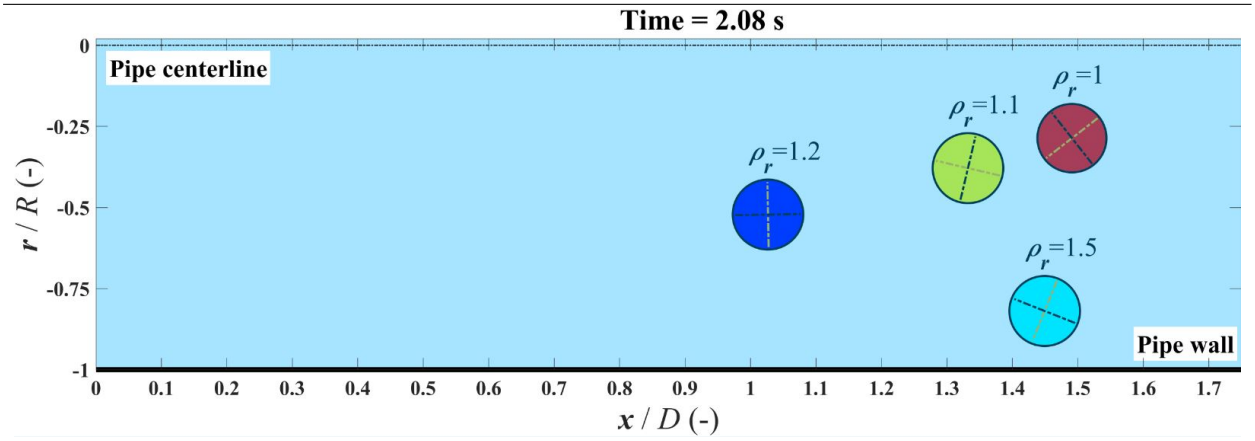

Figure 5.11: Effects of particle-liquid density ratio on the radial equilibrium position of a migrating particle in a viscous flow: $d_p = 4$ mm; $Re = 350$.

5.5.4 Effects of pipe Reynolds number

The migration trajectories of a neutrally-buoyant 4 mm particle, released at a radial position r/R = -0.5, are illustrated in Figure 5.12 for different pipe Reynolds numbers. As Re increases from 350 to 3,500, the particle motion tends to gradually shift towards the wall of the pipe. At Reynolds numbers of 700 and 1,400, the particle trajectory exhibits minor fluctuations, ultimately stabilizing at a fixed position. However, at a Reynolds number of 3,500 well within the transitional regime, the trajectory fluctuations are such that a stable equilibrium position is not attained; instead, an equilibrium region emerges within which the particle exhibits irregular upward and downward movement. Analysis of particle migration behaviour becomes more challenging at higher Reynolds numbers given the increasing turbulence.

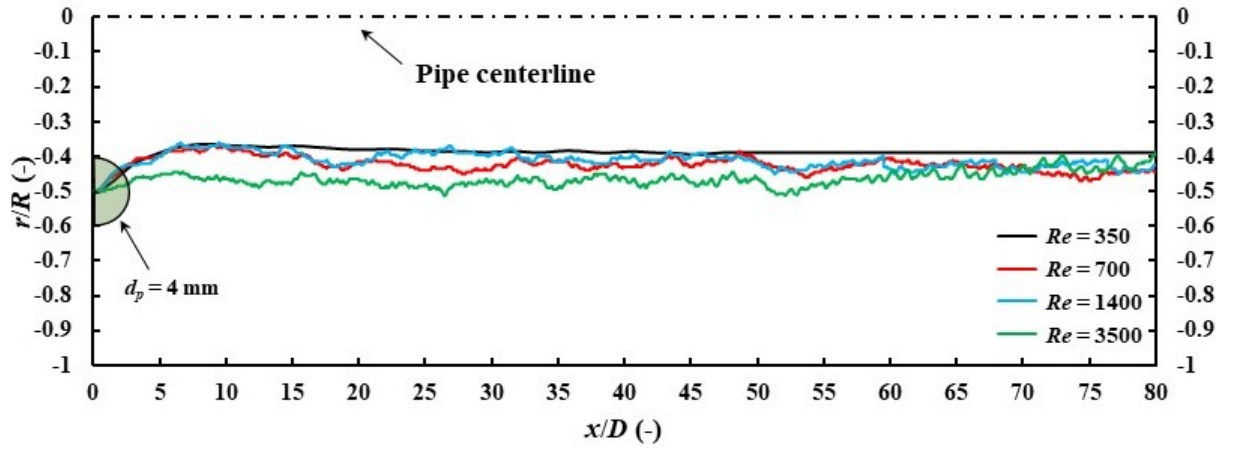

Figure 5.12: Effects of the pipe Reynolds number on the migration trajectories of a neutrally-buoyant particle: $d_p = 4$ mm; $Re = 350$.

5.5.5 Effects of fluid rheology

The migration trajectories of a neutrally-buoyant particle in a non-Newtonian power-law fluid are presented in Figure 5.13 for a range of values of the power-law index ($0.6 \leq n \leq 1.4$). For a given value of n, particles of a given size (4, 10 mm) originating from different initial positions converge on the same equilibrium position, suggesting a direct correlation between equilibrium position (r_{eq}) and n. The precise location of r_{eq} shifts towards the centreline as n increases. Particle migration is governed by the force exerted on the particle by the fluid, which is directly proportional to the local fluid viscosity, contingent upon the local shear rate within the power-law fluid. The power-law index modulates this force via its influence on the local viscosity.

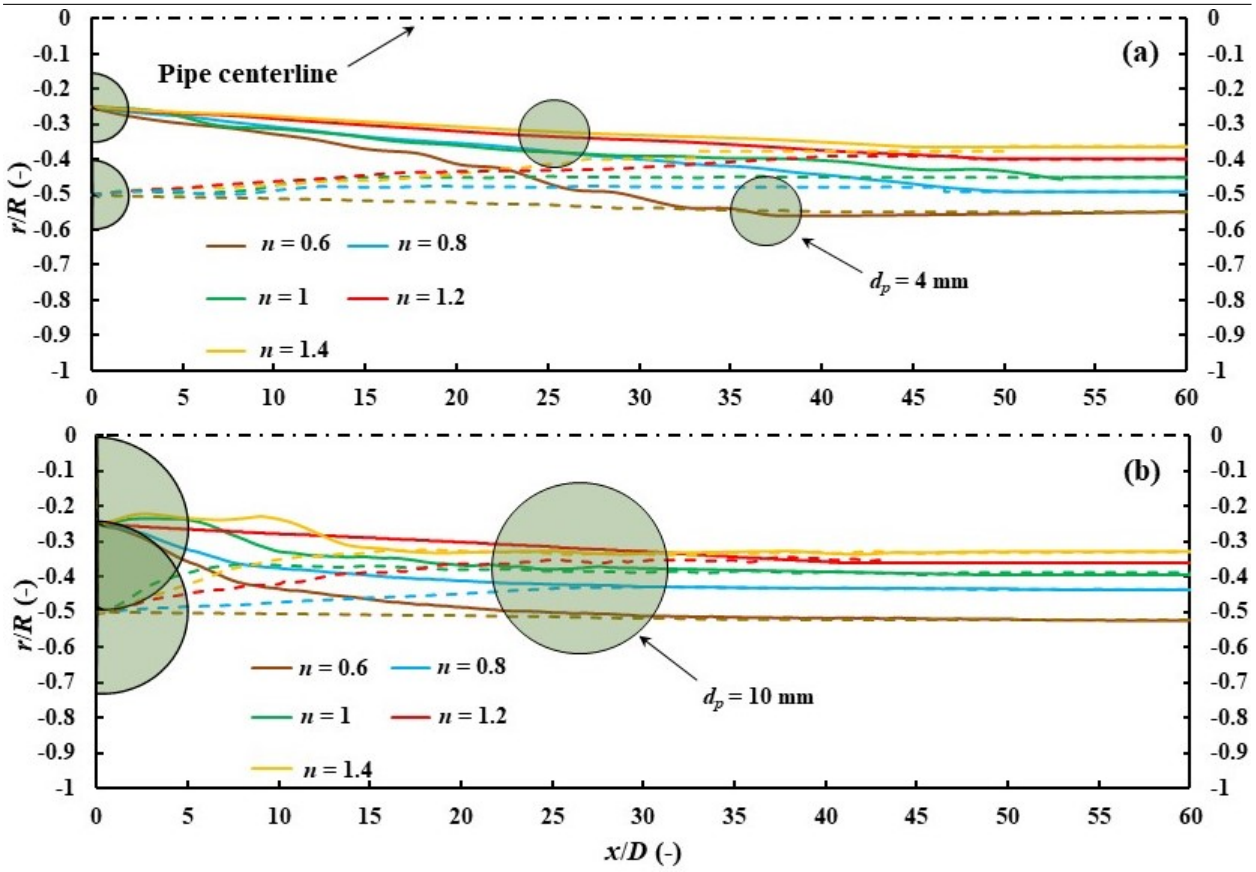

Figure 5.13: Effects of the non-Newtonian power-law index on the equilibrium radial position of a neutrally-buoyant particle, illustrated for two different particle sizes and two different initial particle positions: $\rho_r = 1$, $Re = 350$.

5.5.6 Effects of particle shape

The preceding investigation focused on the behaviour of spherical particles. In engineering applications, however, particles are often non-spherical. Here, we explore the migration behaviour of ellipsoid particles defined by their major axis (a) and minor axis (b), with the aspect ratio ($\alpha = b/a$) serving as a descriptor of particle shape. Typical migration trajectories of neutrally-buoyant particles with varying α values released from two distinct initial positions are depicted in

Figure 5.14(a). The angle (θ) representing the orientation of the particle major a-axis relative to the horizontal is initially set to zero at the particle starting position. Clearly, akin to the behaviour of spherical particles discussed above, for a given aspect ratio an ellipsoidal particle converges towards the same equilibrium position regardless of its initial release point. The difference in equilibrium position between particles of different aspect ratio is small. The equilibrium position plotted as a function of particle aspect in Figure 5.14(b), shows a very shallow curve with a gentle minimum near $\alpha = 0.5$. The angle of orientation θ also does not affect the equilibrium radial position of the particle.

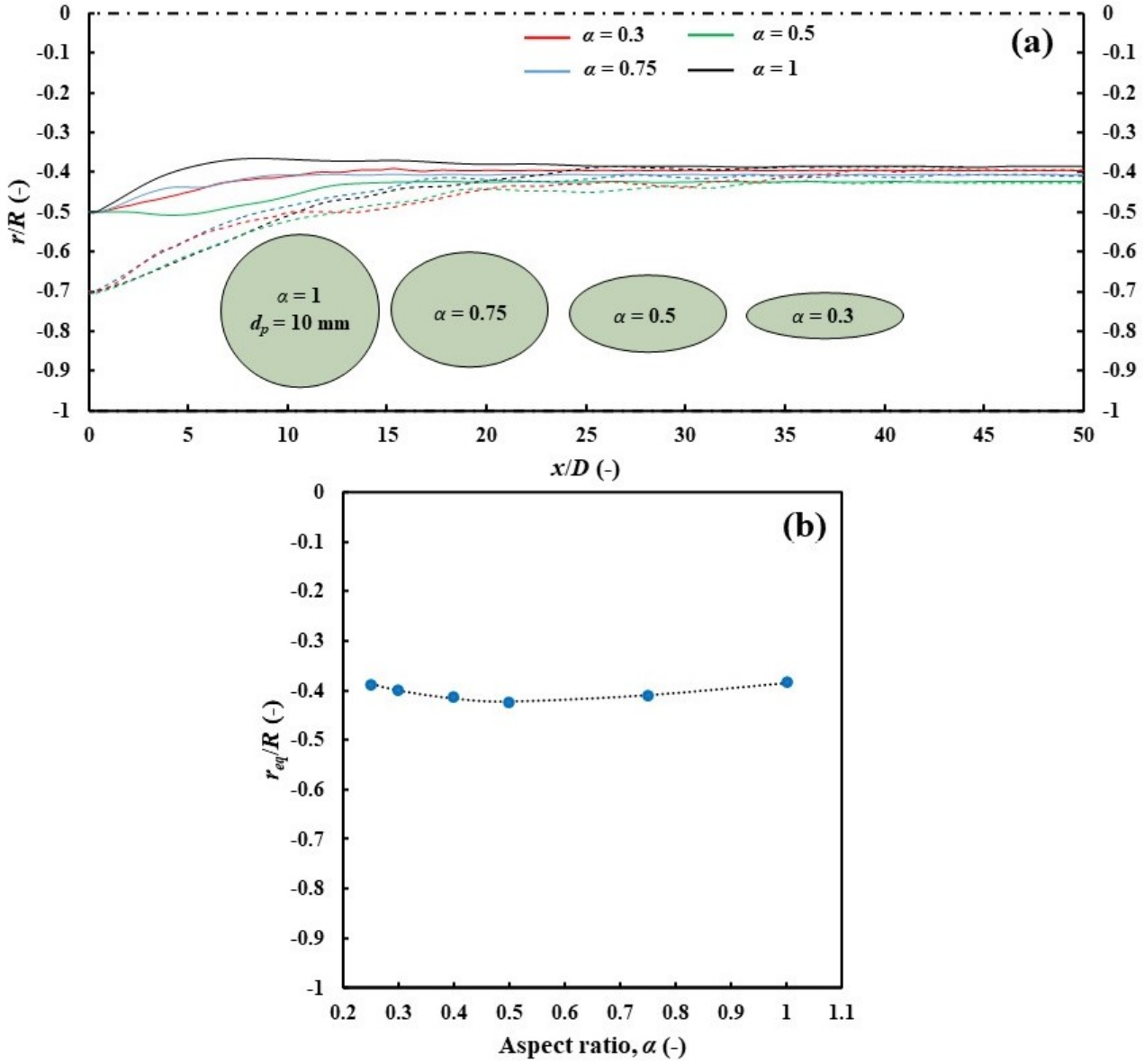

Figure 5.14: Effects of the shape of a neutrally-buoyant particle on: (a) its migration trajectory; (b) its equilibrium radial position. Note that all particles have the same mass and volume; $\rho_r = 1$, $Re = 350$.

The effects of α on the angular velocity of a neutrally-buoyant particle are also illustrated in Figure 5.15 (snapshot), which combines the SPH-DEM simulation data for particles with α values in the range 0.3 - 1. The sphere (α = 1) acquires a steady rotational motion immediately upon

introduction in the flow, superimposed on its steady translational motion, as depicted in Figure 5.16(a). The steady translational velocity of the particle increases significantly for lower α values. The ellipsoidal particles exhibit large fluctuations in angular velocity, which gradually diminish in amplitude as the particle progresses along the pipe.

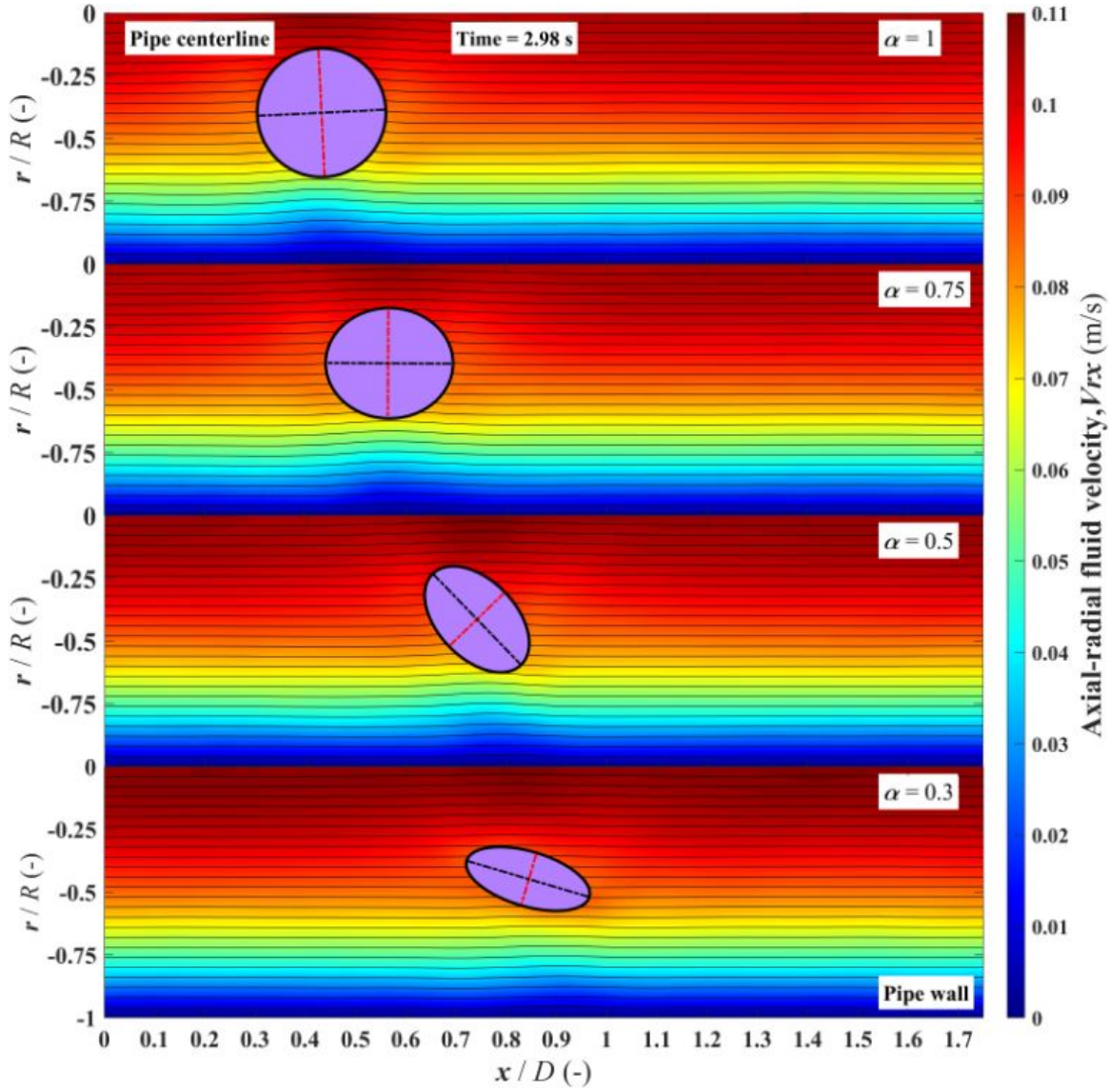

Figure 5.15: Effects of particle aspect ratio (α = 0.3 - 1) on the angular velocity of a neutrally-buoyant particle migrating in viscous flow (snapshot).

After some time, the maximum angular velocity of each ellipsoidal particle reaches a stable value which is higher for lower values of α, corresponding with the equilibrium radial position of the particle. Note that the sphere also exhibits fluctuations, but these are comparatively very small, and acquires its radial equilibrium position much faster than the ellipsoidal particles. This periodic rotational behaviour which is partially represented in Figure 5.16(a) is even more visible and striking in Figure. 5.15(snapshot). The period of the particle rotational motion is plotted as a function of aspect ratio in Figure 5.16(b). Notably, particles with a larger α display shorter rotation periods. The phenomena discussed here are consistent with the observations reported in plane Poiseuille flow in a 2D channel, simulated using LBM by Wen et al. (2019) and distributed Lagrange multiplier/fictitious domain by Chen et al. (2012).

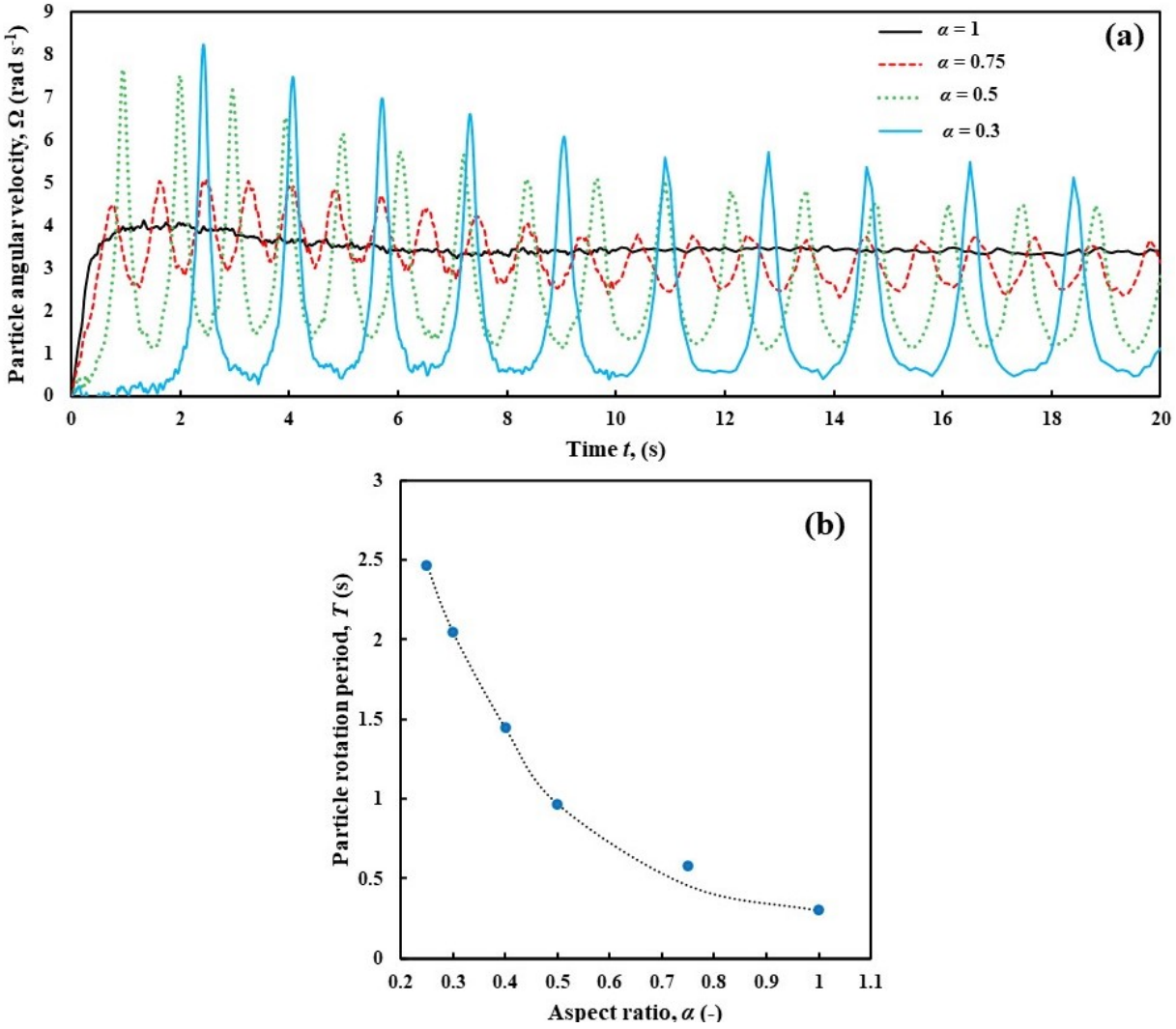

Figure 5.16: Effects of aspect ratio of neutrally-buoyant particle on its rotational motion during migration: (a) angular velocity; (b) particle rotation period; $\rho_r = 1$, $Re = 350$.

To further investigate the flow field perturbations induced by particle migration, the vorticity and radial velocity fields of the fluid surrounding a neutrally-buoyant particle (sphere or ellipsoid) are presented in Figures 5.17 and 5.18. The motion of a sphere introduces a significant vorticity field accompanied by a sharp radial velocity gradient in Figure 5.17. A distinctive butterfly-like pattern emerges around the sphere, characterized by a positive radial velocity on the left side and negative velocity on the right side of comparable magnitudes. Such a pattern is also observed in the case of

the ellipsoid (Figure 5.18). The asymmetry of the radial velocity field around the ellipsoid particle is responsible for the significant fluctuations in its rotational velocity discussed above in Figure 5.16.

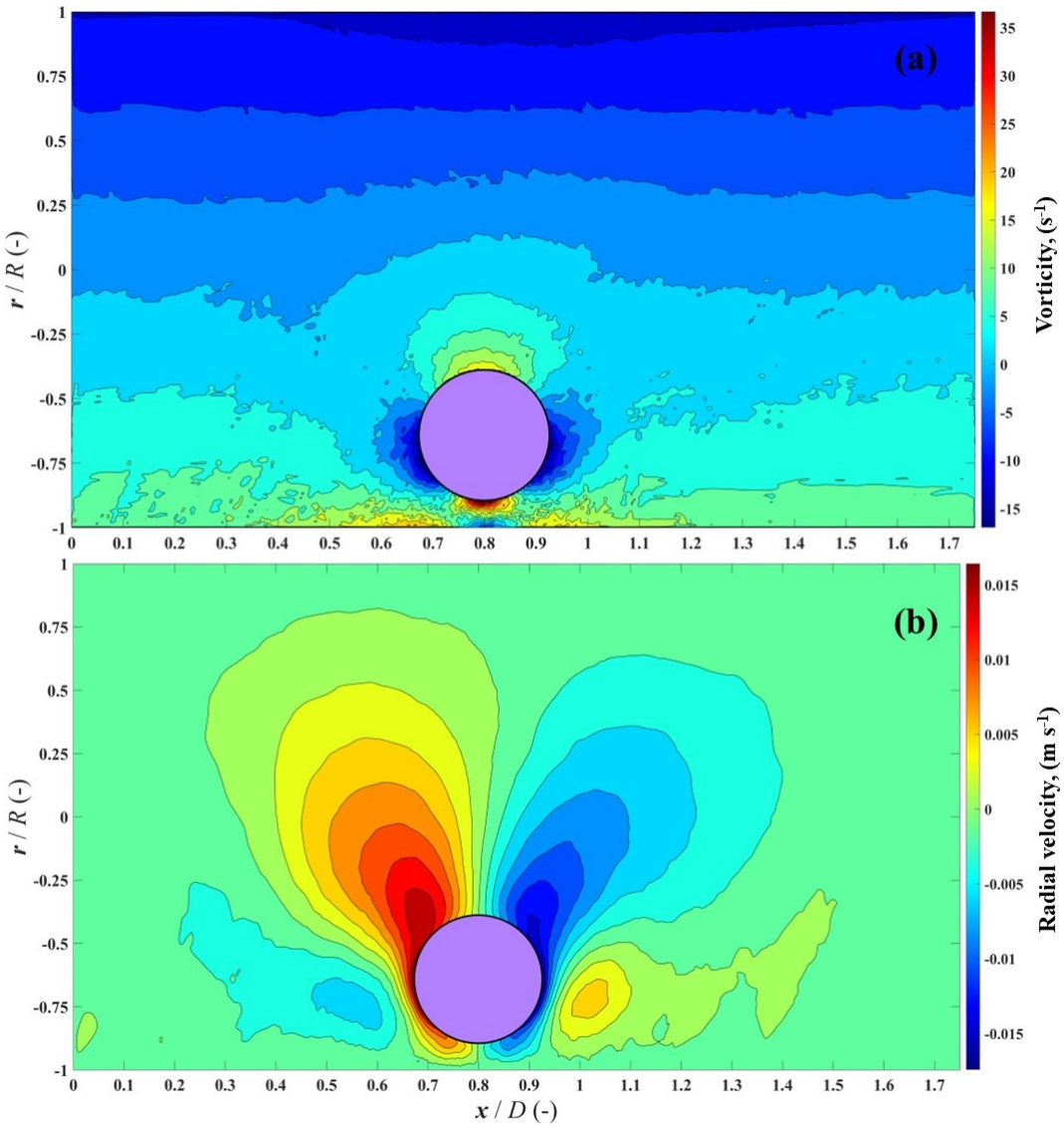

Figure 5.17: Typical (a) vorticity and (b) radial velocity of fluid around a neutrally-buoyant sphere at its equilibrium radial position: $d_p = 10$ mm,$\rho_r = 1$, $Re = 350$.

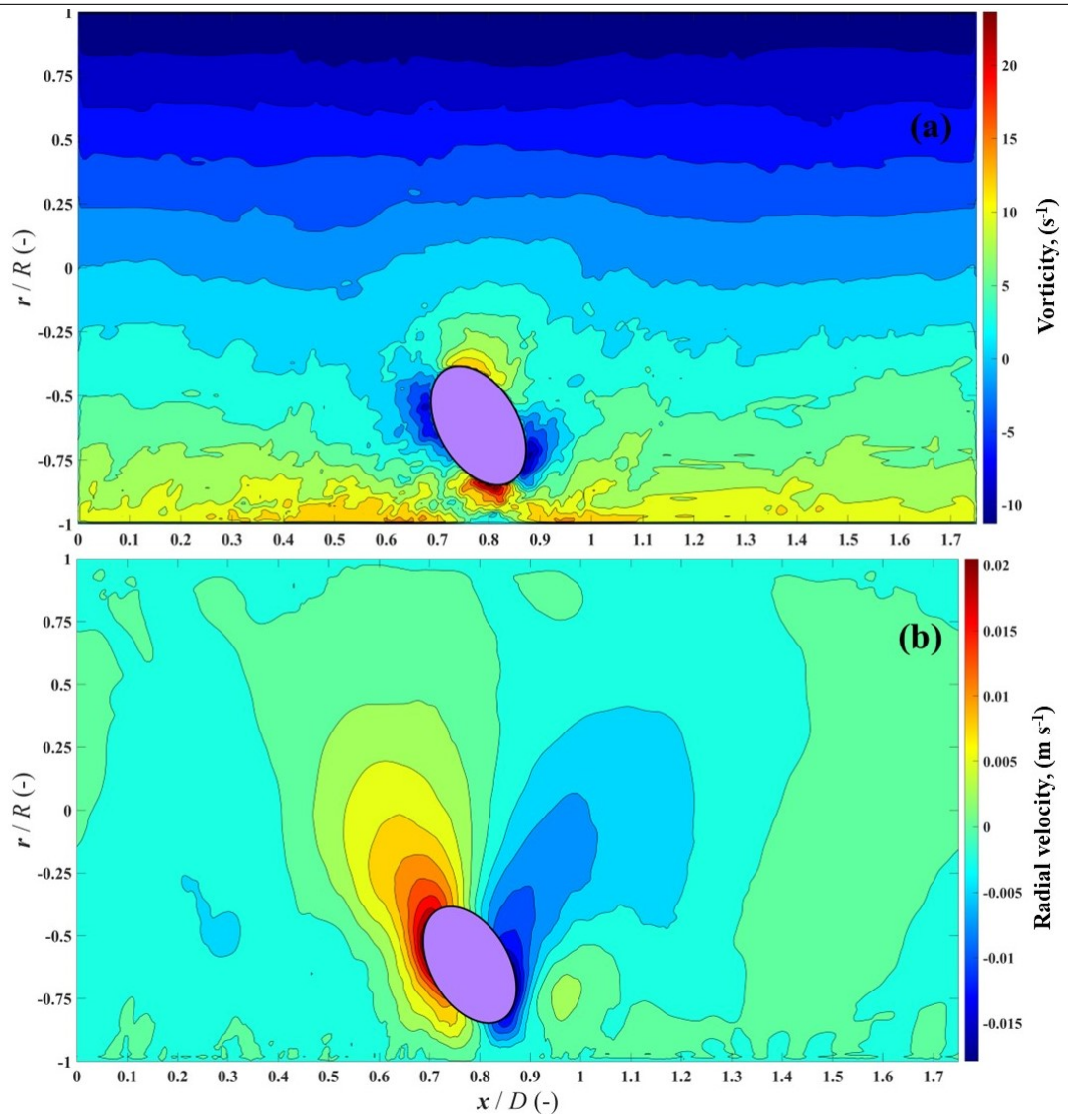

Figure 5.18: Typical (a) vorticity and (b) radial velocity of fluid around a neutrally-buoyant ellipsoid ($\alpha = 0.5$) at its equilibrium radial position: $\rho_r = 1$, $Re = 350$.

5.6 Conclusion

A series of simulations were conducted based on the technique of smoothed particle hydrodynamics (SPH) coupled with the discrete element method (DEM) to investigate the detailed dynamics

of radial migration of a single particle in horizontal viscous pipe flow. Extensive validation procedures were undertaken, including comparisons with established theoretical solutions for single-phase flow and experimental observations obtained from high-speed digital imaging of particle motion in a pipe flow loop. This SPH-DEM coupling was shown to be superior to using SPH alone for handling particle-liquid flow. The work served to demonstrate the robustness and accuracy of the SPH-DEM framework in predicting the detailed aspects of particle migration dynamics in both Newtonian and non-Newtonian fluids. Results showed that neutrally-buoyant particles of spherical and ellipsoidal shape exhibit lateral migration in viscous flow which is symmetrical about the pipe centreline, and each attains the same stable radial equilibrium position regardless of its point of introduction in the flow. Such an equilibrium position becomes less well defined in transitional flow due to the gradual onset of turbulence. A detailed SPH-DEM parametric study showed that the particle equilibrium position is influenced by a number of factors, including particle size and shape, particle-fluid density ratio, pipe Reynolds number and fluid rheology, and the effects have been delineated. Particle density had the most effect on particle equilibrium position, followed by particle size, whilst particle shape had remarkable effects on particle spin dynamics. This study has helped highlight the versatility and accuracy of the SPH-DEM methodology for simulating complex multiphase flow problems.

Nomenclature

Symbols

D	Pipe diameter, m
d_p	Particle diameter, m
h	Kernel smooth length, m
n	Power-law index
r	Radial position, m
R	Pipe radius, m
r_{eq}	Equilibrium radial position, m
Re	Pipe Reynolds number
S_p	Numerical particle distance, m
t	Time, s
u_z	Axial fluid velocity, m s^{-1}
u_{mean}	Mean mixture velocity, m s^{-1}
x	axial pipe direction, m

Greek Symbols

α	particle aspect ratio
ν	kinematic viscosity, m^2 s^{-1}
μ_f	viscosity, kg m^{-1} s^{-1}
ρ_f	liquid density, kg m^{-3}
ρ_s	particle density, kg m^{-3}
ρ_r	particle to liquid density ratio
Ω	particle angular velocity, rad s^{-1}

Chapter Six

NUMERICAL INVESTIGATION OF SOLID-LIQUID FLOWS IN HORIZONTAL PIPES USING SPH-DEM COUPLING

The main data of this chapter was published in the Journal of *Physics of Fluids* and *Chemical Engineering Sicence* . The contribution of the authors is listed as following:

Paper 1: Lian, X., Savari, C., Li, K., Barigou, M., 2023. Coupled smoothed particle hydrodynamics and discrete element method for simulating coarse food particles in a non-Newtonian conveying fluid. Physics of Fluids 35(4).

- **Xue Lian**: Conceptualization (equal); Data curation (equal); Formal analysis (lead); Investigation (lead); Methodology (equal); Validation (equal); Visualization (lead); Writing – original draft (equal); Writing – review & editing (equal).
- **Chiya Savari**: Conceptualization (supporting); Data curation (supporting); Formal analysis

(supporting); Methodology (supporting); Visualization (supporting); Writing – original draft (supporting); Writing – review & editing (equal).

- **Kun Li**: Conceptualization (supporting); Data curation (supporting); Formal analysis (supporting); Methodology (supporting); Visualization (supporting); Writing – original draft (supporting); Writing – review & editing (equal).

- **Mostafa Barigou**: Conceptualization (lead); Funding acquisition (lead); Investigation (equal); Methodology (lead); Project administration (lead); Resources (lead); Supervision (lead); Validation (lead); Writing – review & editing (equal).

Paper 2: Yang Z J., Lian X., Savari C., Barigou, M., 2024. Evaluating the effectiveness of CFD-DEM and SPH-DEM for complex pipe flow simulations with and without particles[J]. Chemical Engineering Science: 119788.

- **ZhuangJian Yang**: Conceptualization, Data curation, Formal analysis, Investigation, Software, Validation, Visualization, Writing – original draft.

- **Xue Lian**: Conceptualization, Data curation, Formal analysis, Investigation, Software, Validation, Visualization, Writing – original draft.

- **Chiya Savari**: Conceptualization, Formal analysis, Investigation, Methodology, Validation, Visualization, Writing – review & editing.

- **Mostafa Barigou**: Conceptualization, Formal analysis, Funding acquisition, Methodology, Project administration, Resources, Supervision, Validation, Writing – review & editing.

6.1 Introduction

Pipe transport of food materials is a common operation in food manufacture. For example, continuous in-line processing of particulate foods relies on the conveying of particle-liquid mixtures through pipes. Typically, the challenge in a heat-hold-cool process is to ensure a safe and uniform level of sterility whilst preventing over-processing. Often, in such processes, the food particles are coarse solids (up to 20 mm), their loading is high, and the carrier fluid is viscous of non-Newtonian rheology (Barigou et al., 2003; Fairhurst et al., 2001). Compared to single-phase flow, the dynamical behaviour of these particle-liquid flows is e size, flowrate, particle concentration). Particle flow behaviour critically affects extremely varied and complex and depends on many factors including particle properties (size, shape, density), liquid properties (density, rheology) and other process parameters (pipproduct heating, cooling and microbial sterilization. Moreover, information on the two-phase flow pressure drop and particle residence time distribution is also necessary for process optimization. Thus, knowledge of the detailed two-phase flow behaviour is necessary for optimum food processing as the final product quality is highly dependent on the usually complex flow patterns involved. Understanding this complexity and being able to model it, would undoubtedly represent a big step forward towards improving current food engineering practices. To achieve this aim, advanced and reliable experimental and numerical methodologies are required.

Imaging of food flows is very challenging because of their opacity which prevents the use of leading laser-based optical measurement techniques such as particle image velocimetry (PIV) and laser Doppler velocimetry (LDV), except for unrealistically dilute situations (Mühlich et al., 2016; Nouri et al., 2005; Stebel et al., 2020; Takei et al., 2004). Positron emission particle tracking (PEPT) is able to visualize concentrated opaque particle-liquid flows by providing the long-term three-dimensional (3D) trajectories of all components, whilst being non-invasive (Barigou, 2004). In PEPT, a tiny radiolabeled tracer is utilized to track the flow components in space and time with comparable accuracy to LDV and PIV (Guida et al., 2010a; Pianko-Oprych et al., 2009). PEPT

has been extensively used to study single-phase as well as complex multiphase flows and the data provided have been successfully exploited to inform, drive and validate various modelling methodologies (Li et al., 2022; Li et al., 2023b; Savari et al., 2022; Savari et al., 2021; Sheikh et al., 2022a, b). The technique, however, is very expensive to run and not widely available which makes any available data scarce and precious. Hence, the need for the development of advanced theoretical/numerical modelling strategies to reduce reliance on experimental work in such a challenging field.

Various modelling approaches have been attempted over the years, each having its own advantages and disadvantages, focusing on certain aspects of the flow and oversimplifying others. There are two main approaches, mesh-based and particle-based, to simulate the carrier fluid in a particle-liquid flow. In mesh-based computational fluid dynamics (CFD) methods, the fluid is treated as a continuum and a mesh is used to describe the flow domain. In many cases, the two-fluid or Eulerian-Eulerian (E-E) model has been used to study particle-liquid food flow in pipes under different flow regimes and solid loadings (Chen et al., 2011; Eesa et al., 2008; Jiradilok et al., 2006; Treinen et al., 2015). Data in the form of radial velocity profiles and radial solid phase distributions determined by different experimental techniques were used to validate the simulations. However, as this numerical approach relies on a mesh to evaluate the development of the flow field and structural deformation, the large deformation of the mesh can lead to mesh skewness which affects the accuracy of the predictions. This limitation is even more challenging when the mesh needs to be modified in complex flow geometries due to topological changes and the meshing process can be extremely complicated (Markauskas et al., 2017). Moreover, in this approach the distribution of local flow properties in a domain is represented without reference to the history of the fluid or particle trajectories. Thus, where localized particle effects are dominant such as in heterogenous dense flows of coarse particles, such effects cannot be accurately modelled by conventional mesh-based CFD approaches.

Smoothed particle hydrodynamics (SPH) is a more recent mesh-free alternative to traditional CFD

techniques and is a fully Lagrangian particle-based method. The continuum is divided into a set of computational particles, and an appropriate set of governing equations, such as Navier-Stokes are solved for each computational particle. This technique has shown a lot of promise and has been recently used in a number of studies to simulate single-phase and particle-liquid flows in different geometries (Cao et al., 2014; Han et al., 2020; Pazouki et al., 2015) In contrast to traditional mesh-based CFD approaches, SPH promises to be particularly efficient in solid-liquid flows where particle and flow characteristic dimensions are comparable. It has the added advantage of being able to model stresses within fluid and solid, but not particle-particle or particle-wall contact forces. The discrete element method (DEM), however, is a robust numerical approach for modelling particulate systems, where particles are treated as individual entities and their interactions are usually modelled using established contact laws (Munjiza, 2004). Thus, complete quantitative information about the time evolution and spatial distribution of local solid fraction, particle kinematics and both collisional stresses and streaming stresses can be obtained. Such detailed, physically sound information cannot be obtained through continuum modelling such as CFD.

A number of other modelling techniques exist such as lattice Boltzmann method (LBM) (Krüger et al., 2017), finite element method (FEM) (Reddy, 2005), boundary element method (BEM) (Gaul et al., 2013), and coarse-grained molecular dynamics (CGMD) (Hadley et al., 2012) However, there is currently no one single modelling methodology which can effectively tackle these complex particle-liquid flows. The continuum approach used in CFD is more efficient in handling the fluid phase, low solid concentrations and small particles, whilst DEM is much better at modelling high solid concentrations, but it cannot handle the continuous phase well. LBM, on the other hand, is able to handle complex boundary conditions such as those found on the endothelium, and can also be applied to microscale flow phenomena, but it is not efficient for particles with complex shapes; whilst SPH is a relatively general method which can be applied to both fluid and solids, can handle surface flows well, but it has some limitations in dealing with solid boundaries. The best solution, therefore, lies in a methodology which can exploit the strengths of each technique

and assemble these methods in an optimised hybrid fashion. Selecting methods which are particle-based facilitates their linking in a hybrid fashion. In particular, the SPH and DEM algorithms are almost identical, essentially the only difference being the routines needed to calculate the forces used for updating particle trajectories, which simplifies code development and makes it more efficient.

A coupled SPH-DEM framework, therefore, should be able to appropriately and efficiently handle the interactions between the carrier fluid and solid particles to yield flow details such as the rotational angular velocity (or spin) of the particles and Lagrangian trajectories of both particles and fluid. The coupled SPH-DEM model is highly robust and flexible with regard to the shape and size of the solid particles considered compared to conventional mesh-based CFD approaches (Sasson et al., 2016) and has recently been successfully applied to simulate different flow systems including packed beds (Natsui et al., 2018), particle sedimentation (Robinson et al., 2014) and debris flow (Liu et al., 2021). However, few studies have been validated due to the lack of appropriate experimental data, and food flows have not been investigated in this way. Here, the PEPT experimental method, which is a fully Lagrangian measurement technique, provides a unique opportunity to examine the capability of the SPH-DEM methodology to simulate the complex pipe flow of particle-liquid food suspensions.

In this chapter, a coupled SPH-DEM scheme is used to investigate the behaviour of coarse model food particles in a viscous non-Newtonian conveying fluid inside a horizontal pipe. The model is fully validated by PEPT-measured radial profiles of particle velocity and solid phase as well as particle passage time distribution and pressure drop, under varying conditions of solid loading. A detailed analysis of localized particle-liquid dynamics is obtained from the simulation results for different conditions of the two-phase flow. Such information is invaluable to inform the protocols of food particle transport and processing in pipelines.

6.2 Experimental

6.2.1 Pipe flow rig

Particle-liquid flow was driven by a vortex pump (T21-32 HF4 LB1, Turo vortex pump, EGGER, Switzerland) through a 10 m long flow loop of 40 mm internal diameter, schematically represented in Figure 6.1. Food particles were represented by model nearly neutrally-buoyant calcium alginate beads, fabricated in-house using the protocol reported by Fairhurst et. al. (2001), being nearly spherical with 4.0 mm diameter. The carrier fluid was a 0.80 wt. % aqueous carboxymethylcellulose (CMC) solution of non-Newtonian rheology used to mimic the usual behaviour of industrial food fluids. The rheological properties of the carrier fluid were determined before each experiment and checked at the end using a rheometer (Discovery Hybrid Rheometer, HR-2, TA Instruments). The mixture was circulated via a large cone-bottom tank where particles were kept in suspension by a mechanical mixer. Flow was studied in a 4 m long horizontal section of the flow loop. Flow visualisation by the PEPT technique was conducted over a pipe length of 0.40 m which was located 3 m downstream of the inlet and 0.6 m upstream of the outlet to ensure that the flow was fully developed and was not affected by pipe bends (Munson et al., 2016). The particle-liquid flowrate was measured by an ultrasonic Doppler flowmeter (UDF D5500, Doppler flowmeter, Micronics), and the mean particle delivery concentration in the pipe was measured with a bucket and stopwatch method. The mean delivery concentration of solids was in the range 10 – 40 vol. %, with mean mixture velocities of 0.056 - 0.092 m s-1. The experimental conditions are summarized in Table 6.1.

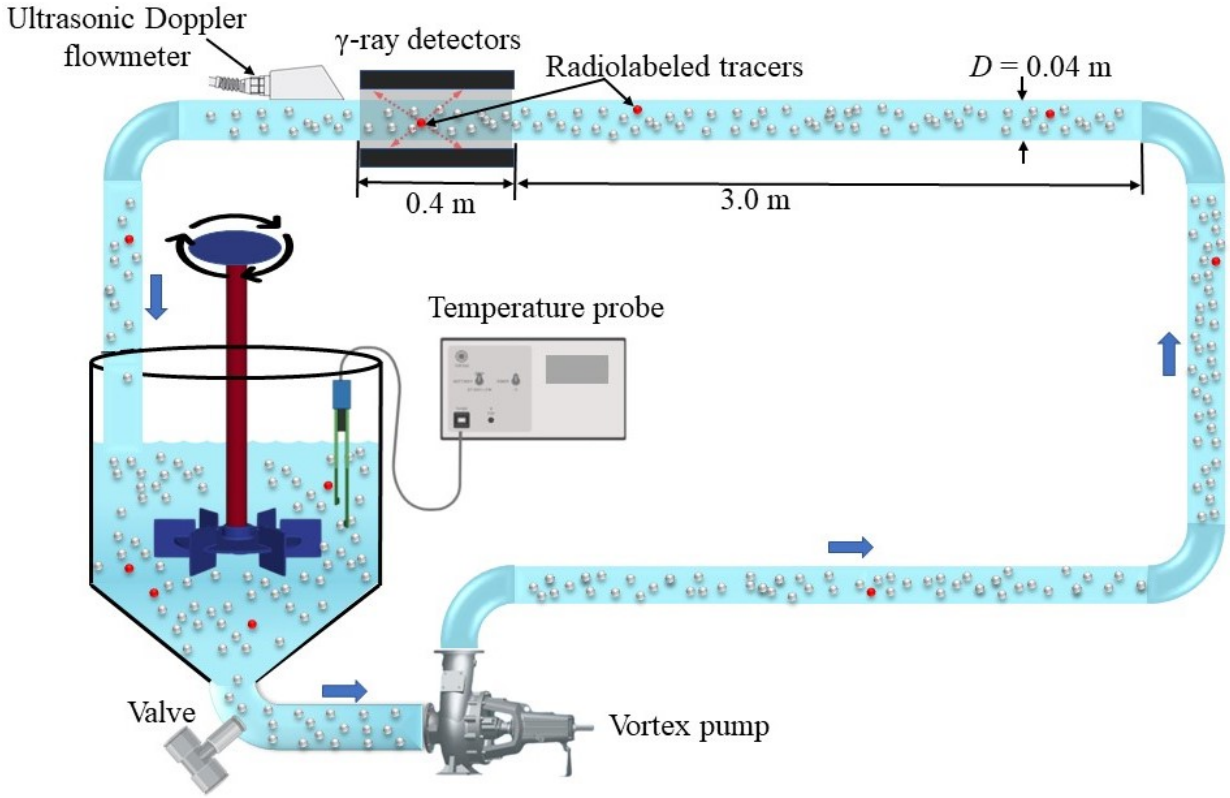

Figure 6.1: Schematic of experimental pipe flow loop and PEPT setup.

6.2.2 Positron emission particle tracking

PEPT is a non-invasive flow measurement technique. In PEPT, a tiny tracer radiolabelled by a positron-emitting radionuclide (here 18F) is introduced in the flow. The tracer position is then determined by detecting a set of coincident gamma rays associated with the annihilation of emitted positrons with nearby electrons. PEPT can be used to visualise flow in opaque flow/apparatus, a unique advantage, and its accuracy is on a par with leading laser-based optical methods (Pianko-Oprych et al., 2009). Detailed information about PEPT technology and data processing algorithms has been reported in our earlier papers (Barigou, 2004; Guida et al., 2010a, c; Liu et al., 2013; Barigou et al., 2014). In pipe flow, imaging by PEPT consists in letting the particle tracer flow in a

closed loop until it maps the entire area of interest, therefore requiring a statistically representative number of Lagrangian trajectories, typically > 50 (Bakalis et al., 2003; Barigou et al., 2003). In this chapter, since flow was viscous, a long time would have been needed to collect enough trajectories in each experiment with a single particle tracer. Hence, several identical tracers (usually 7-8 tracers) were introduced in the flow loop and simultaneously tracked. In PEPT, both carrier fluid and solid particles can be separately tracked by using suitable radiolabelled tracers, but in this study only the solid phase was tracked using a tiny (100 μm) radiolabelled resin-particle tracer encapsulated within a representative alginate bead.

Table 6.1: Experimental conditions of particle-liquid flows.

Flow case	**CMC** (wt. %)	C_s (vol. %)	d_p (mm)	$u_{\mathbf{mean}}$ (m s^{-1})	**D** (m)	$\boldsymbol{Re}$ $\left(\frac{\rho D u_{\text{mean}}}{\mu}\right)$	ρ_r $\left(\frac{\rho_p}{\rho_f}\right)$
1	0.80	10	4.0	0.056	0.040	11.2	1.01
2	0.80	20	4.0	0.072	0.040	14.4	1.01
3	0.80	30	4.0	0.083	0.040	16.6	1.01
4	0.80	40	4.0	0.092	0.040	18.4	1.01

6.3 PEPT data analysis

PEPT provides 3D Lagrangian trajectories which can be used to calculate particle velocity profiles, particle concentration distribution and particle passage times. In the following sections, the procedures for analysing PEPT data to infer these parameters are presented.

6.3.1 Radial particle velocity profile

PEPT provides data arrays of tracer positions as a function of time in the form of $f(x,y,z,t)$. The local velocity in each direction is estimated using the time derivatives of positions by a differencing approach. Since flow in the pipe is laminar, the principal velocity component is the axial component (u_x) and any radial fluctuations can be ignored. The local axial velocity at each point was estimated from the slope of a straight line fitted to a number of x-positions versus time using regression analysis (Bakalis et al., 2003; Barigou et al., 2003). In this case, 20 points were used covering a small distance of 25 mm. The radial velocity profile was obtained by dividing the pipe cross-section into 20 semi-annular regions of equal area, as shown in Figure 6.2. As the solid particles used were slightly heavier than the carrier fluid (ρ_r = 1.01), 10 regions above and 10 regions below the centreline of the pipe were used to account for axial asymmetry of the flow. The radial velocity profile was constructed by normalising with the mean mixture velocity, u_mean, and the mean and standard deviations were calculated in each region.

6.3.2 Radial particle concentration profile

We previously demonstrated a method by which the Lagrangian PEPT trajectories can be used to determine the spatial distribution of solids, utilising the occupancy of the particle tracer (Guida et al., 2010a; Yang et al., 2022). Traditionally, by dividing the flow domain into a grid, occupancy is defined as the fraction of the total experimental time (t_∞) a tracer spends in each grid cell during the experiment, which makes it dependent on the density of the grid used (Guida et al., 2010a). To mitigate this bias, an ergodic time (t_E) is defined; the time which a tracer would spend in a cell, given the system is single-phase and ergodic. Since the tracer has equal probability of presence anywhere within the pipe flow, the ergodic time can be expressed as the total experimental time divided by the number of cells, i.e., $t_E = t_\infty / N_C$. Thus, the local occupancy (O_E) can therefore be defined as:

$$O_E = \frac{\Delta t}{t_E} \tag{6.1}$$

where, Δt is the time the tracer spends inside a given cell. Guida et al. (2010b) demonstrated that the local occupancy is equal to the ratio of the local particle concentration, c, to the mean particle concentration in the vessel, C, as follows:

$$O_E = \frac{c}{C} \tag{6.2}$$

Using these definitions and dividing the pipe into a 3D grid of equal volume cells, the local particle concentration was estimated and the local radial particle concentration profile constructed. An average radial concentration profile was calculated from the local concentration profiles over 40 equidistant cross-sections along the length of the pipe.

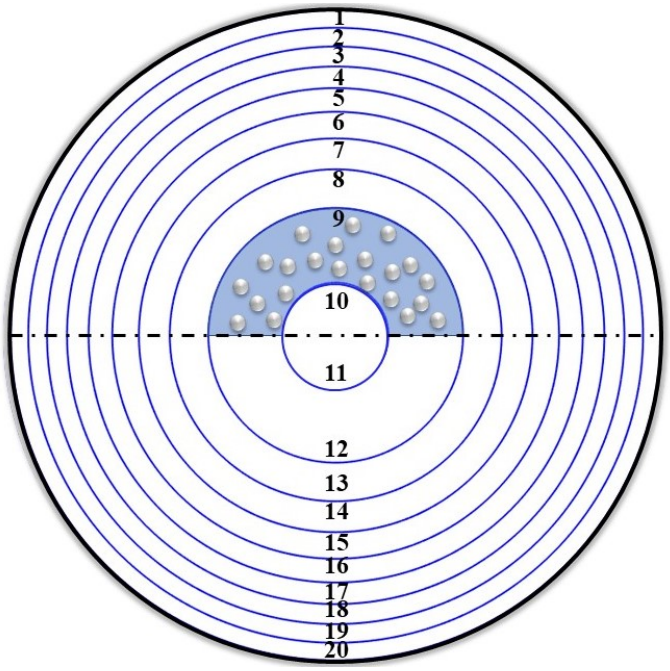

$$\bar{u}_{x,i} = \frac{\sum_j u_{x,j}}{N}$$

$$\sigma_i = \sqrt{\frac{\sum_j \left(u_{x,j} - \bar{u}_{x,i}\right)^2}{N}}$$

$\bar{u}_{x,i}$: mean velocity in region *i;*
$u_{x,j}$: axial velocity of particle *j;*
N: total number of particles in region *i;*
σ_i: standard deviation of region *i.*

Figure 6.2: Division of pipe cross-section into twenty semi-annular regions of equal-area for local PEPT velocity calculations and construction of radial velocity profile. Note that because particles are slightly heavier than the liquid, flow is not axisymmetric.

6.4 Numerical modelling of solid-liquid flow

In section 6.4, numerical methodologies employed for simulating the continuous and discrete are illustrated in following. The non-Newtonian carrier fluid was modelled by the SPH technique whilst the solid particles were modelled by the distributed contact DEM (DCDEM) approach, a variant of DEM, which is able to simulate irregularly shaped solid particles, if necessary. DCDEM models each solid particle using a cluster of numerical particles, keeping the relative positions of these inner constituent particles constant (Koshizuka et al., 1998).

6.4.1 SPH formulation of carrier fluid

The motion of the liquid phase is governed by continuity and momentum conservation equations. Dur to solid phase is introduced to the flow systems, based on Eq. 6.3, which proposed by Monaghan (1992b), add one terms for coupling forces as:

$$\frac{d\mathbf{v}}{dt} = -\frac{1}{\rho}\nabla P + \mathbf{g} + \mathbf{\Gamma} + \mathbf{S}_c = -\sum_b m_b \left(\frac{P_a + P_b}{\rho_a + \rho_b}\right) \nabla_a W_{ab} + \mathbf{g} + (\nu_0 \nabla^2 \mathbf{v})_a + \mathbf{S}_c \tag{6.3}$$

where, $\mathbf{\Gamma}$ represents the dissipative terms; P_a and ρ_a are the pressure and density that correspond to a target particle a, and P_b and ρ_b are the pressure and density corresponding to a given neighbouring particle b. In particle-liquid flow $\mathbf{S}_c = \mathbf{f}_a/m_a$, where $\mathbf{f}_a$ represents the whole coupling force on the liquid particle, because of the DEM particles. The laminar viscous stresses $(\nu_0 \nabla^2 \mathbf{v})_a$ in the momentum conversation can be represented by Eq. 3. Mass continuity in SPH form is given by Eq.6.3 The rheology of carrier fluids are controlled by HBP model.

6.4.2 DEM formulation of dispersed solid phase

In DEM, the suspended solid particles are treated as a discrete phase whose motion is described by Newton's second law:

$$m_i \frac{d^2 \mathbf{r}_i}{dt^2} = \sum_j \mathbf{c}_{ij} + \mathbf{f}_i + m_i \mathbf{g} \tag{6.4}$$

where, m_i represents the mass of particle i at position $\mathbf{r}_i$, $\mathbf{c}_{ij}$ represents the contact force between solid particles and $\mathbf{f}_i$ is the coupling force of the particle-liquid flow acting on solid particle i.

In the coupled SPH-DEM approach, the force exerted on solid particle i by the numerical SPH particles is estimated as (Anderson and Jackson, 1967):

$$\mathbf{f}_i = V_i\left(-\nabla P + \nabla\cdot\tau\right) + \mathbf{f}_d(\boldsymbol{\varepsilon}_i, \mathbf{u}_s) \tag{6.5}$$

where, V_i is the volume of the solid particle. The first two terms account for fluid forces such as shear stress, pressure and buoyancy. The force $\mathbf{f}_d$ is the particle drag force which is affected by the local porosity ε_i and the superficial fluid velocity $\mathbf{u}_s$ given by:

$$\mathbf{u}_s = \varepsilon_i(\mathbf{u}_L - \mathbf{u}_p) \tag{6.6}$$

where, $\mathbf{u}_L$ and $\mathbf{u}_p$ are, respectively, the velocity of the SPH fluid and DEM solid particles. The drag force is defined as (Coulson and Richardson, 1993):

$$f_d = \frac{1}{8}C_d\varepsilon_i^{-\varphi}\pi d_p^2\rho_f|\mathbf{u}_s|\mathbf{u}_s \tag{6.5}$$

where, ρ_f is the fluid density. The drag coefficient C_d and the constant φ are related to the particle Reynolds number, $Re_p = \rho u d_p/\mu$:

$$C_d = \left(0.63 + \frac{4.8}{\sqrt{Re_p}}\right)^2 \tag{6.6}$$

$$\varphi = 3.7 - 0.65\times\exp\left[\frac{-(1.5-\log_{10}Re_p)^2}{2}\right] \tag{6.7}$$

The contact forces are calculated by the DCDEM algorithm, which has been described in section 3.5.

6.4.3 SPH-DEM coupling

The SPH-DEM coupling process is illustrated in the flowchart of Figure 6.3. The governing equations for the liquid and solid phases are solved for each numerical particle. At the pre-processing stage, the physical parameters including the rheological parameters of the carrier fluid, mean mixture velocity and solid particle positions are fed into the framework. The number of solid particles is estimated based on the solids loading and their positions are randomly assigned. The pipe containing the particle-liquid flow is constrained by periodic boundaries at the inlet and outlet. Three types of simulation particles are generated within the simulation domain: fluid, solid and boundary particles. During the course of the simulation, each fluid and solid particle is independently tracked.

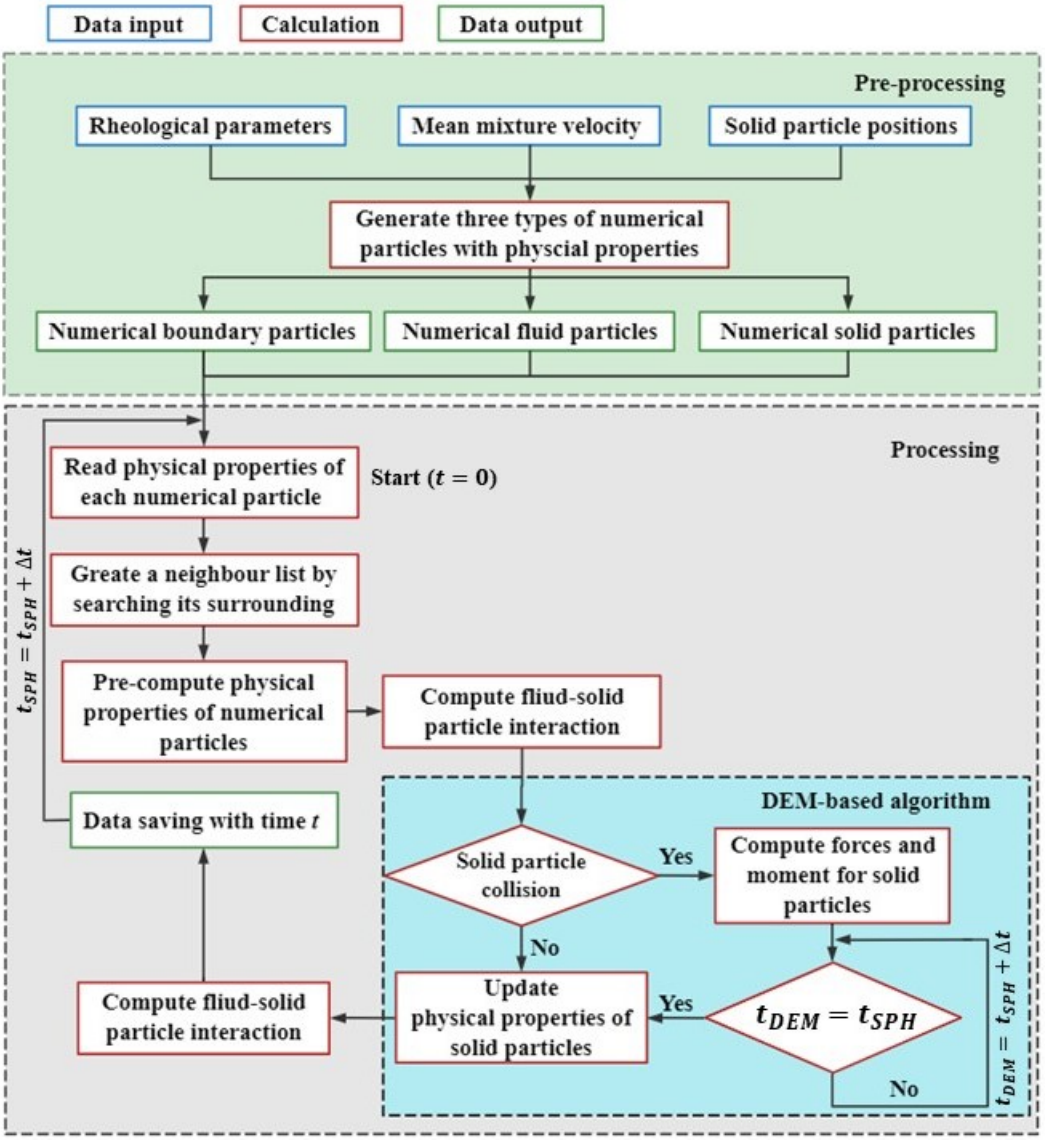

Figure 6.3: Flowchart of SPH-DEM coupling process.

The main numerical calculations are implemented in the processing stage, where the data for each simulation particle is read and a list of neighbouring particles is generated by searching the particle's surrounding (Domínguez et al., 2011). Then, the model variables at each numerical particle are estimated based on the weightings assigned to the neighbouring particles by the kernel function. Once the quantities for each simulation particle are computed in the SPH module within the

time step, the linear and angular accelerations of each solid particle are computed based on the fluid-solid interactions and are fed into the DEM module. A collision condition is checked by the framework, and if a collision happens with other solid particles, DEM calculates the after-collision linear and angular velocities and updates the positions of the particles. In case of no collision, the density, position and velocity of the numerical solid particles are updated by the SPH module. At each time step, all physical information pertaining to the simulation particles is saved and carried forward to the next time step. The modelling parameters used in the SPH-DEM simulations are summarized in Table 6.2; the parameters of the solid phase, i.e., alginate beads, were obtained from Chan et al.(2011).

6.4.4 Simulation set-up

Geometry and initial conditions

Simulations were conducted in 2D using DualSPHysics software. Thus, solid particles are circular rather than spherical and the pipe wall is reduced to two lines on the cylindrical surface. The pipe geometry was identical to that of the experimental pipe, i.e., circular with a 40 cm diameter, as shown in Figure 6.4. Simulations were conducted over a pipe length of 0.07 m. The effects of particle spacing, S_p, for each solid concentration were studied via a sensitivity analysis and the optimum values obtained were: 4, 4, 3 and 2 $\times 10^{-5}$ m, respectively, for 10, 20, 30 and 40 vol. % mean solid loadings. Numerical SPH and DEM particles representing the liquid and solid phases, respectively, which are uniformly distributed with a constant particle spacing,S_p, to ensure smooth density and pressure calculations. The pipe flow is driven by a constant pressure gradient. The number of solid particles is determined based on the solid loading, with their initial positions randomly assigned to reflect realistic dispersion. Initially, all numerical particles, including both numerical SPH and DEM particles, are set to a velocity of zero, ensuring that any observed motion arises solely from the applied pressure gradient and particle-fluid interactions. articles within the

Table 6.2: Modelling parameters used in SPH-DEM simulations.

Solid phase	
Density (kg m^{-3})	1,014
Young's modulus (kPa)	400
Passion ratio (-)	0.5
Restitution coefficient (-)	0.75
Friction coefficient (-)	0.4
Numerical particle spacing, s_p (m)	0.00002-0.00004
Overlap distance (m)	$0.5s_p$
Liquid phase	
Density (kg m^{-3})	1,000
Papanastasiou parameter, m (-)	10
Power-law index, n (-)	0.89
Numerical particle spacing, s_p (m)	0.00002-0.00004
Kernel function	Quintic class 2 Wendland
Kinematic viscosity (Pa s)	0.1
Kernel smooth length, h (m)	$h = 0.1\sqrt{3s_p}$
Time step, Δt_{SPH} (s)	0.00004

flow field. The total simulation time was 15 seconds to ensure that the particle-liquid flow was fully developed.

Boundary conditions

Using periodic boundary conditions at the inlet and outlet of the pipe can substantially reduce the computational effort (Gomez-Gesteira et al., 2012). To enhance computational accuracy near open boundaries, the support domain of the kernel function of a particle is clipped by the nearest open boundary and the remainder of its clipped support applied at the complimentary open boundary (Fourtakas et al., 2016).

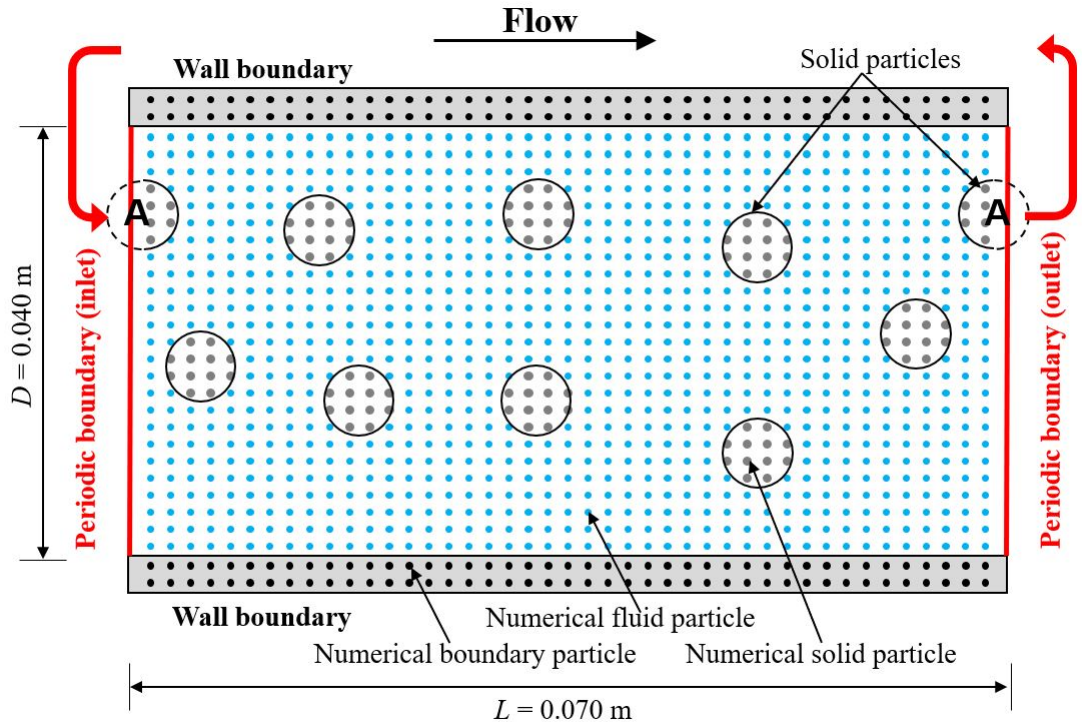

Figure 6.4: Schematic diagram of SPH-DEM setup for simulation of particle-liquid flow. Note how particle (A) moves through the periodic boundaries of the pipe.

The wall boundary is also described by numerical boundary particles (Figure 6.4). In the SPH solid-liquid pipe flow simulation, 20 layers of boundary particles are used to effectively prevent solid particles from penetrating the pipe wall boundary. These boundary particles act as a rigid, impenetrable layer that enforces a no-slip condition on the pipe wall and ensures interaction between

the solid particles and the pipe surface. The multiple layers help maintain numerical stability and prevent unexpected behaviors, such as particle leakage or penetration, that can affect the accuracy of simulations. The dynamic boundary condition (DBC) method assumes that the boundary particles satisfy the same equations as the fluid particles, but they do not move in response to the forces exerted on them (Crespo, et al., 2007). The stability of the DBC method also could be influenced by the time step used in the numerical calculations, which should be suitability short to deal with the highest velocity expected for any fluid particle interacting with the boundary particles.

Simulation time step

To ensure the robustness of the SPH-DEM simulations, the CFL condition needs to be satisfied (Monaghan et al., 1999). There are viscous diffusion and forcing terms in the CFL condition. The simulation time step, $\triangle t_{SPH}$ is estimated as shown in section 3.3.3.

6.5 Results and discussion

6.5.1 Validation of simulations

Single-phase flow of fluids of different rheology

The first step in the validation process evaluated the capability of the SPH module in the framework to simulate the single-phase flow of fluids of different rheology. The simulations were performed at a mean fluid velocity of 0.075 ms^{-1}, typical of the experimental mean particle-liquid mixture velocities used. The SPH-predicted velocity profiles are compared with those obtained from analytical solutions for the various rheologies considered in Figures 6.5 and 6.6. By appropriately selecting the values of the parameters τ_y, m and n in the HBP rheological model, different rheolog-

ical fluids were implemented. Thus, for a Newtonian fluid ($\tau_y = 0$ and $n = 1$) the numerical and theoretical profiles are identical in Figure 6.5(a). For power-law rheology, the simulation results are presented in Figure 6.5(b) for a wide range of cases (e.g., $\tau_y = 0$ and $n = 0.5, 0.8, 1.3, 1.7$), showing an excellent agreement with the theoretical solutions. Simulations of typical Bingham fluids (e.g., $n = 1$ and $m = 100$) with different yield stress values ($\tau_y = 1, 3, 5$ Pa) are depicted in Figure 6.5(c), again exhibiting a high degree of accuracy.

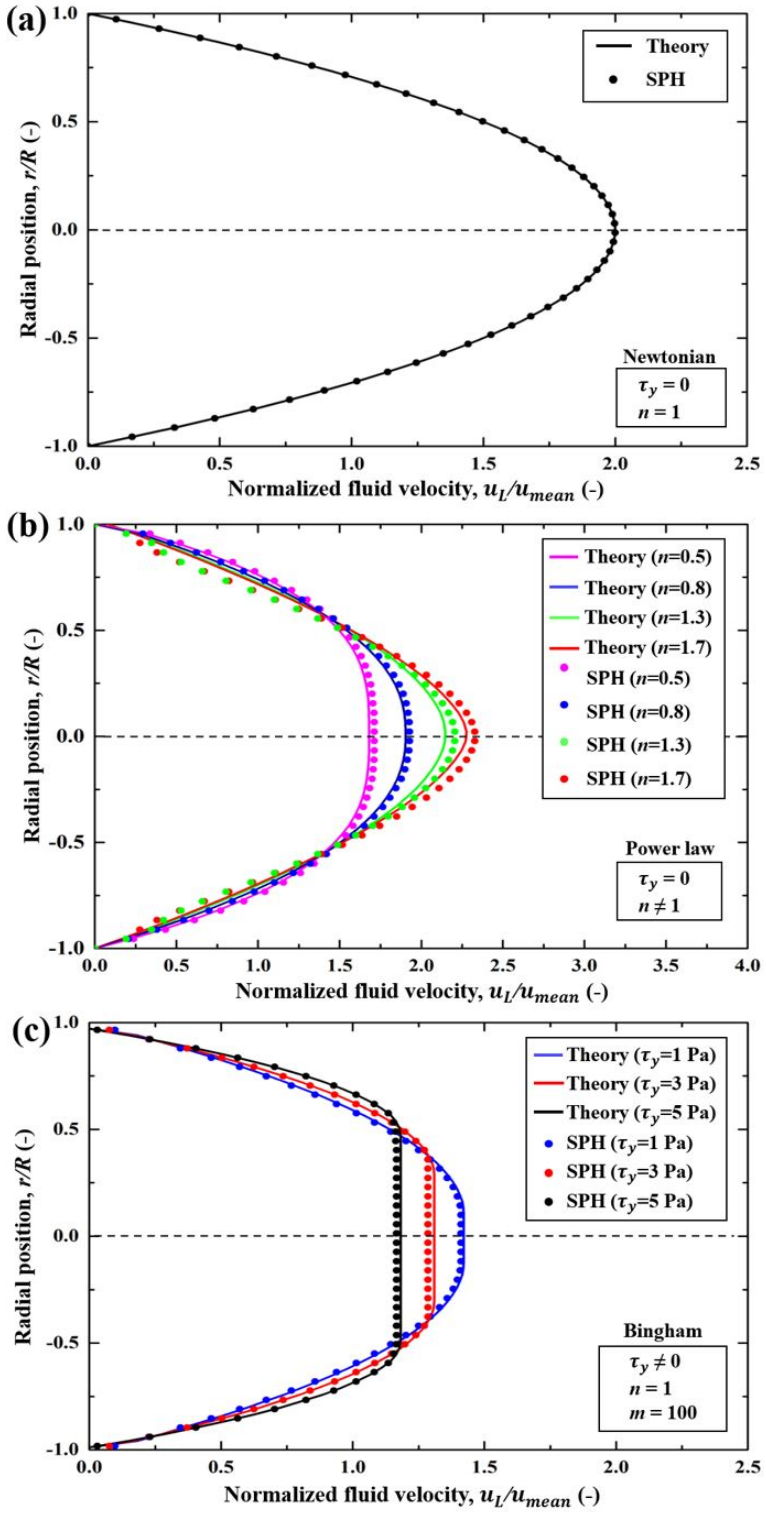

Figure 6.5: Normalized radial velocity profile for single-phase laminar flow of (a) Newtonian, (b) power law and (c) Bingham fluid: SPH predictions and analytical solutions compared.

The rheological behaviour of the CMC solution used in the particle-liquid flow experiments was also represented by the HBP model, where, τ_y = 6.4 Pa, n = 0.89 and m = 10. The SPH-predicted velocity profile shown in Figure 6.6 coincides very well with the analytical solution provided by the well-known Herschel-Bulkley equation. In conclusion, SPH is able to predict the pipe flow of non-Newtonian fluids with a high degree of accuracy.

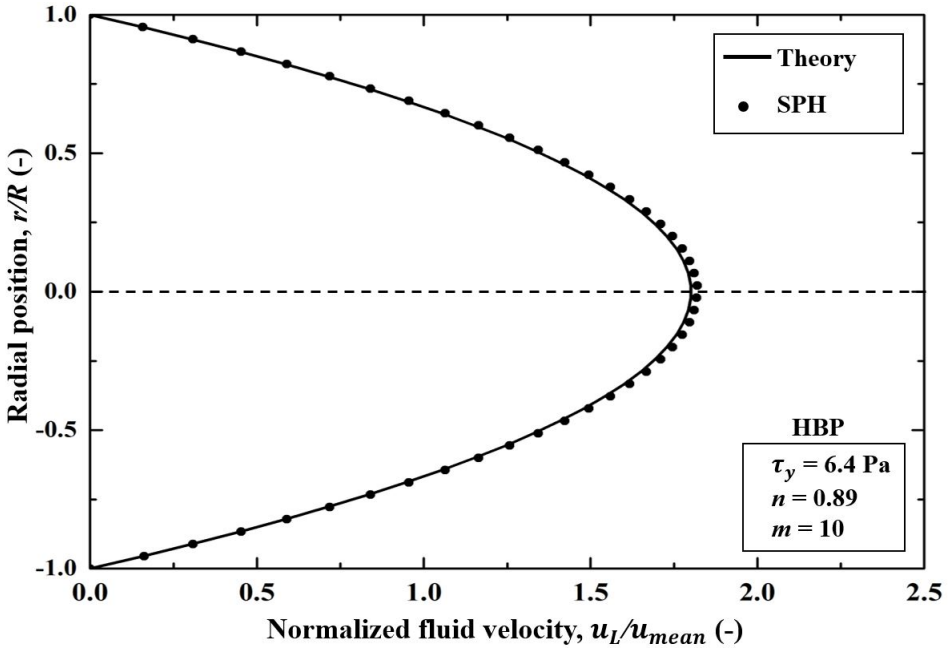

Figure 6.6: Normalized radial velocity profile for single-phase laminar flow of 0.8 wt. % CMC fluid used in experiments: SPH prediction and analytical solution compared.

The SPH-DEM simulations provide the Lagrangian trajectories for both the fluid and solid particles in the flow. Typical trajectories are depicted in Figure 6.7 illustrating the different behaviour of the fluid and particles in different regions of the flow. The SPH-DEM simulations were validated by comparing in each case the predicted local radial particle velocity profile, radial solid phase distribution and particle passage time distributions with those estimated from PEPT experimental data, as shown, respectively, in Figures 6.8-6.10. The simulation results were treated using the same procedure described above for analysing PEPT data to construct radial profiles of local

particle velocity and solid volume fraction, and particle passage times.

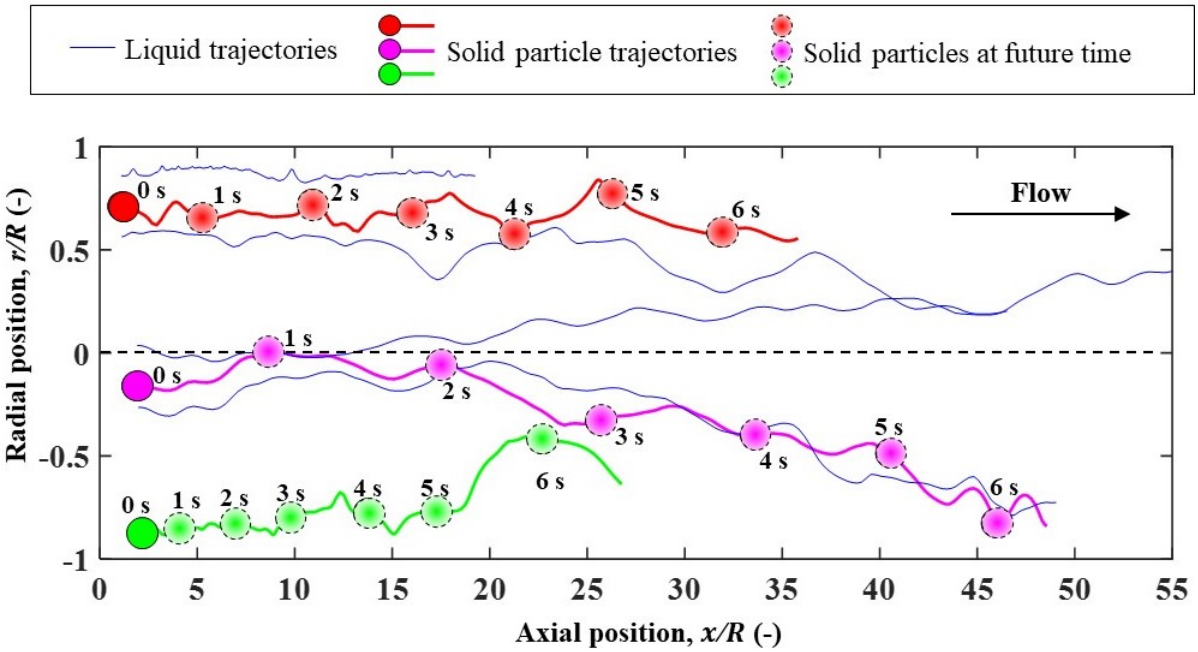

Figure 6.7: Typical SPH-DEM trajectories of liquid and particles over a travel period of 6 s: C_s = 20 vol. %.

Radial particle velocity profile

The SPH-DEM predicted radial particle velocity profiles are compared with PEPT determined profiles in Figure 6.8 at different solid loadings from 10 to 40 vol. %. The local velocity error bars for both simulations and experimental data are too small to be shown. There is a generally good agreement between the SPH-DEM predictions and PEPT measurements at all solid concentrations. The results show the capability of the SPH-DEM coupling to predict particle velocities in a complex two-phase flow consisting of a non-Newtonian carrier fluid with high solid loadings. The plots exhibit a minor asymmetry in the velocity profiles as the maximum appears slightly above the centreline. As the density of the particles is slightly higher than that of the carrier fluid, particle settling effects would be expected to distort the particle velocity profile causing particles to travel

faster in the top part of the pipe.

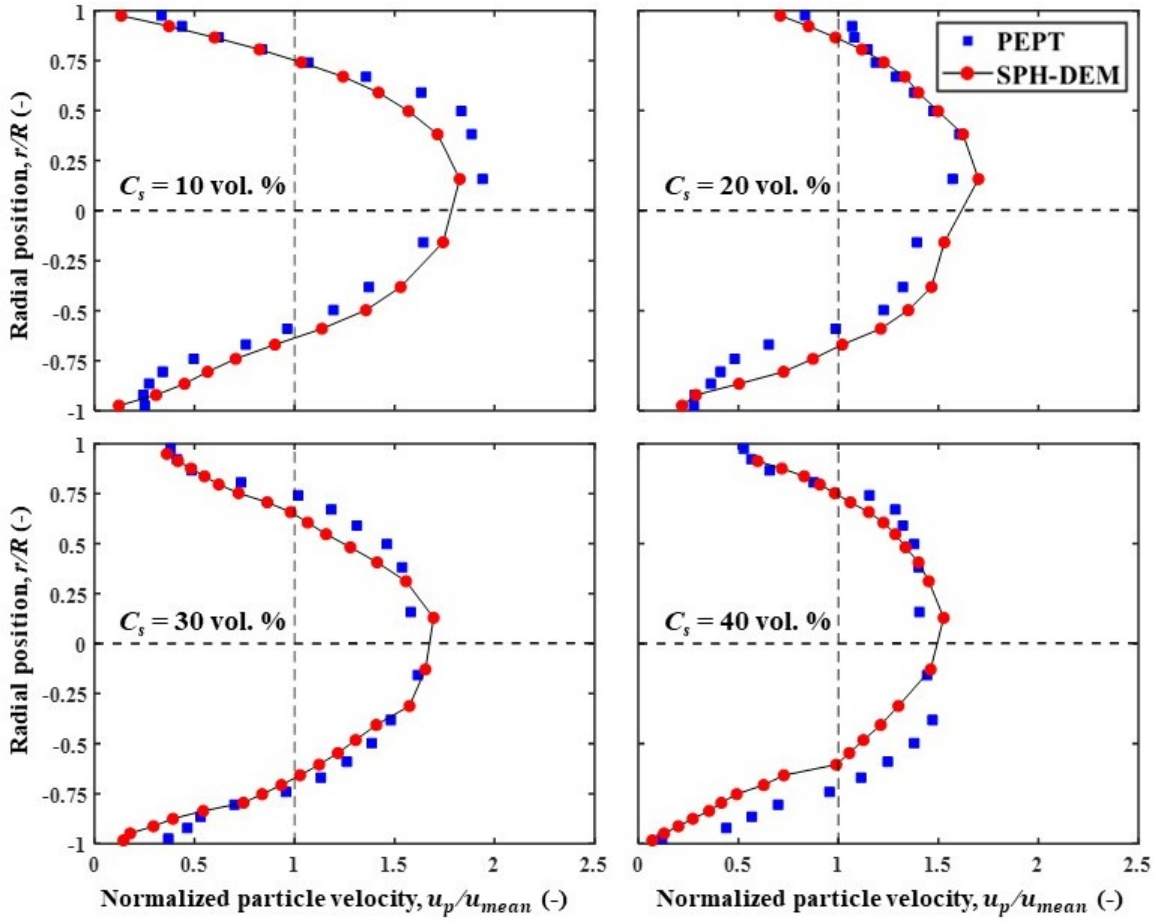

Figure 6.8: Normalized radial particle velocity profile developed at different mean solid concentrations: SPH-DEM predictions and PEPT measurements compared. Note that errors bars are too small to be shown.

Radial solid phase distribution

The SPH-DEM predicted and PEPT determined radial solid phase distributions corresponding to the same particle size and concentrations are compared in Figure 6.9. The local particle concentration in the flow was inferred from the Lagrangian particle trajectories by the method described above in Section 6.3.2, at 20 radial positions over 40 equidistant cross-sections along the length

of the pipe and an average obtained along each radial position. The radial particle concentration profiles thus constructed are shown in Figure 6.9. The error bars indicate the axial standard deviation of the local particle concentration at each radial position along the pipe, reflecting the complex dynamic fluctuating nature of the solid phase distribution. Such variations tend to reduce as the mean particle concentration increases. Comparison of the SPH-DEM predicted and PEPT determined solid phase profiles shows a good agreement, confirming again the capability of the coupled SPH-DEM methodology to deal with such complex flows.

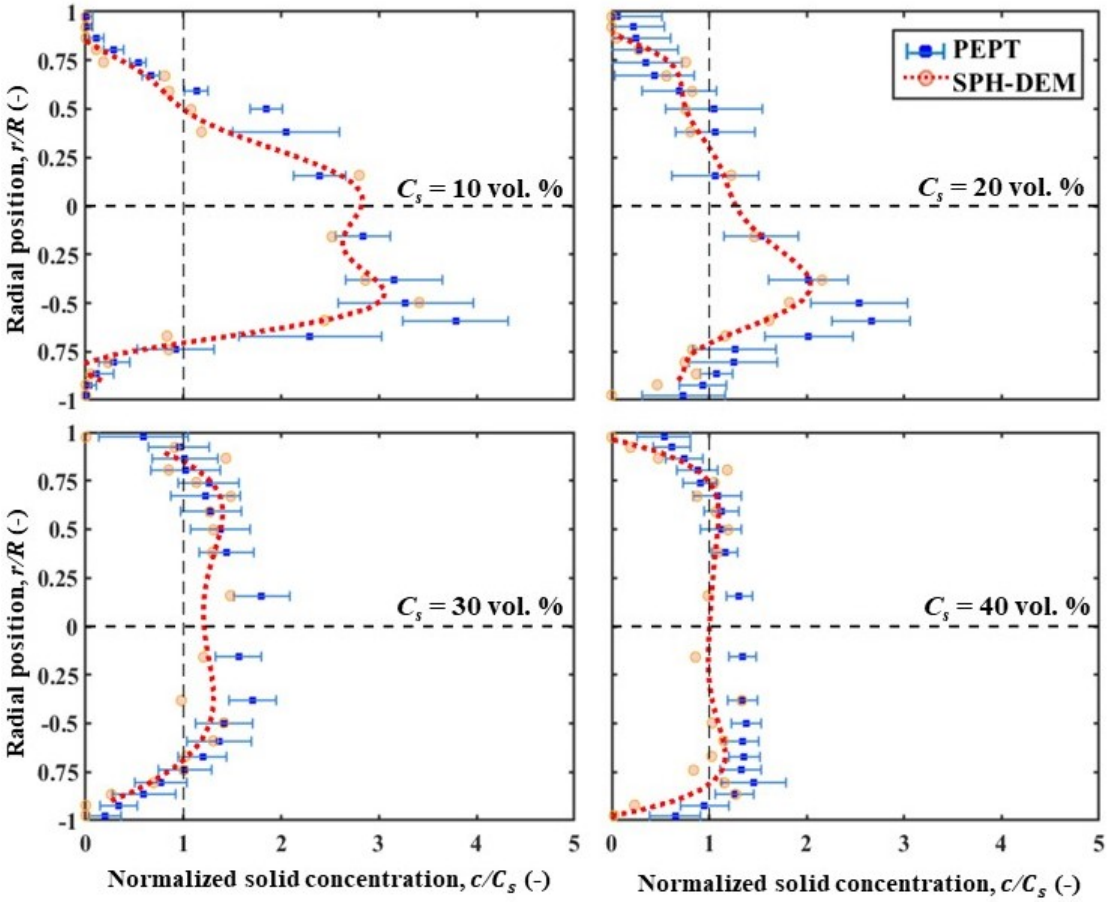

Figure 6.9: Normalized radial particle concentration profile developed at different mean solid concentrations: SPH-DEM predictions and PEPT measurements compared. Error bars indicate the axial standard deviation of the local particle concentration at each radial position along the pipe.

The effects of particle sedimentation, even though small, are apparent in the distorted profiles corresponding to C_s = 10 and 20 vol. %, showing a maximum in the bottom region of the pipe cross-section. Particles become more uniformly distributed across the pipe at higher solid loadings, exhibiting a nearly flat profile at C_s = 40 vol. % as the pipe cross-section fills up with particles (approaching the packing fraction) and inter-particle interactions increase.

Particle passage time distribution

As both SPH-DEM and PEPT provide Lagrangian trajectories of solid particles in the flow, they allow extraction of particle passage times, a very important parameter in pipeline transport of particle-liquid flows, e.g., in continuous inline processing of particulate food mixtures. Each trajectory within the experimental data set was used to extract the particle passage time over a given length of pipe, which was then normalised by the mean mixture passage time estimated from the mean mixture velocity (Table 6.1). The distributions obtained by both methods are presented in Figure 6.10 at the different particle concentrations investigated. Results show a good agreement between the numerical predictions and experimental measurements.

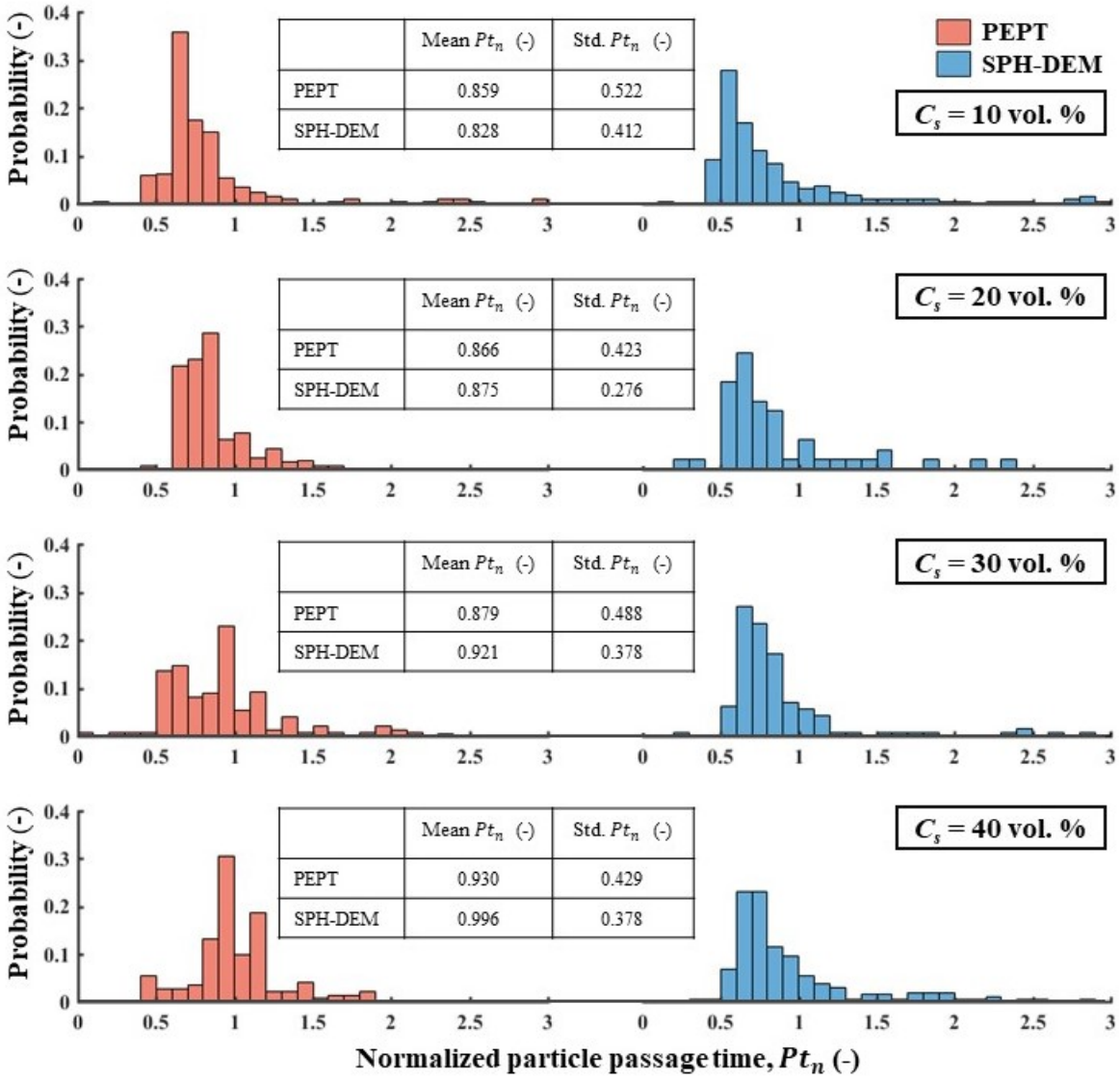

Figure 6.10: Normalized particle passage time distribution at different mean solid concentrations: SPH-DEM predictions and PEPT measurements compared.

Pressure-drop in particle-liquid flow

Prediction of pressure drop is important in the design and operation of pumped flow systems. Some empirical and semi-empirical correlations have been proposed for estimating pressure drop

in particle-liquid pipe flows. Two empirical correlations whose experimental conditions are remarkably close to the flow cases studied here are used to verify the pressure drop estimated from the SPH-DEM simulations. When the difference in density between particles and liquid is small (< 1 %) suspensions can usually be treated as a pseudo-homogeneous fluid whose density is equal to the mean density of the mixture, i.e., the two-phase flow is approximated by a single-phase flow (Chakrabandhu et al., 2005). And Gradeck et al. (2005) developed a correlation to estimate the pressure drop per unit length $\frac{\Delta P}{L}$ in particle-liquid flow consisting of coarse alginate particles (4.4 mm) in a CMC solution, thus:

$$C_f = \frac{1}{2}\frac{d_p}{\rho_{susp} u_{mean}^2}\frac{\Delta P}{L} \tag{6.7}$$

where, C_f is the fanning friction factor, ρ_{susp} is the mean suspension density. In laminar flow the friction factor is given by:

$$C_f = \frac{16}{Re} \tag{6.8}$$

where, Re represents the Reynolds number of the (pseudo-homogeneous) suspension.

Earlier Rasteiro et al. (1993) had developed a semi-theoretical solution to predict the pressure drop in particle-liquid flow based on the kinetic energy loss, J_c, the viscous energy loss, J_v, and the energy loss from particle–particle interactions, J_p, thus:

$$\left[\frac{\Delta P}{L}\right]_{susp} = \Phi_1 J_c + \Phi_2 J_v + \Phi_3 J_p \tag{6.9}$$

$$J_c = \frac{\rho_f \overline{u}^2}{d(1-C_s)} \tag{6.10}$$

$$J_v = \frac{\mu \bar{u}^2}{d^2(1-C_s)^2} \tag{6.11}$$

$$J_p = \frac{(\rho_s - \rho_f) g C_s^2}{(1-C_s)^3} \tag{6.12}$$

Φ_1, Φ_2, and Φ_3 are empirical constants.

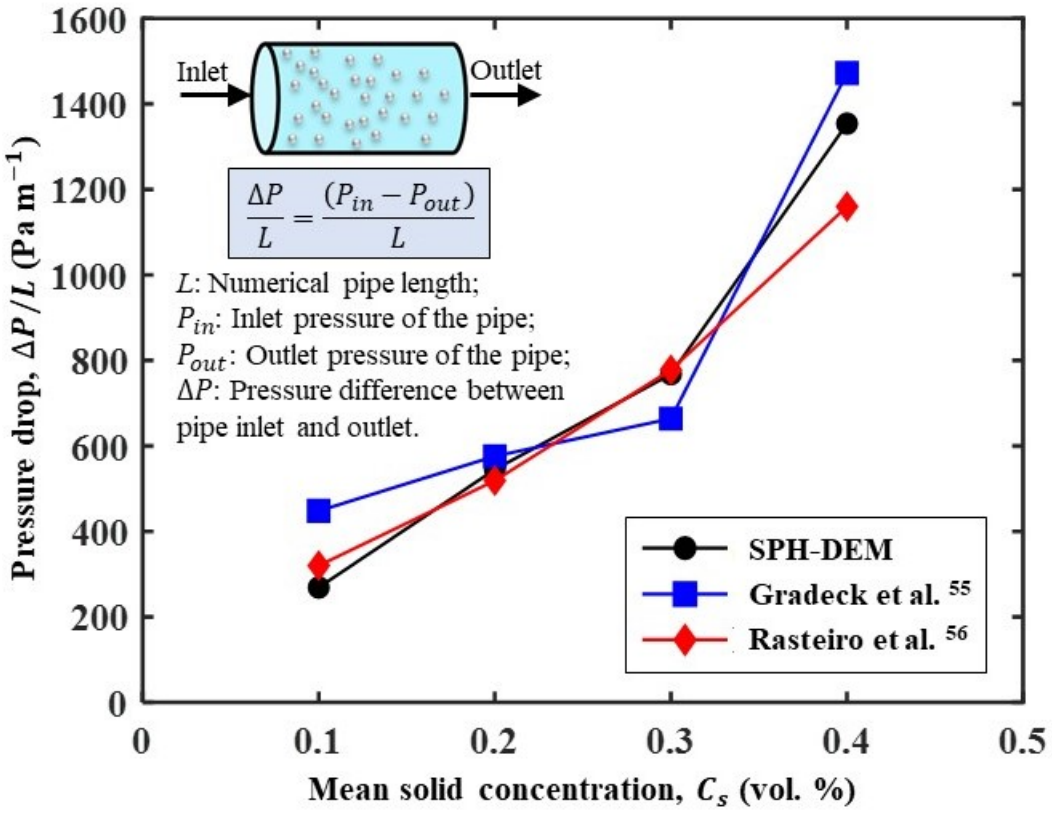

Figure 6.11: SPH-DEM predicted flow pressure drop compared with estimations from literature correlations (Eqs. (6.7) and (6.9)) at different mean solid concentrations.

The pressure drop predicted by SPH-DEM at the different particle concentrations investigated is compared in Figure 6.11 with those estimated from Eqs. (6.7) and (6.9). Whilst there is a fair agreement with Gradeck et al.'s empirical correlation, there is a very good agreement with Rasteiro

et al.'s semi-empirical correlation over the particle concentration range 10 to 30 vol. %. From 30 to 40 vol. % the two results seem to gradually diverge reaching a maximum difference of about 15% at 40 vol. %; such a discrepancy may be attributed to the fact that the correlation is based mostly on data in the concentration range 10 – 20 vol. %. Overall, the SPH-DEM predictions fall within the range of estimations provided by these two correlations, which is further evidence of the accuracy and reliability of the coupled method to simulate these complex flows even under conditions of high concentration which are typical of industrial food processing (Fairhurst et al., 2001).

6.5.2 Localized dynamics of particle-liquid flow

The Lagrangian particle-based nature of the SPH-DEM simulations provide important information on the local hydrodynamic properties of both particles and carrier fluid. One of these properties which can be estimated is the local particle-liquid slip velocity, $u_{slip} = u_p - u_L$. Whilst such a slip velocity can have significant values in dense flows, because the particles here are nearly neutrally-buoyant the values estimated from both experimental and simulated trajectories were, as expected, vanishingly small.

Particle angular velocity or spin

One of these properties which can be estimated is particle angular (or spin) velocity, ω, which is defined as:

$$\omega = \frac{d\theta}{dt} \tag{6.13}$$

where, θ is angular displacement. In a number of applications including food processing, flow

is often accompanied by heating or cooling. Similarly, in chemical reactors mass transfer occurs frequently. The heat/mass transfer coefficient between particle and liquid is critical and directly affected by the local relative (slip) velocity between particle and fluid. The rotational (spin) motion of particles enhances slip and is, thus, also significant in defining heat/mass transfer. It also produces a lift force which affects particle trajectories and, hence, the distribution of particles and flow field (Duchanoy et al., 2003). Thus, to understand particle-liquid flow, both rotational and translational behaviours of particles need to be known. Rigorous studies of particle spin motion are virtually non-existent.

Based on the Magnus effect (Seifert, 2012) particles experience a lift force if the angular velocity is negative, and they sink in the fluid if the angular velocity is positive. The local particle angular velocities simulated at different mean solid concentrations are presented in Figure 6.12(a), whilst the corresponding averaged radial profiles are plotted in Figure 6.12(b). The spin velocities are positive (anticlockwise) in the top half of the pipe cross-section and negative (clockwise) in the bottom half. Particle spin is fastest closest to the wall where the liquid velocity gradients are highest, reducing to zero at the centre of the pipe before switching direction. At the solid loading of 40 vol. %, spin becomes negligible everywhere except close to the wall. As the solid concentration approaches the particle packing fraction, velocity gradients in the core section dramatically weaken and inter-particle interactions increase such that particle spin is prevented.

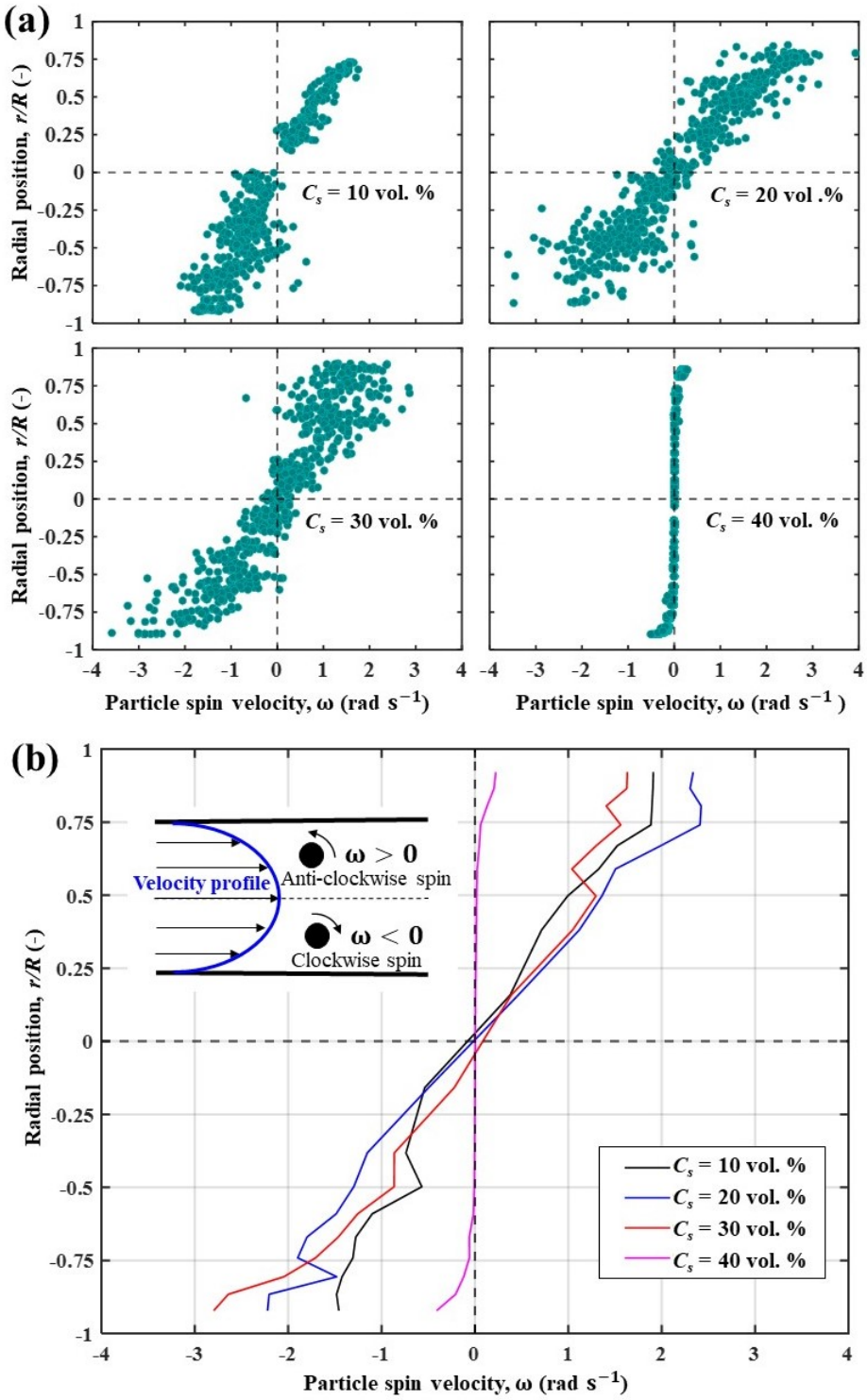

Figure 6.12: Radial particle angular-velocity profiles predicted by SPH-DEM at different mean solid concentrations.

Flow pressure field

Another important parameter which can be extracted from the Lagrangian simulations is the flow pressure field. A typical contour plot is shown in Figure 6.13(a). Enlarged views of the pressure field and isobars surrounding particles located in the top (A) and bottom (B) parts of the pipe, are presented in Figure 6.13(a) and (b). A close inspection of the isobars around particle A shows that the pressure (P2) to the right of the particle is slightly higher than the pressure (P1) to the left. This means that the liquid around particle A exerts a retarding form drag force on particle A which causes the particle to lag behind the liquid. On the other hand, the pressure (P4) to the right of particle B is slightly lower than the pressure (P3) to left. Thus, particle B is subject to an accelerating form drag force causing it to lead the liquid. Such detailed information is valuable for analysing the local behaviour of individual particles as well as particle clusters.

Fluid vorticity

Vorticity is another parameter of fundamental importance which can be extracted from the simulations and is a measure of the rotation or degree of deformation of a fluid and is defined as the curl of the velocity. A typical simulated liquid vorticity contour map is depicted in Figure 6.14. Vorticity values are highest near the pipe walls showing a high degree of fluid deformation, falling to zero in the central region. Vorticity is positive in the top part of the pipe cross-section and negative in the bottom part, confirming the reason for the anticlockwise and clockwise spin of particles in the top and bottom regions, respectively, as discussed above. A close inspection of the vorticity field around a single particle and around two adjacent particles is shown in Figure 6.14(a) and (b). The fluid around a single particle exhibits a symmetrical four-petal shape of vorticity which is deformed when two particles approach each other squeezing the liquid film in between.

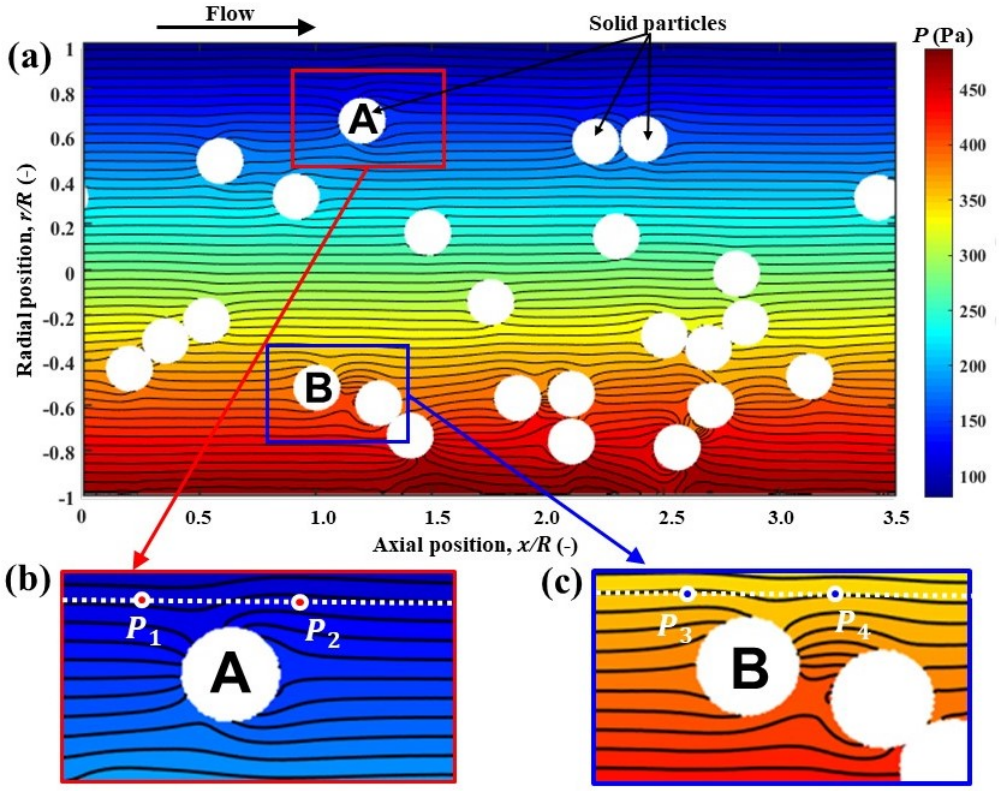

Figure 6.13: Typical SPH-DEM predicted flow pressure field: C_s = 10 vol. %; P1, P2, P3 and P4 indicate local fluid pressure.

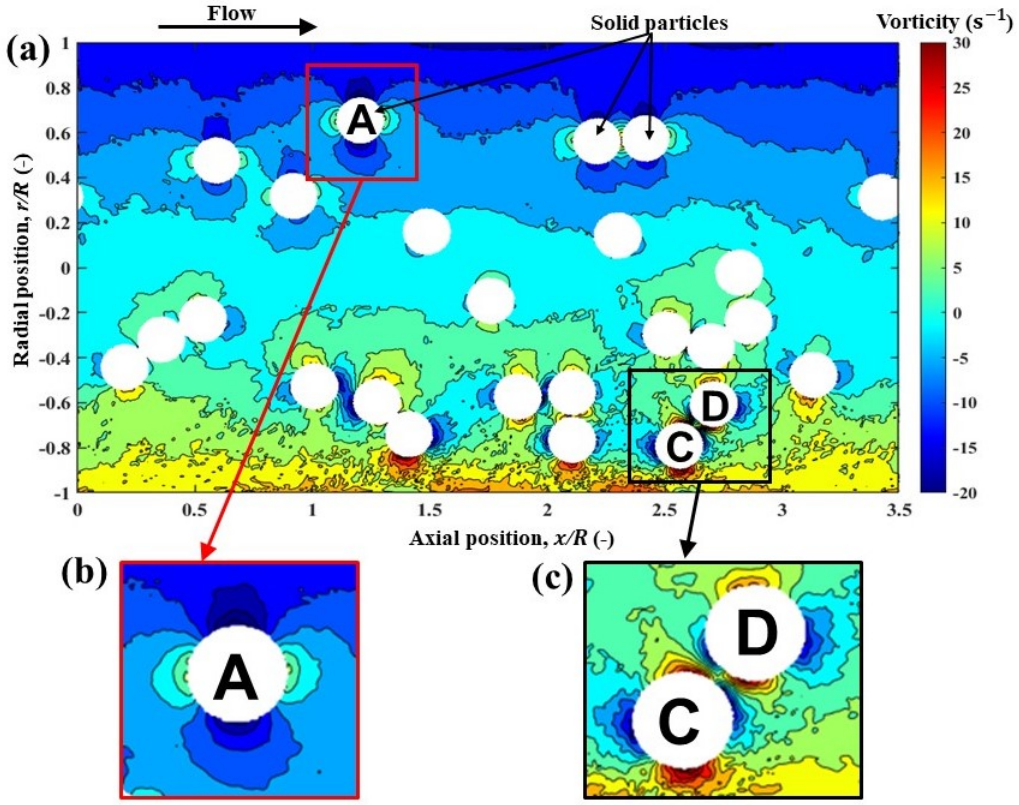

Figure 6.14: Typical SPH-DEM predicted liquid vorticity field: C_s = 10 vol. %.

6.5.3 Parametric study

Different particles sizes (d_p = 0.5-10 mm, d_p/D = 0.0125–0.25) with different density ratio (ρ_r = 1.014, 1.2, 1.5) simulations were conducted at same solid concentration C_s = 20 % and mean mixture velocity U_{mean} = 0.72 m/s. The results are shown and described in the form of plots of solid velocity, liquid velocity, and solids concentration.

Figure 6.15 illustrates the normalized velocity profiles and solid concentration distributions for 0.8 wt% CMC solution with alginate particles of various sizes (d_p = 0.5-10 mm), a density ratio of 1.014, and a solid concentration of 20 %. In Figure 6.15(a), the normalized liquid velocity profiles indicating that fine solid particles (d_p = 0.5 mm) have velocity profiles very similar to the liquid

velocity, with a uniform particle distribution throughout the pipe. This similarity and homogeneity suggests that the flow behaviour is consistent with typical suspension characteristics. However, as the particle size increases to 4 mm and 10 mm, the solid velocity profiles become asymmetric relative to the central axis, as seen in Figure 6.15(b). This asymmetry is due to the effect of gravity, which causes more particles to accumulate at the bottom of the pipe, thus increasing particle collisions and resistance, which decreases the flow rate at the bottom. Although the solid velocity profile is asymmetric, the liquid velocity profile remains similar to the solid velocity profile due to slip velocity effects. Figure 6.15(c) presents the normalized solid concentration (C_s) distributions, highlighted that larger particles show a more significant concentration gradient, with higher concentrations observed near the bottom of the pipe.

From Figure 6.16(a) and Figure 6.15(a), in both figures, it is observed that the normalized liquid velocity profiles for fine solid particles (0.5 mm) are almost identical to the liquid velocity profiles. However, as the particle size increased, significant differences emerge. In Figure 6.16(a), the velocity profiles show a more pronounced asymmetry compared to Figure 6.15(a), due to the higher density ratio, which enhance the gravitational settling of particles. As shown in Figure 6.16(c), the concentration gradient near the bottom of the pipe is sharper and the particle accumulation more intense compared to Figure 6.15(c). The lower solid concentration in top of pipe allows particles to settle more freely, resulting in a sharper concentration profile and more significant settling. In contrast, the radial position corresponding to the highest concentration at the bottom of the pipe gradually moves closer to the pipe centre line due to the large concentration of particles at the bottom of the pipe and the increased collisions and interactions between particles.

The density of solid particles is a fundamental parameter in particle-liquid flow systems since it has a deep impact on all aspects of flow behaviour and system dynamics.The relative density of solid particles compared to liquids determines whether the particles float, sink, or are suspended. The rate of settling or rising of small particles in liquids is governed by Stokes' law, while large particles are governed by more complex drag equations. This settling rate depends directly on the

density difference between the particle and the liquid. With the particle density increase to ρ_r = 1.5, even fine particle (0.5 mm) begin to accumulate at the bottom in certain numbers in Figure 6.17(c),and a slight asymmetry appears in the velocity profiles of the liquid and solid particles in this special case. Comparison of the Figures 6.15-6.17, theses three plots shows that the effect of density ratio on the large size of the particles is more obvious, with the number of particles on top of the pipe decreasing as the density ratio increases. In suspensions, the stability is strongly influenced by the density of the particles. Denser particles are more likely to settle, leading to layer and phase separation, while less dense particles are more likely to remain in suspension, thus promoting the formation of a homogeneous mixture. The slip velocity is also affected by the particle density. Denser particles typically experience higher slip velocities, leading to more significant differences in movement between the particles and the fluid.

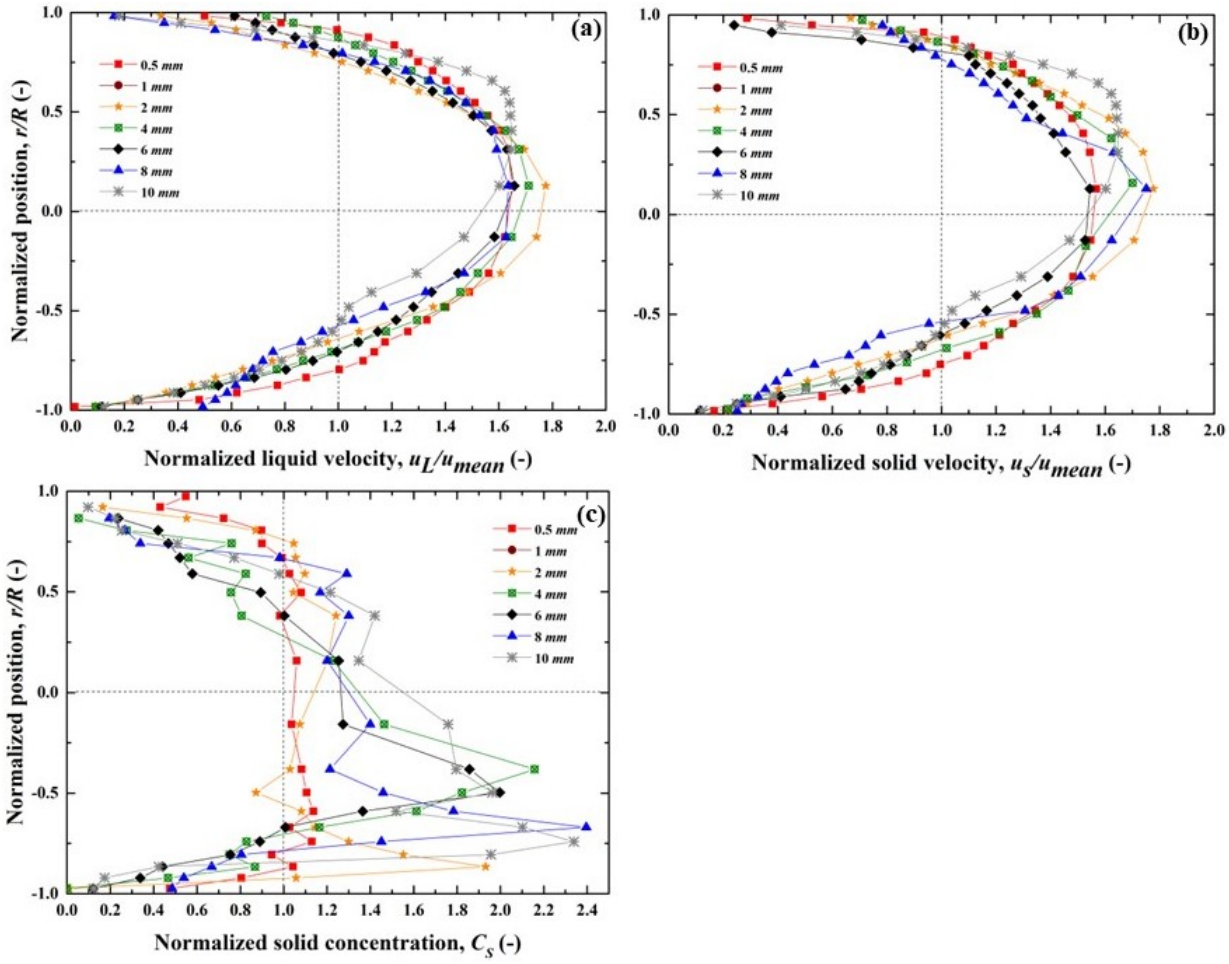

Figure 6.15: Effects of particle size on radial profiles of (a) liquid velocity, (b) solid velocity, and (c) solid concentration, C_s = 20 %, ρ_r = 1.014.

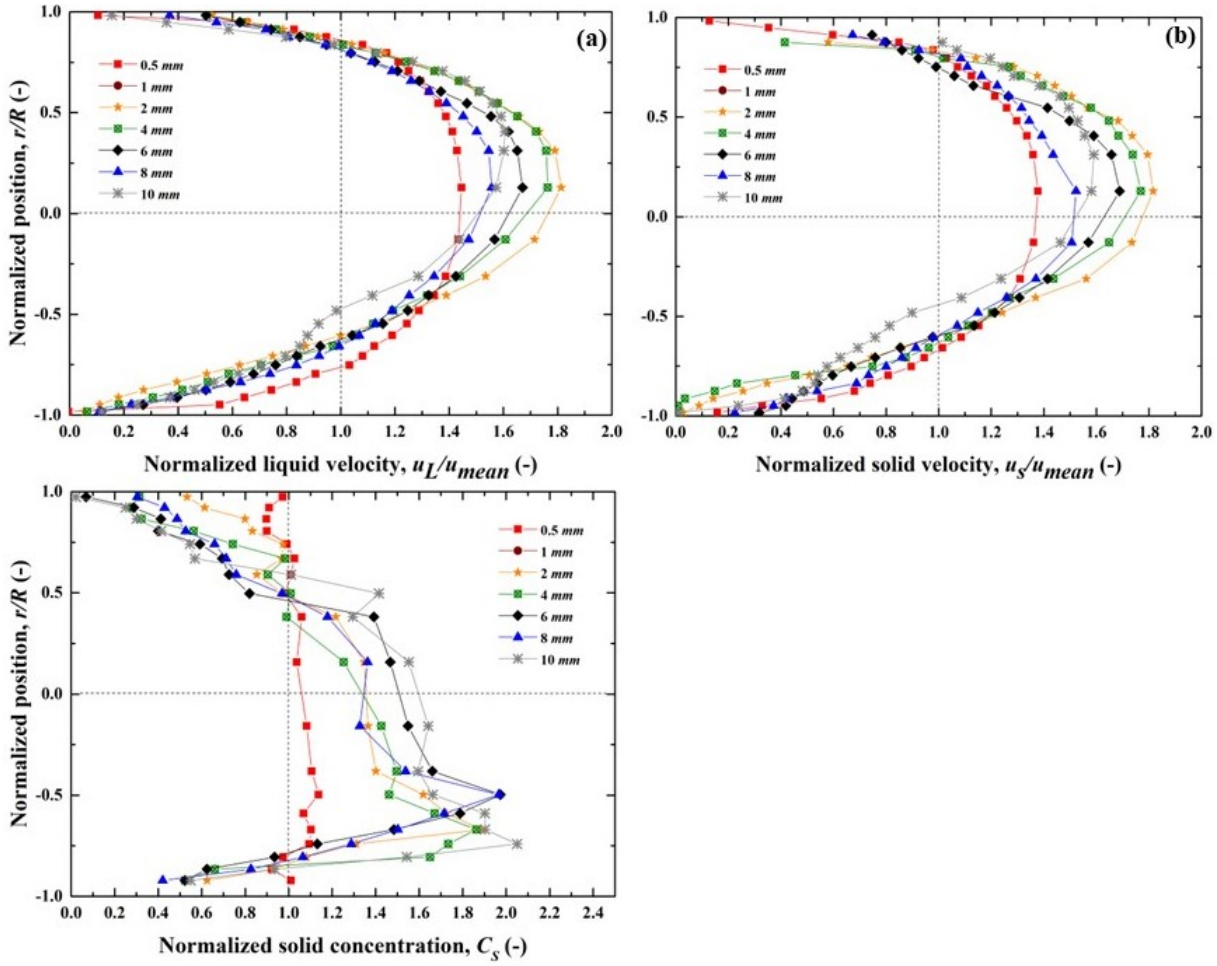

Figure 6.16: Effects of particle size on radial profiles of (a) liquid velocity, (b) solid velocity, and (c) solid concentration, C_s = 20 %, ρ_r = 1.2.

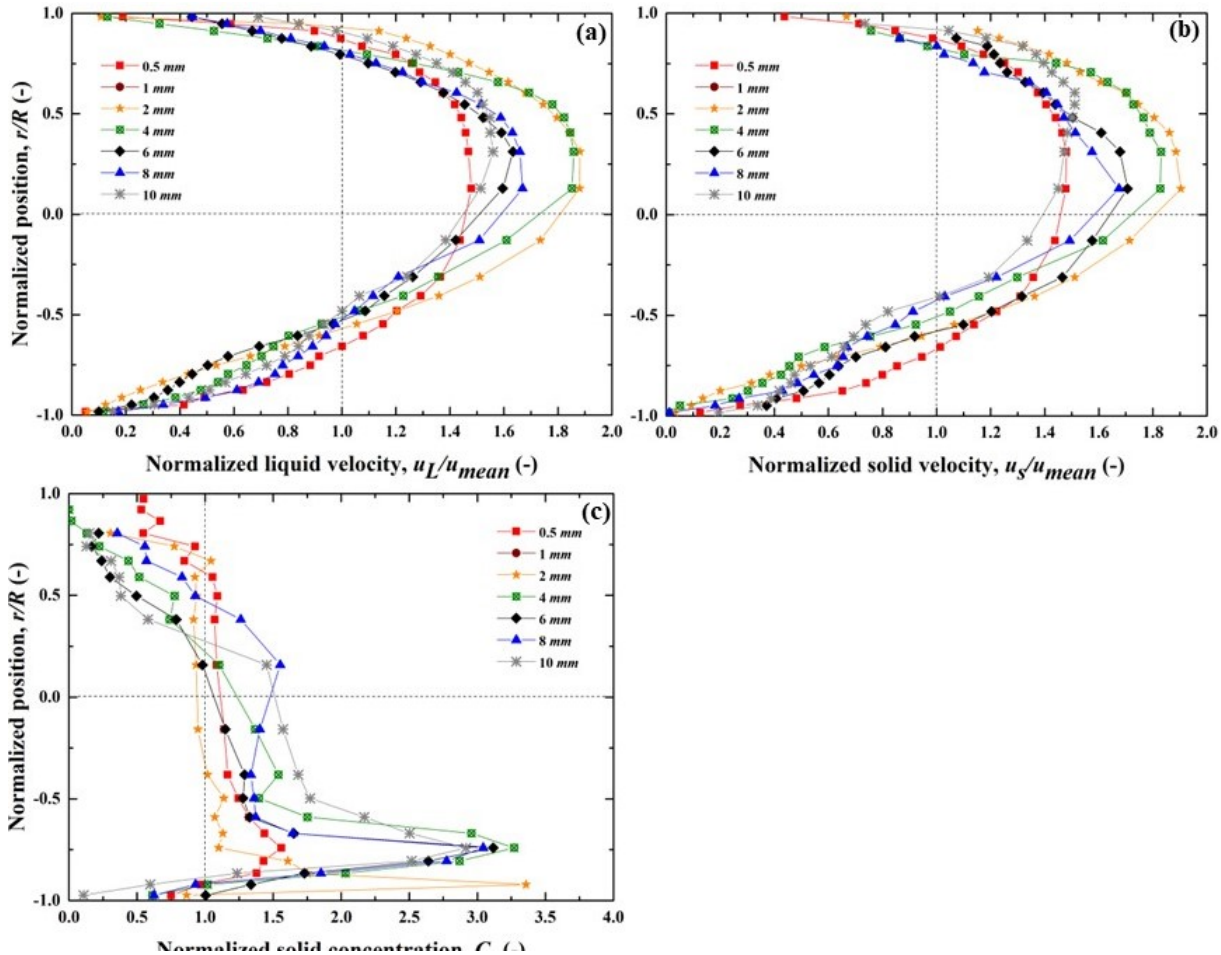

Figure 6.17: Effects of particle size on radial profiles of (a) liquid velocity, (b) solid velocity, and (c) solid concentration, C_s = 20 %, ρ_r = 1.5.

6.6 Comparison of SPH-DEM and FVM-DEM

Results plotted in Figure 6.18 are for two particle concentrations 10 and 30 vol.%, with mixture Reynolds number, $Re_{mean} = 14$, conveyed by a 0.8 wt.% CMC solution in 3D simulations. Validation of the numerical simulations is conducted through comparison with PEPT measurements. At the lower concentration (C_s = 10 vol.%), the FVM-DEM approach produces reasonable predictions of the velocity profile but fails to accurately predict the spatial particle distribution. The near axial

symmetry observed in the FVM-DEM particle velocity and volume concentration profiles suggest inadequate estimation of particle gravity settling effects. This discrepancy warrants further investigation and improvement. However, at high solid loading (C_s = 30 vol%), the FVM-DEM method manages to predict particle velocity and concentration distribution to a good degree of accuracy. In contrast, the SPH-DEM method is more successful in predicting the particle velocity and concentration profiles at both low and high solid loadings, indicating a superior capability over FVM-DEM in the laminar regime.

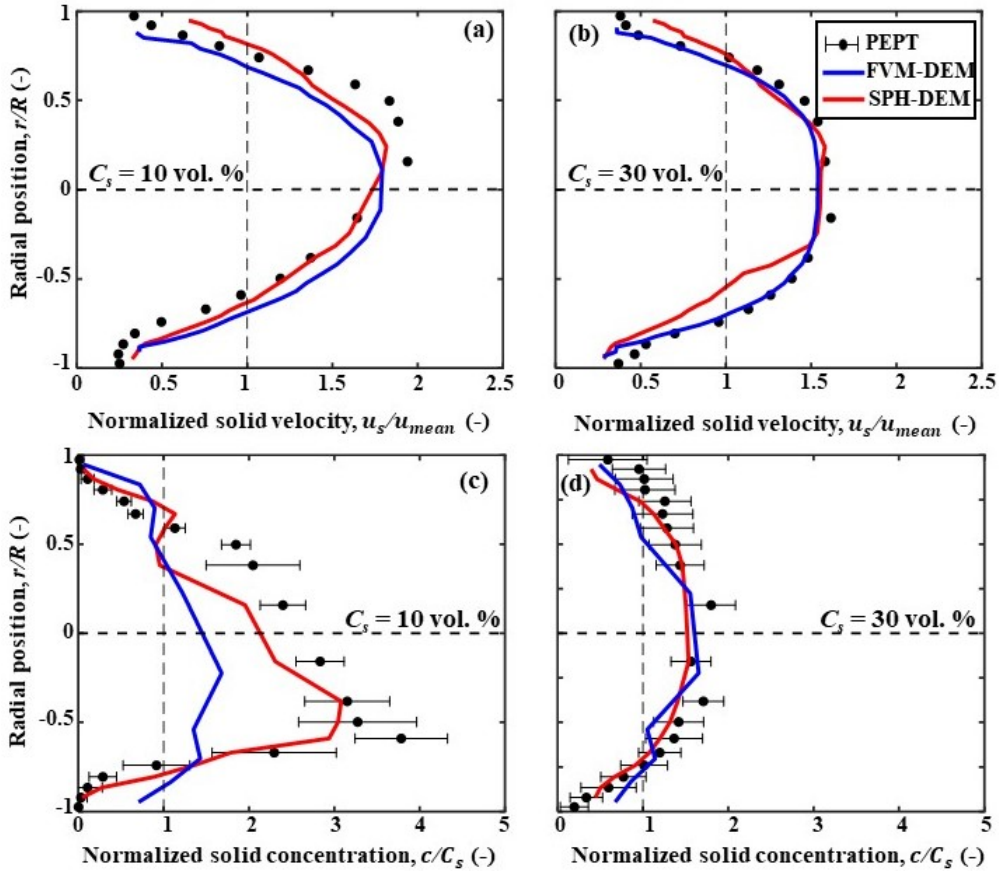

Figure 6.18: FVM-DEM and SPH-DEM predictions compared to PEPT measurements in laminar particle-laden flow (d_p = 4 mm and ρ_r = 1.014, Re = 14): (a) particle velocity profile (C_s = 10 vol.%); (b) particle velocity profile (C_s = 30 vol.%); (c) particle concentration distribution (C_s = 10 vol.%); (d) particle concentration distribution (C_s = 30 vol.%). Note velocity error bars are too small to be shown.

The case displayed in Figure 6.19 is for 30 vol.% solids conveyed by a 36 wt.% sugar solution, at a mean mixture Reynolds number of 7,800. Bar some slight deviations near the wall, the FVM-DEM method demonstrates a close match with PEPT results over most of the pipe cross-section, accurately estimating particle and liquid velocities, as well as particle concentration. The predictions of particle velocity and concentration distributions by SPH-DEM agree well with PEPT results, albeit with slight discrepancies near the pipe wall. However, the liquid velocity profile exhibits a

significant deviation from the PEPT profile away from the central core region. Thus, the FVM-DEM model framework appears to be better at handling particle-laden turbulent flows compared to SPH-DEM. At lower Reynolds numbers, the agreement between FVM-DEM and SPH-DEM improves somewhat, as exemplified in Figure 6.20.

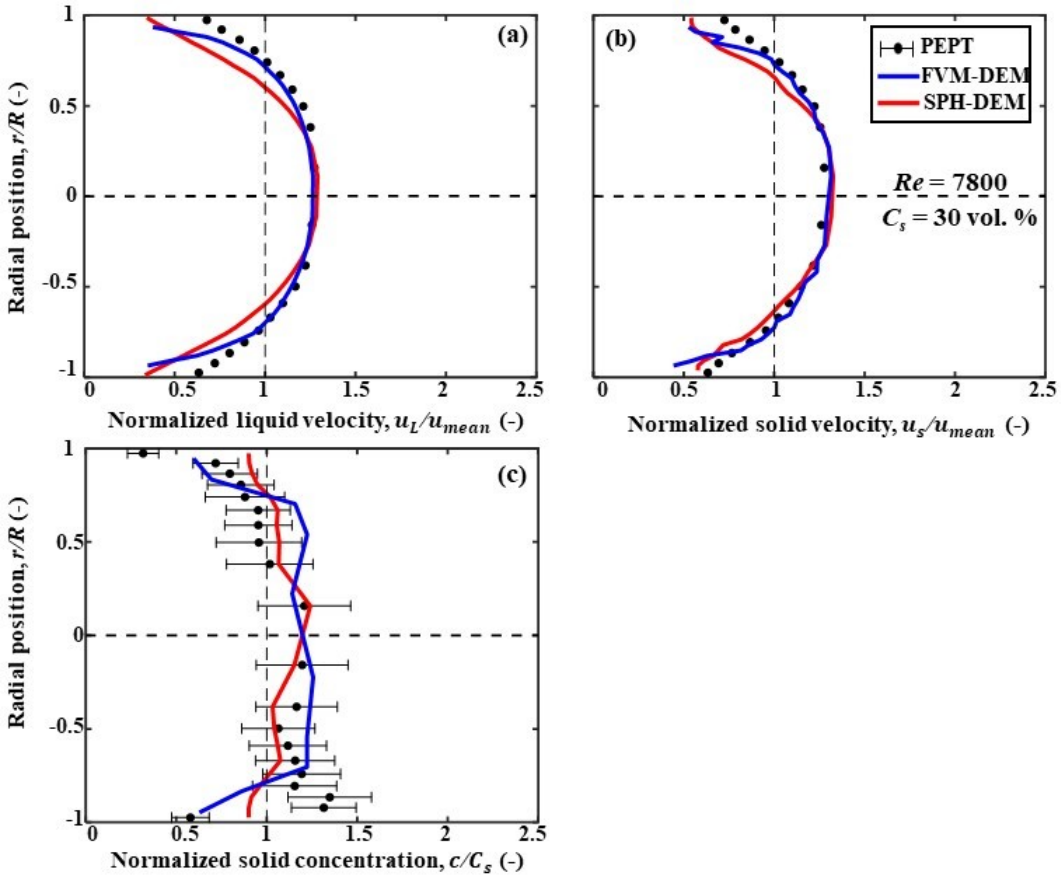

Figure 6.19: FVM-DEM and SPH-DEM predictions compared to PEPT measurements in turbulent particle-laden flow (d_p = 4 mm, C_s= 30 vol.%, ρ_r = 1.014 = 1.02, Re = 7,800): (a) liquid velocity profile; (b) particle velocity profile; (c) particle concentration distribution. Note velocity error bars are too small to be shown.

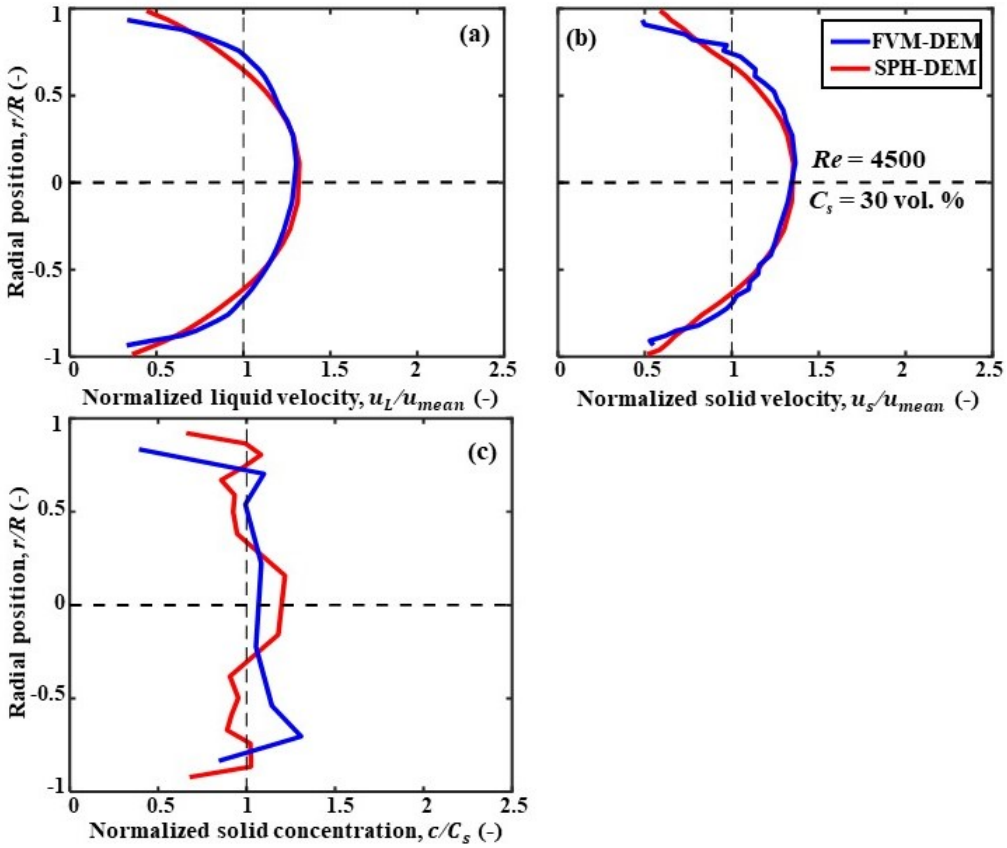

Figure 6.20: FVM-DEM and SPH-DEM predictions compared in turbulent particle-laden flow (d_p = 4 mm, C_s= 30 vol.%, ρ_r = 1.02 Re = 4,500): (a) liquid velocity profile; (b) particle velocity profile; (c) particle concentration distribution.

Computational cost serves as a crucial metric for assessing the cost-effectiveness of numerical simulations in practical applications. Recent advancements in computer science have led to significant increases in both CPU and GPU computational power, making the implementation of CPU-GPU solutions possible. An illustrative study utilizing 12 CPUs (Intel® Xeon® Silver 4214 Processor) and a GPU (NVIDIA® GeForce® RTX 2080) was used to estimate the computational time for different numerical FVM-DEM and SPH-DEM simulations, as summarised in Table 6.3. The utilization of GPU further reduced the processing time. However, for particle-laden flow (C_s=30 vol.%), a much longer computation time ($\sim$3 orders of magnitude greater) was necessary, which

could be moderately reduced ($\sim$16%) with the aid of GPU.

SPH-DEM proved very inefficient compared to FVM-DEM, requiring $\sim$250 times longer without GPU and $\sim$13 times longer with GPU for single-phase flow, and $\sim$16 times and $\sim$6 times more computational time without and with GPU, respectively, for particle-liquid flow. It is noteworthy that in the case of SPH-DEM, the use of GPU technology produced much greater improvements performance compared to CPU alone, proving highly suitable for meeting the computational demands of large-scale smoothed particle simulations (Winkler et al., 2017; Xiong et al., 2013). Thus, mesh-based CFD demonstrates high cost-effectiveness compared to SPH.

Table 6.3: Simulation time comparison between FVM-DEM and SPH-DEM methods

	Number of mesh/numerical particles	Simulation time (hr)	
		CPU	CPU-GPU
FVM-DEM	255,592	23.6	19.7
SPH-DEM	795,488	372	127

6.7 Conclusion

A Lagrangian-Lagrangian particle-based SPH-DEM numerical approach was applied to simulate the horizontal laminar pipe flow of coarse particle-liquid food suspensions. SPH-DEM was able to predict the single-phase flow of various non-Newtonian fluid rheologies including the carrier fluid used to convey food particles with a high degree of accuracy, as validated by analytical solutions of radial velocity profiles. The particle-liquid flow simulations were also successfully validated using experimental measurements obtained by a technique of positron emission particle tracking. The radial particle velocity profiles, radial solid phase distributions as well as particle passage time distributions were accurately predicted at solid loadings varying from 10 to 40 vol. %. Radial

particle velocity profiles are asymmetric, with the maximum being located above the centreline. Such asymmetry disappears at high solid concentrations, and the maximum moves to the centre.

Simulations yielded detailed information on the local dynamics of the two-phase flows investigated, including translational as well as rotational particle slip velocities, flow pressure field and fluid vorticity. Whilst local translational particle slip velocities, as expected for nearly-neutrally buoyant particles, were vanishingly small, particle angular (slip) velocities were significant. Spin is positive (anticlockwise) in the top half of the pipe cross-section and negative (clockwise) in the bottom half. Particle spin is fastest closest to the wall where liquid velocity gradients are highest, reducing to zero at the centre of the pipe before switching direction. As solid loading increases, approaching the particle packing fraction, spin becomes negligible everywhere except close to the wall.

The pressure drop predicted by SPH-DEM at different particle concentrations showed a very good agreement with empirical correlations from the literature, which is further evidence of the accuracy and reliability of the coupled method to simulate these complex flows even under conditions of high concentration which are typical of industrial food processing. With further development, the framework has potential for simulating flows involving particles with more complex physical properties and fluids with more complex rheologies.

Nomenclature

Symbols

c	Local solid volume concentration (–)
C_s	Mean solid volume concentration (–)
c_n	Normalized solid phase concentration (–)
D	Pipe diameter (m)
d_p	Particle diameter (m)
E	Young modulus (Pa)
h	Kernel smooth length (–)
L	Pipe length (m)
m	Papenastasiou parameter (–)
n	Power law index (–)
O_E	Local occupancy (–)
P	Pressure (Pa)
P_{tn}	Normalized particle passage time (–)
r	Radial position (m)
R	Pipe radius (m)
Re	Reynolds number (–)
s_p	Numerical particle spacing (m)
u_L	Liquid velocity (m s^{-1})
u_{mean}	Mean mixture velocity (m s^{-1})
u_f	Superficial velocity (m s^{-1})
u_s	Solid particle velocity (m s^{-1})
u_{slip}	Slip velocity (m s^{-1})
Δt_{SPH}	Time step of simulation (ms)
Δt	Tracer spent time in each cell (s)

ΔP	Pressure difference (Pa)
t_{PEPT}	PEPT experiment runtime (s)
t_c	Ergodic time (s)
W	Kernel function

Greek Symbols

ω	Angular velocity (rad s^{-1})
θ	Angular displacement (rad)
μ	Apparent viscosity (Pa s)
μ_{eff}	Effective viscosity (Pa s)
σ	Standard deviation (–)
ρ_f	Fluid density (kg m^{-3})
ρ_p	Particle density (kg m^{-3})
ρ_r	Particle to fluid density ratio (–)
ν_p	Poisson coefficient of particle (–)
τ_y	Yield stress (Pa)

Chapter Seven

APPLICATION OF SPH APPROACH TO MODELLING VISCOPLASTIC FLUID IN STIRRED VESSELS

7.1 Introduction

In the field of chemical engineering, the design and optimization of industrial stirred vessels are crucial for ensuring efficient and effective chemical processing (Hemrajani et al., 2003; Zlokarnik, 2008). Since many industrial applications involve stirred tanks with no-Newtonian rheology, hence the investigation of non-Newtonian mixing systems is required to improve final products. Different from Newtonian fluids, non-Newtonian fluids exhibit complex flow behavior with viscoelastic, shear-thinning, or shear-thickening properties, which brings unique challenges to the design and operation of mixing vessels (Wang et al., 2018). Understanding the flow behavior of non-Newtonian fluids in stirred vessels is critical in various industrial processes such as polymer processing, food manufacturing, and pharmaceutical production. Therefore, a detailed understanding of the interactions between fluid rheology, mixing mechanisms and vessel geometry is required

to optimize mixing performance and ensure product consistency. Mixing of non-Newtonian fluids result in a homogeneous region termed the "cavern" around the impeller, while the fluids elsewhere in the vessel remain essentially stagnant or exhibit sluggish movement. Moreover, poor heat and mass transfer rates and high temperature gradients can occur when stagnant zones are existed and, if gassed, anoxia may occur during fermentation (Solomon et al., 1981). Several studies with experimental and numerical methods have been conducted using various impellers to evaluate cavern size as a function of the power drawn by yield stress fluids for different types of impellers, such as Rushton turbine, pitched blade turbine, disk turbine, Lightnin A315 and Scaba 6SRGT impeller (Barigou, 2004; Elson, 1990; Galindot et al., 1992).

One of the earliest experimental methods involves flow visualization techniques such as particle image velocimetry (PIV) (Guida et al., 2010a; Li et al., 2011) and laser-induced fluorescence (LIF) (Barigou, 2009; Busciglio et al., 2014). These methods provide qualitative insights into flow patterns and mixing efficiency but lack quantitative data on fluid rheology. Ultrasonic Doppler Velocimetry (UDV) enables the measurement of flow velocity profiles in stirred vessels with high spatial and temporal resolution. It has been utilized to study non-Newtonian fluid flows, providing insights into velocity gradients, shear rates, and flow homogeneity (Bouillard et al., 2001). Additionally, Positron Emission Particle Tracking (PEPT) has been utilized as a non-intrusive Lagrangian flow visualization technique to obtain complete 3D velocity and concentration fields of both continuous and dispersed phases in opaque mixing equipment (Guida 2019,2010). In this present, PEPT data was used to determine the accuracy of numerical model. Despite this, most of the literature on mechanically agitated fluid mixers is focused on the study of turbulent Newtonian flows (Li et al., 2023a; Savari et al., 2022).

Computational fluid dynamics (CFD) is a widely used tool for simulating fluid behaviour in stirred vessels, and the Lagrangian meshfree approach has emerged as a promising alternative to traditional grid-based methods. Viscoplastic fluids are characterized by their yield stress, which causes them to behave as solids until a certain threshold is reached, at which point they begin to flow

like a liquid. This makes their behaviour in stirred vessels particularly challenging to model, as it requires capturing the complex fluid-solid transitions that occur during the mixing process. Conventionally, mixing processes have been modeled by grid-based Eulerian methods (Liu et al., 2013; Shi et al., 2018). In recent years, Lagrangian methods have been gradually integrated into grid-based methods, which gives a way to Euler-Lagrangian methods (Kim et al., 2021; Lapin et al., 2006). However, these methods raise different issues as they usually employ multi-level algorithms and are categorized as difficult and complex numerical methods (Yang et al., 2024; Zhang et al., 2005). More recently, a pure Lagrangian meshfree approach based on the particle method has been introduced and developed to simulate the mixing process (Nikolić et al., 2016). In this context, the application of the Lagrangian meshfree approach, Smoothed Particle Hydrodynamics (SPH), for simulating viscoplastic fluids within stirred vessels has garnered considerable attention. SPH is one of the most well-known particle-based method, which initially proposed by Lucy (1977) and then further developed by Gingold and Monaghan (1982).

The Lagrangian meshfree approach, SPH, offers several advantages over both traditional grid-based Euler and Euler-Lagrangian methods for modeling viscoplastic fluids in stirred vessels. For example, SPH can handle large deformations and complex geometries more efficiently, and it can accurately capture the complex fluid-structure interactions and moving boundaries that occur during mixing (Sefid et al., 2015). Additionally, SPH also can easily couple with other particle-based method like DEM to simulate particle-laden flows, which are important in many industrial applications (Lian et al., 2023). Although the SPH method may causing some complexities, it is a general easy and appropriate way to study mixing flow, free surface and moving boundary problems (Shadloo et al., 2016), which will simultaneously be applied in the present study. Due to its Lagrangian nature, SPH is a proper way to model mixing processes, and there is no need to model convective terms in SPH modeling because these convective terms are satisfied by the motion of the particles. Hence the false diffusion introduced by the modeling of mesh-based method does not occur in SPH modeling. Moving boundary and fluid–structure interaction are other complex problems for

the mesh-based methods, in which the motion of the rigid body should be defined by moving mesh, sliding mesh, or immersed boundary methods. However, in the SPH and mesh-free methods, the motion of the rigid bodies can be modeled easily (Sefid et al., 2015). All of the above-mentioned qualities show that SPH is a convenient method to model mixers involving rotating blades and with free surface flow.

In this chapter, a SPH algorithm is developed to simulate mixing processes involving rotating blades in stirred vessels. We will discuss the application of the Lagrangian meshfree approach to modeling viscoplastic fluids in stirred vessels and review the fundamental concepts of the method and discuss its advantages and limitations. A number of case studies that demonstrate the effectiveness of the Lagrangian meshfree approach in simulating viscoplastic fluid mixing in stirred vessels and discuss some of the challenges and future directions for this exciting area of research.

7.2 Experimental

7.2.1 Stirred vessels

Laminar flows, with non-Newtonian fluid flows, were performed in a flat-based stirred vessel of standard configuration, with diameter $T = 150$ mm and four equidistant wall baffles of width $W_b = 0.1T$, as illustrated in Figure 7.1(a). The height of mixing flows in the vessel was set at $H = T$ and agitated by 6-blade pitched-turbine (PBT) and Rushton disc turbine (RDT) of diameter $D_{\text{imp,PBT}} = T/3$ and $D_{\text{imp,RDT}} = T/1.82$, respectively. The impeller height $H_{\text{imp}} = 0.12T$, off-bottom clearance $C_{\text{imp}} = 0.33T$. Detailed geometry information of impellers were summarized in Table 7.1 . The single-liquid flows were operated at different impeller rotation speeds (60 to 200 rpm) and the impeller Reynolds number (Re_{imp}) was under the transient regime in particular between 70.3 and 277.8. These flows which used PBT were operated in the down-pumping (PBTD)

mode. In this paper, different aqueous solutions of Carbopol 980 and Carboxymethyl cellulose (CMC) were used as typical viscoplastic fluids for the experimental mixing studies. The rheology was controlled by the concentrations and PH values (Curran et al., 2002).

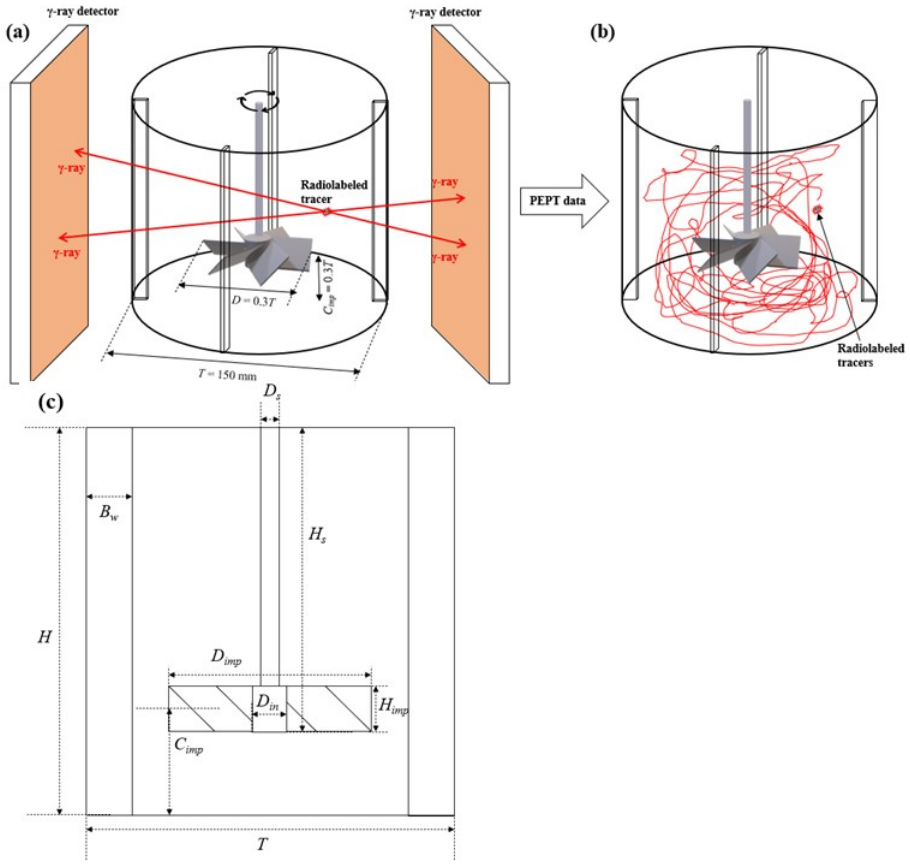

Figure 7.1: (a) PEPT experiment set-up, (b)a typical Lagrangian PEPT 3D trajectory and (c) stirred tank configuration.

Table 7.1: Geometric dimensions of PBT and RDT

Impeller Type	**PBT**	**RDT**
Stirred Diameter, D_{imp}	50	104
Inclined angle, θ (°)	60	-
Clearance, C_{imp}	50	50
Height, H_{imp}	18	-
Thickness, W_{imp}	15	50
Rotation speed, N (rpm)	200	60

7.2.2 Positron emission particle tracking (PEPT)

PEPT is a non-invasive imaging technique, which is applied to track a tiny radiolabelled tracer within the flow, providing a 3D long-term Lagrangian trajectory with time and space information (Barigou, 2004). PEPT is particularly useful for studying complex fluid flows in various applications such as chemical, environmental, and biomedical studies. PEPT has a comparable accuracy with the leading optical techniques (e.g., PIV and LDV), but has advantages to image opaque fluids and inside opaque equipment (Pianko-Oprych et al., 2009). Currently PEPT is widely used to study flow and mixing in pipes and vessels. More details can be found in our previous work (Guida et al., 2010a; Li et al., 2023b; Lian et al., 2023; Savari et al., 2022; Sheikh et al., 2022; Yang et al., 2024). As illustrate in Figure 7.1(b), an extremely tiny neutrally-buoyant radiolabelled particle was assumed as liquid tracer, whose behaviour almost follow the liquid phase motion. The long-term PEPT Lagrangian trajectory of liquid phase was recorded up to 6 hours, long enough to allow the liquid tracer to map all regions of the cavern including those close to the cavern boundary where, due to the poor mixing, the probability of visit can be very low.

7.2.3 Particle image velocimetry (PIV)

Using PIV to obtain the velocity map, the liquid were seeded by 10 μm hollow silver coated particles. The seeding particles were illuminated using a dual head Nd: YAG 532 nm pulsed laser (New Wave Research Inc. USA). Images were recorded simultaneously using a single-frame, cross-connected CCD camera (PowerView Plus 4MP, TSI, USA), which captures seven pairs of images per second with a resolution of 2048 x 2048 pixels. Camera frames and synchronization of laser is supported by the TSI Laserpulse 610035 synchronizer. The recorded images were sliced into small interrogation areas (IA) of 16×16 pixels (0.92×0.92 mm^2) and processed through a recursive Nyquist grid. The effect of the number of PIV images on the flow field measurement has been tested by Guida et al. (2010), and 200 image pairs were stated to be enough to obtain the converged average velocities. 500 pairs of PIV images were recorded in each experiment. The laser sheet was set at 85° which is on the windward side of the baffle to avoid light obstruction by the baffle in front of the camera.

7.3 Simulations

In this study, the SPH methodology was employed to simulate the single-phase flow within the tank. The rheological behaviour was modelled using the HBP model, as described by Han et al. (2020). Detailed descriptions of the simulation procedures are provided in the subsequent sections.

7.3.1 Simulation set-up

Geometry and impeller motion

The simulations were executed in a 3D domain using the DualSPHysics platform for 20 seconds. The configuration of non-Newtonian flows was set up in a standard flat-based stirred vessel using SPH numerical particles, as depicted in Figure 7.2. The surface cells of stirred tank, including the tank wall (blue), baffles (grey), and impeller (red), are represented by numerical boundary particles. Figure 7.2(b) is displayed with 40% transparency to enhance the visualization. The Standard Triangle Language (STL) file of impeller was created by AutoCAD, the side-view and top-view of impeller STL file depicted in Figure 7.2(c) and Figure 7.2(d), respectively. Figure 7.2 illustrates the process of preparing and using a 3D impeller model for SPH simulations by generating body-fitted particles on the SPH framework. Initially, a targeted 3D STL file of the impeller is created by AutoCAD software. This STL file is then used to generate input files which are stored in the source folder of DualSPHysics. The STL file is defined with accurate position information based on experimental conditions. Moving boundary particles are created on the surface of the STL file to simulate the motion of impeller. The motion of the impeller is prepared based on its rotational speed, and Visualization ToolKit (VTK) files are generated to capture this motion. These VTK files provide data on the forces and velocities exerted by the impeller on the numerical fluid particles. This data is crucial for analysing the fluid dynamics and performance of the impeller within the simulated environment. Initially, the impeller was kept stationary with zero velocity and then gradually accelerated to a predefined rotational speed. Similarly, the velocities of all numerical SPH particles were initially set to zero to ensure that any motion observed in the simulation was naturally occurring based on impeller motion and fluid dynamics.

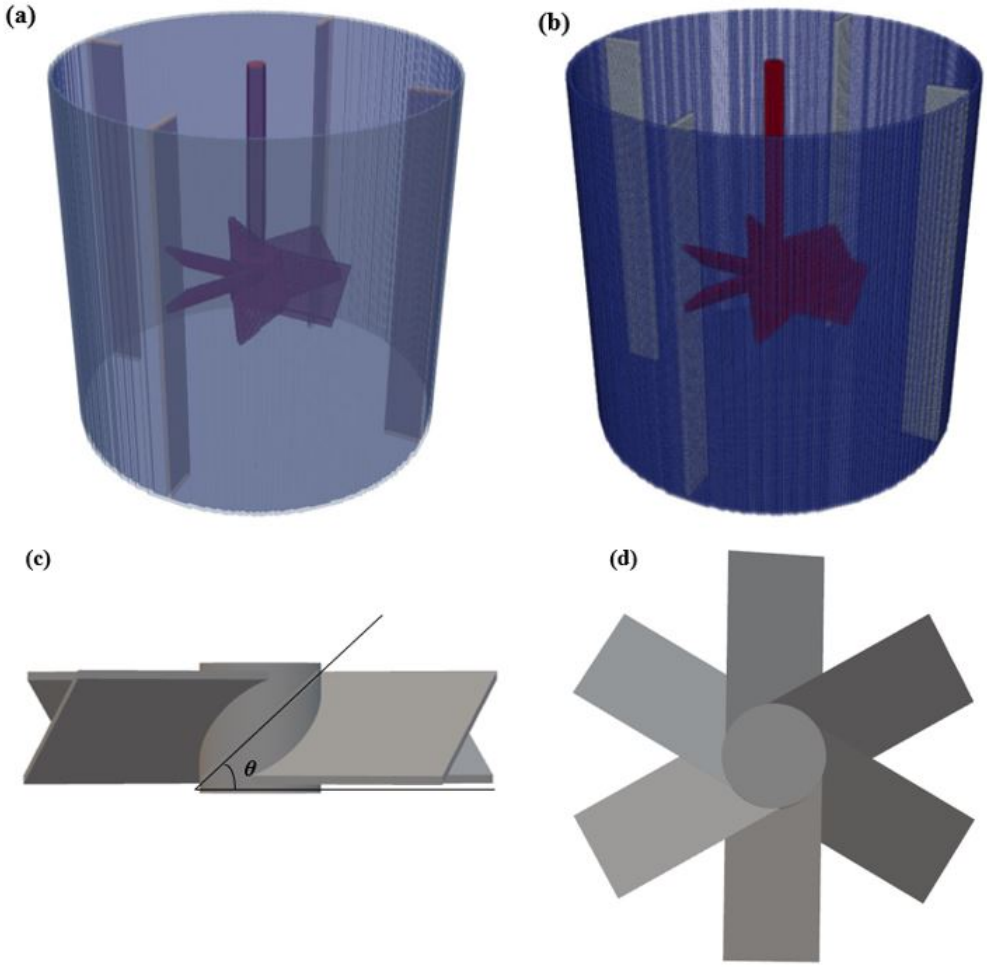

Figure 7.2: (a) The stirred tank surface cells including tank wall (blue), baffles (grey) and PBT impeller (red). (b) Cells are filled with SPH boundary particles with 40% transparency, which is added for better visualisation. (c-d) Side-view and top-view of STL file of impeller.

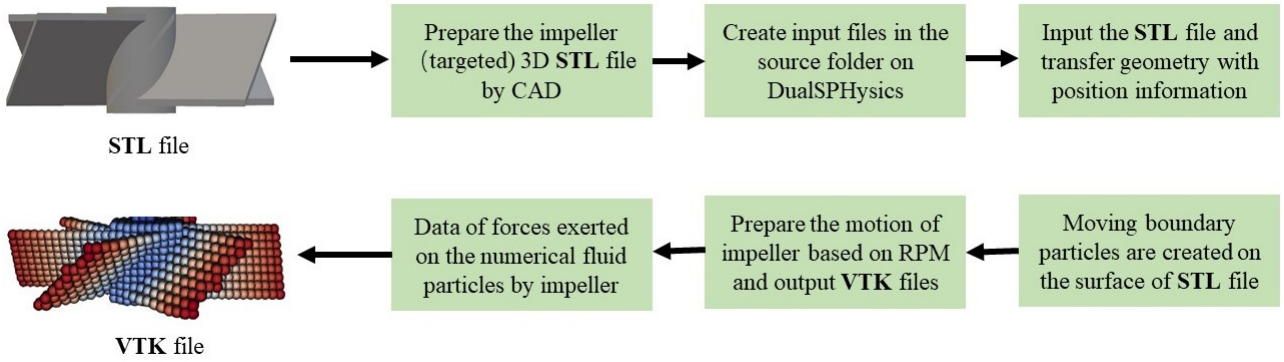

Figure 7.3: The flow chart to generate body-fitted particles on SPH framework.

Boundary conditions

As shown in Figure 7.2(a) and (b), the wall boundary of baffled tank is also described by numerical boundary particles. The dynamic boundary condition (DBC) is a standard conventional condition to model solid surfaces in SPH simulations, such as the buffer and tank wall (Crespo et al., 2007). However, a small unphysical gap between the fluid and solid boundaries can arise when DBC is used, due to a reduction in the precision of pressure calculations along the boundary. Here, a modified dynamic boundary condition (mDBC) was introduced wherein the density of solid particles is acquired through linear extrapolation from ghost positions situated within the fluid domain (English et al., 2022). Through mDBC, the separation between the fluid and boundary is diminished, leading to pressure convergence in undisturbed conditions, including cases involving a sharply cornered bed configuration. The mDBC was used where the boundary interface is located half a particle spacing from the layer of boundary particles closest to the fluid. For each boundary particle, a ghost node was projected into the fluid across the boundary interface.

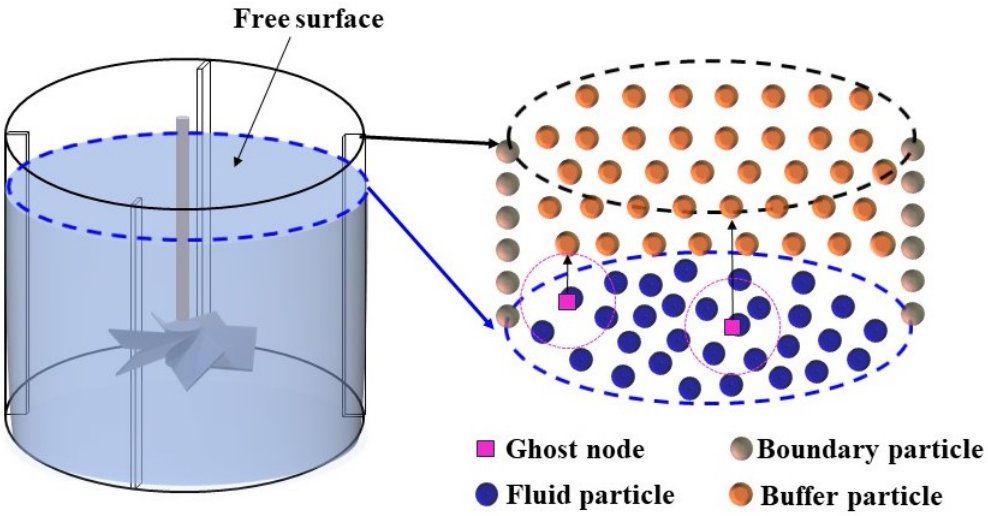

Figure 7.4: Sketch of the implemented open boundary formulation in the stirred tank.

The open boundaries are used to simulate the free surface interface between the fluid and air. Figure 7.4 illustrates the open boundary formulation implemented in a stirred tank. The free surface of the fluid is marked with a blue dashed line, indicating the interface where the fluid is exposed to air. In the close-up view, different particle types are depicted: fluid particles, boundary particles, buffer particles, and ghost nodes. These particles are essential for accurately modeling the fluid dynamics and interactions at the boundaries. The positions of the ghost nodes are determined by reflecting the boundary particles into the fluid along a direction perpendicular to the open boundary. Traditional particle interpolation methods are not adequate when calculating the amount of fluid at ghost nodes due to the proximity of these nodes to open boundaries. This proximity can lead to inadequate kernel support and make standard interpolation methods inconsistent. In this paper, the first order kernel and particle consistency were retrieved via the model developed by Liu and Liu (2006). The multi-dimensional first-order Taylor series approximation of field function $A(r)$ multiplied by the kernel function calculated at particle K, $W_K(r)$. The first order derivatives, $W_{K,\beta}(r)$, are defined as:

$$\int A(r)W_K(r)dr = A_K \int W_K(r)dr + A_{K,\beta} \int (r - r_K)W_K(r)dr \tag{7.1}$$

$$\int A(r)W_{K,\beta}(r)dr = A_K \int W_{K,\beta}(r)dr + A_{K,\beta} \int (r - r_K)W_{K,\beta}(r)dr \tag{7.2}$$

where, β represents an index from 1 to D_i, which is the total number of dimensions. Eq. 7.1 and 7.2 form a system of $D_i + 1$ equations with $D_i + 1$ unknowns, specifically A_K and $A_{K,\beta}$. In particle notation, the solution to this system is calculated by:

$$A_K = \frac{\begin{vmatrix} \sum_b A_b W_{Kb} \Delta V_b & \sum_b (r_b - r_K) W_{Kb} \Delta V_b \\ \sum_b A(r) W_{Kb,\beta} \Delta V_b & \sum_b (r_b - r_K) W_{Kb,\beta} \Delta V_b \end{vmatrix}}{\begin{vmatrix} \sum_b W_{Kb} \Delta V_b & \sum_b (r_b - r_K) W_{Kb} \Delta V_b \\ \sum_b W_{Kb,\beta} \Delta V_b & \sum_b (r_b - r_K) W_{Kb,\beta} \Delta V_b \end{vmatrix}} \tag{7.3}$$

$$A_{K,\beta} = \frac{\begin{vmatrix} \sum_b W_{Kb} \Delta V_b & \sum_b A_b W_{Kb} \Delta V_b \\ \sum_b W_{Kb,\beta} \Delta V_b & \sum_b A_b W_{Kb,\beta} \Delta V_b \end{vmatrix}}{\begin{vmatrix} \sum_b W_{Kb} \Delta V_b & \sum_b (r_b - r_K) W_{Kb} \Delta V_b \\ \sum_b W_{Kb,\beta} \Delta V_b & \sum_b (r_b - r_K) W_{Kb,\beta} \Delta V_b \end{vmatrix}} \tag{7.4}$$

The value of A_0 at the open boundary is calculated by corrected values of A and $A_{K,\beta}$ at the ghost nodes:

$$A_0 = A_K + (r_0 - r_K) \cdot \tilde{\nabla} A_{K,\beta} \tag{7.5}$$

where $\tilde{\nabla} A_{K,\beta}$ refers to the corrected gradient calculated at the ghost nodes.

Simulation time step

To ensure the robustness of the SPH simulations, the Courant- Friedrichs-Lewy (CFL) condition needs to be satisfied (Monaghan et al., 1999). There are viscous diffusion and forcing terms in the CFL condition.

PEPT and SPH Eulerian velocity field

Both PEPT experiments and SPH simulations provide time-resolved 3D Lagrangian data. To compare the experimental and simulation results, identical data processing methods were used to construct Eulerian flow velocity maps. As illustrated in Figure 7.5, the entire tank was divided into 50×50×50 equal volume cells for this purpose. The local velocity in each cell was calculated by time-average velocity at every detection point within the cell and then averaging by the number of detection points. The calculation functions are defined as follows:

$$v_{\text{cell}}^{k} = \frac{1}{n_{\text{SPH}}} \cdot \sum_{i=1}^{n_{\text{SPH}}} v_{\text{SPH}}^{i} \tag{7.6}$$

$$v_{\text{cell}}^{k} = \frac{1}{n_{L}} \cdot \sum_{i=1}^{n_{L}} v_{\text{tracer}}^{i} \tag{7.7}$$

The Eulerian flow velocity maps can be reconstructed by calculating the velocity in each cell.

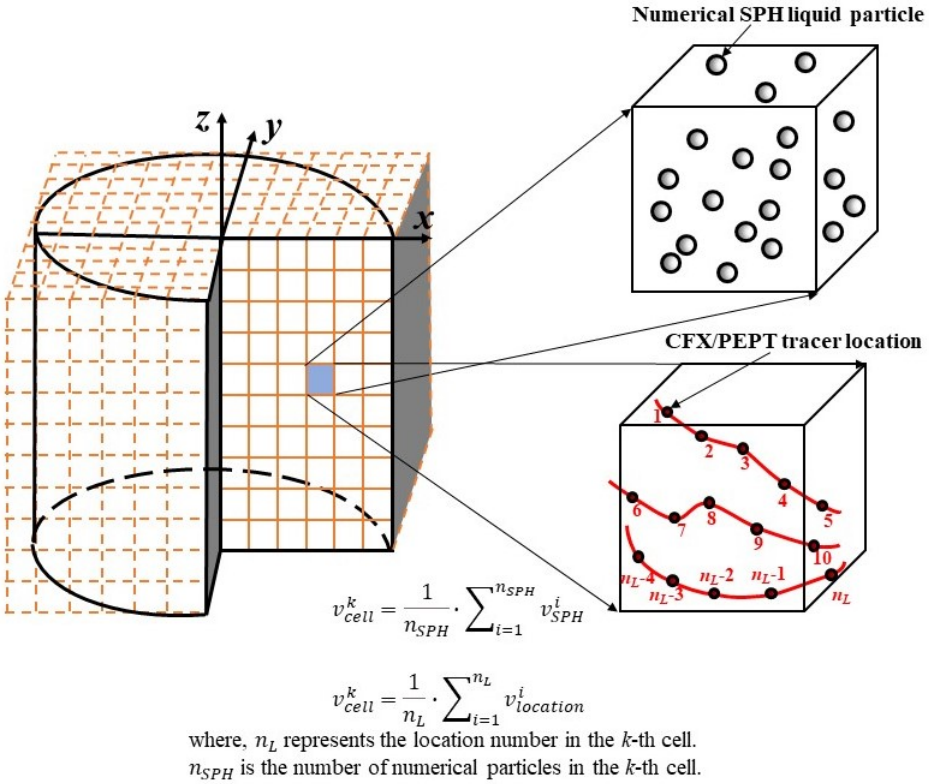

Figure 7.5: Illustration of Cartesian grid of equal volume unites used for analysis of PEPT Lagrangian data and SPH data. The dashed lines show cells outside flow domain: 50 × 50 × 50 cells used for postprocessing data to output Eulerian velocity field.

In SPH simulations, the instantaneous velocity fields are obtained at every time step and revolution. During data processing, it is necessary to average the velocity fields over several revolutions to achieve a stable Eulerian velocity field distribution. Therefore, taking one case as an example, the velocity (u_θ) distribution at various average numbers of revolutions was examined in a 150 mm tall vessel containing a 0.1 wt% Carbopol solution, stirred with a PBT impeller. As shown in the Figure 7.6, the velocity distribution for a single time step exhibits significant fluctuations. Each subplot shows that the velocity profiles become more consistent as the number of averaged revolutions increases, suggesting that a stable Eulerian velocity field distribution can be obtained by averaging over more revolutions. When the number of averaged revolutions reaches 10-15, the

velocity distribution remains almost unchanged. In subsequent case studies, the velocity curves were obtained by averaging at least 15 rotations.

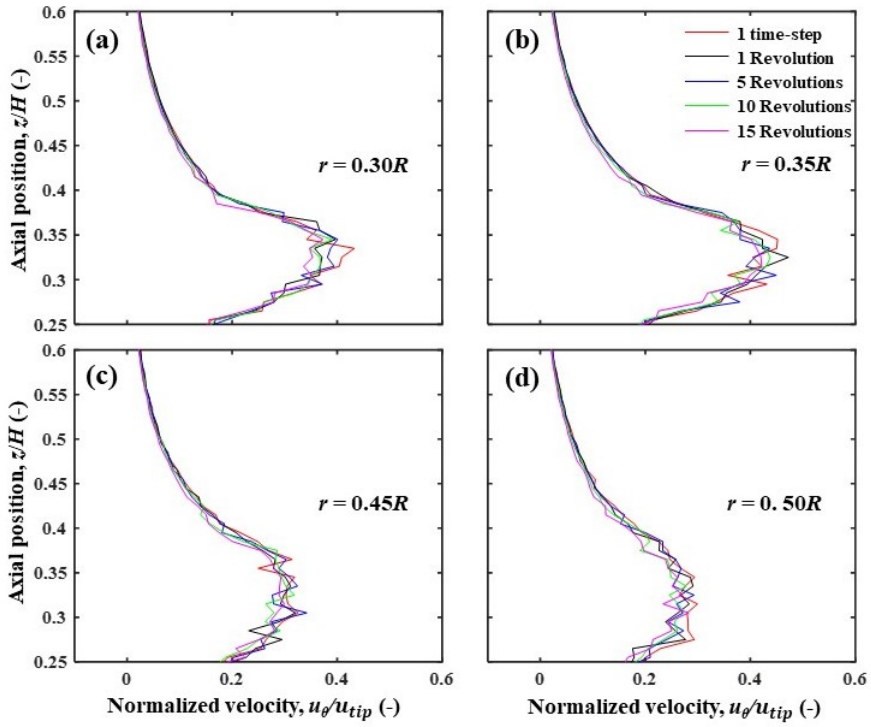

Figure 7.6: Impact of averaged revolutions on normalized velocity (u_θ) profiles at different radial positions in SPH simulations.

7.4 Validation

In this section, we initially validate the rheology model used in the SPH calculation framework. Subsequently, the validated rheology model parameters were fed into the SPH framework. Finally, we assess the performance of the SPH model in simulating stirred vessels using experimental data obtained from PEPT. The experimental parameters and rheological properties for the six main cases studied in this work are reported in Table 7.2. These cases involved different vessel heights, carrier fluids and impeller types to provide a fully validated SPH framework. Radial and axial velocity of

Caes1 and Case 2 were provided by PIV method. The velocity fields of Case 3 was obtained by PEPT measurement. The cavern size and shape of Case 4-6 were obtained by PLIF measurement, the details of these four case can be found in previosly published paper (Adams et al., 2007).

7.4.1 Rheology model

As indicated before, the fluid rheologies have been modelled using the HBP model. The experimental shear rate versus effective viscosity (μ_{eff}) and shear stress (τ) are presented along the curve fitted by the HBP model in Figure 7.7(a) and (b). As depicted in these figures, the fitted HBP model curves are shown for 0.1 wt% Carbopol and 0.2 wt% CMC solutions, and the model parameters are provided. Figure 7.7 also shows the shear thinning behavior of the fluid, i.e., the effective viscosity decreases with increasing shear rate. The HBP model results are in good agreement with the experimental rheological data, especially at lower shear rates, where the shear stress decreases drastically and then tends to flatten down. The comparison between HBP model and experimental data highlights the ability of the HBP model to accurately capture the rheological behavior of both Carbopol and CMC solutions across a range of shear rates. The close agreement between experimental data and model predictions demonstrates the robustness of the HBP model parameters in describing the shear-thinning behavior of these non-Newtonian fluids.

Table 7.2: Rheological and physical properties of the main cases and experimental parameters.

Case	Vessel height, T (mm)	Carrier fluids	Impeller type	PH	HBP rheological parameters			N (rpm)(Re)	Experiment
					Consistency index, k	Behaviour index, n	Yield stress, τ_0(Pa)		
1	190	0.2 wt% CMC	RDT	-	0.2424	0.6	-	60 (105.8)	PIV
2	190	0.2 wt% CMC	RDT	-	0.2424	0.6	-	120 (277.8)	PIV
3	150	0.1 wt% Carbopol	PBT	4.6	0.36	0.56	1.37	200 (76.3)	PEPT/PLIF
4	150	0.1 wt% Carbopol	PBT	4.6	0.35	0.57	1.29	200 (70.3)	PLIF
5	150	0.1 wt% Carbopol	PBT	4.6	0.54	0.56	2.63	6 (7.3)	PLIF
6	150	0.1 wt% Carbopol	PBT	4.6	0.37	0.57	1.41	63 (20.4)	PLIF
7	150	0.1 wt% Carbopol	PBT	4.6	0.37	0.58	1.97	200 (163.2)	PLIF

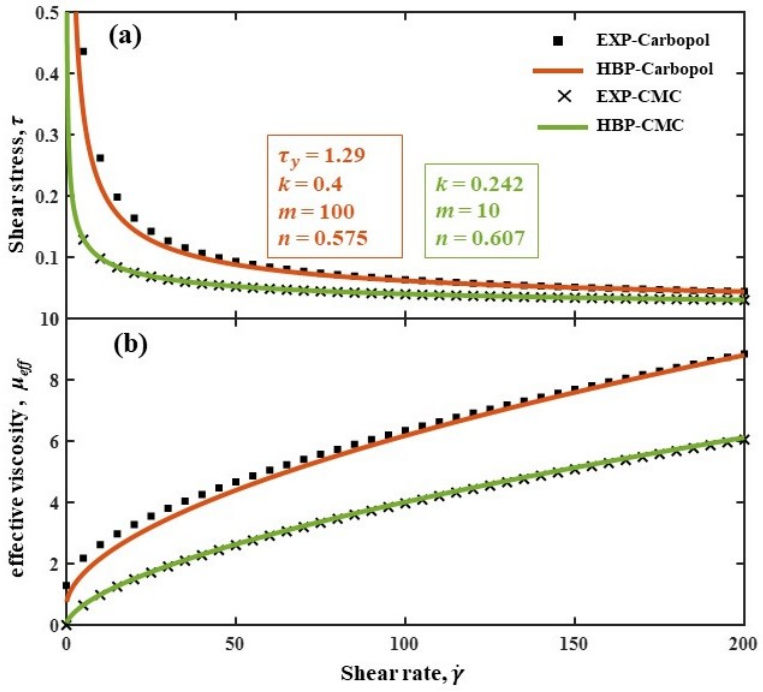

Figure 7.7: Comparison of HBP model parameters for a 0.1 wt% Carbopol and 0.2 wt% CMC solutions with experimental data, (a) shear stress versus shear rate; (b) effective viscosity versus shear rate.

In this section, we initially validate the rheology model within SPH calculation framework. Subsequently, feeding the validated rheology model parameters into the SPH model. Finally, we assess the performance of the SPH model in simulating stirred vessels using experimental data obtained from PEPT. A detailed quantitative comparison between the SPH predictions and PEPT data was conducted at the positions depicted in Figure 7.8 and Figure 7.9, the distribution of velocity field in a 0.1 wt% Carbopol solution with PBT impeller at transient regime (Case 3) were compared. Especially, the SPH-predicted the azimuthally-averaged distributions of the local velocity components, u_z, u_r and u_θ, are generally in very good agreement with the PEPT measurements. The velocity is gradually decrease with the distance of impeller. The value of maximum velocity in the flow domain is about $0.42u_{tip}$ occurs at the position of $z/H = 0.33$, same with the height of impeller

center. The ability of SPH model was accessed by experimental data, SPH is able to predict the velocity distribution, especially the area close to the impeller at radial and theta direction.

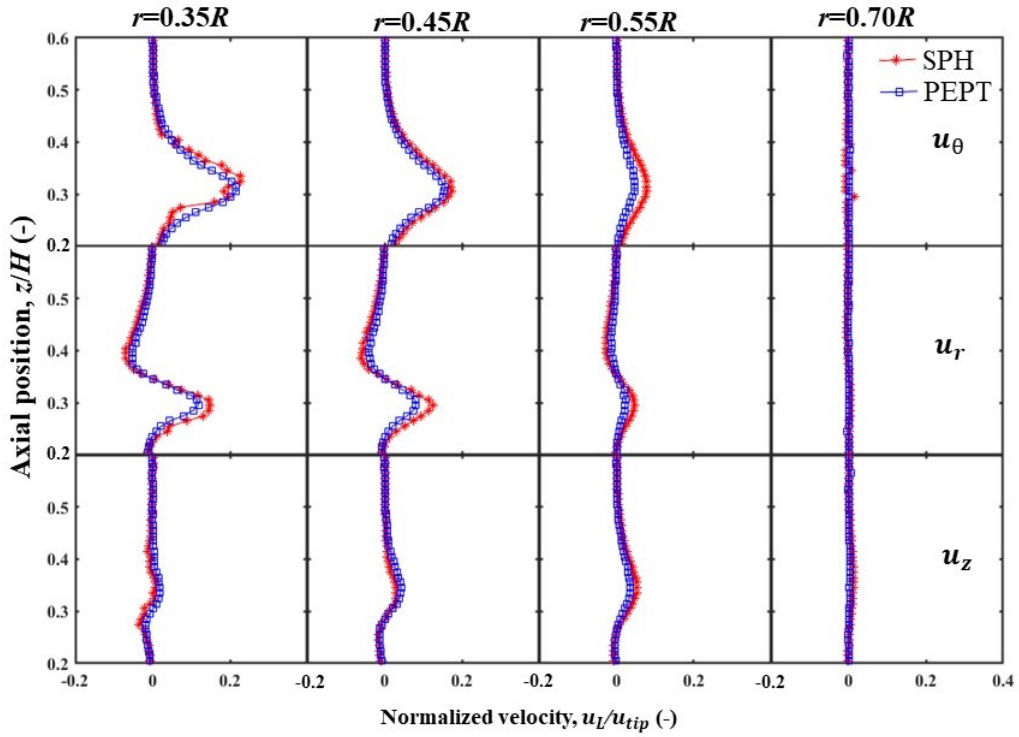

Figure 7.8: Radial distribution of velocity in 0.1 wt% Carbopol solution with PBT impeller at transient regime, SPH and PEPT compared: N = 200 rpm, Re_{imp} = 73.

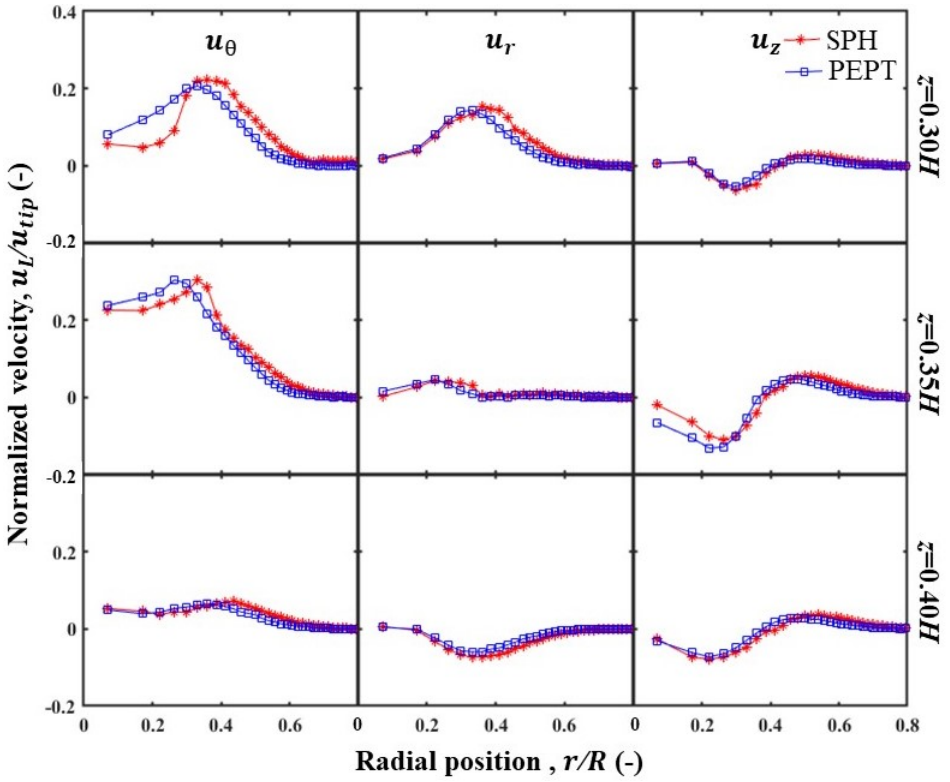

Figure 7.9: Axial distribution of velocity in 0.1 wt% Carbopol solution with PBT impeller at transient regime - SPH and PEPT compared: N = 200 rpm, Re_{imp} = 73.

Figure 7.10 presents a comparison of the velocity fields in Case 3, where the impeller speed is 200 RPM, corresponding to a Reynolds number of 76.3. The top row shows the velocity fields obtained from SPH simulations, while the bottom row displays the velocity fields from PEPT experiments. Both SPH and PEPT results show a high concentration of positive u_θ near the impeller blades, which decreases radially outward. The radial velocity u_r from both methods show a similar pattern, with negative values indicating fluid moving towards the impeller shaft. The axial velocity fields also exhibit comparable trends between SPH and PEPT, with positive velocities above the impeller and negative velocities below it. Overall, the comparison demonstrates good agreement between SPH simulations and PEPT measurements, validating the accuracy of the SPH method in capturing the complex flow dynamics within the stirred tank. This agreement is crucial for understanding the

mixing performance and optimizing the design and operation of stirred tanks in various industrial applications.

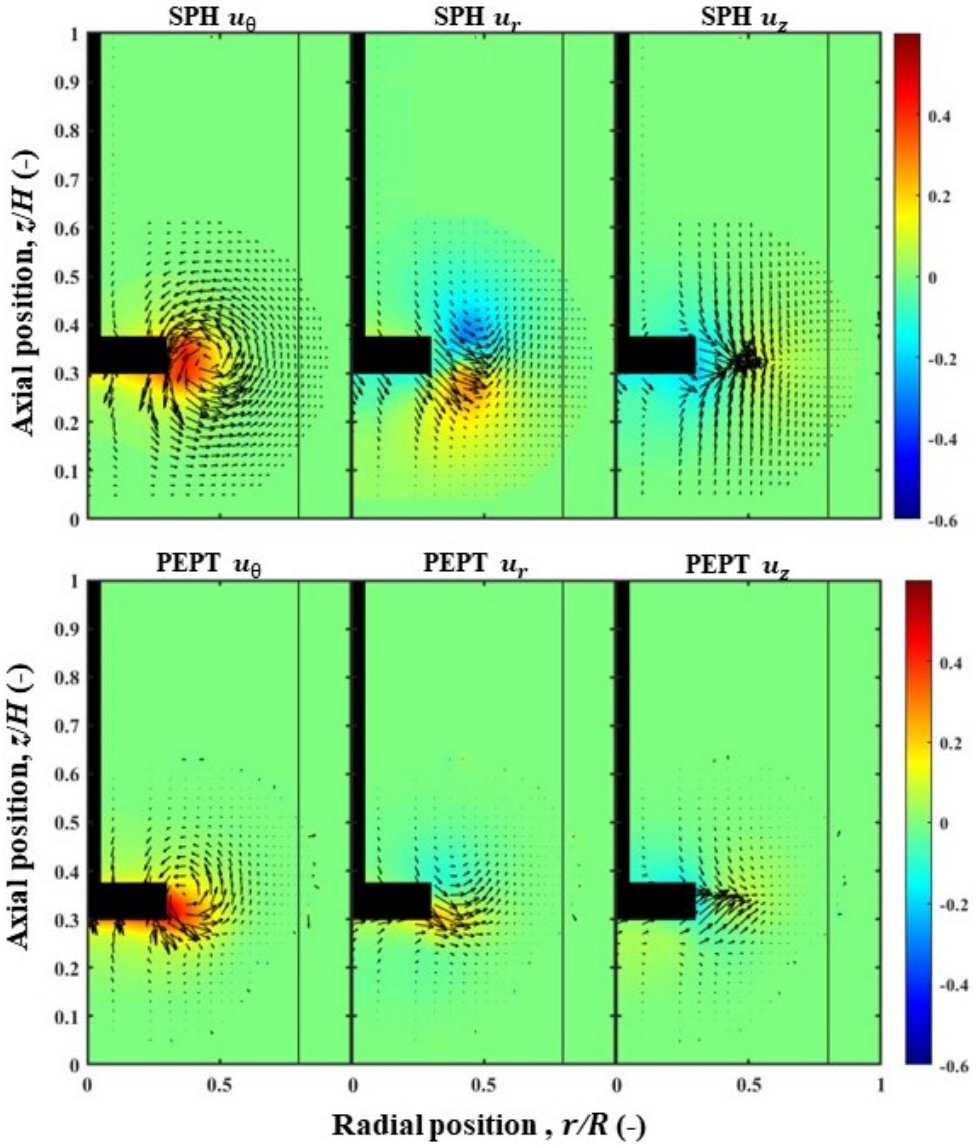

Figure 7.10: Velocity field in 0.1 wt% Carbopol solution with PBT impeller at transient regime - SPH and PEPT compared: N = 200 rpm, Re_{imp} = 76.3.

As illustrated in Figure 7.11, the distribution of velocity in a 0.2 wt% CMC solution using a RDT impeller, comparing results from SPH simulations and PIV data. Two different rotational speeds

are analyzed, at 60 rpm, both SPH and PIV results show similar trends in the velocity profiles. The axial velocity exhibits a positive peak near the impeller region, indicating upward flow, while the radial velocity shows a characteristic outward flow pattern. At 120 rpm, the velocity profiles are more pronounced due to the increased impeller speed. The SPH and PIV data demonstrate good agreement as well, with both axial and radial velocity components following similar patterns as in the lower speed case but with higher magnitudes. The comparison highlights the consistency between SPH simulations and PIV measurements.

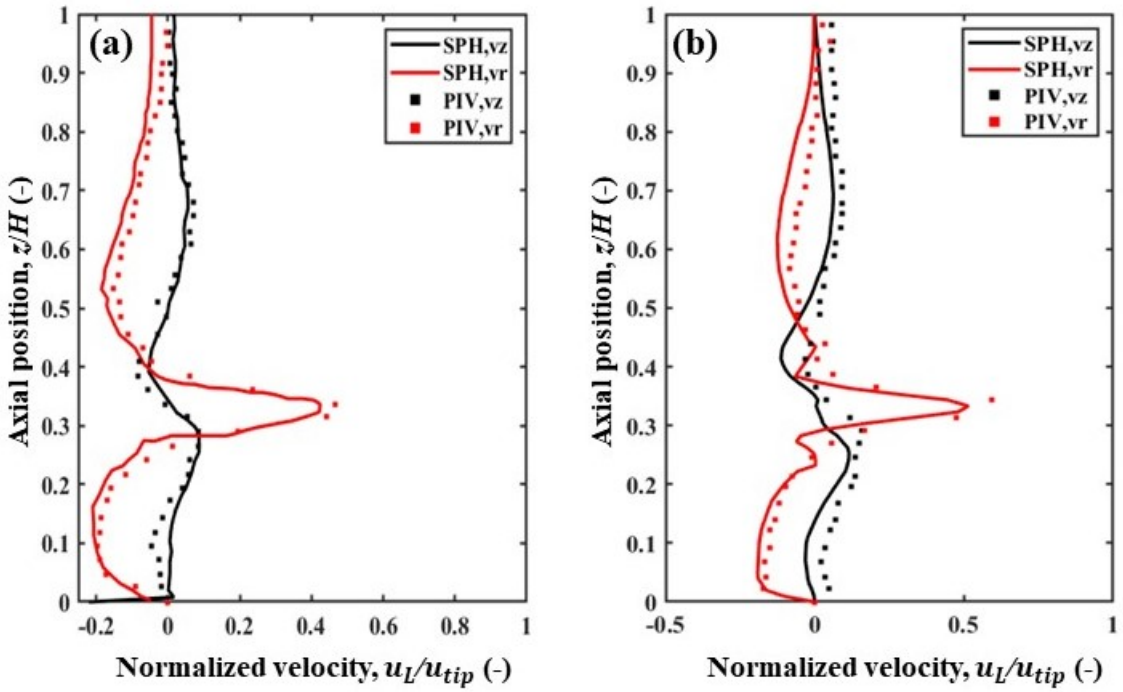

Figure 7.11: Distribution of velocity in 0.2 wt% CMC solution with RDT impeller at transient regime, SPH and PIV compared: (a) $N = 60$ rpm, $\mathrm{Re}_{\mathrm{imp}} = 105.8$, $\theta = 85°$; (b) $N = 120$ rpm, $\mathrm{Re}_{\mathrm{imp}} = 277.8$, $\theta = 85°$.

7.4.2 Cavern prediction

A constant impeller speed of N = 200 rpm was used, and two rheological parameters were kept constant when the effect of one parameter was investigated. The tangential velocity on the cavern boundary is defined as 1% impeller tip speed (Saeed et al., 2007). As shown in Figure 7.12, that at lower Reynolds numbers (i.e. Re = 7.3 and Re = 20.4), the cavern shape is close to spherical shape. The predicted cavern size and shape of SPH simulations are agreed very well with the PLIF measurement results, which shows the accuracy of SPH simulation in mixing flow at transient regime. Increasing the Reynolds number to Re = 70.3, two circulation loops develop inside the cavern, i.e. a larger flow loop above the impeller and a smaller one below it. The performance of SPH cavern prediction are not at same level about the lager and smaller loops in tank, obviously, the upper large loop is more accurate than the lower half one. The cavern reaches the tank wall and tank base at Re = 163.3, which is well captured and described by the SPH model, though the height of cavern was tiny difference with experimental data. In short, the accuracy of SPH model of cavern formation in the mixing of viscoplastic fluids in stirred vessels is affected significantly by the positions of the interfaces between the numerical liquid particles and numerical moving boundary particles, therefore, great care must be taken in setting the locations of moving boundary particle for simulating the cavern size and shape.

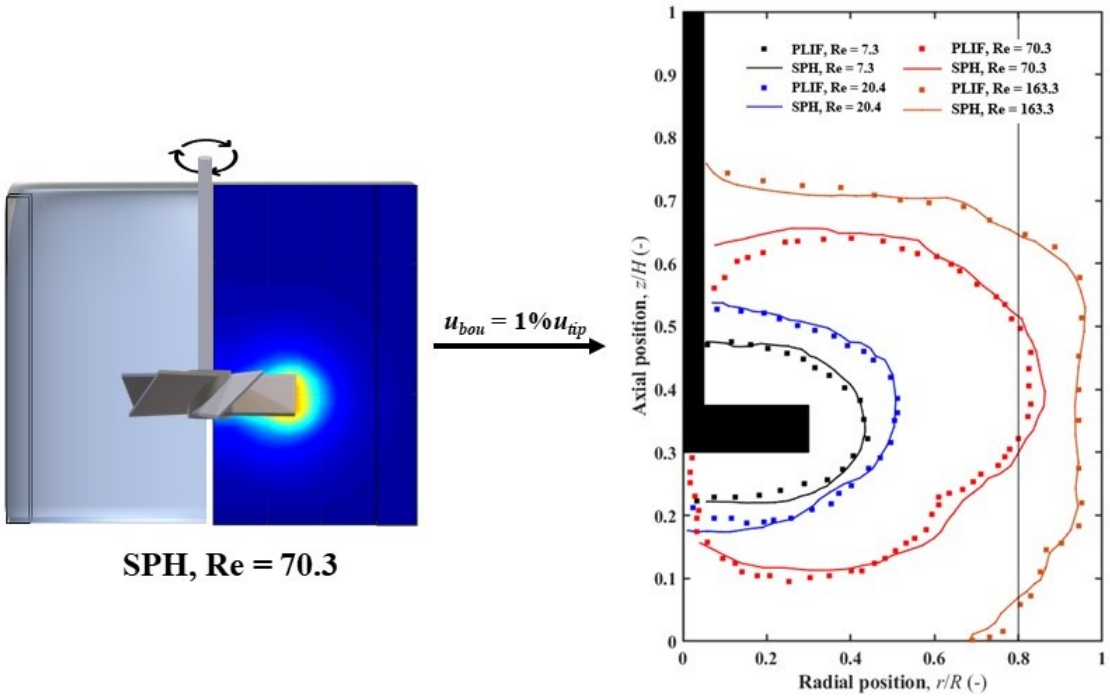

Figure 7.12: Cavern predicting of SPH simulations of 0.1 wt% Carbopol solution with PBT impeller at different Reynolds number.

7.5 Results and discussion

As a powerful tool, SPH model has been employed in many studies to investigate the complex mixing of viscoplastic fluids in multiphase flow and free surface flow over the past several years, but the research on mixing flow are limited by the transient and turbulent model within SPH framework. In order to use the SPH predictions confidently in practical applications, extensive validations need to be carried out. It has been discussed in this section, and the SPH modelling of non-Newtonian fluid mixing in stirred vessels has been well validated in velocity fields in section 7.4.

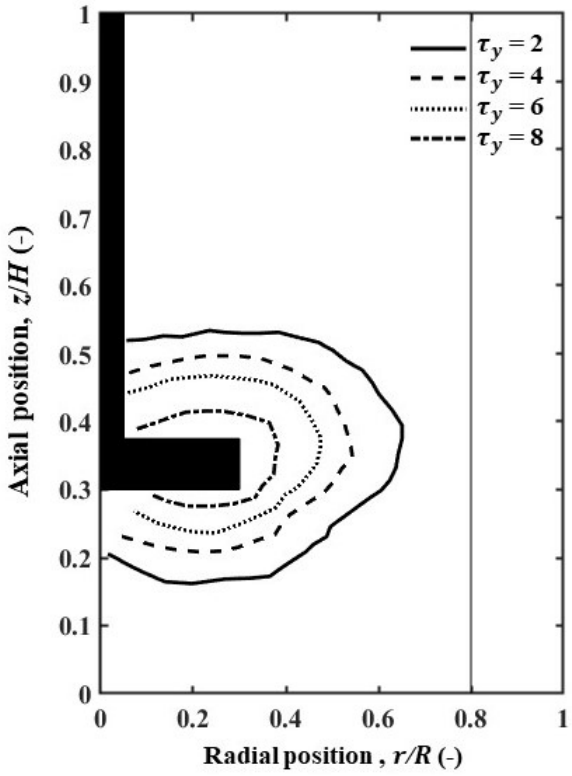

Figure 7.13: Cavern predicting of SPH simulations of 0.1 wt% Carbopol solution with PBT impeller at different yield stress.

Using the well validated SPH approaches and models to conduct parametric studies of non-Newtonian mixing flows in stirred tank. A constant impeller speed of N = 200 rpm was used and two rheological parameters were kept constant when the effect of one parameter was investigated. The predicted caverns from SPH simulations for a 0.1 wt% Carbopol solution using a PBT impeller at various yield stresses were shown in Figure 7.13. Four yield stress levels (τ_y = 2, 4, 6, and 8 Pa) are represented by different line styles. The contours of each case show the extent and shape of the caverns formed at each yield stress level. As the yield stress increases from 2 to 8 Pa, the size of the cavern decreases, indicating less fluid motion and mixing at higher yield stresses. This behavior is characterized by the inward contraction of the contours, especially noticeable near the impeller region. The impact of yield stress on the mixing efficiency within the tank, with higher yield stresses

resulting in smaller and more confined caverns. This information is critical for optimizing mixing processes in industrial applications involving non-Newtonian fluids. Figure 7.14 depicts the caverns predicted by SPH simulations at various consistency coefficients (k). The contours show the extent and shape of the caverns formed at each consistency coefficient. As the consistency coefficient increases from 0.4 to 2.2, the size of the cavern increases, indicating more extensive fluid motion and mixing at higher consistency coefficients. The impact of the consistency coefficient on the mixing efficiency within the tank, with higher consistency coefficients resulting in larger and more extensive caverns.

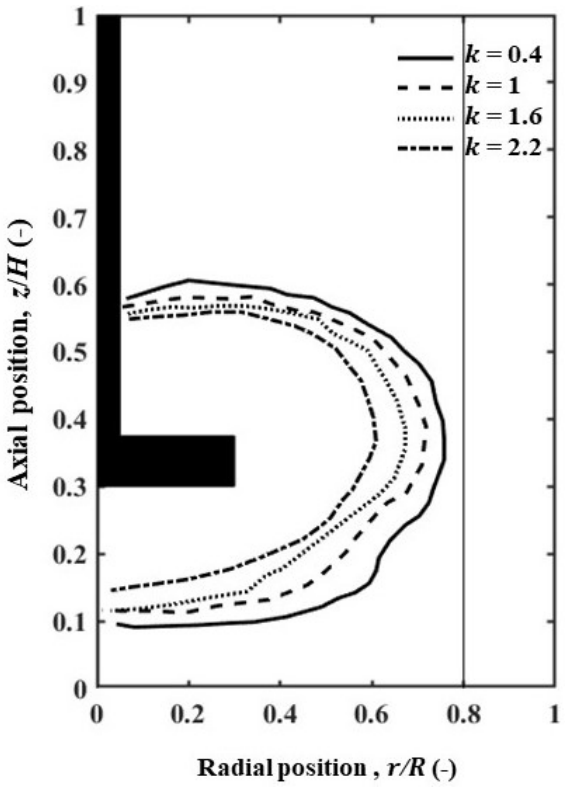

Figure 7.14: Cavern predicting of SPH simulations of 0.1 wt% Carbopol solution with PBT impeller at different Reynolds number.

7.6 Conclusion

A series of simulations were conducted based on the technique of smoothed particle hydrodynamics (SPH) to investigate the detailed dynamics of radial migration of viscoplastic fluid in stirred vessels. A three-dimensional HBP-SPH model has been successfully developed for simulating the mixing flow of non-Newtonian fluids in a mixing vessel. The model's accuracy and reliability were thoroughly validated using pointwise Lagrangian particle tracking measurements through Positron Emission Particle Tracking (PEPT). This validation confirmed that the model accurately predicts the free surface dynamics and the formation of pseudo-caverns within the fluid. The robustness of this model was demonstrated across a range of scales and rheological properties, showcasing its capability to handle various fluid behaviors and mixing scenarios. The HBP-SPH model proved to be not only accurate but also flexible, making it a valuable tool for simulating more complex systems involving moving boundaries. The developed HBP-SPH model represents a significant advancement in the computational modeling of non-Newtonian fluid dynamics within mixing vessels. Its ability to accurately capture complex flow patterns and adapt to different fluid properties makes it an essential tool for optimizing industrial mixing processes and can be extended to meet more complex fluid dynamics challenges.

Chapter Eight

Conclusions and future work

8.1 Conclusions

The work presented in this thesis primarily focuses on three research directions: (i) exploring the capabilities and performance of the meshfree particle-based Smooth Particle Hydrodynamics (SPH) coupled with the Discrete Element Method (DEM) in simulating single-phase and particle-liquid pipe flows, (ii) applying the SPH method to simulate Newtonian and non-Newtonian fluids in mechanically agitated stirred vessels with varying impeller types and Reynolds numbers, where the velocity fields provided by SPH show good agreement with Positron Emission Particle Tracking (PEPT) experimental data, and (iii) using the SPH-DEM methodology to study the role of various parameters on the Lagrangian migration trajectories of particles, particularly their final equilibrium radial positions in horizontal flows. The conclusions from these three main research areas are summarized as follows:

In this study, the capabilities and performance of mesh-based FVM and meshfree particle-based SPH in simulating single-phase Newtonian and non- Newtonian flows are compared. Through a comprehensive analysis encompassing laminar and turbulent flow regimes, various fluid rheologies light on the strengths and limitations of each approach. In single-phase flow, the FVM

method demonstrated excellent concordance with theoretical models and provided accurate predictions across various scenarios including laminar and turbulent regimes. Meanwhile, the SPH method, despite approximations in boundary conditions, excelled in capturing complex fluid dynamics, especially in laminar flows. The ability of SPH to simulate turbulent flows is limited at present because of the lack of appropriate turbulence models. This is an area which needs further development. In laminar regime, SPH is able to capture accuracy velocity distribution in pipe flow. The turbulent SPH simulations are limited to by turbulence model in SPH framework. The chapter 4 has proved that the HBP rheology model in SPH is flexible and excellent to predict different non-Newtonian flow behaviors. HBP model successfully applied in SPH provides a foundation for the study of complex flows such as solid-liquid two-phase flows and mixed flows.

A series of simulations were also conducted based on the technique of SPH coupled with the DEM to investigate the detailed dynamics of radial migration of a single particle in horizontal viscous pipe flow. Extensive validation procedures were undertaken, including comparisons with established theoretical solutions for single-phase flow and experimental observations obtained from high-speed digital imaging of particle motion in a pipe flow loop. This SPH-DEM coupling was shown to be superior to using SPH alone for handling particle-liquid flow. The work served to demonstrate the robustness and accuracy of the SPH-DEM framework in predicting the detailed aspects of particle migration dynamics in both Newtonian and non-Newtonian fluids. Results showed that neutrally-buoyant particles of spherical and ellipsoidal shape exhibit lateral migration in viscous flow which is symmetrical about the pipe centreline, and each attains the same stable radial equilibrium position regardless of its point of introduction in the flow. Such an equilibrium position becomes less well defined in transitional flow due to the gradual onset of turbulence. A detailed SPH-DEM parametric study showed that the particle equilibrium position is influenced by a number of factors, including particle size and shape, particle-fluid density ratio, pipe Reynolds number and fluid rheology, and the effects have been delineated. Particle density had the most effect on particle equilibrium position, followed by particle size, whilst particle shape had remark-

able effects on particle spin dynamics. This study has helped highlight the versatility and accuracy of the SPH-DEM methodology for simulating complex multiphase flow problems.

The SPH-DEM numerical approach was also used to simulate the horizontal laminar pipe flow of coarse particle-liquid food suspensions. SPH-DEM was able to predict the single-phase flow of various non-Newtonian fluid rheologies including the carrier fluid used to convey food particles with a high degree of accuracy as validated by analytical solutions of radial velocity profiles. The particle-liquid flow simulations were also successfully validated using experimental measurements obtained by a technique of PEPT. The radial particle velocity profiles, radial solid phase distributions as well as particle passage time distributions were accurately predicted at solid loadings varying from 10 to 40 vol. %. Radial particle velocity profiles are asymmetric, with the maximum being located above the centreline. Such asymmetry disappears at high solid concentrations, and the maximum moves to the centre.

Simulations yielded detailed information on the local dynamics of the two-phase flows investigated, including translational as well as rotational particle slip velocities, flow pressure field and fluid vorticity. Whilst local translational particle slip velocities, as expected for nearly-neutrally buoyant particles, were vanishingly small, particle angular (slip) velocities were significant. Spin is positive (anticlockwise) in the top half of the pipe cross-section and negative (clockwise) in the bottom half. Particle spin is fastest closest to the wall where liquid velocity gradients are highest, reducing to zero at the centre of the pipe before switching direction. As solid loading increases, approaching the particle packing fraction, spin becomes negligible everywhere except close to the wall. The pressure drop predicted by SPH-DEM at different particle concentrations showed a very good agreement with empirical correlations from the literature, which is further evidence of the accuracy and reliability of the coupled method to simulate these complex flows even under conditions of high concentration which are typical of industrial food processing. With further development, the framework has the potential for simulating flows involving particles with more complex physical properties such as viscoelastic deformability, shape anisotropy, or surface adhe-

sion properties, and fluids with more complex rheologies, including viscoelasticity, shear-thinning, or time-dependent viscosity.

A series of simulations using the SPH technique have been carried out to investigate the detailed dynamics of mixing viscous fluids in stirred vessels.A three-dimensional HBP-SPH model was successfully developed for simulating the mixed flow of a non-Newtonian fluid in a stirred vessel. The accuracy and reliability of the model were fully validated by Lagrangian particle point tracking measurements using PEPT technique. Even the shape and size of the cavern were validated by PLIF measurements. The validation results show that the model accurately predicts free surface dynamics and the formation of pseudo-cavities in the fluid. The model shows robustness over a range of scales and rheological properties, demonstrating its ability to handle a wide range of fluid behaviour and mixing situations. The HBP-SPH model proved to be both accurate and flexible, and is an important tool for modelling more complex systems involving moving boundaries. The developed HBP-SPH model represents a significant advancement in computational modelling of non-Newtonian fluid dynamics within mixing vessels. Its ability to accurately capture complex flow patterns and adapt to different fluid properties makes it essential for optimising industrial mixing processes and addressing more complex fluid dynamics challenges.

8.2 Future work

The main work of this thesis is focused on SPH modeling techniques for particulate flow as well as mixed flow in different geometries. Although this work has achieved important steps towards the understanding of the particle velocity and concentration distributions in the pipe have been explored, it also raised new research challenges.

There is a lack of quantitative studies on particle-particle collision mechanisms, as well as on the mechanical mechanisms of particle-pipe wall interactions. The exploration of particle collision

forces is very challenging for both experimental and existing simulation techniques. However, it is a very practical work, especially for applications in material transport and chemical production.

The natural data properties of SPH have great potential to be combined with machine learning to obtain velocity distributions of complex flows more cost-effectively. Based on the previously work of our group, it is possible to using SPH trajectories as the input of RNN machine learning model. Then, the data after trained will give a good prediction of velocity filed and vorticity field.

Looking ahead, the broadening of SPH application fields depends on the improvement of turbulence modeling techniques in SPH framework. Meeting this challenge will require a great effort to develop robust methods that can accurately capture turbulence phenomena in a variety of situations. By overcoming these obstacles, we can open new areas of fluid dynamics research and extend the utility of SPH to a wider range of engineering and scientific applications. In summary, future work should focus on expanding the application of the SPH method in simulating solids suspended in viscoelastic fluids. This can be achieved by examining simpler flow problems to validate accuracy of the method and reliability. Furthermore, investigating non-Newtonian mixing flows resembling those found in stirred vessels will provide insights into the behaviour of solids in realistic flow fields. Additionally, studying multiple particle systems and exploring different constitutive equations will enhance the capabilities of the method and broaden its applicability. These efforts would contribute to the development of the SPH method as a robust tool for simulating and comprehending the dynamics of solids in viscoelastic fluid systems.

References

Adams, Luke Wayne (2009). "Experimental and computational study of non-turbulent flow regimes and cavern formation of non-Newtonian fluids in a stirred tank". PhD thesis. University of Birmingham.

Adams, Luke Wayne and Mostafa Barigou (2007). "CFD analysis of caverns and pseudo-caverns developed during mixing of non-Newtonian fluids". In: *Chemical Engineering Research and Design* 85.5, pp. 598–604.

Almutairi, Zeyad, Fayez M Al-Alweet, Yusif A Alghamdi, Omar A Almisned, and Othman Y Alothman (2020). "Investigating the characteristics of two-phase flow using electrical capacitance tomography (ECT) for three pipe orientations". In: *Processes* 8.1, p. 51.

Altomare, Corrado, Alejandro JC Crespo, Jose M Domínguez, Moncho Gómez-Gesteira, Tomohiro Suzuki, and Toon Verwaest (2015). "Applicability of Smoothed Particle Hydrodynamics for estimation of sea wave impact on coastal structures". In: *Coastal Engineering* 96, pp. 1–12.

Altschul, Stephen F, Thomas L Madden, Alejandro A Schäffer, Jinghui Zhang, Zheng Zhang, Webb Miller, and David J Lipman (1997). "Gapped BLAST and PSI-BLAST: a new generation of protein database search programs". In: *Nucleic Acids Research* 25.17, pp. 3389–3402.

Amanullah, A, SA Hjorth, and AW Nienow (1998). “A new mathematical model to predict cavern diameters in highly shear thinning, power law liquids using axial flow impellers”. In: *Chemical Engineering Science* 53.3, pp. 455–469.

Anderson, T Bo and ROY Jackson (1967). “Fluid mechanical description of fluidized beds. Equations of motion”. In: *Industrial & Engineering Chemistry Fundamentals* 6.4, pp. 527–539.

Atherton, Tim J and Darren J Kerbyson (1999). “Size invariant circle detection”. In: *Image and Vision Computing* 17.11, pp. 795–803.

Atkinson, Callum, Sebastien Coudert, Jean-Marc Foucaut, Michel Stanislas, and Julio Soria (2011). “The accuracy of tomographic particle image velocimetry for measurements of a turbulent boundary layer”. In: *Experiments in Fluids* 50, pp. 1031–1056.

Aubin, Joelle, David F Fletcher, and Catherine Xuereb (2004). “Modeling turbulent flow in stirred tanks with CFD: the influence of the modeling approach, turbulence model and numerical scheme”. In: *Experimental Thermal and Fluid Science* 28.5, pp. 431–445.

Bailey, Robert T (2017). “Managing false diffusion during second-order upwind simulations of liquid micromixing”. In: *International Journal for Numerical Methods in Fluids* 83.12, pp. 940–959.

Bakalis, Serafim, PW Cox, W Wang-Nolan, David Parker, and PJ F FRYER (2003a). “Use of Positron-Emission Particle Tracking (PEPT) Technique for Velocity Measurements in Model Food Fluids”. In: *Journal of Food Science* 68.9, pp. 2684–2692.

Bakalis, Serafim, PW Cox, W Wang-Nolan, David Parker, and PJ F RYER (2003b). “Use of Positron-Emission Particle Tracking (PEPT) Technique for Velocity Measurements in Model Food Fluids”. In: *Journal of Food Science* 68.9, pp. 2684–2692.

Baker, Roger C (2002). *An introductory guide to flow measurement*. Vol. 2. John Wiley & Sons.

Baker, Stephen, Jonathan Hardy, Kenneth E Sanderson, Michael Quail, Ian Goodhead, Robert A Kingsley, Julian Parkhill, Bruce Stocker, and Gordon Dougan (2007). "A novel linear plasmid mediates flagellar variation in Salmonella Typhi". In: *PLoS Pathog* 3.5, e59.

Bakker, André, Ahmad H HAIDARI, and Lanre M OSHINOWO (2001). "Realize greater benefits from CFD". In: *Chemical Engineering Progress* 97.3, pp. 45–53.

Balmforth, Neil J, Ian A Frigaard, and Guillaume Ovarlez (2014). "Yielding to stress: recent developments in viscoplastic fluid mechanics". In: *Annual Review of Fluid Mechanics* 46, pp. 121–146.

Barigou, Mostafa (2004). "Particle tracking in opaque mixing systems: An overview of the capabilities of PET and PEPT". In: *Chemical Engineering Research and Design* 82.9, pp. 1258–1267.

– (2009). "10 Solid–liquid mixing". In: *Food Mixing: Principles and Applications*, p. 199.

Barigou, Mostafa, Fabio Chiti, Paulina Pianko-Oprych, Antonio Guida, Luke Adams, Xianfeng Fan, David J Parker, and Alvin William Nienow (2009). "Using positron emission particle tracking (PEPT) to study mixing in stirred vessels: validation and tackling unsolved problems in opaque systems". In: *Journal of Chemical Engineering of Japan* 42.11, pp. 839–846.

Barigou, Mostafa, PG Fairhurst, PJ Fryer, and J-P Pain (2003). "Concentric flow regime of solid–liquid food suspensions: theory and experiment". In: *Chemical Engineering Science* 58.9, pp. 1671–1686.

Barth, Timothy, Raphaèle Herbin, and Mario Ohlberger (2018). "Finite volume methods: foundation and analysis". In: *Encyclopedia of computational mechanics second edition*, pp. 1–60.

Bartosik, Artur (2020). "Validation of friction factor predictions in vertical slurry flows with coarse particles". In: *Journal of Hydrology and Hydromechanics* 68.2, pp. 119–127.

Belytschko, T., Y. Krongauz, D. Organ, M. Fleming, and P. Krysl (1996). "Meshless methods: An overview and recent developments". In: *Computer Methods in Applied Mechanics and Engineering* 139.1, pp. 3–47.

Benito, JJ, F Urena, and L Gavete (2001). "Influence of several factors in the generalized finite difference method". In: *Applied Mathematical Modelling* 25.12, pp. 1039–1053.

Benito, JJ, F Urena, L Gavete, and R Alvarez (2003). "An h-adaptive method in the generalized finite differences". In: *Computer Methods in Applied Mechanics and Engineering* 192.5-6, pp. 735–759.

Bird, R Ryron, Robert C Armstrong, and Ole Hassager (1977). *Dynamics of Polymeric Liquids, Volume 1: Fluid Mechanics*. Wiley.

Boac, Josephine M, RP Kingsly Ambrose, Mark E Casada, Ronaldo G Maghirang, and Dirk E Maier (2014). "Applications of discrete element method in modeling of grain postharvest operations". In: *Food Engineering Reviews* 6, pp. 128–149.

Bose, Sayan and Moloy Banerjee (2015). "Effect of non-Newtonian characteristics of blood on magnetic particle capture in occluded blood vessel". In: *Journal of Magnetism and Magnetic Materials* 374, pp. 611–623.

Bouillard, J, B Alban, P Jacques, and C Xuereb (2001). "Liquid flow velocity measurements in stirred tanks by ultra-sound Doppler velocimetry". In: *Chemical Engineering Science* 56.3, pp. 747–754.

Brandt, Luca and Filippo Coletti (2022). “Particle-laden turbulence: progress and perspectives”. In: *Annual Review of Fluid Mechanics* 54, pp. 159–189.

Brown, David AR, Pip N Jones, John C Middleton, George Papadopoulos, and Engin B Arik (2003). “Experimental methods”. In: *Handbook of Industrial Mixing: Science and Practice*, pp. 145–256.

Bryer, Denis William and Ronald Charles Pankhurst (1971). *Pressure-probe methods for determining wind speed and flow direction*. H.M.S.O.

Buchhave, Preben (1992). “Particle image velocimetry—status and trends”. In: *Experimental Thermal and Fluid Science* 5.5, pp. 586–604.

Bureau, Lionel, Gwennou Coupier, and Thomas Salez (2023). “Lift at low Reynolds number”. In: *The European Physical Journal E* 46.11, p. 111.

Busciglio, Antonio, F Grisafi, F Scargiali, and A Brucato (2014). “Mixing dynamics in uncovered unbaffled stirred tanks”. In: *Chemical Engineering Journal* 254, pp. 210–219.

Canelas, Ricardo B, Alejandro JC Crespo, Jose M Domínguez, Rui ML Ferreira, and Moncho Gómez-Gesteira (2016). “SPH–DCDEM model for arbitrary geometries in free surface solid–fluid flows”. In: *Computer Physics Communications* 202, pp. 131–140.

Cao, XY, FR Ming, and AM Zhang (2014). “Sloshing in a rectangular tank based on SPH simulation”. In: *Applied Ocean Research* 47, pp. 241–254.

Chakrabandhu, Krittalak and Rakesh K Singh (2005). “Rheological properties of coarse food suspensions in tube flow at high temperatures”. In: *Journal of Food Engineering* 66.1, pp. 117–128.

Chan, Eng-Seng, Tek-Kaun Lim, Wan-Ping Voo, Ravindra Pogaku, Beng Ti Tey, and Zhibing Zhang (2011). “Effect of formulation of alginate beads on their mechanical behavior and stiffness”. In: *Particuology* 9.3, pp. 228–234.

Chen, Feng, Eric C Drumm, and Georges Guiochon (2011). “Coupled discrete element and finite volume solution of two classical soil mechanics problems”. In: *Computers and Geotechnics* 38.5, pp. 638–647.

Chen, Jian, Ognjen Orozovic, Kenneth Williams, Jingjing Meng, and Chengzhi Li (2020). “A coupled DEM-SPH model for moisture migration in unsaturated granular material under oscillation”. In: *International Journal of Mechanical Sciences* 169, p. 105313.

Chen, Shih-Di, Tsorng-Whay Pan, and Chien-Cheng Chang (2012). “The motion of a single and multiple neutrally buoyant elliptical cylinders in plane Poiseuille flow”. In: *Physics of Fluids* 24.10.

Chen, Xi-Zhong, De-Pan Shi, Xi Gao, and Zheng-Hong Luo (2011). “A fundamental CFD study of the gas–solid flow field in fluidized bed polymerization reactors”. In: *Powder Technology* 205.1, pp. 276–288.

Cheng, Pengxin, Nan Gui, Xingtuan Yang, JiyuanTu, and Shengyao Jiang (2018). “Application of lattice Boltzmann methods for the multiphase fluid pipe flow on graphical processing unit”. In: *The Journal of Computational Multiphase Flows* 10.3, pp. 109–118.

Chhabra, Raj P and John Francis Richardson (2011). *Non-Newtonian flow and applied rheology: engineering applications*. Butterworth-Heinemann.

Chu, Yu-Ming, Fatemeh Salehi, M Jafaryar, and Quang-Vu Bach (2020). "Simulation based on FVM for influence of nanoparticles on flow inside a pipe enhanced with helical tapes". In: *Applied Nanoscience*, pp. 1–11.

Chung, KHK, MJH Simmons, and Mostafa Barigou (2009). "Local gas and liquid phase velocity measurement in a miniature stirred vessel using PIV combined with a new image processing algorithm". In: *Experimental Thermal and Fluid Science* 33.4, pp. 743–753.

Clough, Ray W (1960). "The finite element in plane stress analysis". In: *Proc. 2nd ASCE Confer. On Electric Computation, 1960*.

– (2004). "Early history of the finite element method from the view point of a pioneer". In: *International Journal for Numerical Methods in Engineering* 60.1, pp. 283–287.

Cook, Benjamin Koger (2001). "A numerical framework for the direct simulation of solid-fluid systems". Thesis.

Coudert, Sébastien, Jean-Marc Foucaut, Jim Kostas, Michel Stanislas, P Braud, C Fourment, J Delville, Murat Tutkun, Faraz Mehdi, and P Johansson (2011). "Double large field stereoscopic PIV in a high Reynolds number turbulent boundary layer". In: *Experiments in Fluids* 50, pp. 1–12.

Coulson, John Metcalfe, John Francis Richardson, John Rayner Backhurst, and John Hadlett Harker (1990). *Chemical Engineering: Fluid flow, heat transfer and mass transfer*. Vol. 1. Pergamon press.

Crespo, A JC, M Gómez-Gesteira, and Robert A Dalrymple (2007). "Boundary conditions generated by dynamic particles in SPH methods". In: *Computers, Materials and Continua* 5.3, pp. 173–184.

Crimaldi, JP (2008). “Planar laser induced fluorescence in aqueous flows”. In: *Experiments in Fluids* 44, pp. 851–863.

Cummins, Sharen J and Paul W Cleary (2011). “Using distributed contacts in DEM”. In: *Applied Mathematical Modelling* 35.4, pp. 1904–1914.

Cundall, Peter A and Otto DL Strack (1979). “A discrete numerical model for granular assemblies”. In: *Geotechnique* 29.1, pp. 47–65.

Curran, SJ, RE Hayes, A Afacan, MC Williams, and Philippe A Tanguy (2002). “Properties of carbopol solutions as models for yield-stress fluids”. In: *Journal of Food Science* 67.1, pp. 176–180.

Dalrymple, Robert A and Benedict D Rogers (2006). “Numerical modeling of water waves with the SPH method”. In: *Coastal Engineering* 53.2-3, pp. 141–147.

De Chant, Lawrence J (2005). “The venerable 1/7th power law turbulent velocity profile: a classical nonlinear boundary value problem solution and its relationship to stochastic processes”. In: *Applied Mathematics and Computation* 161.2, pp. 463–474.

Deb, Surya and Danesh Tafti (2014). “Investigation of flat bottomed spouted bed with multiple jets using DEM-CFD framework”. In: *Powder Technology* 254, pp. 387–402.

Dehnen, Walter and Hossam Aly (2012). “Improving convergence in smoothed particle hydrodynamics simulations without pairing instability”. In: *Monthly Notices of the Royal Astronomical Society* 425.2, pp. 1068–1082.

Dennis, SCR, SN Singh, and DB Ingham (1980). “The steady flow due to a rotating sphere at low and moderate Reynolds numbers”. In: *Journal of Fluid Mechanics* 101.2, pp. 257–279.

Domínguez, JM, AJC Crespo, M Gómez-Gesteira, and JC2869628 Marongiu (2011). "Neighbour lists in smoothed particle hydrodynamics". In: *International Journal for Numerical Methods in Fluids* 67.12, pp. 2026–2042.

Domínguez, Jose M, Georgios Fourtakas, Corrado Altomare, Ricardo B Canelas, Angelo Tafuni, Orlando García-Feal, Ivan Martínez-Estévez, Athanasios Mokos, Renato Vacondio, and Alejandro JC Crespo (2022). "DualSPHysics: from fluid dynamics to multiphysics problems". In: *Computational Particle Mechanics* 9.5, pp. 867–895.

Drain, Leslie E (1980). "The laser Doppler techniques". In: *Chichester*.

Drescher, Andrew (1991). *Analytical methods in bin-load analysis*. Elsevier. ISBN: 0444883681.

Drew, Donald A (1993). "Analytical modeling of multiphase flow". In: *Particulate Two-phase Flow*.

Duan, Guangtao, Bin Chen, Seiichi Koshizuka, and Hao Xiang (2017). "Stable multiphase moving particle semi-implicit method for incompressible interfacial flow". In: *Computer Methods in Applied Mechanics and Engineering* 318, pp. 636–666.

Duchanoy, Christophe and Thibauld RG Jongen (2003). "Efficient simulation of liquid–solid flows with high solids fraction in complex geometries". In: *Computers & Fluids* 32.10, pp. 1453–1471.

Durst, F., S. Ray, B. Ünsal, and O. A. Bayoumi (June 2005). "The Development Lengths of Laminar Pipe and Channel Flows". In: *Journal of Fluids Engineering* 127.6, pp. 1154–1160.

Eckmann, David M and James B Grotberg (1991). "Experiments on transition to turbulence in oscillatory pipe flow". In: *Journal of Fluid Mechanics* 222, pp. 329–350.

Edwards, Iwan, Sean A Axon, Mostafa Barigou, and E Hugh Stitt (2009). “c”. In: *Industrial & Engineering Chemistry Research* 48.2, pp. 1019–1028.

Eesa, M and Mostafa Barigou (2008). “Horizontal laminar flow of coarse nearly-neutrally buoyant particles in non-Newtonian conveying fluids: CFD and PEPT experiments compared”. In: *International Journal of Multiphase Flow* 34.11, pp. 997–1007.

– (2010). “Enhancing radial temperature uniformity and boundary layer development in viscous Newtonian and non-Newtonian flow by transverse oscillations: A CFD study”. In: *Chemical Engineering Science* 65.6, pp. 2199–2212.

Eloot, Sunny, Frank De Bisschop, and Pascal Verdonck (2004). “Experimental evaluation of the migration of spherical particles in three-dimensional Poiseuille flow”. In: *Physics of Fluids* 16.7, pp. 2282–2293.

Elson, TP (1990). “The growth of caverns formed around rotating impellers during the mixing of a yield stress fluid”. In: *Chemical Engineering Communications* 96.1, pp. 303–319.

Elson, TP, DJ Cheesman, and AW Nienow (1986). “X-ray studies of cavern sizes and mixing performance with fluids possessing a yield stress”. In: *Chemical Engineering Science* 41.10, pp. 2555–2562.

El-Emam, Mahmoud A., Ling Zhou, Weidong Shi, Chen Han, Ling Bai, and Ramesh Agarwal (2021). “Theories and Applications of CFD–DEM Coupling Approach for Granular Flow: A Review”. In: *Archives of Computational Methods in Engineering* 28.7, pp. 4979–5020.

English, A, JM Domínguez, R Vacondio, AJC Crespo, PK Stansby, SJ Lind, and M Gómez-Gesteira (2019). “Correction for dynamic boundary conditions”. In: *Proceedings of the 14th International SPHERIC Workshop, Exeter, UK*, pp. 25–27.

English, Aaron, JM Domínguez, Renato Vacondio, AJC Crespo, PK Stansby, SJ Lind, Luca Chiapponi, and M Gómez-Gesteira (2022). "Modified dynamic boundary conditions (mDBC) for general-purpose smoothed particle hydrodynamics (SPH): application to tank sloshing, dam break and fish pass problems". In: *Computational Particle Mechanics* 9.5, pp. 1–15.

Fairhurst, PG, Mostafa Barigou, PJ Fryer, JP Pain, and DJ Parker (2001). "Using positron emission particle tracking (PEPT) to study nearly neutrally buoyant particles in high solid fraction pipe flow". In: *International Journal of Multiphase Flow* 27.11, pp. 1881–1901.

Fang, Lide, Yueyuan Liu, Shaochong Wang, Jixun Zhao, Yousef Faraj, Mengyuan Tian, and Zihui Wei (2021). "Dual-modality UDV-PIV system for measurement of solid-liquid flow in sewage facilities". In: *Flow Measurement and Instrumentation* 82, p. 102063.

Feng, James, Howard H Hu, and Daniel D Joseph (1994). "Direct simulation of initial value problems for the motion of solid bodies in a Newtonian fluid. Part 2. Couette and Poiseuille flows". In: *Journal of Fluid Mechanics* 277, pp. 271–301.

Fester, Veruscha, Baudouin Mbiya, and Slatter (2008). "Energy losses of non-Newtonian fluids in sudden pipe contractions". In: *Chemical Engineering Journal* 145.1, pp. 57–63.

Fluent, ANSYS (2011). "Ansys fluent theory guide". In: *Ansys Inc., USA* 15317, pp. 431–432.

Fourtakas, Georgios, Jose M Dominguez, Renato Vacondio, and Benedict D Rogers (2019). "Local uniform stencil (LUST) boundary condition for arbitrary 3-D boundaries in parallel smoothed particle hydrodynamics (SPH) models". In: *Computers & Fluids* 190, pp. 346–361.

Fourtakas, Georgios and BD Rogers (2016). "Modelling multi-phase liquid-sediment scour and resuspension induced by rapid flows using Smoothed Particle Hydrodynamics (SPH) accelerated with a Graphics Processing Unit (GPU)". In: *Advances in Water Resources* 92, pp. 186–199.

Furuichi, N, Y Terao, Y Wada, and Y Tsuji (2015). “Friction factor and mean velocity profile for pipe flow at high Reynolds numbers”. In: *Physics of Fluids* 27.9, p. 095108.

Galindot, Enrique and Alvin W Nienow (1992). “Mixing of highly viscous simulated xanthan fermentation broths with the Lightnin A-315 impeller”. In: *Biotechnology Progress* 8.3, pp. 233–239.

Gaul, Lothar, Martin Kögl, and Marcus Wagner (2013). *Boundary element methods for engineers and scientists: an introductory course with advanced topics*. Springer Science & Business Media.

Gebhardt, Joerg, Wilhelm Daake, and Peter Ude (2018). “Reliable measurement of surface temperature: a step to widespread non-invasive T-measurement in industry”. In: *Sensors and Measuring Systems; 19th ITG/GMA-Symposium*. VDE, pp. 1–4.

Gingold, RA and JJ Monaghan (1982). “Kernel estimates as a basis for general particle methods in hydrodynamics”. In: *Journal of Computational Physics* 46.3, pp. 429–453.

Gingold, Robert A and Joseph J Monaghan (1977). “Smoothed particle hydrodynamics: theory and application to non-spherical stars”. In: *Monthly Notices of The Royal Astronomical Society* 181.3, pp. 375–389.

Gomez-Gesteira, Moncho, Benedict D Rogers, Alejandro JC Crespo, Robert A Dalrymple, Muthukumar Narayanaswamy, and José M Dominguez (2012). “SPHysics–development of a free-surface fluid solver–Part 1: Theory and formulations”. In: *Computers & Geosciences* 48, pp. 289–299.

Gomez-Gesteira, Moncho, Benedict D Rogers, Robert A Dalrymple, and Alex JC Crespo (2010). “State-of-the-art of classical SPH for free-surface flows”. In: *Journal of Hydraulic Research* 48.sup1, pp. 6–27.

González-Montellano, Carlos, EM Baguena, Álvaro Ramírez-Gómez, and P Barreiro (2014). "Discrete element analysis for the assessment of the accuracy of load cell-based dynamic weighing systems in grape harvesters under different ground conditions". In: *Computers and Electronics in Agriculture* 100, pp. 13–23.

Gosman, AD and E Loannides (1983). "Aspects of computer simulation of liquid-fueled combustors". In: *Journal of Energy* 7.6, pp. 482–490.

Gotoh, Hitoshi, Songdong Shao, and Tetsu Memita (2004). "SPH-LES model for numerical investigation of wave interaction with partially immersed breakwater". In: *Coastal Engineering Journal* 46.1, pp. 39–63.

Gradeck, Michel, BFZ Fagla, Christophe Baravian, and Michel Lebouché (2005). "Experimental thermomechanic study of Newtonian and non-Newtonian suspension flows". In: *International Journal of Heat and Mass Transfer* 48.16, pp. 3469–3477.

Guerrero, Esteban, Felipe Muñoz, and Nicolás Ratkovich (2017). "Comparison between eulerian and vof models for two-phase flow assessment in vertical pipes". In: *CT&F-Ciencia, Tecnología y Futuro* 7.1, pp. 73–84.

Guida, Antonio, Alvin W Nienow, and Mostafa Barigou (2010a). "PEPT measurements of solid–liquid flow field and spatial phase distribution in concentrated monodisperse stirred suspensions". In: *Chemical Engineering Science* 65.6, pp. 1905–1914.

– (2010b). "The effects of the azimuthal position of the measurement plane on the flow parameters determined by PIV within a stirred vessel". In: *Chemical Engineering Science* 65.8, pp. 2454–2463.

Guida, Antonio, Alvin W Nienow, and Mostafa Barigou (2011). "Mixing of dense binary suspensions: Multi-component hydrodynamics and spatial phase distribution by PEPT". In: *AIChE Journal* 57.9, pp. 2302–2315.

– (2010c). "Shannon entropy for local and global description of mixing by Lagrangian particle tracking". In: *Chemical Engineering Science* 65.10, pp. 2865–2883.

Hadley, Kevin R and Clare McCabe (2012). "Coarse-grained molecular models of water: a review". In: *Molecular simulation* 38.8-9, pp. 671–681.

Han, Zheng, Bin Su, Yange Li, Jie Dou, Weidong Wang, and Lianheng Zhao (2020). "Modeling the progressive entrainment of bed sediment by viscous debris flows using the three-dimensional SC-HBP-SPH method". In: *Water Research* 182, p. 116031.

Han, Zheng, Bin Su, Yange Li, Wei Wang, Weidong Wang, Jianling Huang, and Guangqi Chen (2019). "Numerical simulation of debris-flow behavior based on the SPH method incorporating the Herschel-Bulkley-Papanastasiou rheology model". In: *Engineering Geology* 255, pp. 26–36.

Hemrajani, Ramesh R and Gary B Tatterson (2003). "Mechanically stirred vessels". In: *Handbook of Industrial Mixing: Science and Practice*, pp. 345–390.

Hertz, Heinrich (1882). "Ueber die Berührung fester elastischer Körper". In: *J reine und angewandte Mathematik*.

Hirt, Cyril W and Billy D Nichols (1981). "Volume of fluid (VOF) method for the dynamics of free boundaries". In: *Journal of Computational Physics* 39.1, pp. 201–225.

Hooper, JD and AR Musgrove (1997). "Reynolds stress, mean velocity, and dynamic static pressure measurement by a four-hole pressure probe". In: *Experimental Thermal and Fluid Science* 15.4, pp. 375–383.

Horabik, Józef and Marek Molenda (2016). “Parameters and contact models for DEM simulations of agricultural granular materials: A review”. In: *Biosystems Engineering* 147, pp. 206–225.

Hosokawa, Shigeo and Akio Tomiyama (2013). “Bubble-induced pseudo turbulence in laminar pipe flows”. In: *International Journal of Heat and Fluid flow* 40, pp. 97–105.

Hossein, Fria, Cong Duan, and Panagiota Angeli (2024). “Advanced ultrasound techniques for studying liquid–liquid dispersions in confined impinging jets”. In: *Physics of Fluids* 36.8.

Hu, Junjie and Zhaoli Guo (2017). “A numerical study on the migration of a neutrally buoyant particle in a Poiseuille flow with thermal convection”. In: *International Journal of Heat and Mass Transfer* 108, pp. 2158–2168.

Hu, Xiao, Jianzhong Lin, and Xiaoke Ku (2019). “Inertial migration of circular particles in Poiseuille flow of a power-law fluid”. In: *Physics of Fluids* 31.7.

Irgens, Fridtjov (2014). *Rheology and non-newtonian fluids*. Vol. 1. Springer.

Jahanmiri, Mohsen (2011). *Particle image velocimetry: Fundamentals and its applications*. Report. Citeseer.

Jammy, Satya P, Christian T Jacobs, and Neil D Sandham (2019). “Performance evaluation of explicit finite difference algorithms with varying amounts of computational and memory intensity”. In: *Journal of Computational Science* 36, p. 100565.

Jiang, Di, Di Huang, Gutian Zhao, Wenlai Tang, and Nan Xiang (2019). “Numerical simulation of particle migration in different contraction–expansion ratio microchannels”. In: *Microfluidics and Nanofluidics* 23, pp. 1–11.

Jiradilok, Veeraya, Dimitri Gidaspow, Somsak Damronglerd, William J. Koves, and Reza Mostofi (2006). “Kinetic theory based CFD simulation of turbulent fluidization of FCC particles in a riser”. In: *Chemical Engineering Science* 61.17, pp. 5544–5559.

Joseph, DD and D Ocando (2002). “Slip velocity and lift”. In: *Journal of Fluid Mechanics* 454, pp. 263–286.

Kalyon, Dilhan M and Seda Aktaş (2014). “Factors affecting the rheology and processability of highly filled suspensions”. In: *Annual Review of Chemical and Biomolecular Engineering* 5, pp. 229–254.

Karnis, Alkibiadis (1966). “The flow of suspensions through tubes.” In: *McGill University*.

Kefayati, GHR and RR Huilgol (2017). “Lattice Boltzmann method for the simulation of the steady flow of a Bingham fluid in a pipe of square cross-section”. In: *European Journal of Mechanics-B/Fluids* 65, pp. 412–422.

Kelessidis, VC, R Maglione, C Tsamantaki, and Y Aspirtakis (2006). “Optimal determination of rheological parameters for Herschel–Bulkley drilling fluids and impact on pressure drop, velocity profiles and penetration rates during drilling”. In: *Journal of Petroleum Science and Engineering* 53.3-4, pp. 203–224.

Kim, Jihwan, Ji-Hyeong Lee, Hoyoung Jang, Jeyun Byun, and Young Seok Joo (2021). “Numerical investigation of scour by incompressible SPH coupled with coarse-grained DEM”. In: *Soil Dynamics and Earthquake Engineering* 151, p. 106998.

Kim, Shin Hyuk, Jay H Lee, and Richard D Braatz (2021). “Multi-scale fluid dynamics simulation based on MP-PIC-PBE method for PMMA suspension polymerization”. In: *Computers & Chemical Engineering* 152, p. 107391.

King, R Peter (2002). *Introduction to practical fluid flow*. Elsevier.

Kong, Dali, Mengmeng Zhou, Shuai Wang, Kun Luo, Debo Li, and Jianren Fan (2021). "Eulerian-Lagrangian simulation of chemical looping combustion with wide particle size distributions". In: *Chemical Engineering Science* 245, p. 116849.

Koo, Bonchan (2022). "Comparison of finite-volume method and method of characteristics for simulating transient flow in natural-gas pipeline". In: *Journal of Natural Gas Science and Engineering* 98, p. 104374.

Koshizuka, Seiichi, Atsushi Nobe, and Yoshiaki Oka (1998). "Numerical analysis of breaking waves using the moving particle semi-implicit method". In: *International Journal for Numerical Methods in Fluids* 26.7, pp. 751–769.

Koshizuka, Seiichi and Yoshiaki Oka (1996). "Moving-particle semi-implicit method for fragmentation of incompressible fluid". In: *Nuclear Science and Engineering* 123.3, pp. 421–434.

Krüger, Timm, Halim Kusumaatmaja, Alexandr Kuzmin, Orest Shardt, Goncalo Silva, and Erlend Magnus Viggen (2017). "The lattice Boltzmann method". In: *Springer International Publishing* 10.978-3, pp. 4–15.

Kruggel-Emden, Harald, Erdem Simsek, Stefan Rickelt, Siegmar Wirtz, and Viktor Scherer (2007). "Review and extension of normal force models for the discrete element method". In: *Powder Technology* 171.3, pp. 157–173.

Kuznik, Frédéric, Christian Obrecht, Gilles Rusaouen, and Jean-Jacques Roux (2010). "LBM based flow simulation using GPU computing processor". In: *Computers & Mathematics with Applications* 59.7, pp. 2380–2392.

Lapin, Alexei, Joachim Schmid, and Matthias Reuss (2006). “Modeling the dynamics of E. coli populations in the three-dimensional turbulent field of a stirred-tank bioreactor—A structured–segregated approach”. In: *Chemical Engineering Science* 61.14, pp. 4783–4797.

Lareo, C, RM Nedderman, and PJ Fryer (1997). “Particle velocity profiles for solid-liquid food flows in vertical pipes Part II. Multiple particles”. In: *Powder Technology* 93.1, pp. 35–45.

Le Guer, Y, P Reghem, I Petit, and B Stutz (2003). “Experimental study of a buoyant particle dispersion in pipe flow”. In: *Chemical Engineering Research and Design* 81.9, pp. 1136–1143.

Leary, KCP and MW Schmeeckle (2017). “The importance of splat events to the spatiotemporal structure of near-bed fluid velocity and bed load motion over bed forms: Laboratory experiments downstream of a backward facing step”. In: *Journal of Geophysical Research: Earth Surface* 122.12, pp. 2411–2430.

Leimkuhler, Benedict J, Sebastian Reich, and Robert D Skeel (1996). “Integration Methods for Molecular Dynamics”. In: *Mathematical Approaches to Biomolecular Structure and Dynamics*. Springer, pp. 161–185.

Li, Huabing, Xiaoyan Lu, Haiping Fang, and Yuehong Qian (2004). “Force evaluations in lattice Boltzmann simulations with moving boundaries in two dimensions”. In: *Physical Review E* 70.2, p. 026701.

Li, Kun, Chiya Savari, and Mostafa Barigou (2022). “Computation of Lagrangian coherent structures from experimental fluid trajectory measurements in a mechanically agitated vessel”. In: *Chemical Engineering Science* 254, p. 117598.

– (2023a). “Predicting complex multicomponent particle–liquid flow in a mechanically agitated vessel via machine learning”. In: *Physics of Fluids* 35.5.

Li, Kun, Chiya Savari, Hamzah A Sheikh, and Mostafa Barigou (2023b). "A data-driven machine learning framework for modeling of turbulent mixing flows". In: *Physics of Fluids* 35.1.

Li, Liangchao, Jiajun Wang, Lianfang Feng, and Xueping Gu (2017). "Computational fluid dynamics simulation of hydrodynamics in an uncovered unbaffled tank agitated by pitched blade turbines". In: *Korean Journal of Chemical Engineering* 34, pp. 2811–2822.

Li, Ming-zhi, Yan-ping He, Ya-dong Liu, and Chao Huang (2018). "Hydrodynamic simulation of multi-sized high concentration slurry transport in pipelines". In: *Ocean Engineering* 163, pp. 691–705.

Li, Zhipeng, Yuyun Bao, and Zhengming Gao (2011). "PIV experiments and large eddy simulations of single-loop flow fields in Rushton turbine stirred tanks". In: *Chemical Engineering Science* 66.6, pp. 1219–1231.

Lian, Xue, Chiya Savari, Kun Li, and Mostafa Barigou (2023). "Coupled smoothed particle hydrodynamics and discrete element method for simulating coarse food particles in a non-Newtonian conveying fluid". In: *Physics of Fluids* 35.4.

Liang, Qiuhua, Xilin Xia, and Jingming Hou (2015). "Efficient urban flood simulation using a GPU-accelerated SPH model". In: *Environmental Earth Sciences* 74, pp. 7285–7294.

Liptak, Bela G (2003). *Instrument Engineers' Handbook, Volume One: Process Measurement and Analysis*. CRC press.

Liu, Chun, Zhixiang Yu, and Shichun Zhao (2021). "A coupled SPH-DEM-FEM model for fluid-particle-structure interaction and a case study of Wenjia gully debris flow impact estimation". In: *Landslides* 18, pp. 2403–2425.

Liu, Kuan-Shuo, Tony Wen-Hann Sheu, Yao-Hsin Hwang, and Khai-Ching Ng (2017). "High-order particle method for solving incompressible Navier–Stokes equations within a mixed Lagrangian–Eulerian framework". In: *Computer Methods in Applied Mechanics and Engineering* 325, pp. 77–101.

Liu, Li and Mostafa Barigou (2013). "Numerical modelling of velocity field and phase distribution in dense monodisperse solid–liquid suspensions under different regimes of agitation: CFD and PEPT experiments". In: *Chemical Engineering Science* 101, pp. 837–850.

– (2014). "Experimentally validated computational fluid dynamics simulations of multicomponent hydrodynamics and phase distribution in agitated high solid fraction binary suspensions". In: *Industrial & Engineering Chemistry Research* 53.2, pp. 895–908.

Liu, MB and GR2593940 Liu (2010). "Smoothed particle hydrodynamics (SPH): an overview and recent developments". In: *Archives of Computational Methods in Engineering* 17, pp. 25–76.

Liu, MB and Gui-Rong Liu (2006). "Restoring particle consistency in smoothed particle hydrodynamics". In: *Applied Numerical Mathematics* 56.1, pp. 19–36.

Liu, Wenwei and Chuan-Yu Wu (2021). "Inertial migration of a non-neutrally buoyant particle in a linear shear flow with thermal convection". In: *Physical Review Fluids* 6.6, p. 064306.

Lixing, ZHOU (2010). "Advances in studies on turbulent dispersed multiphase flows". In: *Chinese Journal of Chemical Engineering* 18.6, pp. 889–898.

Lo, Edmond YM and Songdong Shao (2002). "Simulation of near-shore solitary wave mechanics by an incompressible SPH method". In: *Applied Ocean Research* 24.5, pp. 275–286.

Loh, WW, RC Waterfall, J Cory, and GP Lucas (1999). “Using ERT for multi-phase flow monitoring”. In: *1st World Congress on Industrial Process Tomography, Buxton, Greater Manchester*, pp. 47–53.

Lu, Guang, JR Third, and CR Müller (2015). “Discrete element models for non-spherical particle systems: From theoretical developments to applications”. In: *Chemical Engineering Science* 127, pp. 425–465.

Lucas, GP, J Cory, RC Waterfall, WW Loh, and FJ Dickin (1999). “Measurement of the solids volume fraction and velocity distributions in solids–liquid flows using dual-plane electrical resistance tomography”. In: *Flow Measurement and Instrumentation* 10.4, pp. 249–258.

Lucy, Leon B (1977). “A numerical approach to the testing of the fission hypothesis”. In: *Astronomical Journal* 82, pp. 1013–1024.

Lyu, Hong-Guan and Peng-Nan Sun (2022). “Further enhancement of the particle shifting technique: Towards better volume conservation and particle distribution in SPH simulations of violent free-surface flows”. In: *Applied Mathematical Modelling* 101, pp. 214–238.

Machin, Thomas D, Hsin-Yu Wei, Richard W Greenwood, and Mark JH Simmons (2018). “In-pipe rheology and mixing characterisation using electrical resistance sensing”. In: *Chemical Engineering Science* 187, pp. 327–341.

Mahmud, Tariq, Jennifer N Haque, Kevin J Roberts, Dominic Rhodes, and Derek Wilkinson (2009). “Measurements and modelling of free-surface turbulent flows induced by a magnetic stirrer in an unbaffled stirred tank reactor”. In: *Chemical Engineering Science* 64.20, pp. 4197–4209.

Markauskas, D, H Kruggel-Emden, R Sivanesapillai, and H Steeb (2017). “Comparative study on mesh-based and mesh-less coupled CFD-DEM methods to model particle-laden flow”. In: *Powder Technology* 305, pp. 78–88.

Markauskas, Darius, Harald Kruggel-Emden, and Viktor Scherer (2018). “Numerical analysis of wet plastic particle separation using a coupled DEM-SPH method”. In: *Powder Technology* 325, pp. 218–227.

Marrone, Salvatore, MAGD Antuono, A Colagrossi, G Colicchio, D Le Touzé, and Giorgio Graziani (2011). “δ-SPH model for simulating violent impact flows”. In: *Computer Methods in Applied Mechanics and Engineering* 200.13-16, pp. 1526–1542.

Matas, JP, JF Morris, and Elisabeth Guazzelli (2004). “Lateral forces on a sphere”. In: *Oil & Gas Science and Technology* 59.1, pp. 59–70.

Mazumder, Sandip (2015). *Numerical methods for partial differential equations: finite difference and finite volume methods*. Academic Press.

McKetta, John J (2022). *Encyclopedia of Chemical Processing and Design: Volume 37-Pipeline Flow: Basics to Piping Design*. Routledge.

McLean, Doug (2012). *Understanding aerodynamics: arguing from the real physics*. John Wiley & Sons.

Menter, Florian R, Martin Kuntz, and Robin Langtry (2003). “Ten years of industrial experience with the SST turbulence model”. In: *Turbulence, Heat and Mass Transfer* 4.1, pp. 625–632.

Messa, Gianandrea Vittorio, Michael Malin, and Stefano Malavasi (2014). “Numerical prediction of fully-suspended slurry flow in horizontal pipes”. In: *Powder Technology* 256, pp. 61–70.

Messa, Gianandrea Vittorio and Václav Matoušek (2020). “Analysis and discussion of two fluid modelling of pipe flow of fully suspended slurry”. In: *Powder Technology* 360, pp. 747–768.

Meyers, Robert A (1992). “Encyclopedia of physical sciences and technology”. In: *San Diego: Academic Press*.

Mindlin, Raymond David (Apr. 2021). “Compliance of Elastic Bodies in Contact”. In: *Journal of Applied Mechanics* 16.3, pp. 259–268.

Ming, FR, PN Sun, and AM Zhang (2017). “Numerical investigation of rising bubbles bursting at a free surface through a multiphase SPH model”. In: *Meccanica* 52, pp. 2665–2684.

Molki, Arman, Lyes Khezzar, and Afshin Goharzadeh (2013). “Measurement of fluid velocity development in laminar pipe flow using laser Doppler velocimetry”. In: *European Journal of Physics* 34.5, p. 1127.

Monaghan, JJ (1989). “On the problem of penetration in particle methods”. In: *Journal of Computational Physics* 82.1, pp. 1–15.

Monaghan, Joe J (1992). “Smoothed particle hydrodynamics”. In: *Annual Review of Astronomy and Astrophysics* 30, pp. 543–574.

– (1994). “Simulating free surface flows with SPH”. In: *Journal of Computational Physics* 110.2, pp. 399–406.

– (2005). “Smoothed particle hydrodynamics”. In: *Reports on Progress in Physics* 68.8, p. 1703.

Monaghan, Joe J and Jules B Kajtar (2009). “SPH particle boundary forces for arbitrary boundaries”. In: *Computer Physics Communications* 180.10, pp. 1811–1820.

Monaghan, Joseph J (2012). “Smoothed particle hydrodynamics and its diverse applications”. In: *Annual Review of Fluid Mechanics* 44, pp. 323–346.

Monaghan, Joseph J and Andrew Kos (1999). “Solitary waves on a Cretan beach”. In: *Journal of Waterway, Port, Coastal, and Ocean engineering* 125.3, pp. 145–155.

Monaghan, Joseph J and John C Lattanzio (1985). “A refined particle method for astrophysical problems”. In: *Astronomy and Astrophysics* 149, pp. 135–143.

Moreira, Andreia Borges, Agnès Leroy, Damien Violeau, and Francisco de Almeida Taveira-Pinto (2020). “Overview of large-scale smoothed particle hydrodynamics modeling of dam hydraulics”. In: *Journal of Hydraulic Engineering* 146.2, p. 03119001.

Moukalled, Fadl, Luca Mangani, Marwan Darwish, F Moukalled, L Mangani, and M Darwish (2016). *The Finite Volume Method*. Springer.

Mühlich, Pascal, William Case, Josef Hörmansperger, Michael Beyrer, and Erich J Windhab (2016). “Particle image velocimetry (PIV) in food powders during vacuum-steam-vacuum (VSV) treatment”. In: *Powder Technology* 299, pp. 1–8.

Munjiza, Antonio A (2004). *The combined finite-discrete element method*. John Wiley & Sons.

Munson, Bruce R, DF Young, and TH Okiishi (2016). “Fluid Mechanics”. In: *Bernoulli Eqn*, pp. 139–155.

Musgrove, AR de L and JD Hooper (1993). “Pressure probe measurement of the turbulent stress distribution in a swirling jet”. In: *Experimental Heat Transfer, Fluid Mechanics and Thermodynamics 1993*. Elsevier, pp. 172–179.

Nadeem, Humair and Theodore J Heindel (2018). “Review of noninvasive methods to characterize granular mixing”. In: *Powder Technology* 332, pp. 331–350.

Natsui, Shungo, Akinori Sawada, Koki Terui, Yusuke Kashihara, Tatsuya Kikuchi, and Ryosuke O Suzuki (2018). “DEM-SPH study of molten slag trickle flow in coke bed”. In: *Chemical Engineering Science* 175, pp. 25–39.

Ng, KC, A Alexiadis, Hailong Chen, and TWH Sheu (2021). “Numerical computation of fluid–solid mixture flow using the SPH–VCPM–DEM method”. In: *Journal of Fluids and Structures* 106, p. 103369.

Nguyen, Nhu HT, Thanh Trung Nguyen, and Quoc T Phan (2022). “Dynamics and runout distance of saturated particle-fluid mixture flow on a horizontal plane: A coupled VOF-DEM study”. In: *Powder Technology* 408, p. 117759.

Nikolić, Dragan D and Patrick J Frawley (2016). “Application of the Lagrangian meshfree approach to modelling of batch crystallisation: Part I—Modelling of stirred tank hydrodynamics”. In: *Chemical Engineering Science* 145, pp. 317–328.

Nouri, JM, D Guerrato, N Stosic, and Y Yan (2005). “Application of LDV and PIV techniques for flow measurements in the suction port of a screw compressor”. In: *IOP Conference Series: Materials Science and Engineering*. Vol. 1180. IOP Publishing, p. 012034.

Pan, Tsorng-Whay and Roland Glowinski (2005). “Direct simulation of the motion of neutrally buoyant balls in a three-dimensional Poiseuille flow”. In: *Comptes Rendus Mécanique* 333.12, pp. 884–895.

Parker, DJ (2017). “Positron emission particle tracking and its application to granular media”. In: *Review of Scientific Instruments* 88.5.

Patel, Dineshkumar, Farhad Ein-Mozaffari, and Mehrab Mehrvar (2015). “Effect of rheological parameters on non-ideal flows in the continuous-flow mixing of biopolymer solutions”. In: *Chemical Engineering Research and Design* 100, pp. 126–134.

Paul, Edward L, Victor A Atiemo-Obeng, and Suzanne M Kresta (2004). *Handbook of Industrial Mixing*. Wiley Online Library.

Pazouki, Arman and Dan Negrut (2015). “A numerical study of the effect of particle properties on the radial distribution of suspensions in pipe flow”. In: *Computers & Fluids* 108, pp. 1–12.

Pellico, Juan, Laurence Vass, Amaia Carrascal-Miniño, Francis Man, Jana Kim, Kavitha Sunassee, David Parker, Philip J Blower, Paul K Marsden, and Rafael TM de Rosales (2024). “In vivo real-time positron emission particle tracking (PEPT) and single particle PET”. In: *Nature Nanotechnology* 19.5, pp. 668–676.

Pianko-Oprych, P, AW Nienow, and Mostafa Barigou (2009). “Positron emission particle tracking (PEPT) compared to particle image velocimetry (PIV) for studying the flow generated by a pitched-blade turbine in single phase and multi-phase systems”. In: *Chemical Engineering Science* 64.23, pp. 4955–4968.

Pinho, FT and JH Whitelaw (1990). “Flow of non-Newtonian fluids in a pipe”. In: *Journal of Non-newtonian Fluid Mechanics* 34.2, pp. 129–144.

Pozorski, Jacek and Michał Olejnik (2023). “Smoothed particle hydrodynamics modelling of multiphase flows: an overview”. In: *Acta Mechanica*, pp. 1–30.

Puri, Anish N, Chin Y Kuo, and Raymond S Chapman (1983). “Turbulent diffusion of mass in circular pipe flow”. In: *Applied Mathematical Modelling* 7.2, pp. 135–138.

Raji, AO and JF Favier (2004). “Model for the deformation in agricultural and food particulate materials under bulk compressive loading using discrete element method. I: Theory, model development and validation”. In: *Journal of Food Engineering* 64.3, pp. 359–371.

Rasteiro, MG, MM Figueiredo, and H Franco (1993). “Pressure drop for solid/liquid flow in pipes”. In: *Particulate Science and Technology* 11.3-4, pp. 147–155.

Razzak, SA, JX Zhu, and S Barghi (2010). “Effects of Particle Shape, Density, and Size on a Distribution of Phase Holdups in a Gas−Liquid−Solid Circulating Fluidized Bed Riser”. In: *Industrial & Engineering Chemistry Research* 49.15, pp. 6998–7007.

Reddy, Junuthula Narasimha (2005). *An introduction to the finite element method*. Vol. 3. McGraw-Hill New York.

Reynolds, Osborne (1883). “XXIX. An experimental investigation of the circumstances which determine whether the motion of water shall be direct or sinuous, and of the law of resistance in parallel channels”. In: *Philosophical Transactions of the Royal Society of London* 174, pp. 935–982.

Riis, Tenna, Jennifer L Tank, Alexander J Reisinger, Antoine Aubenau, Kevin R Roche, Peter S Levi, Annette Baattrup-Pedersen, Anette B Alnoee, and Diogo Bolster (2020). “Riverine macrophytes control seasonal nutrient uptake via both physical and biological pathways”. In: *Freshwater Biology* 65.2, pp. 178–192.

Robinson, Martin, Marco Ramaioli, and Stefan Luding (2014). “Fluid–particle flow simulations using two-way-coupled mesoscale SPH–DEM and validation”. In: *International journal of Multiphase Flow* 59, pp. 121–134.

Robinson, Martin Jeremy (2009). “Turbulence and viscous mixing using smoothed particle hydrodynamics”. Thesis.

Romano, MG, F Alberini, L Liu, MJH Simmons, and EH Stitt (2023). “Comparison between RANS and 3D-PTV measurements of Newtonian and non-Newtonian fluid flows in a stirred vessel in the transitional regime”. In: *Chemical Engineering Science* 267, p. 118294.

Ruiz-Viera, MJ, MA Delgado, JM Franco, MC Sánchez, and C Gallegos (2006). “On the drag reduction for the two-phase horizontal pipe flow of highly viscous non-Newtonian liquid/air mixtures: Case of lubricating grease”. In: *International Journal of Multiphase Flow* 32.2, pp. 232–247.

Saeed, Salwan, Farhad Ein-Mozaffari, and Simant R Upreti (2007). “Using computational fluid dynamics modeling and ultrasonic doppler velocimetry to study pulp suspension mixing”. In: *Industrial & Engineering Chemistry Research* 46.7, pp. 2172–2179.

Safa, Raziyeh, Ataallah Soltani Goharrizi, Saeed Jafari, and Ebrahim Jahanshahi Javaran (2019). “On the evaluation of heat and mass transfer effects on the migration behavior of neutrally buoyant particles in a Couette flow”. In: *International Journal of Heat and Mass Transfer* 144, p. 118659.

Sasson, Marcus, Shuhong Chai, Genevieve Beck, Yuting Jin, and Jalal Rafieshahraki (2016). “A comparison between Smoothed-Particle Hydrodynamics and RANS Volume of Fluid method in modelling slamming”. In: *Journal of Ocean Engineering and Science* 1.2, pp. 119–128.

Savari, Chiya, Kun Li, and Mostafa Barigou (2022). “Multiscale wavelet analysis of 3D Lagrangian trajectories in a mechanically agitated vessel”. In: *Chemical Engineering Science* 260, p. 117844.

Savari, Chiya, Hamzah A Sheikh, and Mostafa Barigou (2021). "Lagrangian Recurrence Tracking: A Novel Approach for Description of Mixing in Liquid and Particle–Liquid Flows". In: *Industrial & Engineering Chemistry Research* 60.50, pp. 18501–18512.

Sefid, Mohammad, Rouhollah Fatehi, and Rahim Shamsoddini (2015). "A modified smoothed particle hydrodynamics scheme to model the stationary and moving boundary problems for Newtonian fluid flows". In: *Journal of Fluids Engineering* 137.3, p. 031201.

Segre, G and A Silberberg (1961). "Radial particle displacements in Poiseuille flow of suspensions". In: *Nature* 189.4760, pp. 209–210.

Seifert, Jost (2012). "A review of the Magnus effect in aeronautics". In: *Progress in Aerospace Sciences* 55, pp. 17–45.

Shadloo, M Safdari, G Oger, and David Le Touzé (2016). "Smoothed particle hydrodynamics method for fluid flows, towards industrial applications: Motivations, current state, and challenges". In: *Computers & Fluids* 136, pp. 11–34.

Shao, Xueming, Zhaosheng Yu, and Bo Sun (2008). "Inertial migration of spherical particles in circular Poiseuille flow at moderately high Reynolds numbers". In: *Physics of Fluids* 20.10.

Sharaf, Omar Z., Ashraf N. Al-Khateeb, Dimitrios C. Kyritsis, and Eiyad Abu-Nada (2019). "Numerical investigation of nanofluid particle migration and convective heat transfer in microchannels using an Eulerian–Lagrangian approach". In: *Journal of Fluid Mechanics* 878, pp. 62–97.

Sharifi, Mohadeseh and Brent Young (2012). "Milk total solids and fat content soft sensing via electrical resistance tomography and temperature measurement". In: *Food and Bioproducts Processing* 90.4, pp. 659–666.

Shepherd, Ian C (1981). “A four hole pressure probe for fluid flow measurements in three dimensions”. In: *Journal of Fluids Engineering* 103, pp. 590–594.

Shi, Pengyu and Roland Rzehak (2018). “Bubbly flow in stirred tanks: Euler-Euler/RANS modeling”. In: *Chemical Engineering Science* 190, pp. 419–435.

– (2020). “Solid-liquid flow in stirred tanks: Euler-Euler/RANS modeling”. In: *Chemical Engineering Science* 227, p. 115875.

Silva, Rui C (2022). “Experimental characterization techniques for solid-liquid slurry flows in pipelines: A review”. In: *Processes* 10.3, p. 597.

Sizkow, Saman Farzi and Usama El Shamy (2021). “SPH-DEM simulations of saturated granular soils liquefaction incorporating particles of irregular shape”. In: *Computers and Geotechnics* 134, p. 104060.

Soleymani, A, E Kolehmainen, and I Turunen (2008). “Numerical and experimental investigations of liquid mixing in T-type micromixers”. In: *Chemical Engineering Journal* 135, S219–S228.

Solomon, J, TP Elson, AW Nienow, and GW Pace (1981). “Cavern sizes in agitated fluids with a yield stress”. In: *Chemical Engineering Communications* 11.1-3, pp. 143–164.

Sozzi, D Angelo and Fariborz Taghipour (2005). “Experimental investigation of flow field in annular ultraviolet reactors using particle image velocimetry (PIV)”. In: *Industrial & Engineering Chemistry Research* 44.26, pp. 9979–9988.

Stebel, Michal, Jacek Smolka, Michal Palacz, Wojciech Adamczyk, and Edyta Piechnik (2020). “Numerical investigation of the fluid flow distribution for the hydrofluidisation food freezing method”. In: *International Journal of Thermal Sciences* 151, p. 106284.

Stevenson, Ryan, Susan TL Harrison, Michael D Mantle, Andrew J Sederman, Tracey L Moraczewski, and Michael L Johns (2010). "Analysis of partial suspension in stirred mixing cells using both MRI and ERT". In: *Chemical Engineering Science* 65.4, pp. 1385–1393.

Sun, Xiaosong and Mikio Sakai (2015). "Three-dimensional simulation of gas–solid–liquid flows using the DEM–VOF method". In: *Chemical Engineering Science* 134, pp. 531–548.

Surana, KS, S Allu, PW Tenpas, and JN Reddy (2007). "k-version of finite element method in gas dynamics: Higher-order global differentiability numerical solutions". In: *International Journal for Numerical Methods in Engineering* 69.6, pp. 1109–1157.

Suzuki, Yuji, Motofumi Ikenoya, and Nobuhide Kasagi (2000). "Simultaneous measurement of fluid and dispersed phases in a particle-laden turbulent channel flow with the aid of 3-D PTV". In: *Experiments in Fluids* 29.Suppl 1, S185–S193.

Szymkiewicz, Romuald and Marek Mitosek (2005). "Analysis of unsteady pipe flow using the modified finite element method". In: *Communications in Numerical Methods in Engineering* 21.4, pp. 183–199.

Tachibana, MJRA (1973). "On the behaviour of a sphere in the laminar tube flows". In: *Rheologica Acta* 12, pp. 58–69.

Tafuni, Angelantonio, JM Domínguez, R Vacondio, and AJC Crespo (2018). "A versatile algorithm for the treatment of open boundary conditions in Smoothed particle hydrodynamics GPU models". In: *Computer Methods in Applied Mechanics and Engineering* 342, pp. 604–624.

Takei, Masahiro, Mitsuaki Ochi, and Yoshifuru Saito (2004). "Image extraction of particle concentration at the plug front using 3D wavelets and comparison with LDV". In: *Powder Technology* 142.1, pp. 70–78.

Talebizadehsardari, Pouyan, Hassan Rahimzadeh, Goodarz Ahmadi, Kiao Inthavong, Mohammad Mehdi Keshtkar, and MA Moghimi (2020). “Nano-particle deposition in laminar annular pipe flows”. In: *Advanced Powder Technology* 31.8, pp. 3134–3143.

Tehrani, MA (1996). “An experimental study of particle migration in pipe flow of viscoelastic fluids”. In: *Journal of Rheology* 40.6, pp. 1057–1077.

Thakur, Subhash C, Jin Y Ooi, and Hossein Ahmadian (2016). “Scaling of discrete element model parameters for cohesionless and cohesive solid”. In: *Powder Technology* 293, pp. 130–137.

Thorn, Richard, Geir A Johansen, and Bjørn T Hjertaker (2012). “Three-phase flow measurement in the petroleum industry”. In: *Measurement Science and Technology* 24.1, p. 012003.

Tian, Shuai and Mostafa Barigou (2016). “Assessing the potential of using chaotic advection flow for thermal food processing in heating tubes”. In: *Journal of Food Engineering* 177, pp. 9–20.

Tijsseling, AS (1996). “Fluid-structure interaction in liquid-filled pipe systems: a review”. In: *Journal of Fluids and Structures* 10.2, pp. 109–146.

Tran-Duc, Thien, Michael H Meylan, and Ngamta Thamwattana (2022). “Dynamical response of a floating plate to water waves using a smoothed particle hydrodynamics algorithm for nonlinear elasticity”. In: *Physics of Fluids* 34.5.

Treinen, J and Justin Jacobs (2015). “The applicability of the Eulerian-Eulerian CFD approach using granular kinetic theory to predict particle settling and migration in viscoplastic fluids”. In: *Proceedings of the 17th International Conference on Transport and Sedimentation of Solid Particles*. Wroclaw University of Environmental and Life Sciences, Wroclaw, Poland, pp. 345–354.

Tsuji, Yutaka, Takao Oshima, and Yoshinobu Morikawa (1985). “Numerical simulation of pneumatic conveying in a horizontal pipe”. In: *KONA Powder and Particle Journal* 3, pp. 38–51.

Uzi, Avi and Avi Levy (2018). “Flow characteristics of coarse particles in horizontal hydraulic conveying”. In: *Powder Technology* 326, pp. 302–321.

Vacondio, Renato, Benedict D Rogers, Peter K Stansby, Paolo Mignosa, and Jon Feldman (2013). “Variable resolution for SPH: a dynamic particle coalescing and splitting scheme”. In: *Computer Methods in Applied Mechanics and Engineering* 256, pp. 132–148.

Verlet, Loup (1967). “Computer" experiments" on classical fluids. I. Thermodynamical properties of Lennard-Jones molecules”. In: *Physical Review* 159.1, p. 98.

Wang, Haigang and Wuqiang Yang (2020). “Application of electrical capacitance tomography in circulating fluidised beds–A review”. In: *Applied Thermal Engineering* 176, p. 115311.

Wang, Haixia and Ting Xue (2023). “Flow parameter measurement of intermittent flow by PIV interface imaging characteristics”. In: *IEEE Sensors Journal* 23.21, pp. 26226–26234.

Wang, Haoliang, Xiangyang Li, Zai-Sha Mao, and Chao Yang (2019). “New invasive image velocimetry applicable to dense multiphase flows and its application in solid–liquid suspensions”. In: *AIChE Journal* 65.9, e16668.

Wang, Peng, Thomas Reviol, Stefan Kluck, Pascal Würtz, and Martin Böhle (2018). “Mixing of non-Newtonian fluids in a cylindrical stirred vessel equipped with a novel side-entry propeller”. In: *Chemical Engineering Science* 190, pp. 384–395.

Wang, Wei, Guangqi Chen, Zheng Han, Suhua Zhou, Hong Zhang, and Peideng Jing (2016). “3D numerical simulation of debris-flow motion using SPH method incorporating non-Newtonian fluid behavior”. In: *Natural Hazards* 81, pp. 1981–1998.

Wangxu, Li, Li Zhenggui, Deng Wanquan, Ji Lei, Qiu Yilong, and Chen Huiyu (2021). "Particle image velocimetry flowmeter for natural gas applications". In: *Flow Measurement and Instrumentation* 82, p. 102072.

Washino, K, HS Tan, MJ Hounslow, and AD Salman (2013). "A new capillary force model implemented in micro-scale CFD–DEM coupling for wet granulation". In: *Chemical Engineering Science* 93, pp. 197–205.

Wei, Xing, Chengliang Rao, Shenshen Chen, and Wenjun Luo (2023). "Numerical simulation of anti-plane wave propagation in heterogeneous media". In: *Applied Mathematics Letters* 135, p. 108436.

Wen, Binghai, Hui Chen, Zhangrong Qin, Bing He, and Chaoying Zhang (2019). "Lateral migration and nonuniform rotation of suspended ellipse in Poiseuille flow". In: *Computers & Mathematics with Applications* 78.4, pp. 1142–1153.

Wendt, John F (2008). *Computational fluid dynamics: an introduction*. Springer Science & Business Media.

Wichterle, K and O Wein (1975). "Agitation of concentrated suspensions". In: *CHISA '75, Paper B* 4.

Winkler, Daniel, Michael Meister, Massoud Rezavand, and Wolfgang Rauch (2017). "gpuSPHASE—A shared memory caching implementation for 2D SPH using CUDA". In: *Computer Physics Communications* 213, pp. 165–180.

Woo, MW, WRW Daud, AS Mujumdar, SM Tasirin, and MZM Talib (2010). "Role of rheological characteristics in amorphous food particle-wall collisions in spray drying". In: *Powder Technology* 198.2, pp. 251–257.

Wren, Jon R and Ronaldo I Borja (1997). "Micromechanics of granular media Part II: Overall tangential moduli and localization model for periodic assemblies of circular disks". In: *Computer Methods in Applied Mechanics and Engineering* 141.3-4, pp. 221–246.

Wright, Stuart F, Ivan Zadrazil, and Christos N Markides (2017). "A review of solid–fluid selection options for optical-based measurements in single-phase liquid, two-phase liquid–liquid and multiphase solid–liquid flows". In: *Experiments in Fluids* 58, pp. 1–39.

Wu, Ke, Dongmin Yang, Nigel Wright, and Amirul Khan (2018). "An integrated particle model for fluid–particle–structure interaction problems with free-surface flow and structural failure". In: *Journal of Fluids and Structures* 76, pp. 166–184.

Wu, Liang, Ming Gong, and Jingtao Wang (2018). "Development of a DEM–VOF model for the turbulent free-surface flows with particles and its application to stirred mixing system". In: *Industrial & Engineering Chemistry Research* 57.5, pp. 1714–1725.

Xiong, Qingang, Bo Li, and Ji Xu (2013). "GPU-accelerated adaptive particle splitting and merging in SPH". In: *Computer Physics Communications* 184.7, pp. 1701–1707.

Xu, Jianzhong, Takao Maeda, Yasunari Kamada, Shogo Nishimura, Guangxing Wu, Chang Cai, et al. (2019). "Laser Doppler Velocimetry (LDV) measurements of airfoil surface flow on a Horizontal Axis Wind Turbine in boundary layer". In: *Energy* 183, pp. 341–357.

Xu, Rui, Peter Stansby, and Dominique Laurence (2009). "Accuracy and stability in incompressible SPH (ISPH) based on the projection method and a new approach". In: *Journal of Computational Physics* 228.18, pp. 6703–6725.

Xu, Ke-Wei, Yongchao Zhang, Dong Liu, Amirah Nabilah Azman, and Hyoung-Bum Kim (2020). "Slug flow development study in a horizontal pipe using particle image velocimetry". In: *International Journal of Heat and Mass Transfer* 162, p. 120267.

Xu, Yuqiang, Zhichuan Guan, Yan Jin, Yang Tian, Yongwang Liu, Chuanbin Xu, and Yucai Shi (2017). "Study of the ultrasonic propagation law in the gas–liquid two-phase flow of deepwater riser through numerical simulation". In: *Journal of Petroleum Science and Engineering* 159, pp. 419–432.

Xu, Zhisong, Zhuguo Li, and Fei Jiang (2021). "The applicability of SPH and MPS methods to numerical flow simulation of fresh cementitious materials". In: *Construction and Building Materials* 274, p. 121736.

– (2022). "Numerical approach to pipe flow of fresh concrete based on MPS method". In: *Cement and Concrete Research* 152, p. 106679.

Yan, Yihuan, Krishna Mohanarangam, William Yang, and Jiyuan Tu (2024). "Experimental measuring techniques for industrial-scale multiphase flow problems". In: *Experimental and Computational Multiphase Flow* 6.1, pp. 1–13.

Yang, Bobby H, Jing Wang, Daniel D Joseph, Howard H Hu, T-W Pan, and Roland Glowinski (2005). "Migration of a sphere in tube flow". In: *Journal of Fluid mechanics* 540, pp. 109–131.

Yang, Zhuangjian, Xue Lian, Chiya Savari, and Mostafa Barigou (2024). "Evaluating the effectiveness of CFD-DEM and SPH-DEM for complex pipe flow simulations with and without particles". In: *Chemical Engineering Science* 288, p. 119788.

Yang, Zhuangjian, Chiya Savari, and Mostafa Barigou (2022). “Numerical and Experimental Investigations of Horizontal Turbulent Particle–Liquid Pipe Flow”. In: *Industrial & Engineering Chemistry Research* 61.32, pp. 12040–12051.

Ye, Ting, Dingyi Pan, Can Huang, and Moubin Liu (2019). “Smoothed particle hydrodynamics (SPH) for complex fluid flows: Recent developments in methodology and applications”. In: *Physics of Fluids* 31.1.

Yeh, Y and HZ Cummins (1964). “Localized fluid flow measurements with an He-Ne laser spectrometer”. In: *Applied Physics Letters* 4.10, pp. 176–178.

Yeoh, Guan Heng and Jiyuan Tu (2019). *Computational techniques for multiphase flows*. Butterworth-Heinemann.

Yu, Zhaosheng, Nhan Phan-Thien, and Roger I Tanner (2004). “Dynamic simulation of sphere motion in a vertical tube”. In: *Journal of Fluid Mechanics* 518, pp. 61–93.

Zade, Sagar, Pedro Costa, Walter Fornari, Fredrik Lundell, and Luca Brandt (2018). “Experimental investigation of turbulent suspensions of spherical particles in a square duct”. In: *Journal of Fluid Mechanics* 857, pp. 748–783.

Zawawi, Mohd Hafiz, A Saleha, A Salwa, NH Hassan, Nazirul Mubin Zahari, Mohd Zakwan Ramli, and Zakaria Che Muda (2018). “A review: Fundamentals of computational fluid dynamics (CFD)”. In: *AIP conference proceedings*. Vol. 2030. AIP Publishing.

Zbib, Hussein, Mohammadreza Ebrahimi, Farhad Ein-Mozaffari, and Ali Lohi (2018). “Comprehensive analysis of fluid-particle and particle-particle interactions in a liquid-solid fluidized bed via CFD-DEM coupling and tomography”. In: *Powder Technology* 340, pp. 116–130.

Zhang, Wenbiao, Chao Wang, Wuqiang Yang, and Chi-Hwa Wang (2014). "Application of electrical capacitance tomography in particulate process measurement–A review". In: *Advanced Powder Technology* 25.1, pp. 174–188.

Zhang, Xinyu and Goodarz Ahmadi (2005). "Eulerian–Lagrangian simulations of liquid–gas–solid flows in three-phase slurry reactors". In: *Chemical Engineering Science* 60.18, pp. 5089–5104.

Zhang, Ya, Yonghao Zhang, Guang Pan, and Sina Haeri (2018). "Numerical study of the particle sedimentation in a viscous fluid using a coupled DEM-IB-CLBM approach". In: *Journal of Computational Physics* 368, pp. 1–20.

Zheng, Enzu, Murray Rudman, Shibo Kuang, and Andrew Chryss (2021). "Turbulent coarse-particle non-Newtonian suspension flow in a pipe". In: *International Journal of Multiphase Flow* 142, p. 103698.

Zhou, Ling, Huan Wang, Deyou Liu, Jiajie Ma, Pei Wang, and Lin Xia (2017). "A second-order finite volume method for pipe flow with water column separation". In: *Journal of Hydro-environment Research* 17, pp. 47–55.

Zhu, H.P., Z.Y. Zhou, R.Y. Yang, and A.B. Yu (2007). "Discrete particle simulation of particulate systems: theoretical developments". In: *Chemical Engineering Science* 62.13, pp. 3378–3396.

Zlokarnik, Marko (2008). *Stirring: Theory and practice*. John Wiley & Sons.